

Functional Porous Polymers as a Material Platform for Heterogeneous Metalla-(Photo)catalysis

vorgelegt von

M. Sc.

Michael Traxler

an der Fakultät II – Mathematik und Naturwissenschaften
der Technischen Universität Berlin
zur Erlangung des akademischen Grades

Doktor der Naturwissenschaften

- Dr. rer. nat. -

genehmigte Dissertation

Promotionsausschuss:

Vorsitzende: Prof. Dr. Maria Andrea Mroginski

Gutachter: Prof. Dr. Arne Thomas

Gutachter: Dr. Jérôme Canivet

Tag der wissenschaftlichen Aussprache: 25. November 2022

Berlin 2022

Acknowledgements

I would like to thank everyone, who has helped me in the one or another way along the path towards this thesis. I am extremely grateful to each and every one of you.

My special thanks I owe Prof. Dr. Arne Thomas for giving me the opportunity to work in his group at the TU Berlin. You gave me the confidence and academic freedom, that pushed me to master these challenging projects and always supported and encouraged me to share the results with the community.

Additionally, I am thankful to Dr. Jérôme Canivet for kindly agreeing to review this thesis and to Prof. Dr. Maria Andrea Mroginski for being the chair of my viva voce.

Many thanks go to the EC²/BIG-NSE not only for the support of my thesis with a scholarship, but for welcoming me in Berlin within this unique international and interdisciplinary group. Special thanks to JP Lonjaret, who had followed my progress and supported me from day one. It was an honor being the student representative of such an amazing graduate school.

My thanks go to all the current and former group members of the AK Funktionsmaterialien. Thank you all for the fantastic time and creating such a great working environment, where neither a pandemic nor an IT hack could break our spirit. I am especially grateful for having had the chance to work with Pradip and Michaela. Without both of your support and ideas this thesis would have not been possible. Moreover, I would like to thank the “Solid state NMR-Gang” Julia, Sarah and Vincent, not only for the great (late-night) work, but also for the fun evenings in the social room. Quoting Vincent: “We would make a great start-up team.” Also, I want to give a shout-out to Anne Svilarov, Christina Eichenauer and Maria Unterweger for the excellent technical and organizational support.

Greatest thanks go out to all the collaborators from various institutions that made this work possible. Here I want to highlight the fruitful work with the group of Bart Pieber. Thank you for trusting into my materials!

Ein riesiger Dank gilt auch Nicole und Seba für die zahlreichen gemeinsamen Abende zu viert. Ihr habt Potsdam auch unter schwierigen Umständen so richtig zur Heimat gemacht! Ich möchte ich auch bei meinen Freunden in Graz und Freistadt bedanken. Judith & Patrik, Brockmann WG und Wolfsrudel – ich bin Euch für eure bis heute andauernde Freundschaft dankbar!

Mein ganz großer Dank gilt natürlich Dir Susi. Du hast mir immer wieder gezeigt, dass ich nur an mich glauben muss, dann kann ich alles erreichen. Ich bin für jeden Tag dankbar den ich mit dir an meiner Seite verbringen darf und freue mich schon unglaublich drauf und bin gespannt, was unsere gemeinsame Reise noch für uns bereithält.

Der größte Dank gebührt meiner Familie! Johannes, du warst immer mein Vorbild und ohne dich als großen Bruder wäre ich nicht hier an diesem Punkt. Aber insbesondere gilt mein Dank meinen Eltern, die mich bei all meinen Entscheidungen bedingungslos unterstützen. Ich kann mich immer auf Eure Liebe verlassen, egal wo ich auch gerade bin.

Ich widme diese Doktorarbeit Euch, Mama und Papa!

I. Abstract

Throughout the last two decades, porous polymeric materials have undergone a remarkable development. Besides the synthesis of novel materials also huge improvements in the application of these materials were made. In addition to the already industrially applied fields of gas separation and sensing, porous polymeric materials have been demonstrated to be applicable in gas storage, drug delivery and in the field of catalysis. Side to side with crystalline framework materials such as covalent organic frameworks (COFs) and metal-organic frameworks (MOFs), improvements in amorphous microporous polymer networks (MPNs) have been made, where each class of materials presents unique properties. COFs for instance show a broad absorption in the visible light spectrum as well as long-range order. This makes them highly suitable as candidates for cooperative photocatalysis where structure-activity relationships play a crucial role. In comparison to that, MPNs offer the possibility to introduce functionalities within a purely hydrocarbon-based skeleton. Due to this remarkable stability, MPNs can be used for a broad scope of reactions without destruction of the scaffold or inducing side reactions.

MPNs have been investigated for more than a decade, however, various fields of application are still not explored in depth. For instance, MPNs are proposed to be promising candidates to function as solid supports for heterogenized homogeneous catalysis. Within this project the immobilization of an iridium pincer complex via the ligand sphere onto a propyl bromide functionalized microporous polymer network was demonstrated by a series of three post-synthetic modification steps. Based on the supporting MPN, single catalytically active sites have been embedded into a chemically robust environment. Throughout the modification steps the material maintained permanent porosity and various analysis techniques confirmed the successful formation of the catalyst material. Testing the modified MPN for continuous-flow dehydrogenation revealed a stable formation of the desired product for more than 6 days without a loss in activity. Moreover, the hydrophobic environment of the MPN protected the catalyst against hydrolysis from co-fed water. These results were published in an article entitled *Anchoring an Iridium Pincer Complex in a Hydrophobic Microporous Polymer for Application in Continuous-Flow Alkane Dehydrogenation* published in the journal *ChemCatChem*.

With the myriad of building blocks available for the synthesis of COFs a broad spectrum of

functionalities has been investigated for various applications. With the long-range π -conjugation, COFs are ideal candidates for visible light driven heterogeneous photocatalysis. In this respect most of these porous and crystalline polymers have been mainly investigated for water splitting or CO₂ reduction, with very few examples targeting organic transformation. In this regard, the application of COFs for C–N cross-coupling reactions was investigated by the development of acridine based COFs that absorb throughout the visible light spectrum. Among the series of framework materials, the fully β -ketoenamine linked material showed the highest activity due to increased charge carrier separation upon irradiation. This framework showed good recyclability and was able to drive the organic transformation under low energy green light as energy source. The results of this work on *Acridine-Functionalized Covalent Organic Frameworks (COFs) as Photocatalysts for Metallaphotocatalytic C–N Cross-Coupling* have been published in *Angewandte Chemie International Edition*. The publication has been acknowledged as *Hot Paper*.

Using the multivariate approach, the incorporation of several functional moieties into the backbone of COFs can be realized. By the combination of functional linkers into the defined backbone structure of the framework material, the synthesis of a fully heterogeneous cooperative metallaphotocatalytic system for carbon–heteroatom cross-couplings was targeted. Therefore, the metallaphotocatalytic system was constructed from an acridine linker that enables absorption throughout the visible light range and a bipyridine unit for the complexation of the nickel catalyst. Both linkers are connected via a set of different trialdehyde nodes that show different amounts of additional hydroxy groups enabling keto/enol tautomerization. Investigations for C–N and C–S cross-couplings showed inverse trends in activity with respect to the number of additional hydroxy groups within the framework. Based on the node, the system can be changed between persistent localized charge-separated species suitable for semi-heterogeneous C–N bond formation and high charge carrier mobility within the framework for efficient fully heterogeneous C–S cross-coupling. For the latter, the fully heterogeneous nature was demonstrated by the recycling of the material over several cycles without any loss in activity. Moreover, the material showed activity throughout the visible light range, catalyzing the organic transformation even using low energetic red light irradiation. The results of this work have been published under the title *Programmable Photocatalytic Activity of Multivariate Covalent Organic Frameworks Used as Metallaphotocatalysts* in *Chemistry – A European Journal*.

II. Kurzzusammenfassung

Im Laufe der letzten zwanzig Jahre hat sich das Feld der porösen Polymere transformiert. Neben der Synthese neuartiger Materialklassen wurden auch neue Meilensteine in der Erforschung von Anwendungsgebieten dieser Materialien erreicht. Neben der industriellen Verwendung als Membranmaterial oder Sensoren wurden Beispiele in den Bereichen der Gasspeicherung, der Verabreichung von Medikamenten und der Katalyse gezeigt. Parallel zu den Fortschritten in kristallinen Gerüstmaterialien, wie kovalent-organischen Gerüststrukturen (COFs) und metall-organischen Gerüststrukturen (MOFs), entwickelte sich auch das Feld von amorphen, mikroporösen Netzwerken (MPNs), wobei jede dieser Materialklassen einzigartige Eigenschaften besitzt. COFs zeichnen sich durch die breite Absorption im Bereich des sichtbaren Lichts aus. Des Weiteren eignen sich diese Gerüststrukturen auf Grund der internen Ordnung auch zur Untersuchung der Struktur-Aktivität-Beziehung. Im Vergleich dazu kann man in MPNs selektiv Funktionalitäten in eine inerte Kohlenwasserstoffumgebung einbetten. Dies führt dazu, dass mit diesen porösen Netzwerken Reaktionen unter Bedingungen möglich sind, die andere Materialien zerstören. Obwohl MPNs seit über einem Jahrzehnt erforscht wurden, sind einige Anwendungsbereiche dieser Materialklasse noch immer wenig untersucht. Unter anderem bieten sich MPNs als vielversprechende Trägermaterialien für homogene Katalysatoren an. In diesem Feld wurde die Immobilisierung eines Iridium Pincer Komplexes über das Ligandengerüst an ein MPN gezeigt, welches mit einer Propylbromid-Gruppe funktionalisiert wurde. Durch diese post-synthetische Modifikation wurden einzelne katalytisch aktive Zentren in die chemisch inerte Umgebung des MPN Trägermaterials eingebettet. Der Festphasenkatalysator blieb hierbei permanent porös und die erfolgreiche Verankerung des molekularen katalytischen Zentrums wurde mit verschiedenen Analysentechniken nachgewiesen. Dieses modifizierte MPN wurde anschließend für die Dehydrierung von Cyclohexan verwendet, wo das Katalysatormaterial eine stabile Aktivität über einen Zeitraum von 6 Tagen zeigte. Darüber hinaus konnte Wasser dem Reaktionsgasgemisch zugesetzt werden, da das hydrophobe MPN das aktive Zentrum davor schützt. Die Ergebnisse wurden in der Fachzeitschrift *ChemCatChem* unter dem Titel *Anchoring an Iridium Pincer Complex in a Hydrophobic Microporous Polymer for Application in Continuous-Flow Alkane Dehydrogenation* veröffentlicht.

Auf Grund der schier unendlichen Anzahl an verfügbaren Bausteinen für die Synthese von COFs wurden bereits eine Vielzahl an Funktionalitäten für verschiedenste Anwendungsbereiche untersucht. Durch die ausgedehnte π -Konjugation sind COFs ausgezeichnete Kandidaten für heterogene Photokatalyse. Bisher wurden diese Materialien hauptsächlich für photokatalytische Wasserspaltung oder CO₂ Reduktion verwendet und nur wenige Berichte waren bekannt, die organische Transformationen zur Anwendung hatten. In Rahmen dieser Arbeit wurde ein auf Acridin basierender COF synthetisiert, welcher durch die Absorption im sichtbaren Licht für C–N Kreuzkupplungen verwendet werden konnte. Aus der Serie an hergestellten Materialien war der β -ketoenamin COF der aktivste Photokatalysator auf Grund von hoher Ladungsträgertrennung unter Bestrahlung mit Licht. Die Gerüststruktur bestach auch durch gute Wiederverwendbarkeit und konnte die Reaktion auch mit energiearmen grünem Licht vorantreiben. Die Ergebnisse über *Acridine-Functionalized Covalent Organic Frameworks (COFs) as Photocatalysts for Metallaphotocatalytic C–N Cross-Coupling* wurden in *Angewandte Chemie International Edition* veröffentlicht, welche den Artikel als *Hot Article* hervorgehoben haben.

Mit Hilfe des multivariaten Syntheseansatzes können verschiedene Funktionalitäten in das Gerüst von COFs eingebaut werden. In diesem Projekt wurde die Synthese eines COF zur kooperativen Festphasen-Metallaphotokatalyse für Kohlenstoff–Heteroatom Kreuzkupplungen entwickelt. Hierfür wurden COFs designt, welche sowohl den lichtabsorbierenden Acridin-Linker als auch einen Bipyridin-Linker welcher den Nickel Co-Katalysator binden kann im Gerüst haben. Diese beiden Bausteine wurden durch eine Reihe von Trialdehyden mit weiteren Hydroxygruppen in die Gerüststruktur eingebunden. Untersuchungen zu C–N und C–S Kupplungen zeigten inverse Aktivitätstrends in Bezug auf die Anzahl an OH-Gruppen. Basierend auf den verwendeten Knotenpunkt kann zwischen lokalisierter Ladungstrennung für semi-heterogene C–N Bindungsknüpfung und hoher Ladungsmobilität für effiziente heterogene C–S Kreuzkupplung gewechselt werden. Für die zweite Reaktion konnte die Heterogenität des Katalysators anhand von Rezyklierungsexperimenten bewiesen werden und die Reaktion lief sogar bei Bestrahlung mit rotem Licht ab. Diese Ergebnisse wurden unter dem Titel *Programmable Photocatalytic Activity of Multivariate Covalent Organic Frameworks Used as Metallaphotocatalysts* in *Chemistry – A European Journal* veröffentlicht.

III. List of Publications

Parts of this dissertation have been published in peer-reviewed journals:

- [1] “Acridine-Functionalized Covalent Organic Frameworks (COFs) as Photocatalysts for Metallaphotocatalytic C–N Cross-Coupling”, Michael Traxler, Sebastian Gisbertz, Pradip Pachfule, Johannes Schmidt, Jérôme Roeser, Susanne Reischauer, Bartholomäus Pieber, Arne Thomas *Angewandte Chemie International Edition* **2022**, *61*, e202117738.

DOI: <https://doi.org/10.1002/anie.202117738>

- Synthesis of linkers and covalent organic frameworks as well as characterization of building blocks and materials. Complete writing of the manuscript.

- [2] “Anchoring an Iridium Pincer Complex in a Hydrophobic Microporous Polymer for Application in Continuous-Flow Alkane Dehydrogenation”, Michaela König, Michael Traxler, Maik Alexander Rudolph, Johannes Schmidt, Hüsseyin Küçükkeçeci, Reinhard Schomäcker, Arne Thomas *ChemCatChem* **2022**, *14*, e202200811.

DOI: <https://doi.org/10.1002/cctc.202200811>

- Synthesis of the iridium pincer complex, model compound and immobilization onto the polymer. Joint design of the dehydrogenation experiments and writing of the manuscript.
- Michaela König and Michael Traxler share first authorship as acknowledged in the publication.

- [3] “Programmable Photocatalytic Activity of Multivariate Covalent Organic Frameworks Used as Metallaphotocatalysts”, Michael Traxler, Susanne Reischauer, Sarah Vogl, Jérôme Roeser, Jabor Rabeah, Christopher Penschke, Peter Saalfrank, Bartholomäus Pieber, Arne Thomas *Chemistry – A European Journal* **2022**, e202202967.

DOI: <https://doi.org/10.1002/chem.202202967>

- Synthesis of linkers and covalent organic frameworks as well as characterization of building blocks and materials. Joint design of the metallaphotocatalysis experiments. Major part of the writing of the manuscript.
- Michael Traxler and Susanne Reischauer share first authorship as acknowledged in the publication.

IV. List of Abbreviations

Table 1. List of Abbreviations.

Abbreviation	Designation
Acr	diaminoacridine
BET	Brunauer-Emmett-Teller
CP/MAS	cross-polarization magic angle spinning
Bpy	2,2'-bipyridine
COD	1,5-cyclooctadiene
COF	covalent organic framework
COP	covalent organic polymer
DAA	diaminoanthracene
DMAc	dimethylacetamide
HMTA	hexamethylenetetramine
DCM	dichloromethane
DHTA	2,4-dihydroxybenzene-1,3,5-tricarbaldehyde
DMF	<i>N,N</i> -dimethylformamide
DMSO	dimethylsulfoxide
EDX	energy deispersive X-rax spectroscopy
EPR	electron paramagnetic resonance
FT-IR	Fourier transform infra-red
HOMO	highest occupied molecular orbital
HTA	2-hydroxybenzene-1,3,5-tricarbaldehyde
ICP-OES	inductively coupled plasma optical emission spectrometry
IUPAC	International Union of Pure and Applied Chemistry
LED	light emitting diode
LUMO	lowest unoccupied molecular orbital
MOF	metal-organic framework

MPN	microporous polymer network
NMR	nuclear magnetic resonance
PAF	porous aromatic framework
PC	photocatalyst
PL	photoluminescence
PPN	porous polymer network
PXRD	powder X-ray diffractometry
QSDFT	quenched state density functional theory
SA	surface area
SBU	secondary building unit
SEM	scanning electron microscopy
TEM	transmission electron microscopy
TGA	thermogravimetric analysis
THF	tetrahydrofuran
TOF	turnover frequency
Tp	1,3,4-triformylphloroglucinol
UV	ultraviolet
vis	visible
XPS	X-ray photoelectron spectroscopy

V. Table of Contents

Acknowledgements	iii
I. Abstract	v
II. Kurzzusammenfassung	vii
III. List of Publications	ix
IV. List of Abbreviation	xi
V. Table of Contents	xiii
Chapter 1: Scope and Outline of the Thesis	1
Chapter 2: Theoretical Background	3
2.1 Porosity	3
2.2 Determination of Porosity	5
2.3 Microporous Polymeric Materials	7
2.4 Microporous Polymer Networks	9
2.5 Covalent Organic Frameworks	13
2.5.1 Strategies to Tune COFs Beyond Two-Component Condensation	17
2.5.2 Application of COFs	19
2.6 Supported Homogeneous Catalysis	21
2.7 Photocatalysis for Organic Transformations	24
2.7.1 General Principles of Photocatalysis	24
2.7.2 Metallaphotocatalytic Cross-Couplings	26
2.7.3 Towards Fully Heterogeneous Metallaphotocatalysis	27
References	29
Chapter 3 Anchoring an Iridium Pincer Complex in a Hydrophobic Microporous Polymer for Application in Continuous-Flow Alkane Dehydrogenation	39
Abstract	40
Specific Contribution	40
Supporting Information	40
Introduction	41

Results and Discussion	42
Conclusion	50
Experimental Section	51
References	54
 Chapter 4	 Acridine-Functionalized Covalent Organic Frameworks (COFs) as Photocatalysts for Metallaphotocatalytic C–N Cross-Coupling
Abstract	58
Specific Contribution	58
Supporting Information	58
Introduction	59
Results and Discussion	60
Conclusion	69
References	70
 Chapter 5	 Programmable Photocatalytic Activity of Multivariate Covalent Organic Frameworks Used as Metallaphotocatalysts
Abstract	76
Specific Contribution	76
Supporting Information	76
Introduction	77
Results and Discussion	79
Conclusion	87
Experimental Section	87
References	89
 Chapter 6	 Summary and Outlook
Appendix	97
Article I	99
Article II	123
Article III	193

Chapter 1:

Scope and Outline of the Thesis

Catalysis plays a crucial role in the chemical industry, with more than 85% of the chemical processes involving the use of a catalyst.^[1] The huge impact of catalysts on the sustainability within the chemical industry can be described by an estimated decrease in energy consumption of more than 50% between 1990 and 2010.^[2] Additional improvements of catalytic improvements forecast a further decrease of up to 40% in energy consumption by 2050. In doing so, 13 exajoules in energy – comparable to the energy consumption of Germany - and one gigaton of carbon dioxide equivalent could be saved annually.

Therefore, the development of novel catalysts, which can improve the industrial standard is of high demand. With the emergence of novel microporous material towards the application in catalysis, it is crucial to extend the scope of these materials towards novel heterogeneously catalyzed reactions. The development of solid porous materials enables the recycling of the active species by simple filtration or centrifugation followed by a washing of the catalyst before it can be reused, or performing the reaction under continuous flow conditions.

Among microporous materials, zeolites are already broadly applied on industrial scale. However, for novel subclasses of porous polymeric materials the gap towards industrial use has yet to be closed. In contrast to zeolites, the set of unique properties of each subclass of porous polymeric materials in combination with the tunability gives rise to the synthesis of tailored materials, which can be fine-tuned to the process at hand. For instance, covalent organic frameworks (COFs) show absorption in the visible light, which makes them of great interest towards photocatalytic applications. On the other hand, microporous polymers show high chemical and thermal stability, while providing a hydrophobic reaction environment. The latter can be used to run reactions under conditions, where water can be prevented to reach the catalytic center, protecting it from poisoning. Using this approach, a catalyst could be combined in a tandem reaction with a second reaction, where water is a side product or a substrate. The combination of two reaction steps would be beneficial, since then no energy intensive separation step is needed between each reaction.

Nature has created efficient ways to utilize sunlight as energy source to drive (bio)chemical processes. Taking nature as role-model, synthetic chemists were also seeking to exploit the sun as infinite and sustainable energy source to drive organic transformations. This not only enables known reactions, but also give alternative reaction pathways or show activity using earth abundant metal catalysts. Based on these properties, photocatalysis has emerged as a valuable tool in the life science industry.^[3] The often mild reaction conditions in photocatalysis allow the application in late stage functionalization.^[4] This approach was found suitable for the synthesis of a broad range of pharmaceutical drugs e.g. elbasvir, a drug used in the treatment of hepatitis C.^[5]

Within the framework of this thesis two classes of porous polymeric materials are investigated for their application in heterogeneous catalysis. Owing to the nature of each class of materials, the materials developed are either investigated in a dehydrogenation reaction or in metallaphotocatalytic cross-coupling reactions. Chapter 2 provides the scientific background to the experimental studies and discussions within this thesis. Chapters 3 - 5 report the publications listed at page ix, reformatted, but with unaltered content. For each publication, supporting information containing experimental details is included in the Appendix. In Chapter 3 the immobilization of an iridium pincer complex within the pore structure of a highly hydrophobic microporous polymer network is presented. The synthesis of the supported catalyst material involved a multi-step modification to enable the anchoring of the organometallic catalyst. The activity of the material was demonstrated for the continuous-flow dehydrogenation of cyclohexane. The introduction of a novel linker into the backbone of a family of porous crystalline covalent organic frameworks was demonstrated in Chapter 4. With the broad absorption in the visible light range, the materials were employed as the first COF for metallaphotocatalytic C–N cross-coupling reaction. Chapter 5 demonstrates the design of a series of multivalent COFs, which provides both a photosensitizer and a linker able to bind a nickel catalyst. These functional units are connected by a series of trialdehydes. Depending on the choice of the connecting moiety either efficient charge carrier mobility or persistent charge separated species are obtained, defining the activity in two different metallaphotocatalyses.

The results of this doctoral thesis are summarized with a discussion of the individual projects in Chapter 6. Moreover, an outlook on the use of porous polymeric materials as support material for a broad platform of different catalysts is given.

Chapter 2:

Theoretical Background

2.1 Porosity

Porosity is describing the ratio between the void/pore volume and the overall volume of a material. The first porous structures were built by the greatest engineer of all time – nature. There are numerous examples of natural substances that exhibit porous architectures, featuring a multitude of purposes like enabling gas/liquid transport, while maintaining a lightweight structure. Examples for that are the stems of trees and grass, bird feathers, butterfly wings or the human bone structure (Figure 1).^[6]

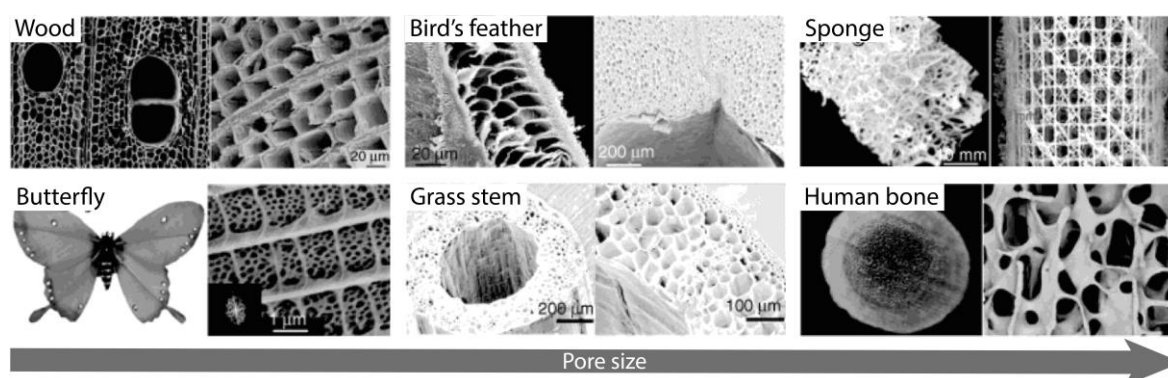


Figure 1. Examples of porous structures in natural systems along different length scales ranging from fractions of micrometers to the millimeter regime.^[6]

Inspired by those structures found in nature, researchers were eager to develop novel synthetic materials with a defined structure on the nanometer level (dimensions of 1-100 nm). There are two general principles on how the nanostructuring can be achieved. On the one hand, the particle size of a material can be reduced to the nanometer regime, increasing the ratio between surface and bulk of a material. On the other hand, nanometer-sized voids (pores) are introduced into a material. This approach results into an increase in surface area, which is available for host-guest interactions.^[7] Both processes result in unique properties that are different from the bulk material. This can result in increased activities e.g. in catalysis or sorption processes.^[8,9]

Chapter 2

The porosity of a material can be categorized on the pore diameter of the voids within a material. Such a classification was introduced by the International Union of Pure and Applied Chemistry (IUPAC) in 1985 for the relevant length scales of sorption processes. Here, porous materials were categorized into three different classes, i.e. microporous (diameter < 2 nm), mesoporous (2-50 nm) and macroporous materials (> 50 nm).^[10]

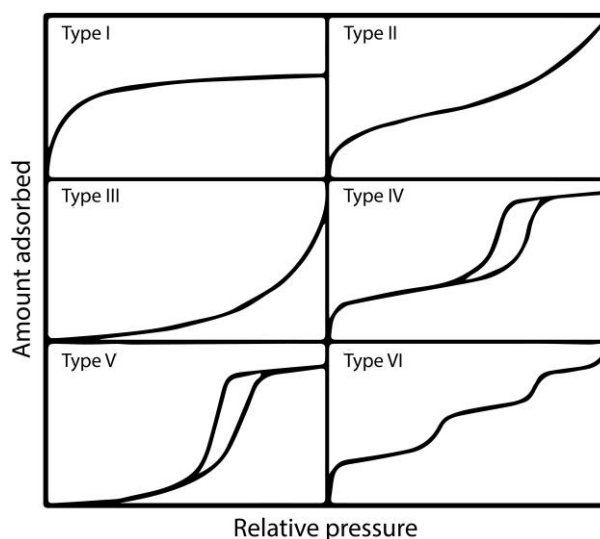
2.2 Determination of Porosity

In order to investigate the size and nature of pores within a material, experiments during which the pores of the host material are filled have to be conducted. For that the pores of the material have to be emptied before introducing a probe species in a controlled manner. This activation step prior to the measurement is performed using reduced pressure and if feasible in terms of stability of the material elevated temperature. Doing so it is ensured that adhesive interactions between any adsorbed species within the porous material and the host itself are overcome. Subsequently, the sample can be treated with the probe gas of choice. The measurement has to be conducted at the normal boiling point of the probing gas, since all models for the calculation of surface area and other relevant values are only valid at that temperature and for relatively low pressures (e.g. N₂ at 77 K). During the measurement the added amount of adsorbate and the pressure change in the measuring cell are recorded for at least one adsorption/desorption cycle. Using this method, the adsorbed amount of probe gas can be plotted against the relative pressure. Depending on the size and geometry of the pores the shape of this isotherms shows a different shape.

The International Union of Pure and Applied Chemistry (IUPAC) classified the different curves in six types of physical adsorption isotherms and additionally four types of hysteresis loops, where the desorption does not follow the reverse pathway of the adsorption (Figure 2).^[10,11] The isotherms are classified by nature of the adsorbing material, which are microporous (Type I), nonporous or macroporous (Types II, III, VI), or mesoporous (Types IV and V). Moreover, the hysteresis loops that are occurring for the mesoporous isotherms are classified by IUPAC into materials with well-defined cylindrical or agglomerations of uniform spheres (Type H1), that with a wide distribution of pore sizes or ink-bottle pores (Type H2), wide slit pores (Type H3) and narrow slit pores (Type H4). The dashed lines in the low pressure range of hysteresis curves indicate possible irreversible gas uptake or swelling of the adsorbent.

Using this measuring technique the accessible surface area of the material can be calculated based on the model developed by Brunauer, Emmett and Teller in the 1940s (BET model).^[12] The BET model is based on the Langmuir adsorption model, which is limited to monolayer adsorption processes, whereas the BET theory takes also multilayer adsorption into consideration.

a)



b)

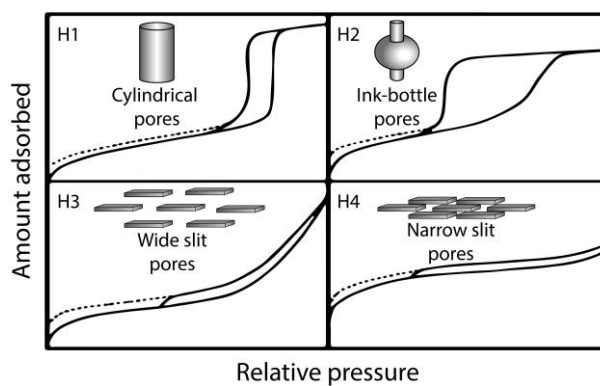


Figure 2. Classification of sorption isotherms (a) and hysteresis types (b) according to IUPAC.^[10,11]

The expansion of the theory is based on following prerequisites: (1) the Langmuir theory is valid for each layer, (2) gas molecules adsorb on infinite layers, (3) no interactions between the adsorbed layers, (4) the enthalpy of adsorption of the first layer is larger than the following ones and (5) the enthalpy of adsorption of the all layers other than the first is the same as the enthalpy of liquefaction. Despite these limitations, the determination of surface areas using gas porosimetry is widely applied, due to a lack of suitable alternatives.

2.3 Microporous Polymeric Materials

Microporous polymeric materials can be classified into four major categories based on the composition of the repeating linking units (Figure 3).^[13] Among the most prominent material class are crystalline, inorganic zeolites. The first report of this class of material dates back to 1765, when the Swedish researcher Cronstedt found the material stilbite. He described this mineral as “boiling stones” ultimately giving this class its name. The framework structure of zeolites are built up by tetrahedral alumina and silica units with cations trapped within the pores to counterbalance the positive charge of the alumina moiety.^[14] Thus, they are exceptionally suited as ion exchange membranes, but due to their porosity they are used as well as solid adsorbents for gas separation and catalytically active materials.^[15] Although the available building blocks are severely limited, more than 170 unique zeolite framework types have been approved. The earliest synthetic preparation of zeolites dates back to the early 1930s.^[16] However, the development of the gel crystallization by Milton and Breck in the 1950s at Union Carbide is perceived as the turning point in zeolites. Their synthesis method opened up avenues for the application of zeolites on industrial scale. Caused by this development, in the following decade zeolite Y and ZSM-5 were discovered, which are on the one hand the most consumed zeolite catalyst and on the other hand the zeolite catalyst most broadly applied in different processes.^[15]

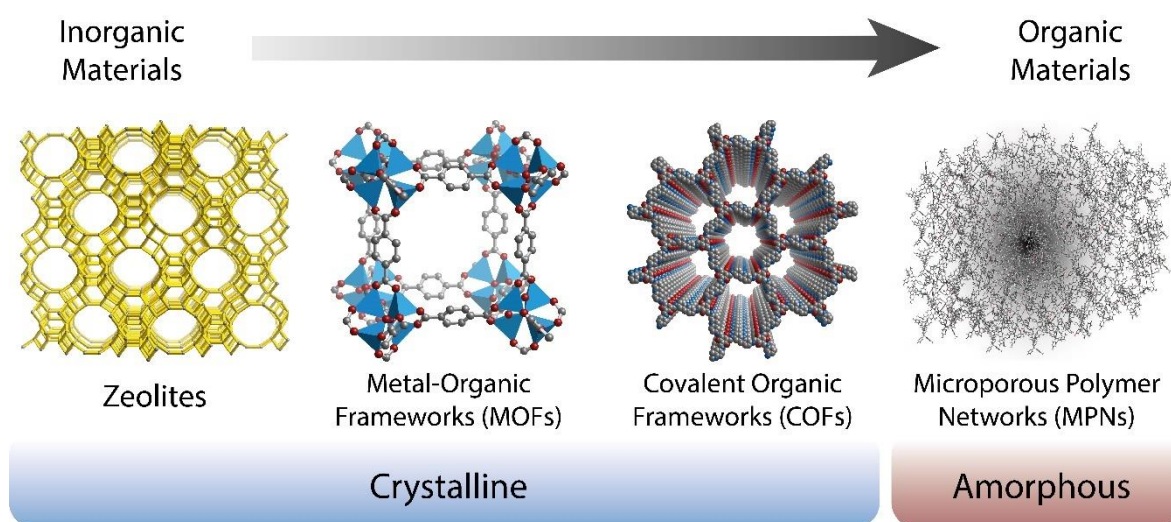


Figure 3. Classes of porous polymeric materials ordered by material character and crystallinity: purely inorganic zeolites, hybrid metal-organic frameworks (MOFs) and fully organic covalent organic frameworks (COFs) as classes of crystalline materials and microporous polymer networks as fully organic amorphous material.^[13]

Compared to zeolites, which are fully inorganic materials, metal-organic frameworks (MOFs) are considered as a hybrid material. Since the first report of this class of porous crystalline material by Yaghi and coworkers in 1995 the field is one of the fastest growing in science.^[17,18] The framework structure is built up by a metal clusters or metal-ligand complexes as inorganic building block (node or secondary building unit [SBU]), which are linked by charged and rigid organic units i.e. carboxylates (linkers). The key to their crystallinity is the reversible bond formation/breaking process (reticulation), which allows for error correction leading to the ordered framework structure. With both a broad library of available organic and inorganic building parts, MOF structures show an extraordinarily high degree of versatility. This led to hundreds of MOF structures and chemistries reported in the last two decades. The only limitation is posed by incompatible functional groups disrupting the reticulation process. However, the conversion of a compatible group to the desired moiety after the framework synthesis renders a possible pathway to the introduction of groups which would normally be not accessible. This so-called post-synthetic modification further expands the design toolbox for MOF materials.^[19] Besides this extraordinary tunability, the ultrahigh permanent porosity with up to more than 90% free volume and enormous internal surface areas, with examples exceeding 8000 m²/g, is a key feature of metal-organic frameworks.^[20] Based on these properties, MOFs render especially suitable for application as media for gas storage (e.g. H₂, CO₂, methane), or membrane materials for separation processes.^[21] Additionally, MOFs are broadly used for applications in biomedicine, as sensors or in various fields of catalysis.^[22]

Compared to zeolites and MOFs, covalent organic frameworks (COFs) and microporous polymer networks (MPNs) are fully organic materials. The main difference between these classes is the order within the polymeric material. While COFs are, as MOFs and zeolites, crystalline materials MPNs are amorphous. This thesis focuses both on catalytic applications of COFs and MPNs. Thus, the properties and applications of these two classes of materials will be discussed in more detail in the following chapters.

2.4 Microporous Polymer Networks

Microporous polymer networks are a class of fully organic materials, that feature a permanent porosity.^[23] They are forming rigid frameworks owing to aromatic moieties in the backbone which are connected by carbon–carbon bonds. Over the years a multitude of different microporous polymer networks have been reported.^[24] Due to a lack of systematics, various name variations, such as porous polymer network (PPN), porous aromatic framework (PAF) or covalent organic polymer (COP) have arisen for this class of materials. For some materials this has even led to different names for the same structure depending on the synthesis method employed in the polymerization reaction (e.g. PPN-6^[25] vs. PAF-1^[26]; Figure 4).

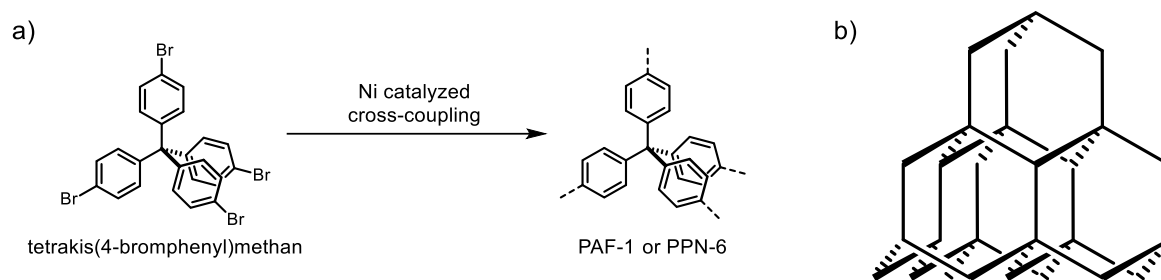


Figure 4. a) Synthesis of PAF-1 or PPN-6 using Yamamoto polymerization of tetrakis(4-bromophenyl)methane. The polymers display different specific surface areas based on the polymerization protocol. b) Idealized diamond-like structure. ^[25,26]

To simplify the matter, within the thesis this class will be designated MPNs, except when referring to distinct literature sources. In a stark contrast to the above-mentioned framework materials (zeolites, MOFs, COFs), microporous polymer networks (MPNs) are building up a non-crystalline structure. This amorphicity originates from the construction of these materials via irreversible carbon–carbon bond formation. With the missing reversibility these types of reactions lead to a non-defined pore structure. Thus, the analytical results are solely giving averaged values of the network structure. The difference of the amorphous and flexible material compared to crystalline framework structures can be typically seen in sorption isotherms. Here, the desorption isotherm branch is not forming a closed loop with the adsorption curve at the origin. This effect of pronounced hysteresis is yet not entirely understood. Most often this phenomenon of the open loop is ascribed to minor structural changes of the material upon dosing of gas into the fully evacuated material. However, there

are debates about if this swelling would indeed be reversible, when employing a stronger vacuum to remove residual entrapped gas molecules. Although this change during measurement imposes strong inaccuracies on the analysis with gas isotherm and BET theory, it is still commonly applied due to a lack of better suitable alternatives.

Among the plethora of different synthesis techniques for MPNs ranging from Suzuki coupling to Friedel-Crafts alkylation, the preparation via a variation of the Sonogashira-Hagihara^[27] coupling, alkyne metathesis or the Yamamoto polymerization^[28] rendered most suitable for the synthesis of highly porous crosslinked porous materials. Based on the Sonogashira-Hagihara chemistry, Cooper *et al.* reported the first synthesis of various porous poly(aryleneethylene) networks with examples exceeding surface areas of 800 m²/g.^[29] The reaction protocols of this reaction was optimized gradually, when Trunk *et al.* reported a series of different polymers using various building blocks in a copper-free Sonogashira reaction to afford materials with a surface area of up to 2550 m²/g.^[30] Another reaction protocol which was applied to the formation of porous polymers was using a dynamic alkyne methatesis reaction. Compared to the irreversible coupling obtained with the Sonogashira protocol, this reaction offers reversible bond formation which allows for error correction. Based on this chemistry MPNs with improved surface areas up to 2300 m²/g were synthesized in 2013.^[31] However, it was nearly a decade until the reversibility of the reaction led to the first crystalline materials, when the group of Zhang reported the successful synthesis of γ -graphyne.^[32] The drawback of both reactions described is that two functionalities are needed for this reaction. In contrast to this, the Yamamoto type polymerization using bis(1,5-cyclooctadiene)nickel(0) strikes with a simplicity of the reaction procedure. Here, solely one multi-halogen functionalized monomer is required to form the respective polymers. This reaction was for the first time used for MPNs in 2009 by the group of Thomas for the polymerization of spirobifluorenes.^[33] Later that year a brominated tetraphenylmethane monomer was used to build up the microporous polymer network denoted as PAF-1.^[26] This material showed a ultrahigh surface area of more than 5000 m²/g. Adaptation of the synthesis protocol employed for PAF-1 by the addition of THF as a co-solvent to DMF led to a decrease in reaction temperature from 80 °C to room-temperature, while the porous nature of the material was still intact.^[25] Recently, the group of Bour demonstrated an alternative route using nickel bromide, 1,5-cyclooctadiene (COD) and activated zinc powder to drive the reaction.^[34] Using this reaction route highly porous

materials were obtained using bench stable and low-cost starting materials to form the active catalyst in situ. Using this method, various MPNs were synthesized and even a gram scale synthesis of PAF-1 was demonstrated.

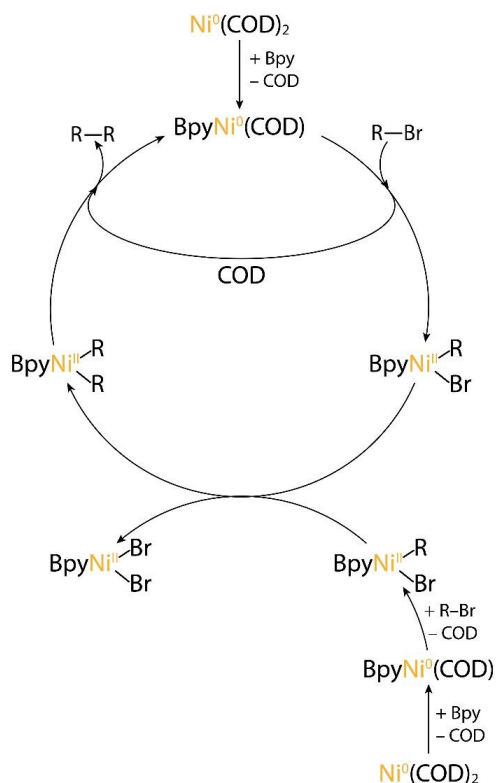


Figure 5. Reaction mechanism for the Yamamoto cross-coupling between aryl bromides.^[35]

On a mechanistic level, the reaction proceeds via a ligand exchange from 1,5-cyclooctadiene (COD) with a 2,2'-bipyridine (Bpy) unit to form the catalytically active nickel(0) species. Oxidative addition of an aryl bromide to the catalyst gives an $(\text{Bpy})\text{Ni}(\text{II})\text{RBr}$ complex. This species undergoes subsequently a disproportionation with a second aliquot to form nickel(II)diaryl and nickel(II)dibromo bipyridine complexes. Subsequently, the diaryl complex undergoes reductive elimination to give back – with an aliquot of COD – the nickel(0) catalyst. However, the NiBr_2 complex is thermodynamically too stable to undergo a pathway of reductive elimination.^[35] Thus, stoichiometric amounts of the nickel complex are needed, which renders also the major drawback of this synthesis procedure (Figure 5). Due to the formation of irreversible strong covalent carbon–carbon bonds, MPNs show generally a high thermal. In this respect MPNs are superseding the majority of MOFs and COFs. Additionally, the strong nondirectional C–C bonds in porous polymers result in a high

stability against hydrolysis, even at elevated temperatures. Furthermore, the parent polymers are built up by a chemically simple structure consisting solely from carbon and hydrogen atoms. Therefore, MPNs are a uniquely suitable platform to introduce isolated functional sites into a chemically “innocent” environment. A broad range of functional groups have already been introduced into the structure of MPNs, with application mostly focusing on gas separation and the storage of e.g. hydrogen or CO₂. Especially intriguing for the use of MPNs is their use as carrier material for the immobilization of molecular catalysts. Using this strategy, single site catalysis, which was gaining increased interests in the last decades, shows a promising field of application.^[36,37] The anchoring of metal-organic catalysts on the backbone of the MPNs would allow to tackle recycling issues in traditional homogeneous catalysis. Moreover, it enables to transfer these catalysts from liquid state solutions to gas phase catalysis, maintaining the unique properties of the molecular catalyst. The strategies and state of the art of the use of porous polymers as support material in heterogenized homogeneous catalysis will be discussed in Chapter 2.6.

2.5 Covalent Organic Frameworks

Compared to the previously described classes of crystalline polymeric materials, covalent organic frameworks are the most recently discovered. Similarly to MOFs, the origin of the crystalline nature of these materials lies upon the reversible bond formation and breaking process, the so-called reticulation. This leads to error correction within the formation of the two- or three-dimensional framework structures, giving rise to the long-range order of this class of materials.^[38,39] However, in contrast to MOFs, where the framework is built up by metal cluster as SBUs that are bound together by organic linkers, COFs are fully organic materials built up solely by covalent bonds between light-weight elements such as, carbon, boron, nitrogen, oxygen or sulfur. The first report of a crystalline porous covalently linked material was described by the group of Yaghi as recent as 2005 (Figure 6).^[40]

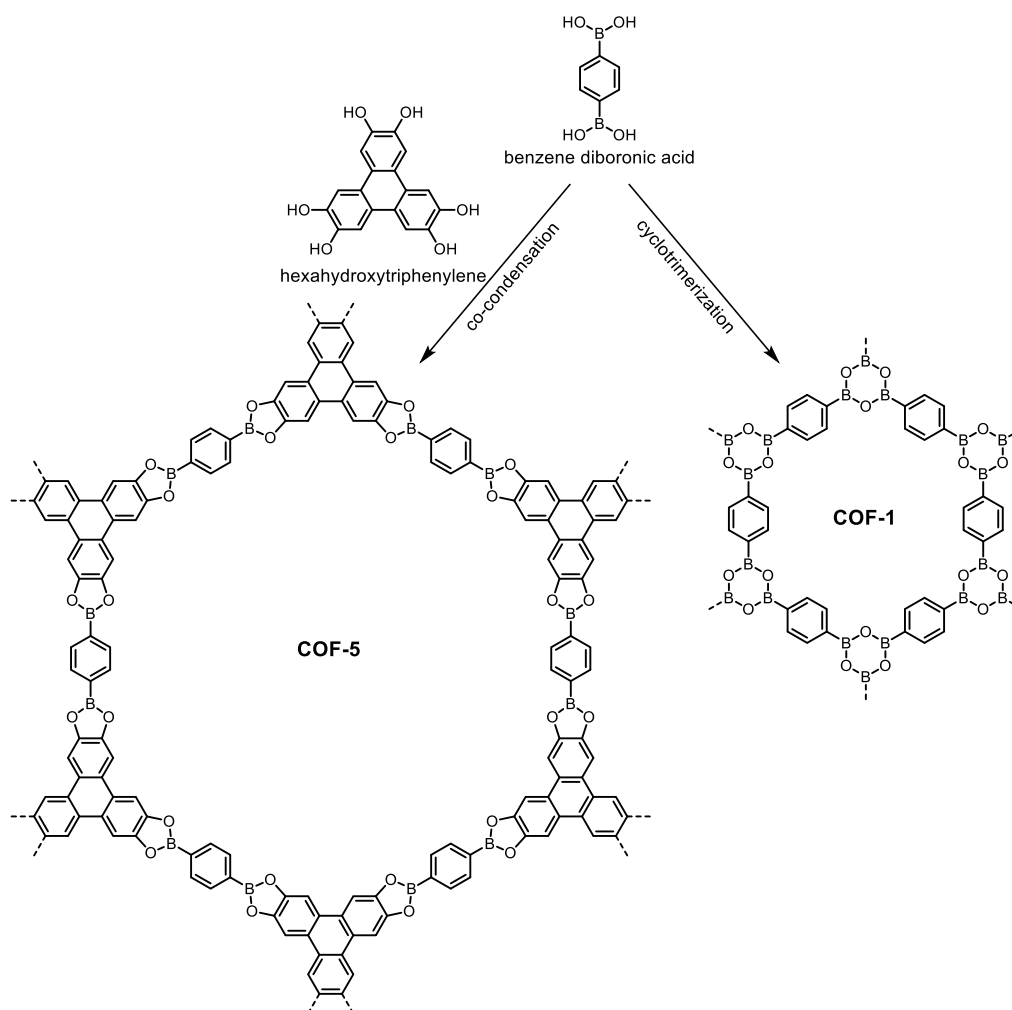


Figure 6. Synthesis of COF-5 by co-condensation (left) and COF-1 by dynamic trimerization (right).^[40]

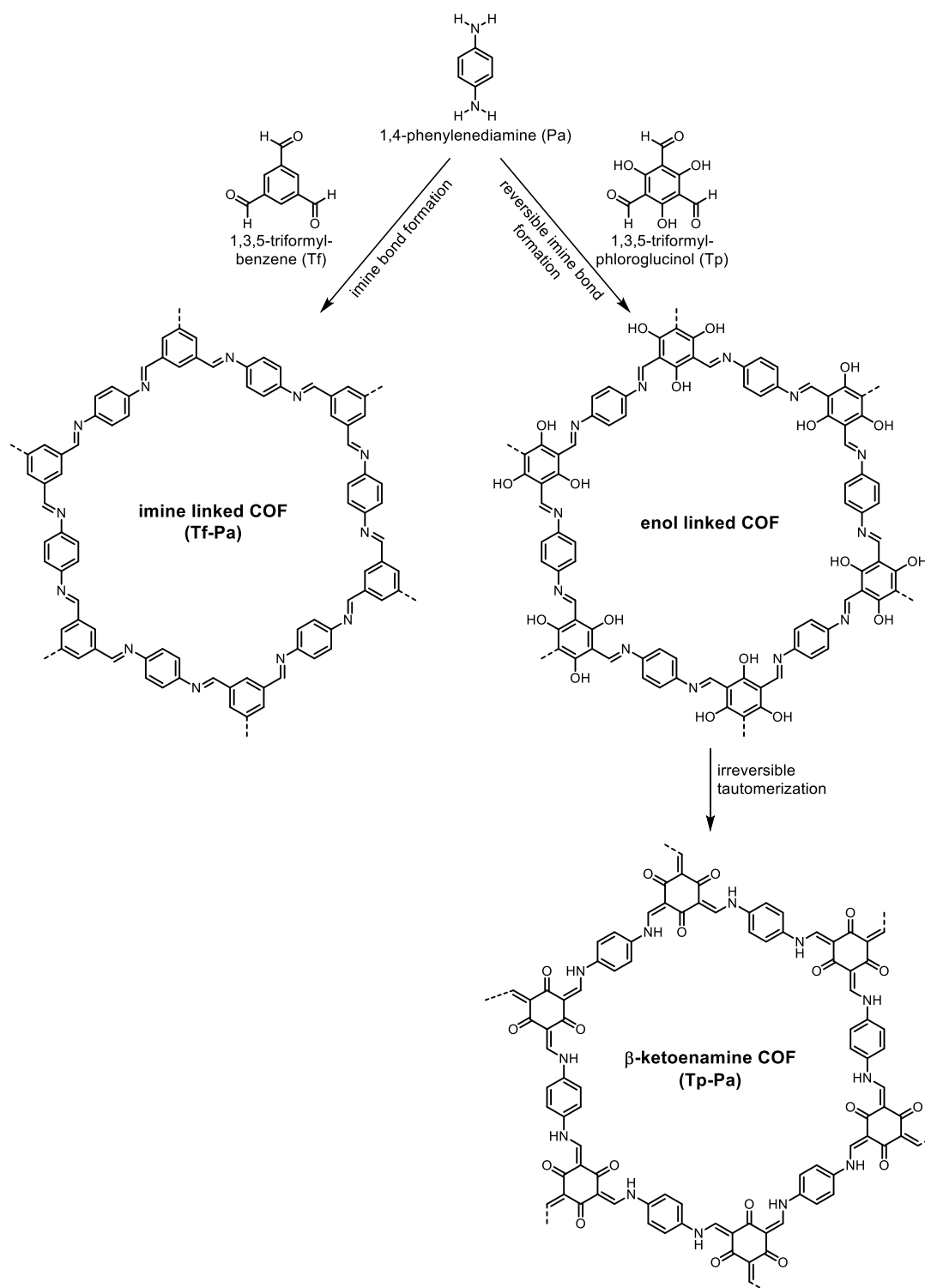


Figure 7. Synthesis of imine based COFs, exemplified for Tf-Pa via Schiff base reaction between 1,4-phenylenediamine and 1,3,5-triformylbenzene (left). Preparation of β -ketoenamine COFs by the use of 1,3,5-triformylphloroglucinol showing first a reversible imine bond formation followed by an irreversible keto-enol tautomerization.^[41,42]

COF-1 and COF-5 are prepared by cyclotrimerization of benzene diboronic acid and co-condensation with hexahydroxytriphenylene to form a boronate ester under solvothermal reaction procedure, respectively. Besides the solvothermal approach for COF synthesis,^[40,43,44] which is still the most commonly used COF preparation method a broad toolbox of framework formation methods is available for reticular chemists. This includes among others ionothermal,^[45,46] mechanochemical,^[47–49] electrochemical,^[50,51] photochemical^[52] or microwave induced COF synthesis.^[53,54] Besides the development of different synthesis methods also a search for reversible reactions to create novel linkages in COFs has driven the field towards a multitude of available linking reactions. Among them, the construction of imine bonds by a reversible Schiff base reaction, which was for the first time reported in 2009, is one of the most intensively investigated method for COF construction, due to the broad diversity of aromatic aldehyde and amines (Figure 7, left).^[55] Noteworthy, also irreversible reactions can be used to build up the framework structures. For example, the β -ketoenamine linked COFs, which are constructed from the reaction of phloroglucinol with amines, is formed by a reversible imine bond formation, followed by an irreversible tautomerization (Figure 7, left).^[42] Using this linkage, COFs with an exceptionally high chemical stability were obtained compared to boronate or imine-based COFs. Furthermore, post-synthetic modification of imine-bonded COFs to form amine,^[56,57] amide,^[58] benzothiazole^[59] or azo^[60] linked frameworks, even broadened the available linkages for COF construction. In addition of the linkages in COFs, the structural diversity can be expanded by different topologies. Based on the choice and connectivity of the linkers for the framework reaction, different arrangements into different 2D and 3D structures are available for COFs. Among them the hexagonal honeycomb topology **hcb** is the most commonly found for 2D COFs obtained by several combination of linkers and linkages.^[61] For stacked 2D monolayer frameworks additionally different stacking modes i.e. AA, AB and ABC, were reported, which is further increasing the structural diversity (Figure 8).

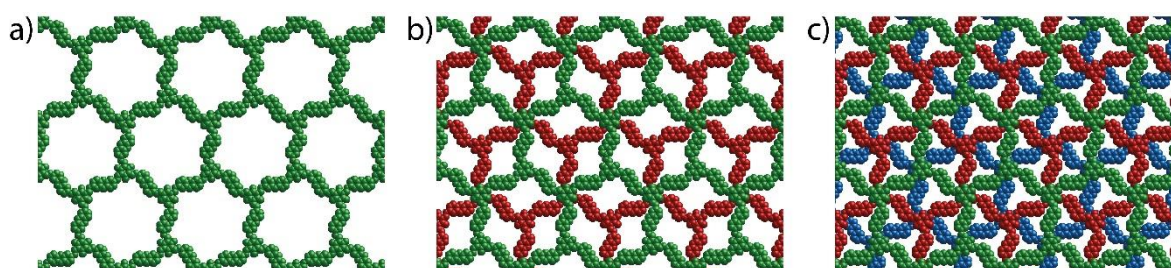


Figure 8. Different stacking modes for COFs in hexagonal honeycomb topology **hcb** (a) staggered, (b) eclipsed AB-stacked and (c) ABC-stacked.

Besides their structural variability, the success of COFs can be attributed to a set of unique properties, superseding other crystalline polymeric materials (Figure 9). Since the framework structure is formed by relatively strong covalent bonds, a majority of COFs show a good stability against various chemicals and solvents as well as increased temperatures. Certain limitations in respect to the stability in acidic and alkaline media have already been tackled in various ways, ranging from new stable linkages (e.g. β -ketoenamine) over to post-synthetic stabilization of the framework by cyclization of the acid/base labile imine bond. With the ordered arrangement of the linkers into the crystalline frameworks, COFs are showing substantial permanent porosity, with certain examples exceeding $4000 \text{ m}^2/\text{g}$.^[62] Additionally, the defined pore geometries allow for detailed structure-activity relationship studies. In contrast to MPNs, the porous structure shows periodic alignment and increased rigidity. Therefore, no structural rearrangements during sorption measurements are occurring. With the extended π -conjugated systems introduced into of a majority of COFs they show unique optical properties, like absorption in the visible light range or photoluminescence. Most interestingly, with the plethora of suitable (functional) linker moieties, in combination with the choices of linkages and possibilities for post-synthetic modifications, a nearly infinite tunability of the COF structures can be obtained.

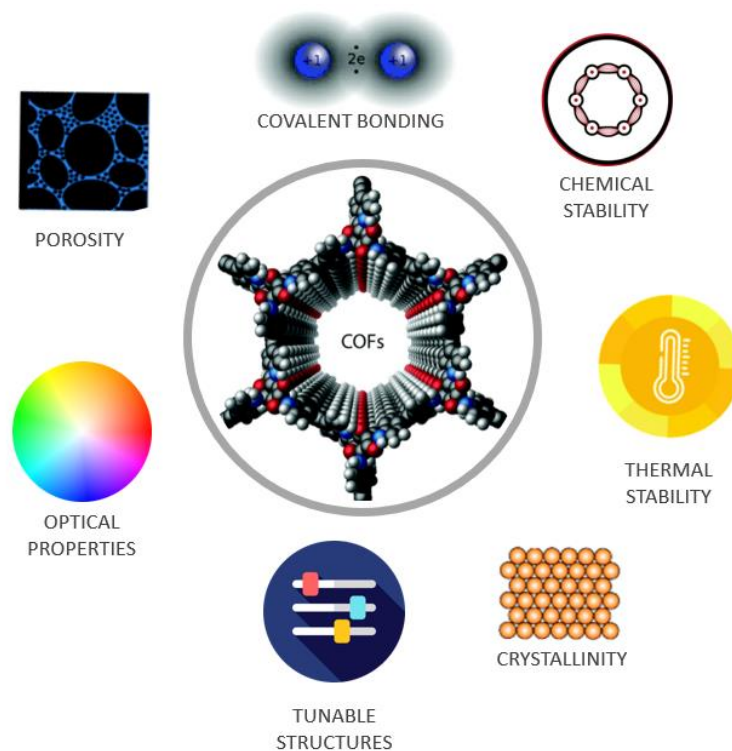


Figure 9. Properties of covalent organic frameworks.

2.5.1 Strategies to Tune COFs Beyond Two-Component Condensation

Even more, strategies to even further increase the structural modularity of COFs were developed in parallel to the development of new linkers and linkages (Figure 10).

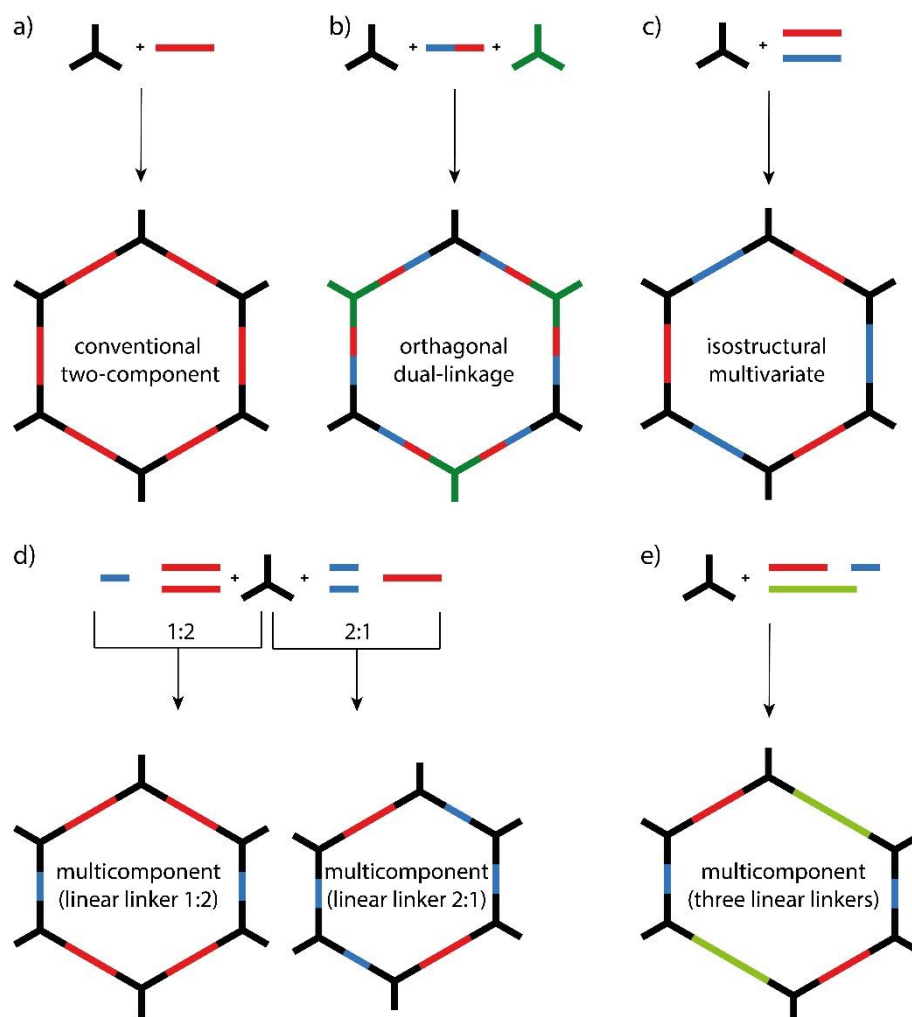


Figure 10. Strategies to introduce functionality into the COFs beyond the two-component condensation.

One approach is the double-stage approach, where COFs consisting of a linker with two functional groups reacts by the formation of two different linkages based on the strategies of orthogonal chemistry (Figure 10b). This synthesis method allows for a dual linkage COF, which enriches the types and functions in COFs, by the introduction of the properties of two linkages. This results in an increase in functionality without post-synthetic modification. The prerequisite towards this synthesis approach is that one of the linkers has to bear two different functional groups (e.g. boroxine and imine). Subsequently, this linker can then

undergo two different reversible reactions with additional tri- or tetratopic linkers bearing the orthogonal functional group in a one pot approach.^[63] This approach was already applied for various orthogonal linkage formation e.g. boroxine/imine,^[63–65] boronate/imine,^[63,64] boronate/hydrazone,^[66] boroxine/triazine^[67] or by Schiff base and Knoevenagel reaction.^[68] In contrast to the orthogonal dual linkage approach, multifunctional COFs can be also designed using topology considerations. Here a single type of linkage is used to introduce different linkers into the COF backbone (Figure 10d,e). These so-called multicomponent COFs are constructed in a similar manner as the traditional synthesis approach, except that more than the topologically necessary linkers are used. In addition to appropriate choice of the molar ratio of two functional groups building up the framework, a suitable stoichiometry of the used linkers is required to close the hexagons or tetragons formed. This is limiting the ratio between the used linkers, e.g. in order to form a distorted hexagonal honeycomb topology. The ratio of the two-connected linkers can only be 2:1 or 1:2 to be able to form up a regular structure when reacting with a 3-connected node moiety (Figure 10d).^[69] Additionally, examples for using three different linear linkers in combination with a tritopic linker were also reported. (Figure 10e). Various examples of this synthesis approach have been reported for different linkage chemistries including boronate ester,^[70–72] imine^[73,74] and β -ketoenamine^[75] based COFs.

In the topology driven multicomponent COFs and orthogonal dual-linkage COFs the additional introduced linkers show a fixed geometrical arrangement in the backbone of the framework structure enabling the investigation of exact structure-activity relationships. In contrast to that, different linkers can also be introduced into the COF backbone by the construction of isostructural mixed linker COF (also multivariate COFs; Figure 10c).^[76] Here multiple linkers that have the same connecting geometry are reacted with a three- or four-connected node moiety. These linkers are bearing different functional side groups that can be gradually introduced in the framework backbone depending on the feed ratio of different linker molecules. With this general strategy a large variety of functionalities can be introduced onto the channel wall of the framework.^[77–81] Without the driving force of orthogonal chemistry or topological arrangements the distribution of functionalities is statistically throughout the material. Nonetheless, due to the simplicity and toleration of different linkages and pore shapes as well as facile post-synthetic modification, this strategy has been used broadly for the synthesis of tailor-made COFs.

2.5.2 Application of COFs

With the broad structural diversity, porosity, absorption in the visible light range and stability of this novel class of materials, COFs are candidates for a multitude of applications (Figure 11).^[39,82]

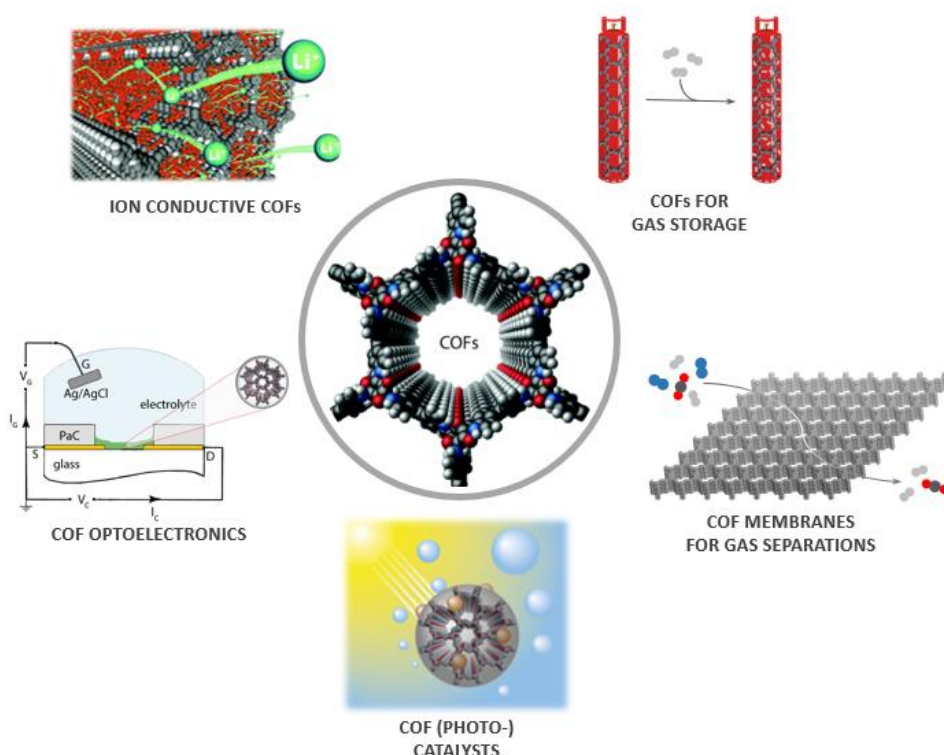


Figure 11. Application of COFs in various fields.

Due to their porous nature the most prominently investigated field is the use in adsorption and separation applications.^[83] Especially interesting is the storage of gases like hydrogen, methane, ammonia or carbon dioxide and the separation and purification of gas mixtures.^[84,85] Moreover, COFs can also be designed for the adsorption and separation of iodine, organic (chiral) compounds or the capture of metal ions from wastewater sources. The channel pores of two-dimensional COFs can also be used for proton or ion conduction processes making them candidates for solid electrolytes in battery technology.^[39,86–90] In this respect COFs are also considered as suitable energy storage materials for batteries as well as supercapacitor applications.^[82] With the unique π -extended systems COFs that can be further tuned with donor-acceptor interactions, the frameworks would create an ideal material platform as semiconductor materials in photoelectronic application.^[91–94] Even more, the

band gaps of COFs can be engineered for efficient photoluminescence,^[72,95,96] which led to the development of light emitting COFs and to the application of these materials as sensors for variable fields ranging from the detection of explosives or toxic metal ions to biosensing.^[97]

A broad field for the application of COFs is their use as catalysts.^[98] Here the materials have proven to be a valuable platform that can be adapted for a broad range of reactions. For instance, the introduction of enzymes or grafting chiral moieties onto the pores of the framework enables enzyme-based transformations or asymmetric catalysis. Moreover, COFs have been successfully used for the introduction of metal atoms for single-site catalysis or to incorporate nanoparticles within the framework material.^[99,100] Depending on the metal (ions) introduced a variety of reactions can be catalyzed. However, the most interesting application within the scope of this thesis is the use of COFs as photocatalysts.^[101] Owing to the long-range π -conjugation and thus visible light absorption, COFs have emerged as a highly suitable candidate as heterogeneous catalyst in light driven transformations. Photocatalytic hydrogen evolution^[102–104] and CO₂ reduction^[105,106] are dominating this field of application. Using COFs as photocatalysts for organic transformations was still an underexplored field of research.^[107] Up to the beginning of this thesis project only a few examples were reported. It is noteworthy, that in the last three years the field has gained significant interest throughout the community with examples for oxidative hydroxylation,^[108,109] N–S cyclization,^[110] C–H functionalization,^[111,112] hydroxylation of aryl chlorides^[113] or tandem addition-cyclization reaction.^[114] The combination of the COF backbone as a photocatalyst with the immobilization of metal ions opened novel pathways for the usage of COFs in metallaphotocatalytic carbon–carbon (C–C)^[115] and carbon–heteroatom (C–X)^[116–119] cross-coupling reactions. The principles of heterogeneous photocatalysis with a particular focus on the metallaphotocatalysis are discussed in the following Chapter 2.7.

2.6 Supported Homogeneous Catalysis

Homogeneous catalysts are a class of molecules that are promoting reactions, where substrates/products are in the same phase as the catalyst itself. Although there are examples for gas phase homogeneous catalysis, the majority of this class are reactions in liquid phase. Such reactions involve a solvent to facilitate fast diffusion, which enables fast reaction rates. The design of small molecular catalysts, that are employed in homogeneous catalysis have gained huge attention over the years, which has led to various subdisciplines including organocatalysis, acid-base catalysis and homogeneous catalysis using metal complexes.^[120] The latter is the most widely applied on industrial scale and activates important reactions, such as C–C cross-couplings, hydroformylation or the oligomerization of olefins using metathesis, that are especially important for the production of pharmaceuticals and fine chemicals.

The advantages of molecular catalysts are their increased selectivity and activity at mild reaction conditions compared to their heterogeneous analogs. This originates from the possibility to design uniform active centers, which prevent side reactions. Moreover, the catalysts can be tuned on the molecular level by the choice of the metal center, as well as the ligand moiety. However, there are major drawbacks when it comes to the reusability of homogeneous catalysts, since the metal complexes are dissolved within the reaction mixture and often employed as pre-catalysts that form in-situ. Therefore, the catalysts can often not be reused, since it is degrading when removed. Moreover, the catalyst remains often in the product because the energy intensive separation processes is more expensive than the small catalyst amounts that are employed in the process.

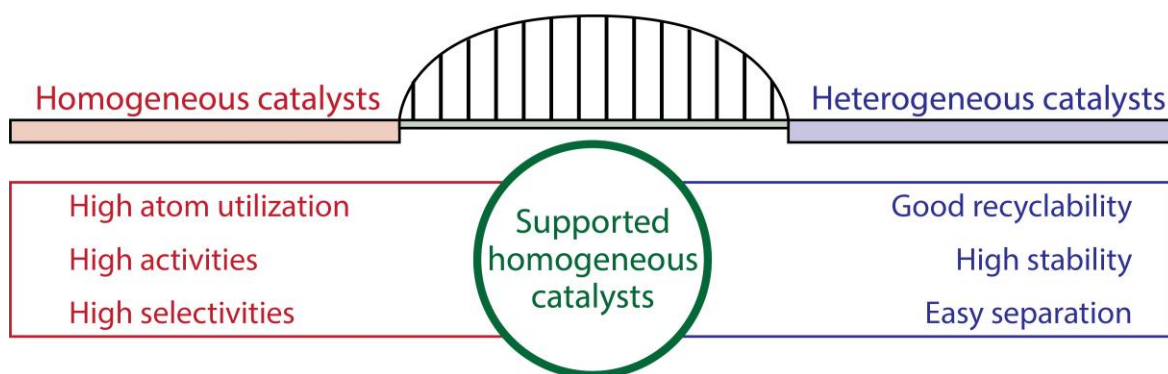


Figure 12. Design principles of supported homogeneous catalysis bridging homogeneous and heterogeneous catalysis.

One method to overcome the limitations between heterogeneous and homogeneous catalysis is to combine both classes of catalysis.^[121] This catalyst design principle is commonly referred to as heterogenization of homogeneous catalysts. The design idea for this is to combine the advantages in tunable activity and selectivity of homogeneous catalysts with the recyclability of the heterogeneous counterparts. The most common way to achieve this is to anchor molecular catalysts onto the surface of a solid support material. By the formation of a covalent bond between the support material and the ligand scaffold of the metal catalyst the active metal center is remained unchanged. A prerequisite for this immobilization strategy is the presence of controlled and uniform anchoring sites on the support material. Moreover, it has to be ensured, that the anchor site at the molecular catalyst is orthogonally reacting with the support material, while maintaining a stable environment at the metal center.^[36,122,123]

Most commonly micro- and mesoporous materials are applied as support materials, since they offer high surface areas for catalytic processes besides enabling a sufficient diffusion of substrates and products. Among the most studied carrier materials is mesoporous silica.^[124,125] Here, the surface hydroxyl groups are reacting with e.g. an alkoxy silane or phosphinite group attached on the ligand in order to immobilize the transition metal catalysts.^[126] Besides the advantage of having a cheap and readily available material, the ill-defined anchoring sites are a substantial drawback. Reports have shown that this can result into an undesired anchoring of the molecular catalyst via the metal center as side reaction. Using a thermal treatment method, the distances between anchoring sites can be decreased in silica materials to afford mostly ligand bound catalysts.^[127]

Another class of material that is currently intensively investigated as support for homogeneous catalysts are MOFs.^[128] In MOFs, the anchoring sites are well-defined owing to the arrangement in crystalline structures.^[129] Among the broad range of available MOF structures, frameworks based on zirconia clusters as metal nodes have been intensively investigated for the anchoring of molecular catalysts.^[130] These MOFs offer open hydroxy sites that are especially prone for anchoring carboxylic acids that can be easily integrated into the ligands of homogeneous catalysts. Examples for this are the immobilization of an iridium pincer complex for the gas phase hydrogenation^[131] or the anchoring of a bipyridine ligand, which can subsequently complex a nickel catalyst for ethene dimerization.^[132] Another approach is the incorporation of ligand scaffolds into the backbone of the linkers of

the MOFs, which was demonstrated among others for the introduction of a palladium pincer complex.^[133] Alternatively, the ligand sphere can be constructed by modifying the linker post-synthetically to form a binding pocket for the immobilization of a metal center to enable e.g. ethylene dimerization.^[134] However, MOFs are often limited in their thermal stabilities and prone to hydrolysis, limiting their application in catalysis significantly.

An alternative to the previously described porous materials are MPNs.^[135] This class of materials has shown especially prone as support for molecular catalysts. They can be designed to afford isolated anchoring points for metal catalysts, while their rigid C–C bonded backbone ensures high thermal and especially chemical stabilities. Using this approach not only the reusability of homogeneous catalysts can be improved, but most interestingly the immobilized catalysts can be used under conditions, which would not be applicable to the homogeneous catalyst. For instance, the immobilization of an iridium pincer complex on a hydroxy functionalized MPN was used for gas phase hydrogenation of alkenes.^[136] Here, the sustainability of the catalytic system is further improved by avoiding the use of solvents, necessary in homogeneous catalysis. Moreover, the polymer backbone offers additional possibilities to further tune the catalyst. By the introduction of hydrophobic or hydrophilic groups the reaction environment can be adjusted to the need of the reaction at hand. This opens the chance to repel certain molecules from the catalyst sites, protecting them against poisoning and offering the possibility towards tandem catalysis. Besides the advances made on the use of MPNs as porous materials for the anchoring of homogeneous metal catalysts, future challenges like pore accessibility have to be tackled to make this approach towards the relevant for chemical industry.^[137]

2.7 Photocatalysis for Organic Transformations

2.7.1 General Principles of Photocatalysis

Over millions of years nature has developed the most elegant ways to utilize sunlight as infinitely available energy source for (bio)chemical processes. Inspired by this role model synthetic chemists were also seeking to explore the use of the more than 100 000 terawatt of solar light reaching the earth for the use in organic reactions.^[138] This concept has successfully been applied in research, where photocatalysts expand the scope of organic transformations, by offering alternative reaction pathways. However, traditional photochemical reactions were mostly powered using high energy ultraviolet (UV) light, where often selectivity problems occurred due to the high photon energies. The recent development of novel molecular photocatalysts (PC) that can absorb visible light has opened new avenues for the application of photocatalysis in organic chemistry. However, this class of PCs is relying on homogeneously used rare metal catalysts, which renders recyclability nearly impossible and decreases therefore the sustainability of this approach. The development of new heterogeneous alternatives has been the focus of research in the recent years.

Knowledge on the fundamentals of the electronic state structure and the transition processes between them is a prerequisite to understand the basics of photocatalytic chemical reactions. The electronic and vibronic states and the transition between them is illustrated in a Jablonski diagram (Figure 1.1). When a chromophore is irradiated with a suitable wavelength it is transitioning from its singlet ground state (HOMO, S_0) to the vibronically activated first singlet excited state (LUMO, S_1). Through vibrational relaxation, which is a non-radiative energy dissipation, the chromophore arrives at the vibrational ground level of the singlet excited state. Typically, the relaxation to the ground state (S_0) proceeds by fluorescence ($S_1 \rightarrow S_0$). This transition within the same spin states is a spin-allowed process and occurs therefore readily. This results in short life-times of the single states ($<10^{-10}$ to 10^{-7} s). An alternative pathway is that molecules can undergo the spin-forbidden process of intersystem crossing (ISC; $S_1 \rightarrow T_1$). The transition from the excited triplet spin state to the ground state is the radiative transition of phosphorescence ($T_1 \rightarrow S_0$). As ISC, phosphorescence is also a spin-forbidden process, due to the transition of states with different spin multiplicity, which results in significantly longer life-times compared to fluorescence ($>10^{-7}$ s).

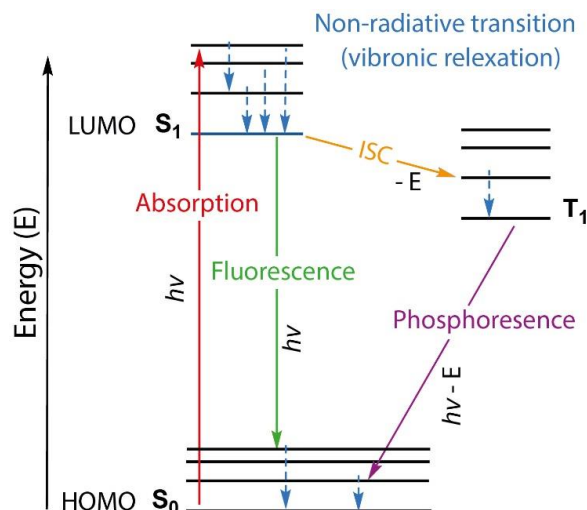


Figure 13. Jablonski diagram for the illustration of a molecule's electronic and vibronic states and the transition between the states.

A crucial factor for photocatalysis are long excited state lifetimes since it gives the excited catalyst sufficient time to conduct the reaction before it relaxes to its ground state (Figure 13). Here the photocatalysts absorb the visible light and reach the excited state (PC^*) that can activate a target molecule (A ; substrate, reagent, co-catalyst or intermediate) through energy or electron transfer. During this process the photocatalyst relaxes to its ground state, while the target molecule is transferred into a reactive intermediate (A^*). This activated species is then itself forming the product by or after dissociation with the photocatalyst. Therefore, the diffusion between the excited state of the PC and the target moiety has to be shorter than the lifetime of PC^* to enable productive photocatalysis.

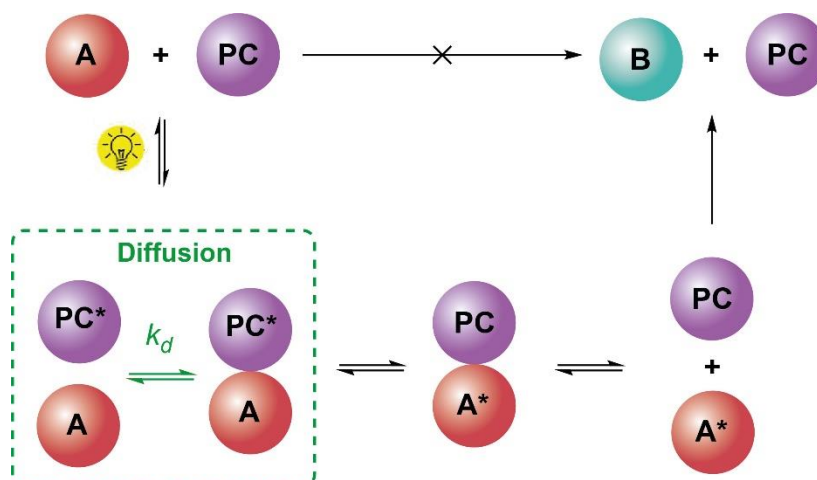


Figure 14. Key events to initiate reactions with a photocatalyst.

2.7.2 Metallaphotocatalytic Cross-Couplings

Metal catalyzed cross-coupling reactions are ranging among the most important reactions in the construction of molecular scaffolds and have since transformed the fields of organic and pharmaceutical chemistry. The major drawback in this regard is the use of a homogeneous palladium catalyst to perform these reactions. Since palladium is among the scarcest metals, the development of alternative cross-coupling pathways, replacing palladium with a more abundant and thus sustainable metal catalyst, is highly needed.^[139] With its close proximity in the periodic table of elements, nickel would provide an attractive alternative for palladium. The abundance in the earth's crust of nickel is compared to palladium 4000 times larger, which makes the prize of the metal much cheaper than the comparable noble metal alternatives. Moreover, nickel also shows a similar chemical behavior to Pd, with the same oxidation states available necessary for the cross-coupling transformations. However, the replacement of the noble metal for cross-coupling reactions renders a challenging task, due to the formation of a thermodynamically stable Ni^{II} species after the oxidative addition of an aryl halide to a Ni^0 complex and subsequent ligand exchange. Therefore, the formation of the desired carbon–heteroatom bond upon reductive elimination is not formed readily.^[140] Conventional methods for the destabilization of the Ni^{II} intermediate are using highly tuned ligands, strong bases in combination with high temperatures, making the process unsustainable.^[141–143] Less than a decade ago, it was shown that this nickel catalysts could perform the cross-coupling reactions very efficiently under mild conditions using photoredox catalysis and light for the destabilization of the intermediate.^[144–146] Since then, the synthesis method has been intensively investigated for different carbon–heteroatom (C–X) and carbon–carbon (C–C) cross-couplings.^[147–149] One major drawback of this procedure is the use of homogeneous photocatalysts and nickel complexes for the reactions. Moreover, the photocatalysts that are commonly applied are Ir or Ru polypyridyl complexes, which are themselves scarce noble metals. In recent years there has been efforts to replace the homogenous noble metal complexes with more sustainable heterogeneous methods, on a pathway towards a single material dual catalyst, which is described in the following chapter.

2.7.3 Towards Fully Heterogeneous Metallaphotocatalysis

Typically, homogeneous Ir or Ru polypyridyl complexes are used, which upon irradiation create the excited species by the donation or acceptance of a single electron in a reductive or oxidative quenching cycle.^[150] Various reports show, that the immobilization of such complexes onto linear polymers,^[151] as well as MOFs^[152,153] and COFs^[115,119] can be realized, by complexation with a framework bound bipyridine unit. Using this approach, the sustainability of the system has been drastically improved by the possibility to recycle the noble metal for multiple reaction cycles. However, creating a noble-metal free alternative was highly desired, which was found when applying semiconductors as photocatalysts. In huge contrast to conventional catalysis, the homogeneous photocatalyst can be substituted with a heterogeneous alternative straightforwardly, since both operate on the same energy and electron transfer processes.^[154]

Conventional homogeneous photocatalytic reactions proceed as single electron transfers. The photocatalyst in the excited state is quenched by either donating or accepting a single electron. The electron transfer can involve a substrate, reagent or co-catalyst. Subsequently, depending on the reaction conditions, the quenching cycle can be closed by either an oxidative or reductive quenching cycle, forming oxidized and reduced species of the photocatalyst during this process. The solid photocatalyst absorbs the light and if the energy is sufficiently large, electrons are excited from the valence band to the conduction band, creating an electron-hole pair. Here the holes and electrons act as the species enabling single electron transfer.

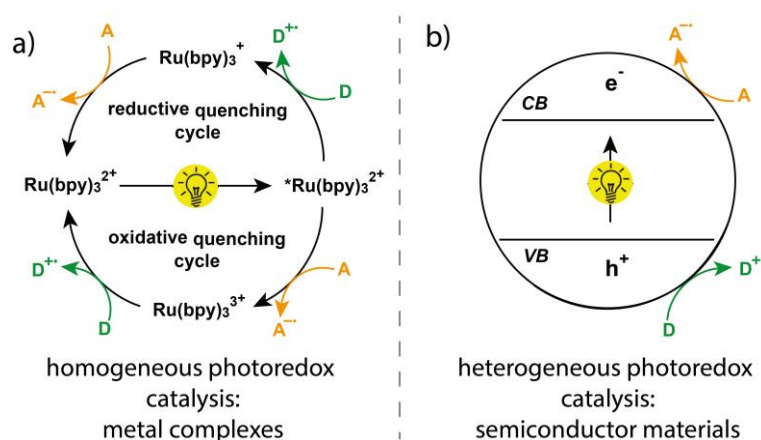


Figure 15. Homogeneous and heterogeneous photoredox catalysis.

This strategy has been demonstrated on a range of materials, including traditional semiconductors like titanium dioxide, which has shown tunability in its photochemical behavior by surface complexation or decoration with organic dyes as sensitizer.^[155,156] Moreover, quantum dots^[157–159] as well as perovskites^[160] carbon nitrides^[161,162] and microporous polymers^[163] can be used as heterogeneous alternatives to the homogeneous Ir and Ru complex photocatalyst. Since covalent organic frameworks can also be considered as a class of semiconductor materials, COFs have been demonstrated as fully organic photocatalyst material for dual-nickel cross-couplings. The optical properties of the material can be tuned by the choice of the size of the conjugated system, the introduction of donor-acceptor structures or the use of a chromophore that absorbs light in the visible range of the spectrum. The group of van der Voort reported in 2021 the synthesis of an imine-linked donor-acceptor COF based on the reticulation of an acenaphthenequinone unit with a triazine based linker to enable C–S coupling.^[116] In the same year a pyrene based cyanovinylene-COF was reported for C–O cross-couplings.^[117] Within the scope of this thesis the introduction of an acridine unit within the backbone of a β -ketoenamine framework material resulted in an efficient photocatalyst, which was used for the semiheterogeneous formation of carbon–nitrogen bonds.^[118]

Moving even one step further, methods for anchoring the nickel catalyst were developed to reach the goal of a fully heterogeneous singular material. Here, similar methods as for the immobilization of the iridium or ruthenium photocatalyst were employed. Mostly, the introduction of a bipyridine ligand site into the materials resulted in an efficient complexing of the transition metal. Using this method - in combination with the approaches for solid noble metal free photocatalysts - fully heterogeneous and recyclable metallaphotocatalyst have been developed as a part of this thesis.

References

- [1] J. M. Thomas, K. D. M. Harris, *Energy Environ. Sci.* **2016**, *9*, 687–708.
- [2] International Energy Agency (IEA), *Technology Roadmap Energy and GHG Reductions in the Chemical Industry via Catalytic Processes*, **2013**.
- [3] L. Candish, K. D. Collins, G. C. Cook, J. J. Douglas, A. Gómez-Suárez, A. Jolit, S. Keess, *Chem. Rev.* **2022**, *122*, 2907–2980.
- [4] R. Cannalire, S. Pelliccia, L. Sancineto, E. Novellino, G. C. Tron, M. Giustiniano, *Chem. Soc. Rev.* **2021**, *50*, 866–897.
- [5] H. G. Yayla, F. Peng, I. K. Mangion, M. McLaughlin, L. C. Campeau, I. W. Davies, D. A. Dirocco, R. R. Knowles, *Chem. Sci.* **2016**, *7*, 2066–2073.
- [6] B. L. Su, C. Sanchez, X. Y. Yang, *Hierarchically Structured Porous Materials: From Nanoscience to Catalysis, Separation, Optics, Energy, and Life Science*, Wiley-VCH, Weinheim, **2011**.
- [7] A. Thomas, *Angew. Chem. Int. Ed.* **2010**, *49*, 8328–8344.
- [8] F. Schüth, W. Schmidt, *Adv. Mater.* **2002**, *14*, 629–638.
- [9] A. Thomas, *Nat. Commun.* **2020**, *11*, 11–13.
- [10] K. S. W. Sing, D. H. Everett, R. A. W. Haul, L. Moscou, R. A. Pierotti, J. Rouquerol, T. Siemieniowska, *Pure Appl. Chem.* **1985**, *57*, 603–619.
- [11] M. Thommes, K. Kaneko, A. V. Neimark, J. P. Olivier, F. Rodriguez-Reinoso, J. Rouquerol, K. S. W. Sing, *Pure Appl. Chem.* **2015**, *87*, 1051–1069.
- [12] S. Brunauer, P. H. Emmett, E. Teller, *J. Am. Chem. Soc.* **1938**, *60*, 309–319.
- [13] A. G. Slater, A. I. Cooper, *Science* **2015**, *348*, aaa8075.
- [14] N. E. R. Zimmermann, M. Haranczyk, *Cryst. Growth Des.* **2016**, *16*, 3043–3048.
- [15] E. M. Flanigen, R. W. Broach, S. T. Wilson, *Zeolites Ind. Sep. Catal.* **2010**, 1–26.
- [16] L. B. McCusker, D. H. Olson, C. Baerlocher, *Atlas of Zeolite Framework Types*, **2007**.
- [17] O. M. Yaghi, G. Li, H. Li, *Nature* **1995**, *378*, 703–706.
- [18] H. C. Zhou, J. R. Long, O. M. Yaghi, *Chem. Rev.* **2012**, *112*, 673–674.
- [19] S. M. Cohen, *Chem. Rev.* **2012**, *112*, 970–1000.
- [20] X. Zhang, Z. Chen, X. Liu, S. L. Hanna, X. Wang, R. Taheri-Ledari, A. Maleki, P. Li, O. K. Farha, *Chem. Soc. Rev.* **2020**, *49*, 7406–7427.
- [21] W. Fan, X. Zhang, Z. Kang, X. Liu, D. Sun, *Coord. Chem. Rev.* **2021**, *443*, 213968.

- [22] I. Stassen, N. Burtch, A. Talin, P. Falcaro, M. Allendorf, R. Ameloot, *Chem. Soc. Rev.* **2017**, *46*, 3185–3241.
- [23] Y. Tian, G. Zhu, *Chem. Rev.* **2020**, *120*, 8934–8986.
- [24] N. Chaoui, M. Trunk, R. Dawson, J. Schmidt, A. Thomas, *Chem. Soc. Rev.* **2017**, *46*, 3302–3321.
- [25] W. Lu, D. Yuan, J. Sculley, D. Zhao, R. Krishna, H. C. Zhou, *J. Am. Chem. Soc.* **2011**, *133*, 18126–18129.
- [26] T. Ben, H. Ren, M. Shengqian, D. Cao, J. Lan, X. Jing, W. Wang, J. Xu, F. Deng, J. M. Simmons, S. Qiu, G. Zhu, *Angew. Chem. Int. Ed.* **2009**, *48*, 9457–9460.
- [27] K. Sonogashira, Y. Tohda, N. Hagihara, *Tetrahedron Lett.* **1975**, 4467–4470.
- [28] T. Yamamoto, A. Morita, Y. Miyazaki, T. Maruyama, H. Wakayama, Z.-H. Zhou, Y. Nakamura, T. Kanbara, S. Sasaki, K. Kubota, *Macromolecules* **1992**, *25*, 1214–1223.
- [29] J. X. Jiang, F. Su, A. Trewin, C. D. Wood, N. L. Campbell, H. Niu, C. Dickinson, A. Y. Ganin, M. J. Rosseinsky, Y. Z. Khimyak, A. I. Cooper, *Angew. Chem. Int. Ed.* **2007**, *46*, 8574–8578.
- [30] M. Trunk, A. Herrmann, H. Bildirir, A. Yassin, J. Schmidt, A. Thomas, *Chem. Eur. J.* **2016**, *22*, 7179–7183.
- [31] Y. Zhu, H. Yang, Y. Jin, W. Zhang, *Chem. Mater.* **2013**, *25*, 3718–3723.
- [32] Y. Hu, C. Wu, Q. Pan, Y. Jin, R. Lyu, V. Martinez, S. Huang, J. Wu, L. J. Wayment, N. A. Clark, M. B. Raschke, Y. Zhao, W. Zhang, *Nat. Synth.* **2022**, *1*, 449–454.
- [33] J. Schmidt, M. Werner, A. Thomas, *Macromolecules* **2009**, *42*, 4426–4429.
- [34] A. J. Porath, M. A. Hettiarachchi, S. Li, J. R. Bour, *Chem. Commun.* **2022**, *58*, 6841–6844.
- [35] T. Yamamoto, S. Wakabayashi, K. Osakada, *J. Organomet. Chem.* **1992**, *428*, 223–237.
- [36] C. Copéret, M. Chabanas, R. Petroff Saint-Arroman, J.-M. Basset, *Angew. Chem. Int. Ed.* **2003**, *42*, 156–181.
- [37] M. D. Korzyński, C. Copéret, *Trends Chem.* **2021**, *3*, 850–862.
- [38] S. Y. Ding, W. Wang, *Chem. Soc. Rev.* **2013**, *42*, 548–568.
- [39] K. Geng, T. He, R. Liu, S. Dalapati, K. T. Tan, Z. Li, S. Tao, Y. Gong, Q. Jiang, D. Jiang, *Chem. Rev.* **2020**, *120*, 8814–8933.
- [40] A. P. Côté, A. I. Benin, N. W. Ockwig, M. O’Keeffe, A. J. Matzger, O. M. Yaghi,

- Science* **2005**, *310*, 1166–1171.
- [41] S. Y. Ding, J. Gao, Q. Wang, Y. Zhang, W. G. Song, C. Y. Su, W. Wang, *J. Am. Chem. Soc.* **2011**, *133*, 19816–19822.
- [42] S. Kandambeth, A. Mallick, B. Lukose, M. V. Mane, T. Heine, R. Banerjee, *J. Am. Chem. Soc.* **2012**, *134*, 19524–19527.
- [43] A. Acharjya, P. Pachfule, J. Roeser, F. J. Schmitt, A. Thomas, *Angew. Chem. Int. Ed.* **2019**, *58*, 14865–14870.
- [44] J. Feng, Y. J. Zhang, S. H. Ma, C. Yang, Z. P. Wang, S. Y. Ding, Y. Li, W. Wang, *J. Am. Chem. Soc.* **2022**, *144*, 6594–6603.
- [45] X. Guan, Y. Ma, H. Li, Y. Yusran, M. Xue, Q. Fang, Y. Yan, V. Valtchev, S. Qiu, *J. Am. Chem. Soc.* **2018**, *140*, 4494–4498.
- [46] J. Maschita, T. Banerjee, G. Savasci, F. Haase, C. Ochsenfeld, B. V. Lotsch, *Angew. Chem. Int. Ed.* **2020**, *59*, 15750–15758.
- [47] B. P. Biswal, S. Chandra, S. Kandambeth, B. Lukose, T. Heine, R. Banerjee, *J. Am. Chem. Soc.* **2013**, *135*, 5328–5331.
- [48] S. Karak, S. Kandambeth, B. P. Biswal, H. S. Sasmal, S. Kumar, P. Pachfule, R. Banerjee, *J. Am. Chem. Soc.* **2017**, *139*, 1856–1862.
- [49] W. Zhao, P. Yan, H. Yang, M. Bahri, A. M. James, H. Chen, L. Liu, B. Li, Z. Pang, R. Clowes, N. D. Browning, J. W. Ward, Y. Wu, A. I. Cooper, *Nat. Synth.* **2022**, *1*, 87–95.
- [50] X. Wang, J. Yang, X. Shi, Z. Zhang, C. Yin, Y. Wang, X. Wang, J. Yang, X. Shi, Z. Zhang, C. Yin, Y. Wang, *Small* **2022**, *18*, 2107108.
- [51] L. Wang, C. Xu, W. Zhang, Q. Zhang, M. Zhao, C. Zeng, Q. Jiang, C. Gu, Y. Ma, *J. Am. Chem. Soc.* **2022**, *144*, 8961–8968.
- [52] S. Kim, H. C. Choi, *Commun. Chem.* **2019**, *21*, 1–8.
- [53] N. L. Campbell, R. Clowes, L. K. Ritchie, A. I. Cooper, *Chem. Mater.* **2009**, *21*, 204–206.
- [54] Y. Zhao, L. Guo, F. Gándara, Y. Ma, Z. Liu, C. Zhu, H. Lyu, C. A. Trickett, E. A. Kapustin, O. Terasaki, O. M. Yaghi, *J. Am. Chem. Soc.* **2017**, *139*, 13166–13172.
- [55] F. J. Uribe-Romo, J. R. Hunt, H. Furukawa, C. Klöck, M. O’Keeffe, O. M. Yaghi, *J. Am. Chem. Soc.* **2009**, *131*, 4570–4571.
- [56] H. Liu, J. Chu, Z. Yin, X. Cai, L. Zhuang, H. Deng, *Chem* **2018**, *4*, 1696–1709.

- [57] L. Grunenberg, G. Savasci, M. W. Terban, V. Duppel, I. Moudrakovski, M. Etter, R. E. Dinnebier, C. Ochsenfeld, B. V. Lotsch, *J. Am. Chem. Soc.* **2021**, *143*, 3430–3438.
- [58] P. J. Waller, S. J. Lyle, T. M. Osborn Popp, C. S. Diercks, J. A. Reimer, O. M. Yaghi, *J. Am. Chem. Soc.* **2016**, *138*, 15519–15522.
- [59] F. Haase, E. Troschke, G. Savasci, T. Banerjee, V. Duppel, S. Dörfler, M. M. J. Grundei, A. M. Burow, C. Ochsenfeld, S. Kaskel, B. V. Lotsch, *Nat. Commun.* **2018**, *9*, 2600.
- [60] Z. B. Zhou, P. J. Tian, J. Yao, Y. Lu, Q. Y. Qi, X. Zhao, *Nat. Commun.* **2022**, *13*, 2180.
- [61] A. M. Evans, M. J. Strauss, A. R. Corcos, Z. Hirani, W. Ji, L. S. Hamachi, X. Aguilar-Enriquez, A. D. Chavez, B. J. Smith, W. R. Dichtel, *Chem. Rev.* **2022**, *122*, 442–564.
- [62] H. M. El-Kaderi, J. R. Hunt, J. L. Mendoza-Cortés, A. P. Côté, R. E. Taylor, M. O’Keeffe, O. M. Yaghi, *Science* **2007**, *316*, 268–272.
- [63] X. Chen, M. Addicoat, E. Jin, H. Xu, T. Hayashi, F. Xu, N. Huang, S. Irle, D. Jiang, *Sci. Rep.* **2015**, *5*, 14650.
- [64] Y. Zeng, R. Zou, Z. Luo, H. Zhang, X. Yao, X. Ma, R. Zou, Y. Zhao, *J. Am. Chem. Soc.* **2015**, *137*, 1020–1023.
- [65] H. Li, Q. Pan, Y. Ma, X. Guan, M. Xue, Q. Fang, Y. Yan, V. Valtchev, S. Qiu, *J. Am. Chem. Soc.* **2016**, *138*, 14783–14788.
- [66] R. R. Liang, A. Ru-Han, S. Q. Xu, Q. Y. Qi, X. Zhao, *J. Am. Chem. Soc.* **2020**, *142*, 70–74.
- [67] Z. Xiao, L. Li, Y. Tang, Z. Cheng, H. Pan, D. Tian, R. Wang, *Energy Storage Mater.* **2018**, *12*, 252–259.
- [68] J. Hu, J. Zhang, Z. Lin, L. Xie, S. Liao, X. Chen, *Chem. Mater.* **2022**, *34*, 5249–5257.
- [69] N. Huang, L. Zhai, D. E. Coupry, M. A. Addicoat, K. Okushita, K. Nishimura, T. Heine, D. Jiang, *Nat. Commun.* **2016**, *7*, 12325.
- [70] H. Yang, Y. Du, S. Wan, G. D. Trahan, Y. Jin, W. Zhang, *Chem. Sci.* **2015**, *6*, 4049–4053.
- [71] L. A. Baldwin, J. W. Crowe, M. D. Shannon, C. P. Jaroniec, P. L. McGrier, *Chem. Mater.* **2015**, *27*, 6169–6172.
- [72] J. W. Crowe, L. A. Baldwin, P. L. McGrier, *J. Am. Chem. Soc.* **2016**, *138*, 10120–10123.

- [73] Z. F. Pang, S. Q. Xu, T. Y. Zhou, R. R. Liang, T. G. Zhan, X. Zhao, *J. Am. Chem. Soc.* **2016**, *138*, 4710–4713.
- [74] T. Banerjee, F. Haase, S. Trenker, B. P. Biswal, G. Savasci, V. Duppel, I. Moudrakovski, C. Ochsenfeld, B. V. Lotsch, *Nat. Commun.* **2019**, *10*, 2689.
- [75] M. Hao, Z. Chen, X. Liu, X. Liu, J. Zhang, H. Yang, G. I. N. Waterhouse, X. Wang, S. Ma, *CCS Chem.* **2022**, *4*, 1–14.
- [76] A. Nagai, Z. Guo, X. Feng, S. Jin, X. Chen, X. Ding, D. Jiang, *Nat. Commun.* **2011**, *2*, 536.
- [77] N. Huang, R. Krishna, D. Jiang, *J. Am. Chem. Soc.* **2015**, *137*, 7079–7082.
- [78] N. Huang, X. Chen, R. Krishna, D. Jiang, *Angew. Chem. Int. Ed.* **2015**, *54*, 2986–2990.
- [79] Q. Xu, S. Tao, Q. Jiang, D. Jiang, *Angew. Chem. Int. Ed.* **2020**, *59*, 4557–4563.
- [80] Y. Xie, T. Pan, Q. Lei, C. Chen, X. Dong, Y. Yuan, J. Shen, Y. Cai, C. Zhou, I. Pinna, Y. Han, *Angew. Chem. Int. Ed.* **2021**, *60*, 22432–22440.
- [81] T. Zhou, X. Huang, Z. Mi, Y. Zhu, R. Wang, C. Wang, J. Guo, *Polym. Chem.* **2021**, *12*, 3250–3256.
- [82] X. Zhao, P. Pachfule, A. Thomas, *Chem. Soc. Rev.* **2021**, *50*, 6871–6913.
- [83] Z. Wang, S. Zhang, Y. Chen, Z. Zhang, S. Ma, *Chem. Soc. Rev.* **2020**, *49*, 708–735.
- [84] H. Furukawa, O. M. Yaghi, *J. Am. Chem. Soc.* **2009**, *131*, 8875–8883.
- [85] S. H. Sang, H. Furukawa, O. M. Yaghi, W. A. Goddard, *J. Am. Chem. Soc.* **2008**, *130*, 11580–11581.
- [86] S. Chandra, T. Kundu, K. Dey, M. Addicoat, T. Heine, R. Banerjee, *Chem. Mater.* **2016**, *28*, 1489–1494.
- [87] H. Xu, S. Tao, D. Jiang, *Nat. Mater.* **2016**, *15*, 722–726.
- [88] K. Chandran Ranjeesh, R. Illathvalappil, S. Dnyaneshwar Veer, J. Peter, V. Chandrakant Wakchaure, K. Vipin Raj, S. Kurungot, S. Santhosh Babu, *J. Am. Chem. Soc.* **2019**, *141*, 14950–14954.
- [89] Y. Du, H. Yang, J. M. Whiteley, S. Wan, Y. Jin, S. H. Lee, W. Zhang, *Angew. Chem. Int. Ed.* **2016**, *55*, 1737–1741.
- [90] Q. Ai, Q. Fang, J. Liang, X. Xu, T. Zhai, G. Gao, H. Guo, G. Han, L. Ci, J. Lou, *Nano Energy* **2020**, *72*, 104657.
- [91] A. M. Evans, A. Giri, V. K. Sangwan, S. Xun, M. Bartnof, C. G. Torres-Castanedo,

- H. B. Balch, M. S. Rahn, N. P. Bradshaw, E. Vitaku, D. W. Burke, H. Li, M. J. Bedzyk, F. Wang, J. L. Brédas, J. A. Malen, A. J. H. McGaughey, M. C. Hersam, W. R. Dichtel, P. E. Hopkins, *Nat. Mater.* **2021**, *20*, 1142–1148.
- [92] M. K. Hota, S. Chandra, Y. Lei, X. Xu, M. N. Hedhili, A. H. Emwas, O. Shekhah, M. Eddaoudi, H. N. Alshareef, *Adv. Funct. Mater.* **2022**, *32*, 2201120.
- [93] Y. Yang, K. Börjesson, *Trends Chem.* **2022**, *4*, 60–75.
- [94] R. B. Rashid, A. M. Evans, L. A. Hall, R. R. Dasari, E. K. Roesner, S. R. Marder, D. M. D’Allesandro, W. R. Dichtel, J. Rivnay, *Adv. Mater.* **2022**, *34*, 2110703.
- [95] S. Halder, D. Chakraborty, B. Roy, G. Banappanavar, K. Rinku, D. Mullangi, P. Hazra, D. Kabra, R. Vaidhyanathan, *J. Am. Chem. Soc.* **2018**, *140*, 13367–13374.
- [96] W. K. Haug, E. M. Moscarello, E. R. Wolfson, P. L. McGrier, *Chem. Soc. Rev.* **2020**, *49*, 839–864.
- [97] X. Liu, D. Huang, C. Lai, G. Zeng, L. Qin, H. Wang, H. Yi, B. Li, S. Liu, M. Zhang, R. Deng, Y. Fu, L. Li, W. Xue, S. Chen, *Chem. Soc. Rev.* **2019**, *48*, 5266–5302.
- [98] J. Guo, D. Jiang, *ACS Cent. Sci.* **2020**, *6*, 869–879.
- [99] P. Pachfule, S. Kandambeth, D. Díaz Díaz, R. Banerjee, *Chem. Commun.* **2014**, *50*, 3169–3172.
- [100] Q. Guan, L. Le Zhou, Y. Bin Dong, *Chem. Soc. Rev.* **2022**, *51*, 6307–6416.
- [101] H. Wang, H. Wang, Z. Wang, L. Tang, G. Zeng, P. Xu, M. Chen, T. Xiong, C. Zhou, X. Li, D. Huang, Y. Zhu, Z. Wang, J. Tang, *Chem. Soc. Rev.* **2020**, *49*, 4135–4165.
- [102] T. Banerjee, K. Gottschling, G. Savasci, C. Ochsenfeld, B. V. Lotsch, *ACS Energy Lett.* **2018**, *3*, 400–409.
- [103] P. Pachfule, A. Acharjya, J. Roeser, T. Langenhahn, M. Schwarze, R. Schomäcker, A. Thomas, J. Schmidt, *J. Am. Chem. Soc.* **2018**, *140*, 1423–1427.
- [104] J. Yang, A. Acharjya, M. Y. Ye, J. Rabeah, S. Li, Z. Kochovski, S. Youk, J. Roeser, J. Grüneberg, C. Penshke, M. Schwarze, T. Wang, Y. Lu, R. van de Krol, M. Oschatz, R. Schomäcker, P. Saalfrank, A. Thomas, *Angew. Chem. Int. Ed.* **2021**, *60*, 19797–19803.
- [105] S. Lin, C. S. Diercks, Y. B. Zhang, N. Kornienko, E. M. Nichols, Y. Zhao, A. R. Paris, D. Kim, P. Yang, O. M. Yaghi, C. J. Chang, *Science* **2015**, *349*, 1208–1213.
- [106] S. Yang, W. Hu, X. Zhang, P. He, B. Pattengale, C. Liu, M. Cendejas, I. Hermans, X. Zhang, J. Zhang, J. Huang, *J. Am. Chem. Soc.* **2018**, *140*, 14614–14618.

- [107] S. Gisbertz, B. Pieber, *ChemPhotoChem* **2020**, *4*, 456–475.
- [108] P. F. Wei, M. Z. Qi, Z. P. Wang, S. Y. Ding, W. Yu, Q. Liu, L. K. Wang, H. Z. Wang, W. K. An, W. Wang, *J. Am. Chem. Soc.* **2018**, *140*, 4623–4631.
- [109] Y. Nailwal, A. D. D. Wonanke, M. A. Addicoat, S. K. Pal, *Macromolecules* **2021**, *54*, 6595–6604.
- [110] J. Yuan, Q. Xia, W. Zhu, C. Wu, B. Wang, B. Liu, X. Yang, Y. Xu, H. Xu, *ChemPhotoChem* **2020**, *4*, 445–450.
- [111] Y. Zhi, Z. Li, X. Feng, H. Xia, Y. Zhang, Z. Shi, Y. Mu, X. Liu, *J. Mater. Chem. A* **2017**, *5*, 22933–22938.
- [112] W. Liu, Q. Su, P. Ju, B. Guo, H. Zhou, G. Li, Q. Wu, *ChemSusChem* **2017**, *10*, 664–669.
- [113] K. Wang, H. Jiang, H. Liu, H. Chen, F. Zhang, *ACS Catal.* **2022**, *12*, 6068–6080.
- [114] S. Liu, W. Pan, S. Wu, X. Bu, S. Xin, J. Yu, H. Xu, X. Yang, *Green Chem.* **2019**, *21*, 2905–2910.
- [115] A. López-Magano, B. Ortín-Rubio, I. Imaz, D. Maspoch, J. Alemán, R. Mas-Ballesté, *ACS Catal.* **2021**, *11*, 12344–12354.
- [116] H. Chen, W. Liu, A. Laemont, C. Krishnaraj, X. Feng, F. Rohman, M. Meledina, Q. Zhang, R. Van Deun, K. Leus, P. Van Der Voort, *Angew. Chemie* **2021**, *133*, 10915–10922.
- [117] W. Dong, Y. Yang, Y. Xiang, S. Wang, P. Wang, J. Hu, L. Rao, H. Chen, *Green Chem.* **2021**, *23*, 5797–5805.
- [118] M. Traxler, S. Gisbertz, P. Pachfule, J. Schmidt, J. Roeser, S. Reischauer, J. Rabeah, B. Pieber, A. Thomas, *Angew. Chem. Int. Ed.* **2022**, *61*, e202117738.
- [119] A. Jati, K. Dey, M. Nurhuda, M. A. Addicoat, R. Banerjee, B. Maji, *J. Am. Chem. Soc.* **2022**, *144*, 7822–7833.
- [120] D. Steinborn, *Fundamentals of Organometallic Catalysis*, Wiley-VCH, Weinheim, **2012**.
- [121] C. Li, Y. Liu, Eds. , *Bridging Heterogeneous and Homogeneous Catalysis*, Wiley-VCH, Weinheim, **2014**.
- [122] M. D. Korzyński, C. Copéret, *Trends Chem.* **2021**, *3*, 850–862.
- [123] M. Rose, *ChemCatChem* **2014**, *6*, 1166–1182.
- [124] A. Corma, H. Garcia, *Adv. Synth. Catal.* **2006**, *348*, 1391–1412.

- [125] K. Motokura, S. Ding, K. Usui, Y. Kong, *ACS Catal.* **2021**, *11*, 11985–12018.
- [126] Z. Huang, M. Brookhart, A. S. Goldman, S. Kundu, A. Ray, S. L. Scott, B. C. Vicente, *Adv. Synth. Catal.* **2009**, *351*, 188–206.
- [127] C. Copéret, F. Allouche, K. W. Chan, M. P. Conley, M. F. Delley, A. Fedorov, I. B. Moroz, V. Mougel, M. Pucino, K. Searles, K. Yamamoto, P. A. Zhizhko, *Angew. Chem. Int. Ed.* **2018**, *57*, 6398–6440.
- [128] A. Bavykina, N. Kolobov, I. S. Khan, J. A. Bau, A. Ramirez, J. Gascon, *Chem. Rev.* **2020**, *120*, 8468–8535.
- [129] J. L. C. Rowsell, O. M. Yaghi, *Microporous Mesoporous Mater.* **2004**, *73*, 3–14.
- [130] Q. Du, R. Rao, F. Bi, Y. Yang, W. Zhang, Y. Yang, N. Liu, X. Zhang, *Surfaces and Interfaces* **2022**, *28*, 101647.
- [131] M. Rimoldi, A. Nakamura, N. A. Vermeulen, J. J. Henkelis, A. K. Blackburn, J. T. Hupp, J. F. Stoddart, O. K. Farha, *Chem. Sci.* **2016**, *7*, 4980–4984.
- [132] S. T. Madrahimov, J. R. Gallagher, G. Zhang, Z. Meinhart, S. J. Garibay, M. Delferro, J. T. Miller, O. K. Farha, J. T. Hupp, S. T. Nguyen, *ACS Catal.* **2015**, *5*, 6713–6718.
- [133] S. A. Burgess, A. Kassie, S. A. Baranowski, K. J. Fritzsche, K. Schmidt-Rohr, C. M. Brown, C. R. Wade, *J. Am. Chem. Soc.* **2016**, *138*, 1780–1783.
- [134] J. Canivet, S. Aguado, Y. Schuurman, D. Farrusseng, *J. Am. Chem. Soc.* **2013**, *135*, 4195–4198.
- [135] F. M. Wissler, Y. Mohr, E. A. Quadrelli, J. Canivet, *ChemCatChem* **2020**, *12*, 1270–1275.
- [136] M. König, M. Rigo, N. Chaoui, T. Tran Ngoc, J. D. Epping, J. Schmidt, P. Pachfule, M. Ye, M. Trunk, J. F. Teichert, M. Drieß, A. Thomas, *Angew. Chem. Int. Ed.* **2020**, *59*, 19830–19834.
- [137] S. Hübner, J. G. De Vries, V. Farina, *Adv. Synth. Catal.* **2016**, *358*, 3–25.
- [138] J. Barber, *Chem. Soc. Rev.* **2009**, *38*, 185–196.
- [139] C. C. C. Johansson Seechurn, M. O. Kitching, T. J. Colacot, V. Snieckus, *Angew. Chem. Int. Ed.* **2012**, *51*, 5062–5085.
- [140] R. Han, G. L. Hillhouse, *J. Am. Chem. Soc.* **1997**, *119*, 8135–8136.
- [141] J. P. Wolfe, S. L. Buchwald, *J. Am. Chem. Soc.* **1997**, *119*, 6054–6058.
- [142] S. Ge, R. A. Green, J. F. Hartwig, *J. Am. Chem. Soc.* **2014**, *136*, 1617–1627.
- [143] J. P. Tassone, E. V England, P. M. Macqueen, M. J. Ferguson, M. Stradiotto,] J P

- Tassone, E. V England, P. M. Macqueen, M. Stradiotto, M. J. F. Erguson, *Angew. Chem. Int. Ed.* **2019**, *58*, 2485–2489.
- [144] J. Twilton, C. C. Le, P. Zhang, M. H. Shaw, R. W. Evans, D. W. C. MacMillan, *Nat. Rev. Chem.* **2017**, *1*, 0052.
- [145] K. L. Skubi, T. R. Blum, T. P. Yoon, *Chem. Rev.* **2016**, *116*, 10035–10074.
- [146] M. N. Hopkinson, B. Sahoo, J. L. Li, F. Glorius, *Chem. Eur. J.* **2014**, *20*, 3874–3886.
- [147] J. A. Milligan, J. P. Phelan, S. O. Badir, G. A. Molander, *Angew. Chem. Int. Ed.* **2019**, *58*, 6152–6163.
- [148] C. Zhu, H. Yue, L. Chu, M. Rueping, *Chem. Sci.* **2020**, *11*, 4051–4064.
- [149] C. Zhu, H. Yue, J. Jia, M. Rueping, *Angew. Chem. Int. Ed.* **2021**, *60*, 17810–17831.
- [150] F. Strieth-Kalthoff, M. J. James, M. Teders, L. Pitzer, F. Glorius, *Chem. Soc. Rev.* **2018**, *47*, 7190–7202.
- [151] Y. Pan, N. Zhang, C. H. Liu, S. Fan, S. Guo, Z. M. Zhang, Y. Y. Zhu, *ACS Catal.* **2020**, *10*, 11758–11767.
- [152] Y. Y. Zhu, G. Lan, Y. Fan, S. S. Veroneau, Y. Song, D. Micheroni, W. Lin, *Angew. Chem. Int. Ed.* **2018**, *57*, 14090–14094.
- [153] G. Lan, Y. Quan, M. Wang, G. T. Nash, E. You, Y. Song, S. S. Veroneau, X. Jiang, W. Lin, *J. Am. Chem. Soc.* **2019**, *141*, 15767–15772.
- [154] D. Friedmann, A. Hakki, H. Kim, W. Choi, D. Bahnemann, *Green Chem.* **2016**, *18*, 5391–5411.
- [155] S. Reischauer, B. Pieber, *iScience* **2021**, *24*, 102209.
- [156] Z. Zhao, S. Reischauer, B. Pieber, M. Delbianco, *Green Chem.* **2021**, *23*, 4524–4530.
- [157] J. A. Caputo, L. C. Frenette, N. Zhao, K. L. Sowers, T. D. Krauss, D. J. Weix, *J. Am. Chem. Soc.* **2017**, *139*, 4250–4253.
- [158] Y. Y. Liu, D. Liang, L. Q. Lu, W. J. Xiao, *Chem. Commun.* **2019**, *55*, 4853–4856.
- [159] Z. Zhang, K. Edme, S. Lian, E. A. Weiss, *J. Am. Chem. Soc.* **2017**, *139*, 4246–4249.
- [160] X. Zhu, Y. Lin, J. San Martin, Y. Sun, D. Zhu, Y. Yan, *Nat. Commun.* **2019**, *10*, 2843.
- [161] I. Ghosh, J. Khamrai, A. Savateev, N. Shlapakov, M. Antonietti, B. König, *Science* **2019**, *365*, 360–366.
- [162] S. Gisbertz, S. Reischauer, B. Pieber, *Nat. Catal.* **2020**, *3*, 611–620.
- [163] C. Cavedon, S. Gisbertz, S. Reischauer, S. Vogl, E. Sperlich, J. H. Burke, R. F. Wallick, S. Schrottke, W.-H. Hsu, L. Anghileri, Y. Pfeifer, N. Richter, C. Teutloff,

H. Müller-Werkmeister, D. Cambié, P. H. Seeberger, J. Vura-Weis, R. M. van der Veen, A. Thomas, B. Pieber, *Angew. Chem. Int. Ed.* **2022**, e202211433.

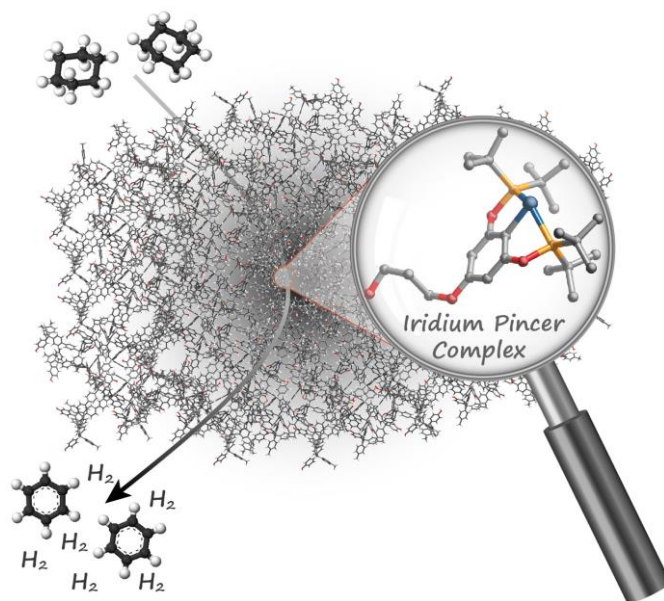
Chapter 3:

Anchoring an Iridium Pincer Complex in a Hydrophobic Microporous Polymer for Application in Continuous-Flow Alkane Dehydrogenation

M. König, **M. Traxler**, M. A. Rudolph, J. Schmidt, H. Küçükkeçeci, R. Schomäcker, A. Thomas

ChemCatChem **2022**, *14*, e202200811.

Accepted manuscript, DOI: <https://doi.org/10.1002/cctc.202200811>



An Iridium pincer complex was anchored in a multi-step post-synthetically modified microporous polymer with a highly hydrophobic character. The immobilized catalyst was applied in continuous-flow dehydrogenation of cyclohexane.

Abstract

An iridium pincer complex $\{p\text{-KO-C}_6\text{H}_2\text{-2,6-[OP}(t\text{-Bu)}_2\text{]}_2\}\text{Ir}(\text{C}_2\text{H}_4)$ is immobilized in a propyl bromide-functionalized microporous polymer network using the concepts of surface organometallic chemistry. The support material enables the formation of isolated active metal sites embedded in a chemically robust and highly hydrophobic environment. The catalyst maintained high porosity and – without prior activation – exhibited high activity in the continuous-flow dehydrogenation of cyclohexane at elevated temperatures. The catalyst shows a stable performance for at least 7 days, even when additional H_2O was co-fed, owing to its hydrophobic nature.

Specific Contribution

All authors contributed extensively to the work presented in this paper. M.K. and A.T. conceived the research project. M.K. conducted the synthesis of monomers as well as polymers, and performed the characterizations. M.K. and M.T. synthesized the pincer complexes, model compound and performed the immobilization onto the polymer. M.T. and M.A.R. designed the dehydrogenation experiments. M.A.R. performed the dehydrogenation experiments and evaluated the data. J.S. performed and evaluated the XPS analyses for all the samples. H.K. performed the SEM analyses as well as EDX experiments. The whole project was administrated by A.T, with the help from M.K. R.S. provided the valuable guidance and helped for the catalytic tests. M.K., M.T. and A.T. wrote the manuscript with the input from the other authors.

Supporting Information

All experimental procedures and analytical data are available in the supporting information in the Appendix or through the website of the Publisher.

DOI: <https://doi.org/10.1002/cctc.202200811>

Introduction

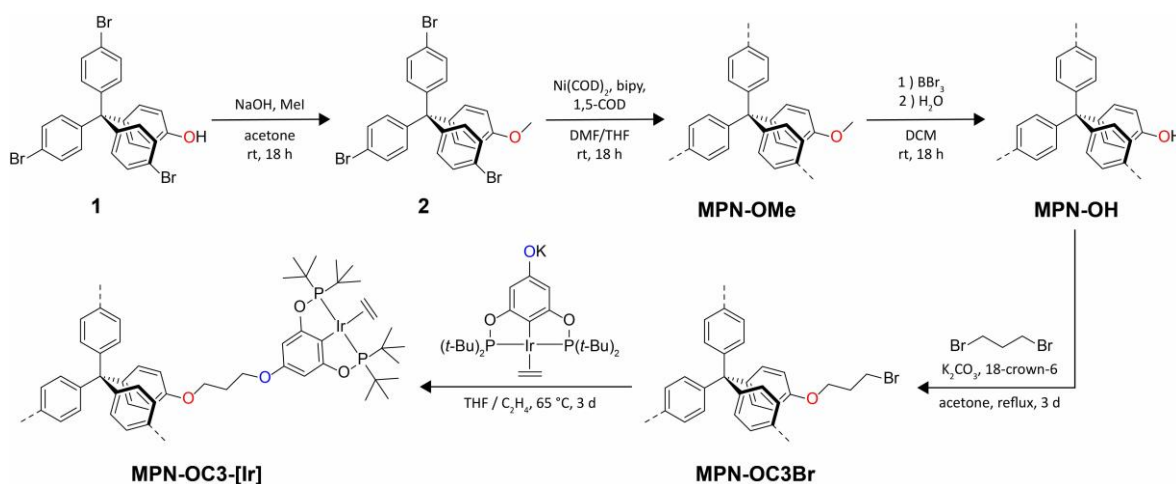
Alkanes can be extracted from various sources, including natural gas, mineral oil, coal, and biomass. Some of these alkanes (C₉–C₁₉) are utilized as fuels, but abundant leftover alkanes have poor application. In comparison, low molecular-weight alkenes and aromatic compounds are essential key intermediates in the synthesis of a multitude of fine chemicals or polymers on an industrial scale. Therefore, the conversion of alkanes to high-value alkenes or arenes is of great commercial interest.^[1] Dehydrogenation reactions are realized industrially on a large scale at high temperatures (400–600 °C) utilizing solid metal catalysts, however with low product selectivities as well as little energy efficacy.^[2] Since their discovery, molecular catalysts featuring tridentate pincer ligands are widely explored and are applied for versatile reactions, such as hydrogenation, coupling, hydrogen transfer, aldol and Michael reactions as well as dehydrogenation or even tandem reactions involving alkane dehydrogenation.^[3–12] In the field of alkane dehydrogenation iridium pincer complexes have received great interest due to their high activity as well as regioselectivity for the formation of terminal olefins, enabled by the relatively mild reaction temperature of around 240 °C compared to currently applied industrial processes.^[13]

Combining homogeneous and heterogeneous catalysis by immobilizing a molecular catalyst onto suitable supports has been investigated widely in recent years. Thereby, the advantages of homogeneous as well as heterogeneous catalysis are combined and well-defined materials with uniform active sites of equal activity towards the reactants can be made accessible for new catalytic applications.^[14,15] Molecular pincer catalysts have been immobilized on different supports, mainly on silica and metal oxides^[2,13,16–23] as well as metal-organic frameworks^[24–28] or even microporous polymer networks^[29] but the resulting materials were mostly investigated for stoichiometric transformation,^[30] coupled with metathesis^[31] or transfer dehydrogenations,^[2,32] whereas direct dehydrogenations remain underexplored.^[13,22] Besides the high porosity and chemical robustness, the advantage of using a microporous polymer network (MPN) as support material is the tunable environment of the catalyst, as the polymer backbone can be versatilely functionalized.

Herein, the immobilization of an organometallic iridium pincer complex on a post-modified high-surface-area MPN is presented (Scheme 1), as well as its application in a catalytic continuous-flow dehydrogenation reaction. The novel MPN provides an inert environment

with isolated anchor points for the immobilization of the metal-organic complex, ensuring the formation of a single-site catalyst.

We and others have recently shown the immobilization of iridium pincer complexes.^[23,29] In these examples the complex has been conveniently anchored via the Ir center to OH-functional groups present on the surface of the support, yielding immobilized Ir(III) pincer complexes, which showed high activity in the hydrogenation of alkenes. However, such catalysts will not be active in the, industrially more important back reaction, i. e. the endothermic dehydrogenation of alkanes. For the latter reaction, the central iridium atom of the pincer catalyst cannot be anchored directly to the support material, as for an effective dehydrogenation reaction an Ir(I) catalyst is required to ensure an Ir(I)-Ir(III) couple.^[13] Therefore, the pincer complex has to be anchored to the support via the organic ligand.^[2] In this study, a synthesis route for the immobilization of a potassium phenolate substituted pincer catalyst onto a propyl bromide-functionalized MPN is presented (Scheme 1). Notably, the catalyst synthesis includes three post-synthetic modification steps on the pre-formed MPN, but can be carried out with high efficiency.



Scheme 1. Synthesis of methoxytetraphenylmethane polymer MPN-OMe, post-synthetic modification towards hydroxy functionalized MPN-OH and alkylated MPN-OC3Br and subsequent immobilization of iridium pincer complex {*p*-KO-C₆H₂-2,6-[OP(*t*-Bu)₂]₂}Ir(C₂H₄) yielding MPN-OC3-[Ir].

Results and Discussion

In our previous work, we developed a synthetic route to provide a highly porous polymer network with isolated, reactive hydroxy functionalities as anchor points for further post-synthetic modifications.^[29] To create such an OH-functionalized network, tris(4-

bromophenyl)-methanol^[33] was synthesized and converted into 4-hydroxyphenyl-tris(4-bromophenyl)methane **1**. To avoid possible interactions with the utilized metal species during polymerization, the hydroxy group was protected by methylation to yield 4-methoxyphenyl-tris(4-bromophenyl)-methane **2**. Subsequently, the protected monomer (**2**) was successfully converted to a methoxy functionalized microporous polymer network **MPN-OMe** with a S_{ABET} of $1014 \text{ m}^2 \text{ g}^{-1}$ using nickel-mediated Yamamoto polymerization.^[34] To recover the hydroxy group the methylated polymer **MPN-OMe** was quantitatively deprotected by successive treatment with BBr_3 and H_2O to yield a microporous polymer **MPN-OH** with a S_{ABET} of $911 \text{ m}^2 \text{ g}^{-1}$ (Figure 1a).

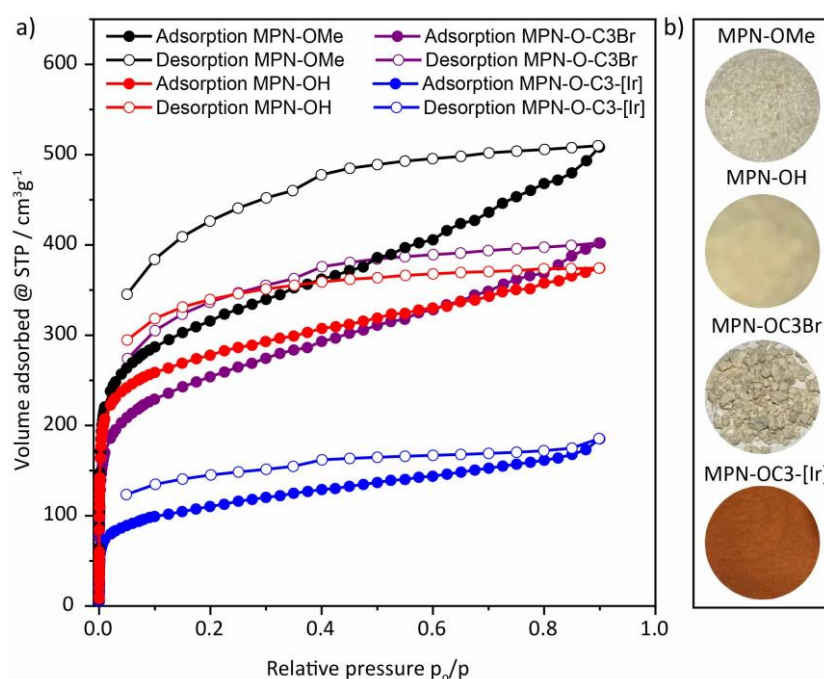


Figure 1. a) Ar sorption analysis at 87 K of **MPN-OMe** (black), **MPN-OH** (red), **MPN-OC3Br** (purple) and **MPN-O-[Ir]** (blue). b) Optical images of **MPN-OMe**, **MPN-OH**, **MPN-OC3Br** and **MPN-OC3-[Ir]**.

As an anchoring point of an iridium pincer complex via its ligand, a small chain alkyl bromide needed to be introduced to the microporous polymer network. In order to find out a suitable chain length, which reacts efficiently with the phenolic OH groups of the polymer, but is sufficiently short not to block the pores of the polymer network, 1,2-dibromoethane, 1,3-dibromopropane and 1,4-dibromobutane were tested in the reaction with the model compound 4-tritylphenol using different reaction protocols. Low yields and slow conversion were obtained when introducing the bromoethyl chain. On the contrary, a reaction protocol

using potassium carbonate and 18-crown-6 gave high conversion rates for the respective bromopropyl and bromobutyl ethers after reflux in acetone, respectively. Therefore, the same reaction protocol was applied for the post-synthetic modification of the **MPN-OH** polymer. For both chain lengths, a nearly quantitative conversion of the hydroxy groups of the microporous polymer was obtained, yielding in the formation of **MPN-OC3Br** and **MPN-OC4Br**. ^{13}C CP/MAS-NMR spectroscopy confirmed the successful attachment of the bromoalkyl chains since new signals in the region between 27 and 32 ppm could be identified as the signals for the aliphatic carbons of the alkyl chains. Furthermore, a low-field shift of the $\text{C}_{\text{Ar}}\text{-O}$ signal from 154 to 157 ppm is observed, which also proves the assumed conversion of hydroxy to ether groups (Figure 2a [**MPN-OC3Br**]; Figure S1 [**MPN-OC4Br**]). Additionally, the complete conversion of the OH group to the respective bromoalkyl ether was confirmed by FT-IR, where the characteristic band around 3500 cm^{-1} , corresponding to O-H stretching, disappeared (Figure S4). Both functionalized polymer networks maintained their microporous characteristics and exhibit a S_{ABET} determined from Ar sorption experiments of $796\text{ m}^2\text{ g}^{-1}$ for **MPN-OC3Br** (Figure 1a) and $781\text{ m}^2\text{ g}^{-1}$ for **MPN-OC4Br** (Figure S5). Such a decrease of the S_{ABET} is expected due to the increase in molecular weight of the repeating units, plus the partial pore blockage of dangling bromoalkyl chains. As both chain lengths yield comparable results, further post-modification steps were carried out on **MPN-OC3Br**.

For anchoring the pincer complex onto the support, a potassium phenolate substituted pincer catalyst was prepared in the next step. The tridentate iridium pincer complex $\{p\text{-KO-C}_6\text{H}_2\text{-2,6-[OP}(t\text{-Bu})_2\text{]}_2\}\text{Ir}(\text{C}_2\text{H}_4)$ was synthesized according to the literature (Scheme S2).^[2] Then, $\{p\text{-KO-C}_6\text{H}_2\text{-2,6-[OP}(t\text{-Bu})_2\text{]}_2\}\text{Ir}(\text{C}_2\text{H}_4)$ was added to a suspension of **MPN-OC3Br** in THF under inert conditions. While stirring for 3 days under C_2H_4 atmosphere the polymer swelled and its color turned from beige to red (Figure 1b). Filtration, extensive washing and drying in vacuum yielded the immobilized iridium pincer complex **MPN-OC3-[Ir]** (Scheme 1). To explore the binding situation of the immobilized pincer complex on the MPN support, a model compound featuring the repeating unit of the porous polymer was synthesized and analyzed by ^1H and ^{13}C liquid state NMR as well (supporting information). The successful immobilization of the iridium pincer complex was again confirmed by solid-state NMR spectroscopy (Figure 2a). In the ^{13}C CP/MAS-NMR spectrum additional peaks in the aromatic region at 168, 160, and 92 ppm are observed attributed to the aromatic

backbone of the pincer ligand. In addition, the signal at 28 ppm can be assigned to the methyl groups of the *tert*-butyl moiety and the signal at 41 ppm can be assigned to the quaternary *tert*-butyl carbon atom. The signal at 35 ppm can be equally assigned to the center aliphatic carbon of the C3-alkyl chain and the coordinated C₂H₄ molecules. When compared to the model compound, the signal at 67 ppm can be assigned to oxygen-connected aliphatic carbons of the alkyl chain. The peak broadening of the aromatic signal at 131 ppm is presumably due to an overlap with the spinning sideband of the signal of the *tert*-butyl methyl groups at 28 ppm.

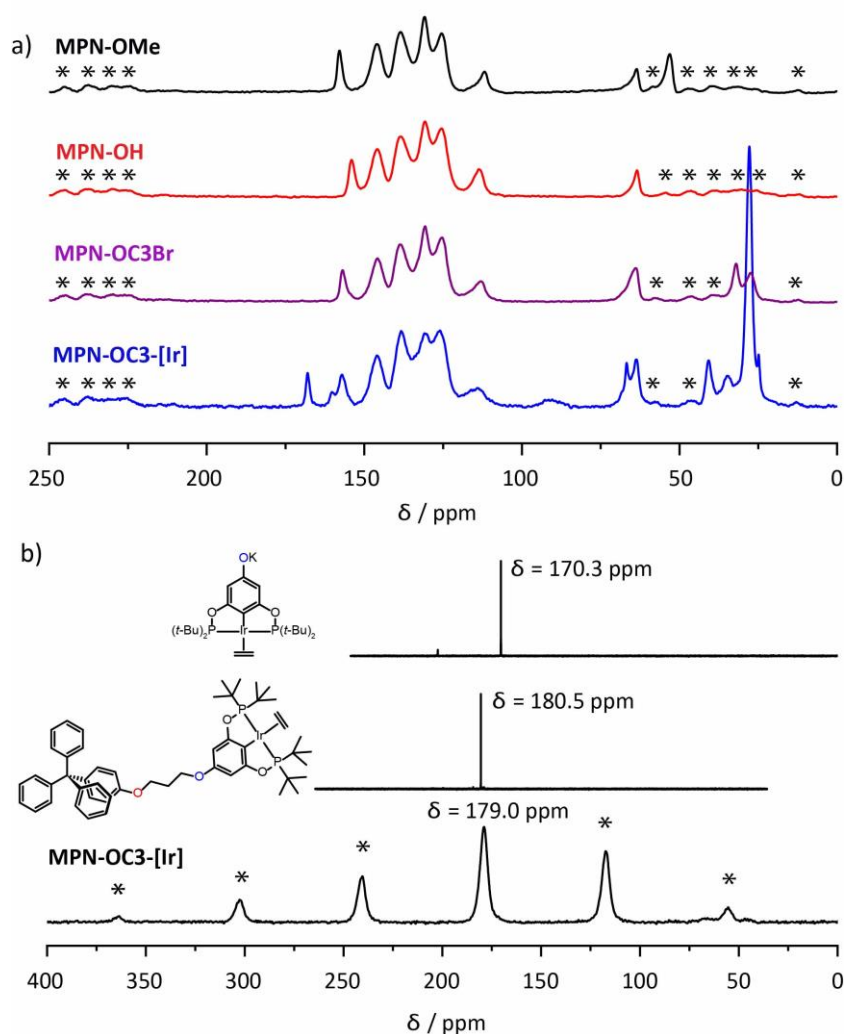


Figure 2. a) Demethylation, post-synthetic modification and immobilization of Ir pincer complex monitored by ¹³C CP/MAS-NMR spectroscopy: **MPN-OMe** (black), **MPN-OH** (red), **MPN-OC3Br** (purple) and immobilized Ir pincer complex **MPN-OC3-[Ir]** (blue). b) ³¹P MAS-NMR spectroscopy of pincer complex $\{p\text{-KO-C}_6\text{H}_2\text{-2,6-[OP(t-Bu)}_2\text{]}_2\}\text{Ir(C}_2\text{H}_4\text{)}$ (top), molecular model compound (middle) and immobilized iridium pincer complex **MPN-OC3-[Ir]** (bottom). Asterisks denote spinning sidebands.

Small amounts of residual THF can be assumed due to the relatively sharp signals at 25 and 67 ppm. The ^{31}P MAS-NMR spectrum further confirms that the pincer ligand stays intact after immobilization as its chemical shift of 179 ppm closely resembles the value of the molecular complex and the designed model compound (Figure 2b).

After immobilization of the iridium pincer catalyst, the porosity of **MPN-OC3-[Ir]** was evaluated by low-pressure argon sorption studies. The material exhibits still a microporous character and the S_{ABET} was determined to be $360 \text{ m}^2 \text{ g}^{-1}$. A decrease of S_{ABET} was expected due to the addition of the iridium complex with its bulky functional groups, which increases the weight of the repeating units and occupies the free volume of the MPN. Also, the apparent pore size calculated from the adsorption isotherm decreased after catalyst immobilization from 0.65 for **MPN-OC3Br** to 0.58 nm for **MPN-OC3-[Ir]** (Figure S7).

X-ray photoelectron spectroscopy (XPS) analysis of the iridium pincer complex, $\{p\text{-KO-C}_6\text{H}_2\text{-2,6-[OP}(t\text{-Bu)}_2\text{]}_2\}\text{Ir}(\text{C}_2\text{H}_4)$, and the immobilized iridium pincer complex, **MPN-OC3-[Ir]**, were conducted to provide further evidence for the anchoring of the catalyst onto the polymer. The molecular metal-organic complex shows two peaks in the O 1s core-level spectrum at 532.0 and 533.3 eV, which both are in the binding energy range of organic oxygen compounds (Figure 3a). Additionally, the characteristic doublet at 131.6 eV in the P 2p spectrum can be assigned to the P–O species. In the Ir 4f spectrum, two different species with characteristic doublets at 60.6 and 63.7 eV, as well as 61.9 and 65.0 eV, can be detected. The set of lower binding energy can be attributed to the unchanged Ir(I) complex, while the peaks for higher binding energy are in the range of Ir(III) species.^[29] This oxidation is most likely resulting from the transfer of the catalyst sample to the XPS measurement chamber and is limited to the outer surface of the material. In addition, the elemental ratio between iridium and phosphorus was determined as 2 : 1.

After the anchoring of the catalyst onto the surface of the microporous polymer network, the O 1s signals slightly shifted to 531.5 and 532.8 eV (Figure 3b). With the absence of a metal-oxygen species at lower binding energies it can be concluded, that the pincer complex is bound via the organic phenyl group rather than the iridium metal center. The P 2p spectrum and Ir 4f spectrum stay nearly identical to that of the molecular pincer catalyst. The extra peak at around 70 eV in the Ir 4f spectrum can be assigned to the Br 3d signal originating from KBr which is the side product of the substitution reaction of the anchoring. Finally, the elemental ratio for iridium and phosphorus in the porous polymer catalyst **MPN-OC3-[Ir]**

stays 2 : 1, which confirms again the successful anchoring of the intact iridium pincer complex onto the porous polymer. In addition, the immobilization of the iridium pincer catalyst on the bromoalkyl modified model compound resulted in identical binding energies in the O 1s, P 2p and Ir 4f spectra **MPN-OC3-[Ir]** (Figure S11).

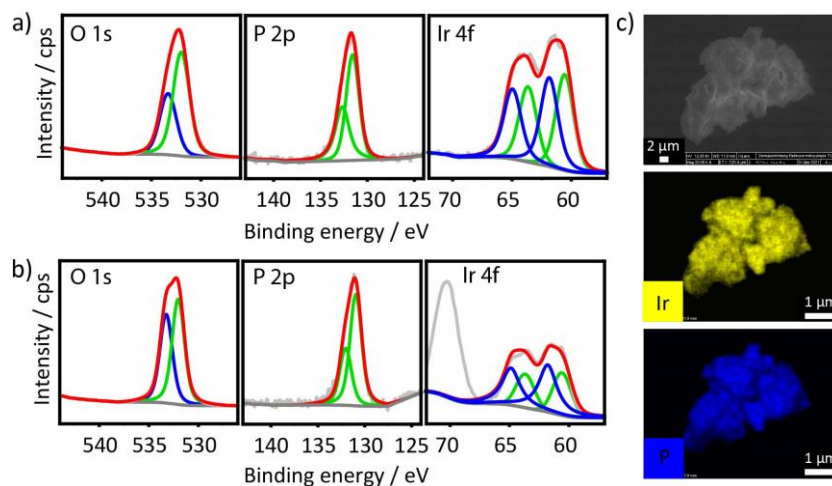


Figure 3. a) O 1s, P 2p and Ir 4f XPS spectra of $\{p\text{-KO-C}_6\text{H}_2\text{-2,6-[OP(t-Bu)}_2\text{]}_2\}\text{Ir(C}_2\text{H}_4\text{)}$. b) O 1s, P 2p and Ir 4f XPS spectra of immobilized iridium pincer complex **MPN-OC3-[Ir]**. (Light grey – measured spectra; red line – fitted spectra; green and blue lines – fitted signals. c) Scanning electron microscopy and energy dispersive X-ray spectroscopic elemental mapping of **MPN-OC3-[Ir]**. Yellow belongs to iridium, blue belongs to phosphorus.

The iridium content was determined by inductively coupled plasma optical emission spectroscopy (ICP-OES) with a value of 7.9 wt%, indicating a functionalization degree of 41 %. A spherical morphology of the MPN is seen by scanning electron microscopy (SEM). Elemental mapping shows the homogeneous distribution of iridium and phosphorus within **MPN-OC3-[Ir]** (Figure 3c). Following the results from solid-state NMR, XPS and SEM, it can be concluded, that the molecular iridium pincer complex has been successfully immobilized onto the microporous polymer support.

The immobilized iridium pincer complex was tested in the catalytic dehydrogenation of cyclohexane to benzene. Gaseous cyclohexane was used in a continuously operated experimental setup to enable simultaneous convenient temporal resolution with adequate experiment duration. To increase the bed height and to avoid potential hot spots, the porous polymer was mixed with SiC as inert material in a 1 : 9 mass ratio.

Two measurements with different temperature programs were conducted. The initial temperature ramp experiment was designed to find a suitable reaction temperature for the

following isothermal stability test. In the first experiment, the catalyst was initially heated to 200 °C with a temperature ramp of 20 K min⁻¹. Subsequently, the activity of the catalyst was determined by holding at this temperature for 15 min. Then, with 4 K min⁻¹ heating ramps followed by holding the temperature for 15 min, the temperature was increased in steps of 20 °C within the stability window of **MPN-OC3-[Ir]** to 340 °C (Figure 4a). The second measurement, using fresh catalyst material, consisted of heating with 5 K/min to 300 °C and holding for more than seven days (Figure 4b). An induction period is observed within the first 30 hours in which the activity of the catalysts is continuously rising. This might be due to an expansion of the highly cross-linked network during time, increasing the accessibility of active sites.

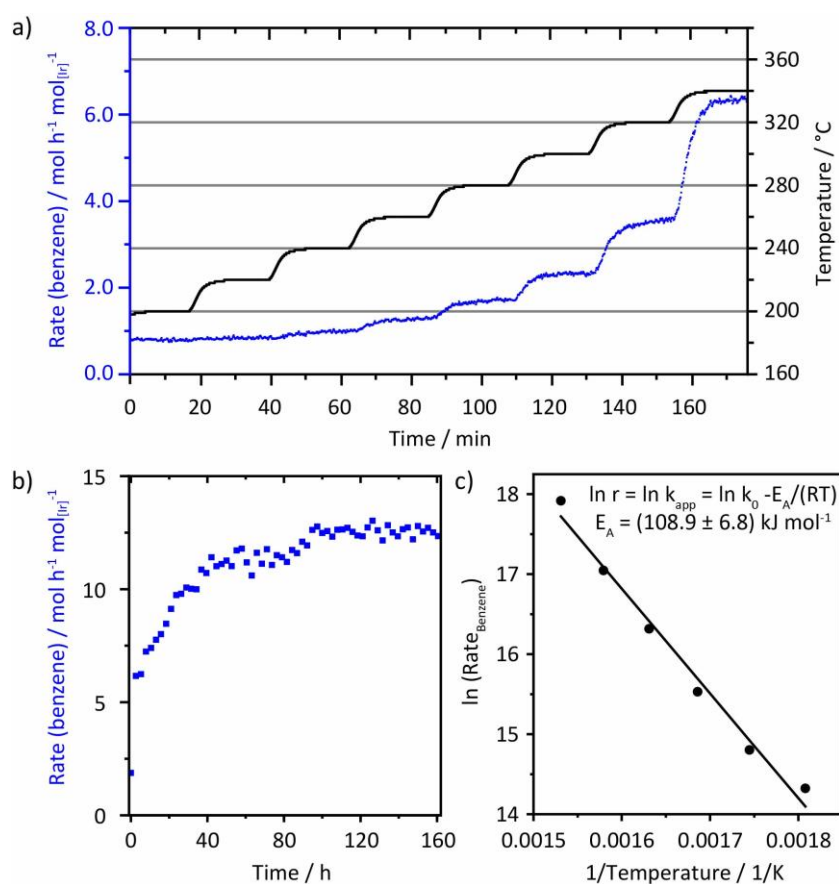


Figure 4. a) Catalytic dehydrogenation of cyclohexane. Temperature ramp measurement: Benzene formation rate depending on the catalyst bed temperature, heating with 4 K/min and holding for 15 min between 200 °C and 340 °C in steps of 20 °C. b) Isothermal stability measurement: Benzene formation rate at 300 °C for 168 h (figure neglects heating with 5 K/min to 300 °C). c) The rates of benzene formation during the steady regimes of each temperature step between 280 and 380 °C (except 380 °C in cycle 1) were averaged for each temperature. The temperature-rate pairs were used in an Arrhenius plot to determine the apparent activation energy of the dehydrogenation of cyclohexane to benzene of $(108.9 \pm 6.8) \text{ kJ mol}^{-1}$.

During both measurements, leakage (i. e. N_2 , H_2O , O_2), combustion (CO_x), and partial dehydrogenation (cyclohexene) were not detected in a significant amount in comparison to the reference baselines. Consequently, total benzene selectivity is perceived. The feed consisting of argon, hydrogen, and cyclohexane was subject to minor fluctuations, but without impact on the formation of benzene. The co-feeding of hydrogen ensures a sufficient H_2 partial pressure for activating the catalyst to a dihydride complex in a plausible associative reaction mechanism, when performing temperature screening experiments starting with zero conversion.^[35] Additionally, the hydrogen feed could also prevent possible C–H bond activation of the support by the iridium pincer complex. Furthermore, no benzene or other organic products could be detected in a reference reaction without the feed of cyclohexane, excluding that products are detected due to a decomposition of the polymer network or ligand.

The temperature ramping dehydrogenation of the **MPN-OC3-[Ir]** catalyst showed an increased formation of benzene, which is elevating with increasing temperature (Figure 4a). At 200 °C the yield of benzene in the dehydrogenation reaction was low. With increasing temperature the conversion of cyclohexane raised stepwise to a steady-state with a turnover frequency (TOF) of $6.3 \text{ mol h}^{-1} \text{ mol}_{[\text{Ir}]}^{-1}$ at 340 °C. It is noteworthy that these temperatures are not accessible with unsupported molecular dehydrogenation catalysts, since the highest temperatures for those is considered 200–240 °C due to thermal instability.^[36] Ramping the catalyst to temperatures beyond the stability window of the microporous dehydrogenation catalyst up to 400 °C led to a further increase in activity, with the highest benzene formation rates peaking as high as $99.5 \text{ mol h}^{-1} \text{ mol}_{[\text{Ir}]}^{-1}$ at a cyclohexane conversion of more than 50 %. However, the initial rates at those temperatures are declining already within the 15 min holding phase (Figure S12). These results are in full agreement with findings from Sheludko et al. that the thermal decomposition product of the supported catalyst is retaining activity, even though at lower conversion rates.^[13] Notably, the catalytic activity of the iridium pincer species is not affected by a co-feed of water (Figure S12, last cycle). This can be explained by the highly hydrophobic environment, which is provided by the microporous polymer network. This renders a further advantage of MPNs compared to other conventional, hydrophilic supports such as silica. The analysis of the temperature dependence of the reaction rates results in an apparent activation energy of $(108.9 \pm 6.8) \text{ kJ mol}^{-1}$ (Figure 4c and supporting information), which is in accordance to

simulations on Pt(111) surfaces.^[37–39] The additionally performed Eyring plot confirms the activation enthalpy to be slightly higher than 100 kJ mol⁻¹ and revealed a positive activation entropy of (55.0±2.4) kJ mol⁻¹ K⁻¹ (Figure S14).

The following isothermal long time catalyst test showed – after an induction period of 24 h – a stable dehydrogenation of cyclohexane to benzene at a rate of 11.4 mol h⁻¹ mol_[Ir]⁻¹ (Figure 4b), which relates to a conversion of 4.4 % of the theoretical maximum conversion based on thermodynamic simulations (Figure S15). This activity is comparable to reported silica-supported metal nanoparticle catalysts for the dehydrogenation of cyclohexane.^[40–42] Additionally, the catalyst showed long-term stability with a turnover number higher than 1600. It should be noted, that the catalyst activity was stable for more than 7 days and no decrease in reaction rate was detected. The catalyst was analyzed after the long-term experiment using SEM and EDX analysis. The elemental mapping revealed, that both iridium and phosphorus are still distributed throughout the catalyst material (Figure S16).

Conclusion

In summary, herein we present a multi-step post-synthetically modified MPN as catalyst for the continuous flow dehydrogenation of cyclohexane to benzene. An iridium pincer complex was immobilized on an alkylated microporous polymer network with a resulting Ir content of 7.9 wt%. The successful immobilization of the intact pincer catalyst could be confirmed by solid-state ¹³C and ³¹P NMR spectroscopy. X-ray photoelectron spectroscopy validated the presence of the expected oxygen, phosphorus, and iridium species. Homogeneous distribution of iridium and phosphorus was confirmed by scanning electron microscopy. After immobilization, the *S*_{BET} decreased from 796 to 360 m² g⁻¹ due to the increased specific weight but without loss of the microporous characteristics. The catalytic performance was demonstrated in the continuous flow dehydrogenation of cyclohexane, where the material showed high long-term stability at a TOF of 11.4 mol h⁻¹ mol_[Ir]⁻¹, which - to our knowledge - was not yet reported for the catalytic dehydrogenation of cyclohexane using an anchored metal organic catalyst. We believe that this highly tunable class of materials ensures the formation of single-site catalytically active species inside a chemically robust, inert, and hydrophobic polymer, offering ample opportunity for the field of surface

organometallic chemistry due to the ability of the formation of tuned environments for the catalyst.

Experimental Section

Materials and methods. All chemicals were of reagent grade and used as received, and all experiments were carried out under Ar atmosphere if stated in the procedure. ^{11}B MAS, $^{13}\text{C}\{^1\text{H}\}$ CP/MAS and ^{31}P MAS measurements were carried out using a Bruker range Avance 400 MHz solid state spectrometer operating at a spinning rate of 10 kHz. Physisorption measurements were conducted at 87 K and Argon as sorption agent at relative pressures up to $p/p_0=0.9$ using an Autosorb-iQ-MP from Quantachrome. X-ray photoelectron spectra were measured on a K-AlphaTM+X-ray Photoelectron Spectrometer System (Thermo Scientific). Scanning electron microscopy images were recorded via ZEISS Gemini SEM 500 using NanoVP mode operating at 15 kV. For the energy dispersive spectroscopy, Bruker Quantax XFlash 6|60 detector was used.

Catalyst preparation. Hydroxytetraphenylmethane polymer **MPN–OH** was synthesized in accordance with a reported procedure.^[29]

MPN–OC3Br. Polymer **MPN–OH** (525 mg, 1.58 mmol), K_2CO_3 (294 mg, 2.13 mmol) and a few crumbs of 18-crown-6 were suspended in acetone (60 mL). 1,3-Dibromopropane (0.98 mL, 9.62 mmol) was added via syringe and the reaction stirred at reflux for 3 days. After cooling down to room temperature the mixture was filtered off and the off-white precipitate washed with abundant amounts of water, acetone, THF and methanol. The product was purified via Soxhlet extraction from methanol overnight and dried at 80 °C in vacuum for 6 h to yield **MPN–OC3Br** as off-white powder. Yield, 620 mg (1.37 mmol repeating units, 87 %). $^{13}\text{C}\{^1\text{H}\}$ CP/MAS-NMR (100 MHz): $\delta=157, 146, 138, 131, 125, 113, 64, 32, 27$ ppm. The potassium phenolate substituted pincer catalyst $\{p\text{-KO-C}_6\text{H}_2\text{-2,6-[OP}(t\text{-Bu)}_2\text{]}_2\}\text{Ir}(\text{C}_2\text{H}_4)$ was prepared according to the literature.^[2]

MPN–OC3–[Ir]. Polymer **MPN–OC3Br** (225 mg, 0.50 mmol) was added to a Schlenk flask and evacuated overnight. Under Ar atmosphere pincer catalyst $\{p\text{-KO-C}_6\text{H}_2\text{-2,6-[OP}(t\text{-Bu)}_2\text{]}_2\}\text{Ir}(t\text{-Bu})$

$\text{Bu}_2\text{]}_2\text{Ir}(\text{C}_2\text{H}_4)$ (400 mg, 0.60 mmol) and THF (80 mL) were added. The THF suspension was degassed by three freeze-pump-thaw cycles. The flask was refilled with ethylene gas at $-78\text{ }^\circ\text{C}$. The reaction stirred at $65\text{ }^\circ\text{C}$ for 3 days. After cooling down to room temperature the solvent was removed via filtration under Ar atmosphere and the orange solid was washed with THF ($6\times 20\text{ mL}$) to remove the excess of metal precursor. The volatiles were removed under high vacuum (10^{-3} mbar), and the orange solid was dried under high vacuum (10^{-3} mbar) overnight. Drying in vacuum overnight (14 h) yielded the product as a red powder. $^{13}\text{C}\{^1\text{H}\}$ CP/MAS-NMR (100 MHz): $\delta=168, 160, 157, 146, 138, 131, 126, 114, 92, 67, 64, 41, 35, 28, 25\text{ ppm}$. $^{31}\text{P}\{^1\text{H}\}$ CP/MAS-NMR (162 MHz): $\delta=179\text{ ppm}$.

The model compound Tritylphenolate Pincer Complex (**10**) was synthesized similar to **MPN-OC3-[Ir]** but using 4-(3-bromo-propyloxy)tetraphenylmethane (**9**) as a representative unit of the polymer **MPN-OC3Br** (see SI).

Procedure for the dehydrogenation of cyclohexane using MPN-OC3-[Ir]. The catalytic performance was examined in a tubular fixed bed reactor (tapered quartz tube with a 4 mm inner diameter) with Swagelok Ultra-Torr fittings and Quick-Connects ensuring gas tightness against atmospheric oxygen and moisture. The reactor was placed vertically in a programmable oven (HTM Reetz). The feed of Argon (29 mL/min, 99.999 %, Air Liquide) and hydrogen (1 mL/min, 99.999 %, Air Liquide) was controlled by mass flow controllers (MFCs, Bronkhorst EL-FLOW) which were calibrated by a flow meter (Analyt-MTC). Argon was bubbled into a doubled walled gas-washing bottle (length 24 cm, frit VitraPOR filter plate with porosity 3) filled with cyclohexane (99.5 %, Roth) which was held at $15\text{ }^\circ\text{C}$ by a thermostat (Lauda Eco RE620). Argon, hydrogen and cyclohexane were used without further purification. The calibration of the cyclohexane feed was conducted measuring the evaporated volume of cyclohexane depending on the time. The decrease in cyclohexane volume in the gas-washing bottle or the difference in residence time of the Argon bubbles within the gas-washing bottle is neglectable. To ensure a stationary feed composition, the MFCs were run one hour in advance of the actual measurement. The feed composition was analysed by a mass spectrometer (GAM 200, InProcess Instruments) with a time resolution of 0.95 measurements of all the 11 channels per second detecting minimal fluctuations. The gas species and their respective channels (mass per charge ratio, m/z) are listed in Table S1.

Cyclohexane and cyclohexene were measured via two channels due to overlapping molecular fractions. To calibrate the signals, a reference measurement excluding MPN-OC3-[Ir] was conducted at room temperature receiving the signal intensities correlated to zero cyclohexane conversion. The catalyst material (15.5 mg of MPN-OC3-[Ir] diluted with SiC (1 : 9 mass related, VWR, 100–500 μm) was mixed and placed on quartz wool (Roth) which was stabilized on the taper under inert conditions. With a bed height of 0.5 cm and a tube diameter of 4 mm, the residence time was 0.5 s.

References

- [1] K. Das, A. Kumar, *Advances in Organometallic Chemistry* **2019**, 72, 1–57.
- [2] Z. Huang, M. Brookhart, A. S. Goldman, S. Kundu, A. Ray, S. L. Scott, B. C. Vicente, *Advanced Synthesis and Catalysis* **2009**, 351, 188–206.
- [3] J. T. Singleton, *Tetrahedron* **2003**, 59, 1837–1857.
- [4] Y. Wang, Z. Huang, X. Leng, H. Zhu, G. Liu, Z. Huang, *J Am Chem Soc* **2018**, 140, 4417–4429.
- [5] M. E. van der Boom, D. Milstein, *Chemical Reviews* **2003**, 103, 1759–1792.
- [6] N. Selander, K. J. Szabó, *Chemical Reviews* **2011**, 111, 2048–2076.
- [7] J. Choi, A. H. R. MacArthur, M. Brookhart, A. S. Goldman, *Chemical Reviews* **2011**, 111, 1761–1779.
- [8] A. Kumar, T. M. Bhatti, A. S. Goldman, *Chemical Reviews* **2017**, 117, 12357–12384.
- [9] L. Maser, L. Vondung, R. Langer, *Polyhedron* **2018**, 143, 28–42.
- [10] M. A. W. Lawrence, K.-A. Green, P. N. Nelson, S. C. Lorraine, *Polyhedron* **2018**, 143, 11–27.
- [11] E. Peris, R. H. Crabtree, *Chemical Society Reviews* **2018**, 47, 1959–1968.
- [12] X. Zhou, S. Malakar, T. Dugan, K. Wang, A. Sattler, D. O. Marler, T. J. Emge, K. Krogh-Jespersen, A. S. Goldman, *ACS Catalysis* **2021**, 11, 14194–14209.
- [13] B. Sheludko, M. T. Cunningham, A. S. Goldman, F. E. Celik, *ACS Catalysis* **2018**, 8, 7828–7841.
- [14] C. Copéret, M. Chabanas, R. Petroff Saint-Arroman, J.-M. Basset, *Angewandte Chemie International Edition* **2003**, 42, 156–181.
- [15] M. D. Korzyński, C. Copéret, *Trends in Chemistry* **2021**, 3, 850–862.
- [16] C. del Pozo, A. Corma, M. Iglesias, F. Sánchez, *Organometallics* **2010**, 29, 4491–4498.
- [17] M. Rimoldi, A. Mezzetti, *Inorganic Chemistry* **2014**, 53, 11974–11984.
- [18] E. K. Huang, W.-M. Cheung, K.-W. Chan, F. L.-Y. Lam, X. Hu, Q.-F. Zhang, I. D. Williams, W.-H. Leung, *European Journal of Inorganic Chemistry* **2013**, 2893–2899.
- [19] J. Ternel, L. Delevoye, F. Agbossou-Niedercorn, T. Roisnel, R. M. Gauvin, C. M. Thomas, *Dalton Transactions* **2010**, 39, 3802.
- [20] M. Rimoldi, A. Mezzetti, *Helvetica Chimica Acta* **2016**, 99, 908–915.

- [21] M. Rimoldi, D. Fodor, J. A. van Bokhoven, A. Mezzetti, *Catalysis Science & Technology* **2015**, *5*, 4575–4586.
- [22] B. Sheludko, C. F. Castro, A. S. Goldman, F. E. Celik, *ACS Catalysis* **2020**, *10*, 12425–12436.
- [23] M. Rimoldi, D. Fodor, J. A. van Bokhoven, A. Mezzetti, *Chemical Communications* **2013**, *49*, 11314–11316.
- [24] S. A. Burgess, A. Kassie, S. A. Baranowski, K. J. Fritzsche, K. Schmidt-Rohr, C. M. Brown, C. R. Wade, *J Am Chem Soc* **2016**, *138*, 1780–1783.
- [25] M. Rimoldi, A. Nakamura, N. A. Vermeulen, J. J. Henkelis, A. K. Blackburn, J. T. Hupp, J. F. Stoddart, O. K. Farha, *Chemical Science* **2016**, *7*, 4980–4984.
- [26] A. M. Rasero-Almansa, A. Corma, M. Iglesias, F. Sánchez, *ChemCatChem* **2013**, *5*, 3092–3100.
- [27] Y. Zhang, J. Li, X. Yang, P. Zhang, J. Pang, B. Li, H.-C. Zhou, *Chemical Communications* **2019**, *55*, 2023–2026.
- [28] B. R. Reiner, N. T. Mucha, A. Rothstein, J. S. Temme, P. Duan, K. Schmidt-Rohr, B. M. Foxman, C. R. Wade, *Inorganic Chemistry* **2018**, *57*, 2663–2672.
- [29] M. König, M. Rigo, N. Chaoui, T. Tran Ngoc, J. D. Epping, J. Schmidt, P. Pachfule, M. Ye, M. Trunk, J. F. Teichert, M. Drieß, A. Thomas, *Angewandte Chemie International Edition* **2020**, *59*, 19830–19834.
- [30] Z. H. Syed, D. M. Kaphan, F. A. Perras, M. Pruski, M. S. Ferrandon, E. C. Wegener, G. Celik, J. Wen, C. Liu, F. Dogan, K. I. Goldberg, M. Delferro, *J Am Chem Soc* **2019**, *141*, 6325–6337.
- [31] Z. Huang, E. Rolfe, E. C. Carson, M. Brookhart, A. S. Goldman, S. H. El-Khalafy, A. H. Roy MacArthur, *Advanced Synthesis and Catalysis* **2010**, *352*, 125–135.
- [32] B. Sheludko, C. F. Castro, C. A. Khalap, T. J. Emge, A. S. Goldman, F. E. Celik, *ChemCatChem* **2021**, *13*, 407–415.
- [33] K. Nikitin, E. Lestini, M. Lazzari, S. Altobello, D. Fitzmaurice, *Langmuir* **2007**, *23*, 12147–12153.
- [34] J. Schmidt, M. Werner, A. Thomas, *Macromolecules* **2009**, *42*, 4426–4429.
- [35] K. Krogh-Jespersen, M. Czerw, N. Summa, K. B. Renkema, P. D. Achord, A. S. Goldman, *J Am Chem Soc* **2002**, *124*, 11404–11416.
- [36] G. E. Dobereiner, R. H. Crabtree, *Chemical Reviews* **2010**, *110*, 681–703.

- [37] B. E. Koel, D. A. Blank, E. A. Carter, *Journal of Molecular Catalysis A: Chemical* **1998**, *131*, 39–53.
- [38] M. Saeys, M. F. Reyniers, M. Neurock, G. B. Marin, *Journal of Physical Chemistry B* **2005**, *109*, 2064–2073.
- [39] M. K. Sabbe, G. Canduela-Rodriguez, M. F. Reyniers, G. B. Marin, *Journal of Catalysis* **2015**, *330*, 406–422.
- [40] Z. Xia, H. Lu, H. Liu, Z. Zhang, Y. Chen, *Catalysis Communications* **2017**, *90*, 39–42.
- [41] Z. Xia, H. Liu, H. Lu, Z. Zhang, Y. Chen, *Catalysis Letters* **2017**, *147*, 1295–1302.
- [42] Z. Xia, H. Liu, H. Lu, Z. Zhang, Y. Chen, *Applied Surface Science* **2017**, *422*, 905–912.

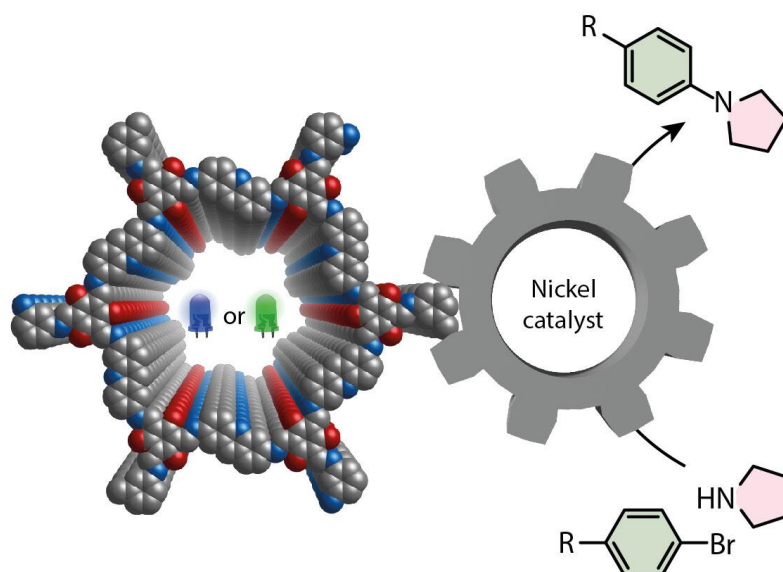
Chapter 4:

Acridine-Functionalized Covalent Organic Frameworks (COFs) as Photocatalysts for Metallaphotocatalytic C–N Cross-Coupling

M. Traxler, S. Gisbertz, P. Pachfule, J. Schmidt, J. Roeser, S. Reischauer, B. Pieber, A. Thomas

Angew. Chem. Int. Ed. **2022**, 61, e202117738.

Accepted manuscript, DOI: <https://doi.org/10.1002/anie.202117738>



A new family of porous crystalline COFs bearing acridine moieties was synthesized and applied as photocatalysts in metallaphotocatalytic C–N cross-coupling. Among these materials the fully β -ketoenamine-linked COF showed the highest catalytic activity and was shown to be recyclable and even catalyzed the cross-coupling efficiently under green light irradiation.

Abstract

Covalent organic frameworks (COFs) are structurally tuneable, porous and crystalline polymers constructed through the covalent attachment of small organic building blocks as elementary units. Using the myriad of such building blocks, a broad spectrum of functionalities has been applied for COF syntheses for broad applications, including heterogeneous catalysis. Herein, we report the synthesis of a new family of porous and crystalline COFs using a novel acridine linker and benzene-1,3,5-tricarbaldehyde derivatives bearing a variable number of hydroxy groups. With the broad absorption in the visible light region, the COFs were applied as photocatalysts in metallaphotocatalytic C–N cross-coupling. The fully β -ketoenamine linked COF showed the highest activity, due to the increased charge separation upon irradiation. The COF showed good to excellent yields for several aryl bromides, good recyclability and even catalyzed the organic transformation in presence of green light as energy source.

Specific Contribution

All authors contributed extensively to the work presented in this paper. M.T., P.P. and A.T. conceived the research project. M.T. conducted the synthesis of linkers as well as COFs and performed the characterizations. S.G. performed and evaluated the photocatalytic experiments. J.S. performed and evaluated the XPS analyses. J. Roeser. performed the simulations of the COFs. S.R. performed the photoluminescence measurements and photocatalytic experiments. J. Rabeah performed the EPR analyses. The whole project was directed by A.T and B.P. with the help from M.T. and P.P., M.T. wrote the manuscript with the input from the other authors.

Supporting Information

All experimental procedures and analytical data are available in the supporting information in the appendix or through the website of the Publisher.

DOI: <https://doi.org/10.1002/anie.202117738>

Introduction

The field of covalent organic frameworks (COFs)—crystalline and porous polymers that are solely consisting of organic building blocks reticulated via covalent bonds—has gained significant attention in the last decade.^[1–6] A variety of building units (linkers) and organic reactions have been applied for the synthesis of COFs with a broad range of functionalities, linkages and variable pore structures.^[7–13] Because these ordered structures have a permanent porosity, long-range π -conjugation, and the possibility to tune the structure of the backbone and integrate functional linkers, COFs have emerged as powerful materials for a plethora of different applications including gas storage and separation, energy storage, optoelectronics and catalysis.^[13–21] The formation of strong covalent bonds between the organic building blocks results in high chemical stability for the framework materials that can be further enhanced by introducing linkers that allow for e.g. tautomerization or hydrogen bond formation.^[22,23]

As an impact of these properties, COFs are promising candidates for heterogeneous photocatalysis using visible-light due to the long-range π -conjugation. Water splitting and CO₂ reduction dominate this application branch, and only few examples using COF photocatalysts in organic synthesis were reported.^[24] These include oxidative hydroxylation,^[25,26] C–H functionalization, cross-coupling reactions,^[27,28] oxidative N–S cyclization^[29] or tandem addition-cyclization reaction.^[30] Recently, the scope of COFs in catalyzing organic transformation has been further expanded to C–S and C–O carbon heteroatom cross-couplings through metallaphotocatalysis.^[31,32] However, COFs have not been applied in carbon-nitrogen (C–N) cross-coupling reactions, which are among the most important reactions in synthetic organic chemistry.^[33] The majority of COFs applied in photocatalysis are limited to short wavelengths (blue light radiation), which can result in deactivation of the nickel co-catalyst,^[34] and other side-reactions^[35] due to the high photon energy. These problems can be overcome using less energetic irradiation sources. Expanding the absorption of COFs in order to harvest long wavelengths requires, for example, increasing π -conjugation by extending the length of the linkers with phenyl or acetylene groups, introduction of donor–acceptor structures, post-synthetic introduction of a chromophore, or the use of organic dyes that absorb visible light as linkers.^[36–38]

The acridine motif is commonly found in organic dyes and enables efficient intersystem crossing upon excitation. This results in long-lived excited states that are crucial for efficient

photocatalysis using low catalyst loadings.^[39,40] Recently, Stolarczyk and co-workers showed that an acridine carbon dot heterostructure can be used for photocatalytic water splitting.^[41] Homogeneous acridines have been explored in dual photocatalysis for decarboxylative *N*-alkylation, decarboxylative conjugate addition or dehydrocarboxylation of carboxylic acids.^[42–44] Further, it has been observed that acridine based small molecules and materials can harvest lower energetic light radiation compared to anthracene compounds, especially in its protonated form.^[40,41,45] However, utilization of acridine-based linkers for the synthesis of crystalline and porous materials such as COFs and MOFs have not been attempted.

Herein, we describe the synthesis of novel COFs bearing acridine moieties in reticulation with three different benzene-1,3,5-tricarbaldehyde derivatives with a variable number of hydroxy groups. The resulting materials were evaluated for their application as photocatalysts in metallaphotocatalytic C–N cross-couplings. Our results indicate that not only a high surface area and crystallinity, but also a β -ketoenamine structure and high charge separation under light irradiation are the key factors for high catalytic activity.

Results and Discussion

We began our investigations by synthesizing a C2-linker bearing the acridine moiety (2,6-diaminoacridine, Acr) by a three step reaction, where 3-nitro-*N*-(4-nitrophenyl)aniline was obtained by a Buchwald–Hartwig amination.^[46] After a palladium catalyzed reduction, the linker was prepared by a Bernthsen-type acridine synthesis using formic acid [Section S3.1, in the Supporting Information].^[47] By changing the amounts of hydroxy groups, we have enabled a different β -ketoenamine to imine ratio in Tp-Acr, DHTA-Acr and HTA-Acr COFs (Figure 1a). In the special case of using the phloroglucinol based linker, the keto-enol tautomerization is irreversible towards the keto form, whereas for DHTA and HTA based COFs the tautomerization shows reversibility.^[48] Tp-Acr and DHTA-Acr COFs were prepared via an acid catalyzed Schiff base reaction, where 2,6-diaminoacridine (Acr, 31.5 mg, 0.15 mmol) was reacted with 1,3,5-triformylphloroglucinol (Tp, 21 mg, 0.1 mmol) or 2,4-dihydroxybenzene-1,3,5-tricarbaldehyde (DHTA, 19.4 mg, 0.1 mmol), respectively, using 6 M acetic acid (0.5 mL) as catalyst and a mixture of 3 mL mesitylene/dioxane (1 : 1) as a solvent. For the HTA-Acr COF, the solvent mixture was changed to 1 : 1 *n*-butanol/*o*-

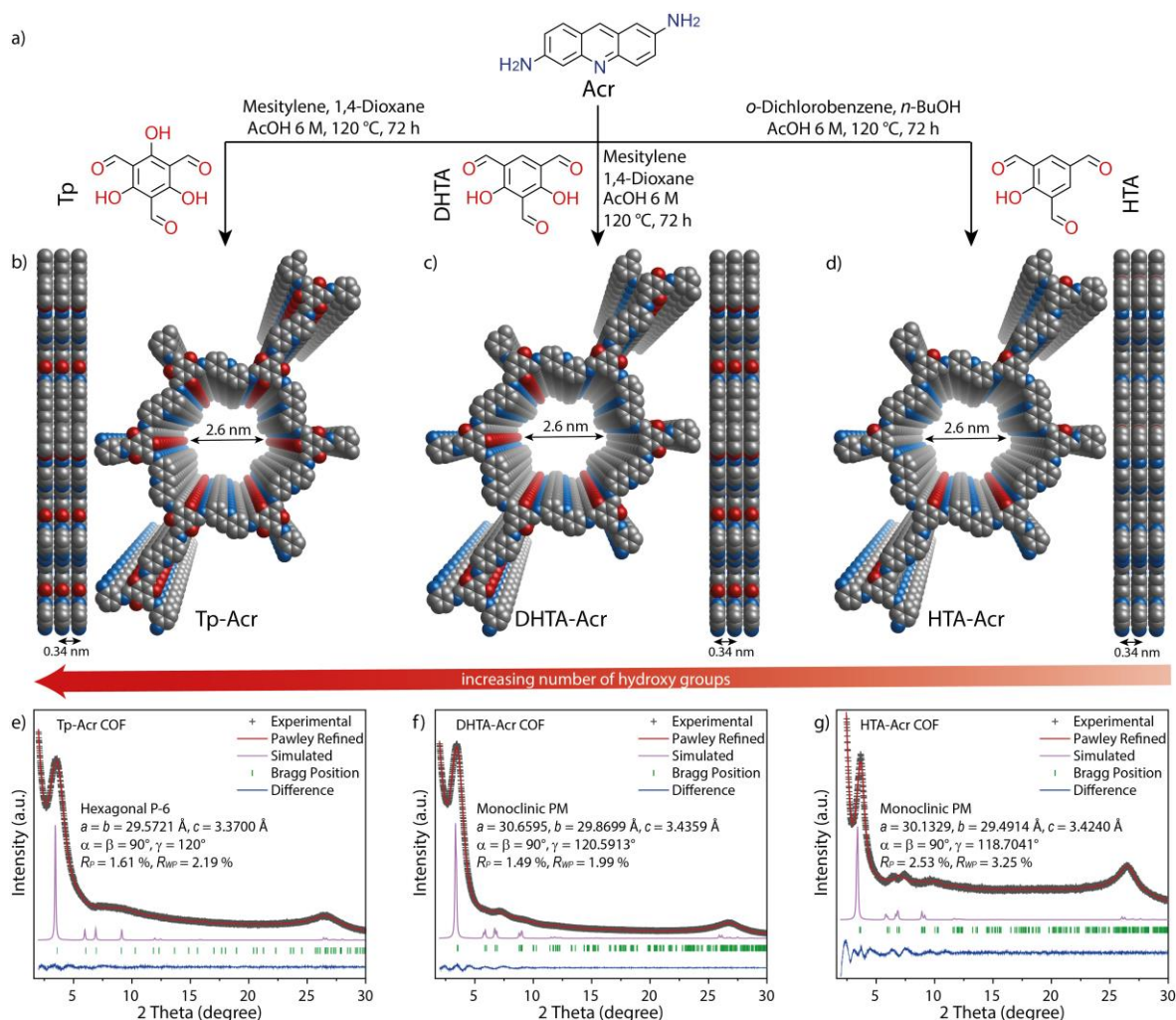


Figure 1. Synthesis and characterization of Tp-Acr, DHTA-Acr and HTA-Acr. a) Scheme of the synthesis of the COFs. b–d) Top and side views of Tp-Acr, DHTA-Acr and HTA-Acr showing the ideal eclipsed (AA) structures. e–g) Experimental, Pawley-refined and simulated powder X-ray diffraction patterns (AA stacking) and difference plot for Tp-Acr, DHTA-Acr and HTA-Acr.

dichlorobenzene (3 mL) in the reaction with 2-hydroxybenzene-1,3,5-tricarbaldehyde (HTA, 17.8 mg, 0.1 mmol), while the amount of 2,6-diaminoacridine and acetic acid was kept constant (Section S3.2). All the precursor mixtures were heated for 72 h at 120 °C and the solid product washed with acetone, methanol (MeOH) and cyclohexane prior to Soxhlet extraction using MeOH to obtain the COFs as dark red solids.

Structural features and crystallinity of the synthesized COFs were determined using powder X-ray diffraction (PXRD) analyses with a Cu K_α radiation. All materials show the most intense reflections in the low angle region at 3.5 2θ degrees for Tp-Acr as well as DHTA-Acr, and 3.6 2θ degrees for HTA-Acr (Figure 1e–g). These can be assigned to the (100) facet of a primitive hexagonal lattice. Additional weak reflections and a broad reflection at around

26.5 2θ degrees can be assigned to the (001) facet and confirm the crystalline π - π stacked 2D structure for all three COFs. According to the geometry of the linkers, structural models with **hcb** topology were constructed for eclipsed (AA) and staggered (AB) stacking sequences (Figure S4–S6). After geometrical optimization, the theoretical PXRD patterns of the structures were calculated and compared to the experimental diffraction pattern. All three COFs showed good agreement for the eclipsed stacking pattern, whereas the simulated staggered pattern did not fit with the measured diffractogram (Figure S7). Additionally, a full Pawley refinement was carried out to fit the final unit cell parameters, which led to acceptably low residual values and profile differences (Figure 1e–g).

All COFs were studied using ^{13}C cross-polarization magic angle spinning nuclear magnetic resonance (CP-MAS NMR) analyses (Figure 2a). The pronounced carbonyl carbon ($\text{C}=\text{O}$) peak in the area of 180–185 ppm for Tp-Acr and DHTA-Acr indicates that these COFs exist dominantly in their keto form. In case of HTA-Acr COF, an equilibrium between the keto- and enol-form was identified via the signals at 179 and 189 ppm, respectively.

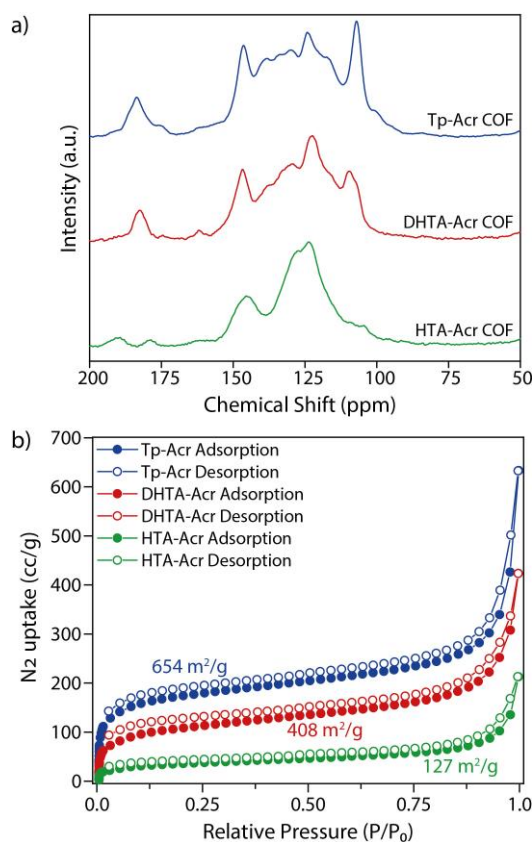


Figure 2. a) ^{13}C CP-MAS NMR spectra of Tp-Acr, DHTA-Acr and HTA-Acr. b) N_2 sorption isotherms for Tp-Acr, DHTA-Acr and HTA-Acr.

Further distinctive peaks are overlapping with the broad multiple signals between 100–150 ppm due to the missing symmetry in the acridine linker. Fourier transform infrared (FT-IR) spectra of the frameworks confirmed the disappearance of characteristic signals of the precursors, while diagnostic bands of the COFs (C=O and C=C bonds at 1550–1580 cm^{-1} and for C–N bonds at around 1270 cm^{-1}) are present (Section S5.1). From the CP-MAS NMR and FTIR data, the structural integrity and formation of acridine COFs has been validated.

The permanent porosity of the acridine based COFs was confirmed using nitrogen sorption measurements at 77 K (Figure 2b). The surface areas were calculated using the Brunauer–Emmett–Teller (BET) method. Among the newly synthesized acridine COFs, Tp-Acr showed the highest BET surface area of 654 $\text{m}^2 \text{g}^{-1}$, compared to 408 $\text{m}^2 \text{g}^{-1}$ for DHTA-Acr COF and 127 $\text{m}^2 \text{g}^{-1}$ for the HTA-Acr COF. This shows that the number of hydroxy groups in the aldehyde linker influences the final accessible surface area of the COFs. The additional keto-/enol groups within the COF structure work as pore-directing “anchors”, improving the stacking of the layers, which results in the increase of surface area.^[49] Additional pore size evaluation revealed for all COFs a distribution close to the simulated one (Figure S11). Scanning electron microscopy (SEM) analyses revealed a rather undefined morphology from aggregated particles of Tp-Acr, DHTA-Acr and HTA-Acr, while transmission electron microscopy (TEM) confirms the presence of a sheet like structure (Figure S12). In order to investigate the chemical stability of Tp-Acr, the COF was immersed in various solvents. PXRD analyses of recovered samples confirmed, that the Tp-Acr COF retained its crystalline structure after 3 days of treatment with acetone, methanol, cyclohexane, dimethylacetamide (DMAc) or water. Moreover, the COF was stable in a basic aqueous environment (1 M NaOH) for 1 day with only a slight loss in crystallinity. No sign of decomposition or dissolution was observed, and the COF could be recovered quantitatively after the treatment (Figure S13 and S14). Additionally, the thermal stability of the COFs was tested using thermogravimetric analysis (TGA), which revealed that the frameworks are - after initial weight loss due to adsorbed solvent molecules - thermally stable up to 300 °C (Figure S15). The chemical stability of the COF in DMAc and basic medium is important as the architectural stability in polar solvents and under basic conditions renders a prerequisite for many photocatalytic reactions, particularly metallaphotocatalytic cross-couplings.^[50]

From the diffuse reflectance ultraviolet-visible (UV/Vis) spectroscopy, it was confirmed that all acridine containing COFs show a very similar absorption behavior in the visible light region. In order to distinctly investigate the effect of the acridine moiety on the optical properties, an isorecticular COF with anthracene edges (Tp-DAA, DAA: 2,6-diaminoanthracene) was synthesized for comparison (Section S6).^[51] It can be clearly seen that the absorption of Tp-DAA COF is blue shifted compared to the acridine COFs. While Tp-DAA exhibits an absorption edge at 620 nm, all acridine COFs show an absorbance over a broad range of the visible light region. The absorption edge is in all cases around 680 nm tailing up to more than 800 nm (Figure 3a). Optical band gaps calculated from Tauc plots are 1.82–1.83 eV for the acridine COFs and 1.98 eV for the anthracene analogue, confirming the impact of acridine moieties for light harvesting in the visible region (Figure 3b). The absorption of the acridine moiety itself determines the photophysical properties with a peak shoulder at 610 nm that can be attributed to aggregation of the acridine units, which is red shifted to the absorption of the acridine linker itself (Figure S16). Such a phenomenon, the formation of so-called “*J*-aggregates”, was previously reported for porphyrin COFs.^[52] Moreover photoluminescence measurements and steady-state time-resolved fluorescence life-time measurements were performed (Section S5.6). The measurements reveal for individual decay components, that Tp-Acr shows the highest life-time compared to other acridine based COFs.

The conduction band electrons of the acridine COF species were monitored by electron paramagnetic resonance (EPR) spectroscopy. To visualize the charge separation and transfer properties, EPR spectra of the COFs have been recorded in the dark and under photocatalytic

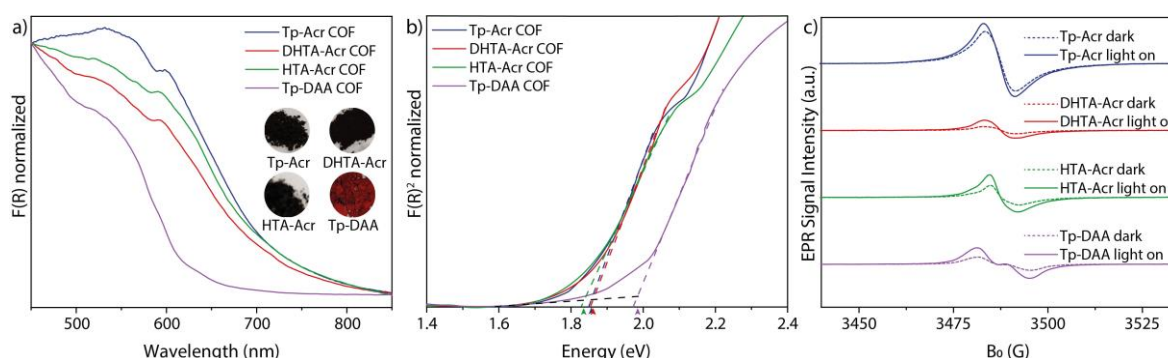


Figure 3. a) UV/Vis diffuse reflectance spectra for Tp-Acr, DHTA-Acr, HTA-Acr and Tp-DAA. The inset shows optical images of the COF powders. b) Tauc plots for Tp-Acr, DHTA-Acr, HTA-Acr and Tp-DAA. c) EPR conduction band e-signals of Tp-Acr, DHTA-Acr, HTA-Acr and Tp-DAA under dark condition (dotted lines) and during visible light irradiation (>420 nm).

reaction conditions. All three acridine based COFs show a singlet signal with Lorentzian line shape at $g=2.007$, which can be attributed to unpaired electrons in the conduction band.^[53] The signal intensities increased upon irradiation with light, since more electrons are excited from the valence band to the conduction band, indicating the formation of electron hole pairs in the COF semiconductors (Figure 3c).^[36,54] A clear trend in signal intensity can be found for the COF materials. The Tp-Acr COF shows by far the highest signal intensity, which suggests that the charge separation efficiency is largely improved in the fully β -keto tautomerized COF material. For DHTA-Acr and HTA-Acr the tautomerization between keto and enol form is likely to result in a decreased stability of the conduction band electrons. Compared to the structurally identical Tp-Acr, the anthracene containing Tp-DAA ($g=2.007$) COF shows a decreased efficiency in charge separation (Figure S18), highlighting the benefit of introducing the acridine moiety into the framework structure.

After confirming the porosity as well as the presence of acridine functionalities in the COF backbones and determining the enhanced light absorption in visible light region as well as the charge separation properties, we sought to study if acridine COFs are suitable photocatalysts for semi-heterogeneous dual nickel/photocatalytic C–N cross-coupling.^[50] Our investigations started by optimizing the amination of 4-bromobenzotrifluoride with pyrrolidine using the Tp-Acr COF as photocatalyst and 440 nm LEDs as light source. Nearly quantitative formation (91 %) of the desired alkyl aryl amine (**1**) was obtained within 16 h when Tp-Acr COF (2 mg mL^{-1}), $\text{NiBr}_2 \cdot 3\text{H}_2\text{O}$ (5 mol%) and three equivalents of the amine coupling partner were used in DMAc (Figure 4, Entry 1). Similarly, DHTA-Acr and HTA-Acr showed full conversion of the substrate with slightly lower selectivity towards the coupling product (Entries 2 and 3). Interestingly, the isorecticular Tp-DAA COF also gave almost quantitative formation of the desired product under these conditions (Entry 4). Shorter reaction times were investigated to better compare the activity of Tp-Acr and Tp-DAA. Within five hours, the acridine COF resulted in 87 % of the desired product, while Tp-DAA gave only 55 % (Entries 5 and 6). These results highlight the advantage of using the acridine based COFs in metallaphotocatalytic C–N cross-coupling and are in full agreement with the charge separation properties found in EPR. When comparing the three acridine COFs, also the higher surface area of Tp-Acr compared to the others might accelerate the photocatalytic performance by increasing the number of accessible active sites and improving mass transfer within the material. However, Tp-DAA shows an even higher

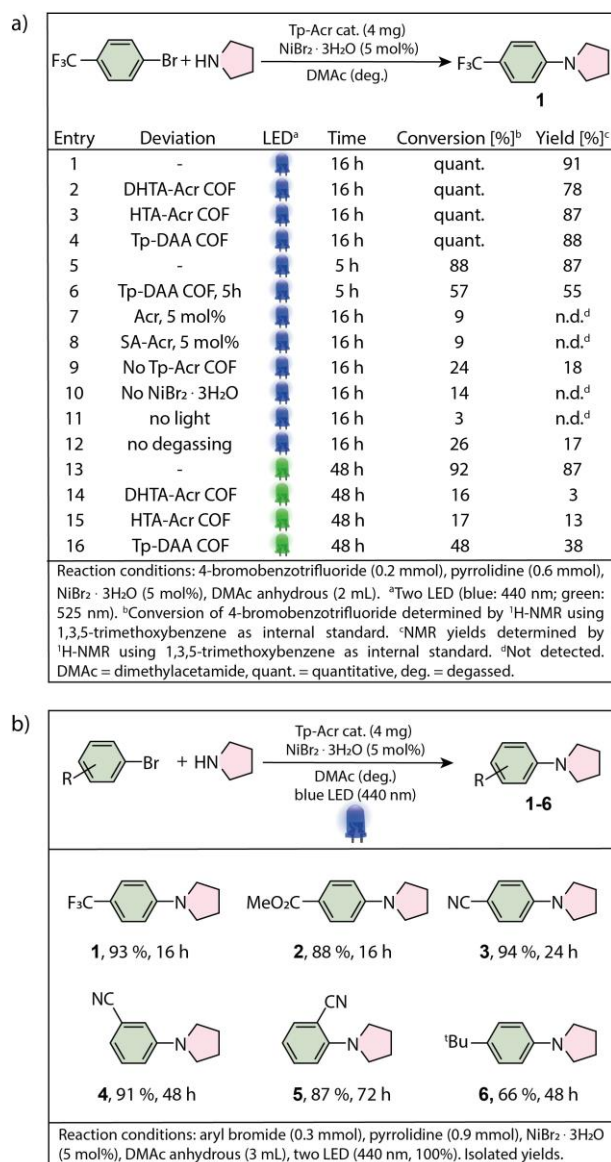


Figure 4. a) Optimized conditions and control experiments using blue and green light. b) Scope of the semi-heterogeneous amination of pyrrolidine and aryl bromides.

surface area than TP-Acr from BET measurements (Figure S20), but a lower activity, thus charge carrier generation and separation seem to be the most decisive parameter for their photocatalytic performance.

Control studies using the linker 2,6-diaminoacridine (Acr) or a model compound (low molecular repeating unit of the COF structure; SA-Acr; Section S7) as photocatalyst showed no formation of the product (Entries 7 and 8), emphasizing that only after incorporation into the COF backbone, the repeating units build up their photocatalytic properties through conjugation. In case of omitting a photocatalyst, still minor product formation (18 %) was

detected (Entry 7). This can be explained by photoexcitation and productive catalysis of nickel-amine complexes by the small portion of UV-light in the emission of the used light source (Figure S1).^[55] Further control studies showed that a nickel source, light and an oxygen free-environment are crucial for the desired coupling (Entry 10–12). With their extended absorption, the acridine COFs were additionally tested as photocatalyst under green light radiation (525 nm LEDs). This is important, because lower excitation energy prevents catalyst deactivation^[34] and the formation of undesired side products in case of certain substrates.^[35] Indeed, the reaction using Tp-Acr as a photocatalyst resulted in 87 % yield of **1** after 48 h (Entry 13). On the contrary, DHTA-Acr and HTA-Acr showed only minor product formation, while using Tp-DAA 38 % of the coupling product was obtained (Entries 14 and 16). These results emphasize that embedding the acridine unit into a fully keto tautomerized COF resulted in a highly efficient photocatalyst both under blue and green light irradiation. With the optimized conditions using the most efficient COF (Tp-Acr) as photocatalyst, the versatility of the semi-heterogeneous catalytic system was evaluated (Figure 4b). The reaction of pyrrolidine with electron deficient aryl bromides generally gave high yields for the corresponding aryl amines (**1–5**). An aryl bromide with electron-donating group (**6**) reacted with slightly less selectivity, which is in agreement with most dual nickel/photocatalytic C–N coupling protocols.^[34,55–58] Nitriles (**3–5**), ester (**2**), trifluoromethyl- (**1**) as well as a bulky aliphatic residue (**6**) were tolerated in the dual catalytic amination. Substrates with an electron withdrawing meta-substituent (**4**) or ortho-substituent (**5**) did also yield the desired products in similar selectivity, although with lower efficiency than the para-substituted analogue (**3**).

A major advantage of COFs is the potential reusability of the solid photocatalyst due to easy separation from the reaction mixture. Therefore, we studied whether the Tp-Acr framework can be recycled (Figure 5). After successful C–N coupling reaction, Tp-Acr COF was recovered by centrifugation and reused for the same reaction. A first set of experiments in which the recovered material was washed with DMAc and lyophilized (Figure 5, blue bars) showed that Tp-Acr can be recycled, but a significant drop in yield of **1** was observed. We hypothesized that the loss in catalytic activity can be attributed to a collapse of the pores of the COF due to removal of DMAc. Performing a solvent exchange with MeOH and hexane prior to drying improved the recyclability significantly (Figure 5, green bars). A catalytic activity of 60 % is retained after 5 cycles of catalysis. To investigate, if the nickel salt can

be reused, the recycling studies were also conducted without adding $\text{NiBr}_2 \cdot 3 \text{H}_2\text{O}$ after the first run (Figure 5, red bars). A significant drop of efficiency after the first cycle was detected, meaning that addition of the nickel catalyst is needed in each cycle. Nevertheless, inductively coupled plasma optical emission spectrometry (ICP-OES) analysis revealed that 25 % of the added nickel is deposited after the first reaction on the COF material that can drive the reaction in subsequent cycles with a yield of up to 10 %.

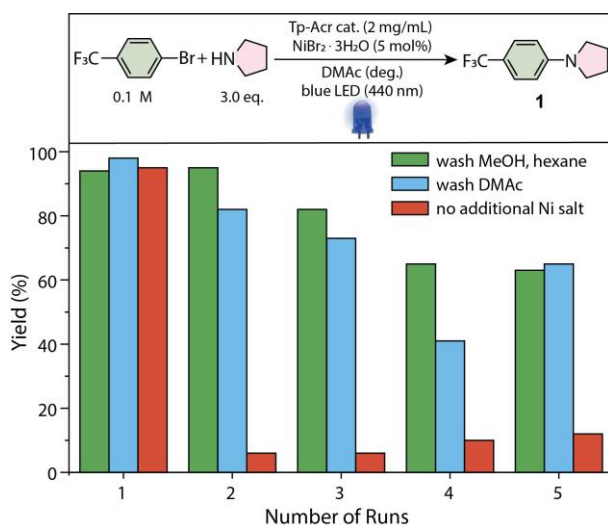


Figure 5. Reusability of Tp-Acr COF in the dual nickel/photocatalytic amination of 4-bromobenzotrifluoride and pyrrolidine (NMR yields determined by ^1H -NMR using 1,3,5-trimethoxybenzene as internal standard, DMAC anhydrous (3 mL), two blue LED [440 nm, 100 %]).

In order to get an understanding of the nickel species adsorbed on the material, the Tp-Acr COF was analyzed by X-ray photoelectron spectroscopy (XPS) after the first and fifth cycle. Ni 2p core-level spectra (Figure S25d-e) of the recycled material confirmed the presence of nickel(II) species with a doublet at 856 eV and 874 eV after the catalysis. Although the crystallinity of the COF is lost due to the intense light irradiation, N 1s XPS core-level spectra show that both the aminic and pyridinic nitrogen species from the COF backbone remain unchanged during the catalysis (Figure S25a-c; S26). The structural integrity of the COF after the cross-coupling reaction was further confirmed by IR spectroscopy (Figure S27). From additional TEM analyses it is clear that the morphology of the materials stays intact throughout the catalysis (Figure S28).

Conclusion

In summary, we report the first successful preparation of crystalline and porous acridine-based COFs by following an acid-catalyzed Schiff base synthesis route using three different 1,3,5-triformylbenzene based linkers. The acridine-based conjugated COFs show light absorption over a broad range of the visible light spectrum. Owing to these properties, the acridine-based COFs were applied for the first time in semi-heterogeneous metallaphotocatalytic C–N cross-couplings. Among the novel COFs, the fully β -ketoenamine tautomerized COF, Tp-Acr, showed a high catalytic activity both under blue and green light radiation for several aryl bromides, which is attributed to higher charge carrier separation efficiency as well as surface area. In addition, it was demonstrated that the COF could be recycled with a small drop in catalytic activity. To the best of our knowledge, this is the first example of a heterogenization of acridine photocatalysts via formation of crystalline organic frameworks.

References

- [1] X. Feng, X. Ding, D. Jiang, *Chem. Soc. Rev.* **2012**, *41*, 6010–6022.
- [2] J. W. Colson, W. R. Dichtel, *Nat. Chem.* **2013**, *5*, 453–465.
- [3] C. S. Diercks, O. M. Yaghi, *Science* **2017**, *355*, eaal1585.
- [4] S. Kandambeth, K. Dey, R. Banerjee, *J. Am. Chem. Soc.* **2019**, *141*, 1807–1822.
- [5] K. Geng, T. He, R. Liu, K. T. Tan, Z. Li, S. Tao, Y. Gong, Q. Jiang, D. Jiang, *Chem. Rev.* **2020**, *120*, 8814–8933.
- [6] Y. Jin, Y. Hu, M. Ortiz, S. Huang, Y. Ge, W. Zhang, *Chem. Soc. Rev.* **2020**, *49*, 4637–4666.
- [7] S. Y. Ding, W. Wang, *Chem. Soc. Rev.* **2013**, *42*, 548–568.
- [8] P. J. Waller, F. Gándara, O. M. Yaghi, *Acc. Chem. Res.* **2015**, *48*, 3053–3063.
- [9] S. Karak, S. Kandambeth, B. P. Biswal, H. S. Sasmal, S. Kumar, P. Pachfule, R. Banerjee, *J. Am. Chem. Soc.* **2017**, *139*, 1856–1862.
- [10] Y. Jin, Y. Hu, W. Zhang, *Nat. Rev. Chem.* **2017**, *1*, 0056.
- [11] O. Yahiaoui, A. N. Fitch, F. Hoffmann, M. Fröba, A. Thomas, J. Roeser, *J. Am. Chem. Soc.* **2018**, *140*, 5330–5333.
- [12] A. Acharjya, P. Pachfule, J. Roeser, F. J. Schmitt, A. Thomas, *Angew. Chem. Int. Ed.* **2019**, *58*, 14865–14870.
- [13] F. Haase, B. V. Lotsch, *Chem. Soc. Rev.* **2020**, *49*, 8469–8500.
- [14] S. H. Sang, H. Furukawa, O. M. Yaghi, W. A. Goddard, *J. Am. Chem. Soc.* **2008**, *130*, 11580–11581.
- [15] Z. Wang, S. Zhang, Y. Chen, Z. Zhang, S. Ma, *Chem. Soc. Rev.* **2020**, *49*, 708–735.
- [16] D. D. Medina, T. Sick, T. Bein, *Adv. Energy Mater.* **2017**, *7*, 1700387.
- [17] J. Guo, D. Jiang, *ACS Cent. Sci.* **2020**, *6*, 869–879.
- [18] Y. Hu, L. J. Wayment, C. Haslam, X. Yang, S. Lee, Y. Jin, W. Zhang, *EnergyChem* **2021**, *3*, 100048.
- [19] X. Zhao, P. Pachfule, A. Thomas, *Chem. Soc. Rev.* **2021**, *50*, 6871–6913.
- [20] M. S. Lohse, T. Bein, *Adv. Funct. Mater.* **2018**, *28*, 1705553.
- [21] B. Liu, H. Sun, J. W. Lee, J. Yang, J. Wang, Y. Li, B. Li, M. Xu, Q. Liao, W. Zhang, D. Han, L. Niu, H. Meng, B. J. Kim, X. Guo, *Energy Environ. Sci.* **2021**, *14*, 4499–4507.
- [22] N. Huang, P. Wang, D. Jiang, *Nat. Rev. Mater.* **2016**, *1*, 16068.

- [23] S. Kandambeth, A. Mallick, B. Lukose, M. V. Mane, T. Heine, R. Banerjee, *J. Am. Chem. Soc.* **2012**, *134*, 19524–19527.
- [24] S. Gisbertz, B. Pieber, *ChemPhotoChem* **2020**, *4*, 456–475.
- [25] P. F. Wei, M. Z. Qi, Z. P. Wang, S. Y. Ding, W. Yu, Q. Liu, L. K. Wang, H. Z. Wang, W. K. An, W. Wang, *J. Am. Chem. Soc.* **2018**, *140*, 4623–4631.
- [26] Y. Nailwal, A. D. D. Wonanke, M. A. Addicoat, S. K. Pal, *Macromolecules* **2021**, *54*, 6595–6604.
- [27] Y. Zhi, Z. Li, X. Feng, H. Xia, Y. Zhang, Z. Shi, Y. Mu, X. Liu, *J. Mater. Chem. A* **2017**, *5*, 22933–22938.
- [28] W. Liu, Q. Su, P. Ju, B. Guo, H. Zhou, G. Li, Q. Wu, *ChemSusChem* **2017**, *10*, 664–669.
- [29] J. Yuan, Q. Xia, W. Zhu, C. Wu, B. Wang, B. Liu, X. Yang, Y. Xu, H. Xu, *ChemPhotoChem* **2020**, *4*, 445–450.
- [30] S. Liu, W. Pan, S. Wu, X. Bu, S. Xin, J. Yu, H. Xu, X. Yang, *Green Chem.* **2019**, *21*, 2905–2910.
- [31] H. Chen, W. Liu, A. Laemont, C. Krishnaraj, X. Feng, F. Rohman, M. Meledina, Q. Zhang, R. Van Deun, K. Leus, P. Van Der Voort, *Angew. Chemie* **2021**, *133*, 10915–10922.
- [32] W. Dong, Y. Yang, Y. Xiang, S. Wang, P. Wang, J. Hu, L. Rao, H. Chen, *Green Chem.* **2021**, *23*, 5797–5805.
- [33] D. G. Brown, J. Boström, *J. Med. Chem.* **2016**, *59*, 4443–4458.
- [34] S. Gisbertz, S. Reischauer, B. Pieber, *Nat. Catal.* **2020**, *3*, 611–620.
- [35] S. Reischauer, V. Strauss, B. Pieber, *ACS Catal.* **2020**, *10*, 13269–13274.
- [36] P. Pachfule, A. Acharjya, J. Roeser, R. P. Sivasankaran, M. Y. Ye, A. Brückner, J. Schmidt, A. Thomas, *Chem. Sci.* **2019**, *10*, 8316–8322.
- [37] S. Lin, C. S. Diercks, Y. B. Zhang, N. Kornienko, E. M. Nichols, Y. Zhao, A. R. Paris, D. Kim, P. Yang, O. M. Yaghi, C. J. Chang, *Science* **2015**, *349*, 1208–1213.
- [38] D. Bessinger, L. Ascherl, F. Auras, T. Bein, *J. Am. Chem. Soc.* **2017**, *139*, 12035–12042.
- [39] W. E. Ford, M. A. J. Rodgers, *J. Photochem. Photobiol. A Chem.* **1991**, *59*, 73–80.
- [40] T. T. Eisenhart, J. L. Dempsey, *J. Am. Chem. Soc.* **2014**, *136*, 12221–12224.
- [41] J. Fang, T. Debnath, S. Bhattacharyya, M. Döblinger, J. Feldmann, J. K. Stolarczyk,

- Nat. Commun.* **2020**, *11*, 5179.
- [42] V. T. Nguyen, V. D. Nguyen, G. C. Haug, H. T. Dang, S. Jin, Z. Li, C. Flores-Hansen, B. S. Benavides, H. D. Arman, O. V. Larionov, *ACS Catal.* **2019**, *9*, 9485–9498.
- [43] V. T. Nguyen, V. D. Nguyen, G. C. Haug, N. T. H. Vuong, H. T. Dang, H. D. Arman, O. V. Larionov, *Angew. Chem. Int. Ed.* **2020**, *59*, 7921–7927.
- [44] H. T. Dang, G. C. Haug, V. T. Nguyen, N. T. H. Vuong, V. D. Nguyen, H. D. Arman, O. V. Larionov, *ACS Catal.* **2020**, *10*, 11448–11457.
- [45] D. Radulescu, G. Ostrogovich, *Chem. Ber.* **1931**, *64*, 2233–2240.
- [46] D. H. O'Donovan, B. Kelly, E. Diez-Cecilia, M. Kitson, I. Rozas, *New J. Chem.* **2013**, *37*, 2408–2418.
- [47] A. Albert, *J. Chem. Soc.* **1948**, *111*, 1225–1230.
- [48] H. Wang, C. Qian, J. Liu, Y. Zeng, D. Wang, W. Zhou, L. Gu, H. Wu, G. Liu, Y. Zhao, *J. Am. Chem. Soc.* **2020**, *142*, 4862–4871.
- [49] S. T. Emmerling, R. Schuldt, S. Bette, L. Yao, R. E. Dinnebier, J. Kästner, B. V. Lotsch, *J. Am. Chem. Soc.* **2021**, *143*, 15711–15722.
- [50] C. Zhu, H. Yue, J. Jia, M. Rueping, *Angew. Chem. Int. Ed.* **2021**, *60*, 17810–17831.
- [51] M. A. Khayum, S. Kandambeth, S. Mitra, S. B. Nair, A. Das, S. S. Nagane, R. Mukherjee, R. Banerjee, *Angew. Chem. Int. Ed.* **2016**, *55*, 15604–15608.
- [52] N. Keller, M. Calik, D. Sharapa, H. R. Soni, P. M. Zehetmaier, S. Rager, F. Auras, A. C. Jakowetz, A. Görling, T. Clark, T. Bein, *J. Am. Chem. Soc.* **2018**, *140*, 16544–16552.
- [53] J. Zhang, G. Zhang, X. Chen, S. Lin, L. Möhlmann, G. Dołęga, G. Lipner, M. Antonietti, S. Blechert, X. Wang, *Angew. Chem. Int. Ed.* **2012**, *51*, 3183–3187.
- [54] D. Hollmann, M. Karnahl, S. Tschierlei, K. Kailasam, M. Schneider, J. Radnik, K. Grabow, U. Bentrup, H. Junge, M. Beller, S. Lochbrunner, A. Thomas, A. Brückner, *Chem. Mater.* **2014**, *26*, 1727–1733.
- [55] C. H. Lim, M. Kudisch, B. Liu, G. M. Miyake, *J. Am. Chem. Soc.* **2018**, *140*, 7667–7673.
- [56] E. B. Corcoran, M. T. Pirnot, S. Lin, S. D. Dreher, D. A. DiRocco, I. W. Davies, S. L. Buchwald, D. W. C. Macmillan, *Science* **2016**, *353*, 279–283.
- [57] I. Ghosh, J. Khamrai, A. Savateev, N. Shlapakov, M. Antonietti, B. König, *Science* **2019**, *365*, 360–366.

- [58] Y. Y. Liu, D. Liang, L. Q. Lu, W. J. Xiao, *Chem. Commun.* **2019**, 55, 4853–4856.

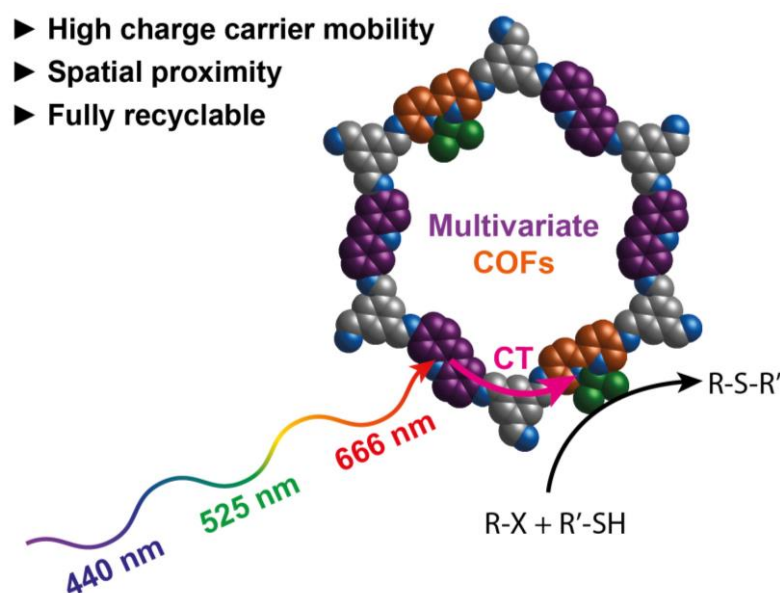
Chapter 5:

Programmable Photocatalytic Activity of Multivariate Covalent Organic Frameworks Used as Metallaphotocatalysts

M. Traxler, S. Reischauer, S. Vogl, J. Roeser, J. Rabeah, C. Penschke, P. Saalfrank, B. Pieber, A. Thomas

Chem. Eur. J. **2022**, e202202967.

Accepted manuscript, DOI: <https://doi.org/10.1002/chem.202202967>



Various multivariate COFs bearing a moiety for photosensitization and complexation of nickel catalysts was synthesized using reticulation with different 1,3,5-triformylbenzene nodes. This enabled the switching between persistent, charge separated species or efficient charge-carrier mobility for different metallaphotocatalytic cross-coupling reactions based on the node unit. The framework showed recyclability and the possibility to drive the reactions using red light irradiation.

Abstract

The multivariate approach allows to incorporate several functionalities into a single covalent organic framework (COF) and consequently allows the construction of bifunctional materials for cooperative catalysis. The well-defined structure of such multivariate COFs is furthermore ideally suited for structure-activity relationship studies. We report a series of multivariate COFs that contain acridine- and 2,2'-bipyridine linkers connected through 1,3,5-benzenetrialddehyde derivatives. The acridine motif is responsible for broad light absorption, while the bipyridine unit enables complexation of nickel catalysts. These features enable usage of the framework materials as catalysts for light-mediated carbon–heteroatom cross-couplings. Variation of the node units shows that the catalytic activity correlates to the keto-enamine tautomer isomerism. This allows switching between high charge-carrier mobility and persistent, localized charge-separated species depending on the nodes, a tool to tailor the materials for specific reactions. Moreover, nickel-loaded COFs are recyclable and catalyze cross-couplings even using red light irradiation.

Specific Contribution

M.T. and S.R. contributed equally to this work and either has the right to list them self first in bibliographic documents. All authors contributed extensively to the work presented in this paper. M.T., S.R., B.P. and A.T. conceived the research project. M.T. conducted the synthesis of linkers as well as COFs and performed characterizations. S.R. evaluated the COFs in cross-couplings. S.V. performed and evaluated the XPS analyses. J. Roeser was responsible for simulations of the COFs. J. Rabeah carried out EPR analyses. C.P. and P.S. conducted theoretical calculations. M.T. and S.R. wrote the manuscript with the input from all authors.

Supporting Information

All experimental procedures and analytical data are available in the supporting information in the appendix or through the website of the Publisher.

DOI: <https://doi.org/10.1002/chem.202202967>

Introduction

Combining two or more catalysts that work in concert to enable the formation of a chemical bond (cooperative catalysis, dual catalysis) has recently become a powerful addition to the synthetic chemist's toolbox.^[1] In particular, the combination of nickel- and photocatalysis (metallaphotocatalysis) has led to the discovery of a number of carbon–heteroatom (C–X) and carbon–carbon (C–C) cross-coupling methods that are carried out under mild conditions using visible-light.^[2–5] These reactions are typically carried out using a photocatalyst in combination with a molecular, homogeneous nickel catalyst. The efficacy of such complex systems depends on a multitude of parameters that are individually optimized to maximize product formation. These include irradiation wavelength, photon flux, activity/selectivity of the nickel catalyst, photoelectronic properties of photocatalysts, base, temperature, solvent and stoichiometry, among others.

The interaction between the catalysts in solution requires persistent excited state lifetimes of the photocatalyst as it must be longer than the time it takes to diffuse to the nickel complex to induce catalysis. Thus, these transformations are limited to photocatalysts that populate triplet excited states with high quantum yields, such as Ir or Ru polypyridyl complexes^[6], and organic compounds that show thermally activated delayed fluorescence.^[7] Similarly, certain semiconducting materials generate sufficiently long-lived charge-separated species.^[8]

Close spatial proximity between the two catalysts is arguably beneficial for electron (or energy) transfer events between the two catalytic species but this parameter is difficult to tune using homogeneous catalysts. Immobilizing the photo- and the nickel catalyst on a support enables controlling the distance between the individual catalysts at the nanoscale. For example, iridium polypyridyl- and nickel bipyridine complexes were integrated in metal–organic frameworks (MOFs),^[9,10] covalent organic frameworks (COFs),^[11,12] and linear polymers.^[13] Indeed, these bifunctional catalysts often showed synergistic effects in terms of higher turnover numbers and catalytic activities in C–C and C–X cross-couplings as compared to using the individual catalysts in solution. A similar trend was observed for MOFs that have incorporated catalysts for dual photo-/Lewis acid catalysis.^[14,15] Decoupling the interaction between the photocatalyst and the nickel catalyst from the limiting rate of diffusion was also shown to increase the arsenal of suitable photocatalysts for metallaphotocatalytic reactions.^[16,17] However, these concepts rely on the immobilization of

photo- and nickel catalysts on a supporting material that potentially influences transmission of the generated charge carriers to the active metal site.

Another appealing strategy is to integrate a nickel catalyst directly into a photocatalytically active polymeric material. Seminal approaches include the incorporation of nickel atoms into carbon nitride materials^[18–21], and a conjugated microporous polymer that contains a bipyridine motif in its repeating unit that can ligate nickel atoms.^[22,23] However, these ill-defined macrostructures do not allow for detailed structure-activity relationship studies to better understand the underlying processes, which renders knowledge-guided improvement of the bifunctional materials difficult.

Covalent organic frameworks (COFs) are well-defined, crystalline, highly porous polymers with tunable structures that are prepared by covalently attaching multiconnected nodes with linear linkers, which can introduce functional groups into the backbone.^[24–28] When a three or higher connected node component is allowed to react with more than one linker unit, several functionalities can be integrated into the backbone of a single COF material (multivariate approach).^[29–34] Owing to their conjugated backbones, COF materials have been shown to serve as valuable photocatalysts.^[35–39] Using the modularity of COFs the optoelectrical properties can be influenced through, for example, the choice of the node component.^[40,41] We have shown that COFs bearing acridine linkers are promising metal-free, heterogeneous photocatalyst that can be combined with homogeneous nickel complexes for metallaphotocatalysis.^[39] Our results suggested that the β -ketoenamine to imine ratio on the node that connects the linkers is a key parameter influencing charge-carrier separation. Others have reported the integration of nickel complexes into a photocatalytically active COF structure to realize visible-light mediated cross-couplings^[42,43] or hydroxylation of aryl chlorides with water.^[44]

Inspired by these studies, we hypothesized that a multivariate COF prepared from an acridine linker, a linking unit that provides coordination sites for nickel, and benzene-1,3,5-tricarbaldehyde derivatives as 3-connected (3-c) nodes would enable detailed structure-activity relationship studies that shine light on parameters that influence the activity of such bifunctional multivariate COF metallaphotocatalysts. Here, we show that the β -ketoenamine to imine ratio significantly varies the efficacy of such COFs as catalysts for C–S and C–N cross-couplings. Our results show that the imine-form leads to high charge carrier mobility that is ideal for activating nickel sites that are ligated at the COF backbone. In contrast, β -

ketoenamine tautomerized COFs have localized, persistent charge-separated species that is key for diffusion limited interaction with homogeneous nickel complexes.

Results and Discussion

Our investigations started with the synthesis of a set of eight multivariate COFs using 2,6-acridinediamine (Acr) as chromophoric linker and 2,2'-bipyridine-5,5'-diamine (Bpy) as metal binding site (Figure 1a). Since both linkers are varying in length, an Acr/Bpy ratio of 2:1 and 1:2 was used to ensure the formation of extended structures of the expected honeycomb topology.^[30] The number of hydroxy groups on the 3-connected benzene-1,3,5-tricarbaldehyde nodes was varied within each series of Acr/Bpy COFs to investigate the influence of the β -ketoenamine to imine ratio on charge-carrier mobility. 1,3,5-triformylphloroglucinol (Tp) was used to synthesize the irreversible keto tautomeric COFs, whereas 1,3,5-triformylbenzene (Tf) carries no tautomerizable group and thus yields a fully imine linked COF (Figure 2e). 2,4-dihydroxybenzene-1,3,5-tricarbaldehyde (DHTA) and 2-hydroxybenzene-1,3,5-tricarbaldehyde (HTA) was used to prepare COF backbones that have reversible tautomeric forms.^[40] All multivariate $\text{Acr}^x\text{-L-Bpy}^y$ COFs (where $x:y = 2:1$ or $1:2$ and $L = \text{Tp, DHTA, HTA or Tf}$) were synthesized by an acid catalyzed Schiff base reaction (detailed information for the synthesis of all COFs can be found in Section S3.2 in the Supporting Information).

The crystallinity of the synthesized COFs was determined by powder X-ray diffraction (PXRD) analyses using $\text{Cu K}\alpha$ radiation (Figure 1b and Figure S5). All materials show an intense reflection in the low angle area at around $3.5^\circ 2\theta$ degrees, which can be assigned to the (100) facet of a primitive hexagonal lattice. Weaker reflections in the $5\text{--}10^\circ 2\theta$ degree range and a broad peak at $26.5^\circ 2\theta$ degrees confirmed the formation of crystalline, π - π stacked two-dimensional structures for all COFs. According to the symmetry of the linkers, the structural models for the multivariate COFs were constructed by generating the expected 2D layers with **hcb** topology. The models were geometrically optimized, and their corresponding theoretical PXRD patterns were compared to the experimentally measured patterns. Theoretical diffraction patterns of models with eclipsed stacking sequences (AA) are in good agreement with the measured diffractograms (Figure S4-S5).

Nitrogen sorption measurements at 77 K confirmed the porosity of all COFs (Figure 1c and Figure S6). Based on the Brunauer-Emmett-Teller (BET) method, surface areas of the COFs

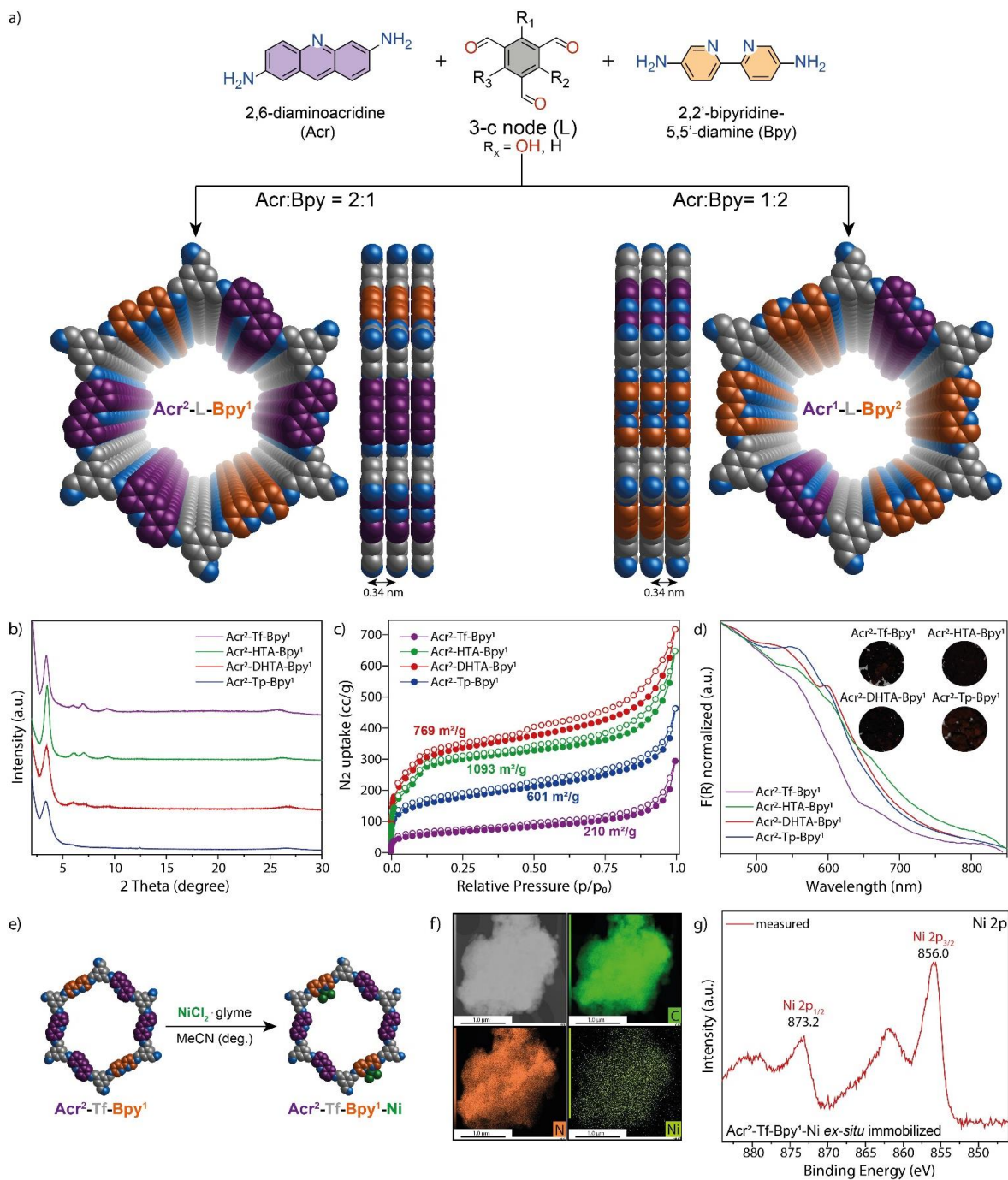


Figure 1. Synthesis and characterization of Acr^x-L-Bpy^y ($x:y = 1:2$ or $2:1$; L = Tp, DHTA, HTA or Tf). (a) Scheme of the synthesis of the COFs; top and side views of Acr^x-L-Bpy^y COFs showing the ideal eclipsed (AA) structures. (b) Experimental X-ray diffraction patterns for Acr²-L-Bpy¹ COFs. (c) N₂ sorption isotherms for Acr²-L-Bpy¹ COFs, calculated BET surface areas are shown in the insets. (d) UV-vis diffuse reflectance spectra for Acr²-L-Bpy¹ COFs. The inset shows optical images of the COF powders. (e) Schematic illustration of the preparation of Acr²-Tf-Bpy¹-[Ni]. (f) TEM image of Acr²-Tf-Bpy¹ and the elemental mapping of carbon, nitrogen and nickel. (g) XPS Ni 2p core-level spectrum of Acr²-Tf-Bpy¹-[Ni].

were determined. Among the series of $\text{Acr}^2\text{-L-Bpy}^1$ COFs, $\text{Acr}^2\text{-HTA-Bpy}^1$ showed the highest specific surface area ($1093 \text{ m}^2/\text{g}$). The fully imine-based COF $\text{Acr}^2\text{-Tf-Bpy}^1$ showed the lowest surface area of $210 \text{ m}^2/\text{g}$. A different trend was found for $\text{Acr}^1\text{-L-Bpy}^2$ COFs, where the highest surface area was obtained using DHTA ($926 \text{ m}^2/\text{g}$) and the lowest using HTA ($175 \text{ m}^2/\text{g}$). The pore size of all $\text{Acr}^2\text{-L-Bpy}^1$ COFs are close to theoretical values (Figure S7).

Fourier transform infrared (FT-IR) spectroscopy confirmed the formation of the framework materials. Characteristic signals of the precursors disappeared, while peaks that can be assigned to C=O and C=C or C=N vibrations, respectively, are present after the COF synthesis (Figure S8-S9). Thermal stability of the multivariate COFs was investigated using thermogravimetric analysis (TGA). After an initial weight loss due to adsorbed moisture and solvent molecules, all materials were thermally stable up to 350°C (Figure S10).

The structural integrity of frameworks was studied by ^{13}C cross-polarization magic angle spinning nuclear magnetic resonance (CP-MAS NMR) analyses (Figure S11). For $\text{Acr}^x\text{-Tp-Bpy}^y$ COFs, a distinct carbonyl carbon (C=O) peak around 180-185 ppm as well the C=C signal at 105 ppm confirm the dominant presence of the keto form.^[45] These two peaks decreased with a lower degree of tautomerization when less hydroxy groups were on the node and completely vanished for $\text{Acr}^x\text{-Tf-Bpy}^y$, indicative of increasing amounts of imine tautomers among the series. Signals between 115-150 ppm confirm the presence heteroaromatic linkers in all COF backbones. Diagnostic signals at 150 and 133 ppm were assigned to the bipyridine motif and confirm an increasing bipyridine:acridine ratio when higher amounts of 2,2'-bipyridine-5,5'-diamine were used for the COF synthesis (Figure S25b).^[46,47]

X-ray photoelectron spectroscopy (XPS) also depicted the gradual reduction of keto-enamine tautomerization in the series of COFs. Deconvolution revealed signals in the N 1s spectrum at 400 eV that can be assigned to the secondary amine group of the keto-enamine linkage. The ratio between these signals gradually decreases with increased number of tautomerizable groups and vanishes for fully imine-based COFs $\text{Acr}^x\text{-Tf-Bpy}^y$ (Figure S12). Aromatic nitrogen atoms of the acridine and bipyridine atoms show a signal with the binding energy of 399 eV in the N 1s spectrum. The different amounts of bipyridine units within the COF backbones can be determined qualitatively, with a more pronounced signal for $\text{Acr}^1\text{-Tp-Bpy}^2$ compared to $\text{Acr}^2\text{-Tp-Bpy}^1$. For the other COFs this peak is overlying with the

signals of the imine and enol bonded nitrogen atoms. To quantitatively determine the amount of Acr and Bpy units in the backbone of the multivalent materials, Acr^x-Tp-Bpy^y COFs were digested in a solution of 0.1 mL of 10 M NaOH in D₂O and 0.5 mL DMSO-d₆ at 120 °C and subsequently analyzed with ¹H-NMR. Integration of the peaks at 7.89 and 7.69 ppm that can be assigned to Bpy and Acr, respectively, show that the amount of substrates used in the synthesis is in agreement with the incorporated ratio of the two linkers, demonstrating no preferential reaction of the linkers (Figure S13).

Using diffuse reflectance ultraviolet-visible (UV-vis) spectroscopy we confirmed that multivariate COFs broadly absorb across the visible-light spectrum (Figure 1d, S15a). The absorption onsets of all COFs are above 700 nm. In comparison, COFs that exclusively contain bipyridine linkers (L-Bpy) absorb less broadly (Figure S24). This shows that the introduction of the acridine moiety is key for efficient solar harvesting.^[39] Using calculations on the level of density functional theory (DFT) we discovered that the introduction of a bipyridine linker into the backbone of the framework is not changing the band gap of the multivariate Acr²-L-Bpy¹ COFs (Section S4.10), confirming our experimental findings.

Before testing the materials in cross-coupling reaction as suitable catalysts, nickel complexation at Acr²-Tf-Bpy¹ was tested *ex situ* by refluxing a suspension of the COF and NiCl₂·glyme in acetonitrile (Figure 1e). After confirming the crystallinity of the material by PXRD (Figure S31), the resulting Acr²-Tf-Bpy¹-Ni was characterized by transmission electron microscopy (TEM) and shows rather undefined morphology of the particles (Figure 1f). Elemental mapping illustrates a homogeneous distribution of nickel, nitrogen and carbon within the material. XPS analysis confirmed successful coordination of Ni^{II} on the bipyridine nitrogen atoms within the COF (Figure 1g). The Ni 2p spectrum showed the presence of nickel with a doublet at 855.7 eV and 873.4 eV, assigned to 2p_{3/2} and 2p_{1/2} signals for Ni^{II} species, respectively. Inductive coupled plasma - optical emission spectroscopy (ICP-OES) was used to quantify the immobilization of the transition metal (Table S9) and showed a nickel loading of 3.59 mg g⁻¹, corresponding to an occupation of 5.1% of bipyridine functionalities.

With the fully characterized Acr^x-L-Bpy^y COFs in hand, we sought to study if these bifunctional materials are suitable as heterogeneous metallaphotocatalysts for carbon–heteroatom cross-couplings in presence of a nickel(II) salt (*in situ* complexation). Indeed, Acr²-Tf-Bpy¹ showed high catalytic activity in the C–S coupling of 4-iodobenzotrifluoride

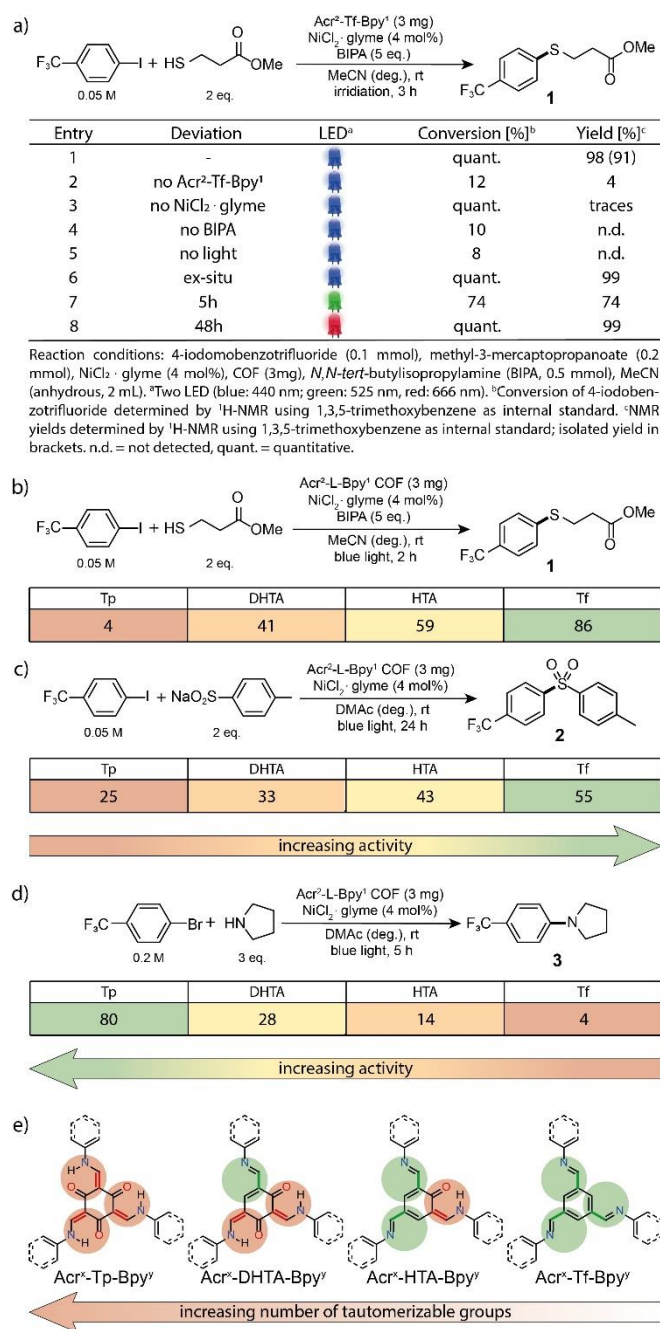


Figure 2. Optimized conditions and control experiments using blue, green and red light for the C–S between 4-iodobenzotrifluoride and 3-mercaptopropionate (a). Screening of Acr²-L-Bpy¹ COFs for the coupling of 4-iodobenzotrifluoride with 3-mercaptopropionate (b) and sodium p-toluenesulfonate (c); NMR yields determined by ¹H-NMR using internal standard. COFs bearing linkers with different tautomerizable groups (d).

with methyl 3-mercaptopropionate. Almost quantitative formation of the desired product (**1**) was achieved within three hours using 440 nm LEDs (Figure 2a, Entry 1). Control studies showed that only small amounts of the coupling product were formed without the Ni^{II} salt, or Acr²-Tf-Bpy¹ (Entry 2,3). No reaction occurred in the absence of a base or light

(Entry 4,5). Nickel complexation can also be carried out prior to catalysis (Entry 6). High energy of blue light potentially causes deactivation of nickel catalysts and can lead to undesired side reactions.^[16] Longer wavelengths do not only serve as a tool to overcome such drawbacks, but also potentially provide better scalable protocols^[48] and enable irradiation through tissue^[49], which is a promising feature towards biological applications. Consequently, we were delighted to see that Acr²-Tp-Bpy¹ shows high catalytic activity using green light (Entry 7) and even results in quantitative product formation after 48 h using red LEDs (Entry 8).

By comparing the series of Acr²-L-Bpy¹ COFs as catalysts, for the same cross-coupling reaction a clear trend regarding the nodes was identified (Figure 2b). Fully tautomerized Acr²-Tp-Bpy¹ showed the lowest catalytic activity with a yield of 4% after 2 h irradiation time. Decreasing the number of hydroxy groups on the node resulted in a gradual increase of the desired product under identical conditions. The same activity pattern was observed in the coupling of 4-iodobenzotrifluoride and sodium *p*-toluenesulfinate (Figure 2c), where the same overall trend was found for Acr¹-L-Bpy² and L-Bpy COFs, showing less than 45 and 36% activity per added nickel center (Table S4). However, the related C–N coupling between pyrrolidine and 4-bromobenzotrifluoride showed a reversed trend (Figure 2d). Here, the keto-tautomer Acr²-Tp-Bpy¹ gave the highest yield, while the corresponding imine-based COF showed low catalytic activity.

This discrepancy can be rationalized by the different involved mechanisms. C–S couplings require coordination of Ni to a bipyridine ligand. In C–N cross-couplings, the secondary amine is added in large excess, because it simultaneously serves as substrate, base and, more importantly, ligand for the first-row transition metal.^[50] As such, this reaction is catalyzed through a homogeneous Ni(pyrrolidine)_n complex that is activated by the COF that only acts as photocatalyst. Hence, the trend in the COF activity results from the fact that the irreversible tautomer stabilizes the conduction band electrons located at the acridine motif, resulting in a persistent charge-separated species that is ideally suited for a diffusion limited dual catalytic interaction with a homogeneous nickel intermediate.^[39] In contrast, in the C–S cross-couplings nickel catalysis requires bipyridine ligation and occurs therefore directly at the COF backbone. Consequently, this transformation benefits from high charge carrier mobility governed by a fully imine-based backbone. These results are supported by electron paramagnetic resonance (EPR) spin trapping experiments that provide evidence for

enhanced formation of spin adducts when a mixture of metalated $\text{Acr}^2\text{-Tf-Bpy}^1\text{-Ni}$, 5,5-dimethyl-1-pyrrolin-*N*-oxid (DMPO) and 4-iodobenzotrifluoride in acetonitrile is irradiated compared to the $\text{Acr}^2\text{-Tp-Bpy}^1\text{-Ni}$ (Figure S19, see Section S4.12 for details).

Next, we aimed to investigate if the high spatiotemporal control that results from the close proximity of the photocatalyst (COF) and the nickel center in combination with the high charge-carrier mobility is superior to related, diffusion limited transformations. We compared the catalytic activity of *in situ* nickel loaded $\text{Acr}^2\text{-Tf-Bpy}^1$ with two other catalytic systems in the cross-coupling of 4-iodobenzotrifluoride with methyl 3-mercaptopropionate (Figure 3). One catalytic system contained a mixture of a photocatalytic COF that only contains acridine units (Tf-Acr; Section S5.3) with a nickel containing bipyridine COF (Tf-Bpy, Section S.5.1) in the ratio of 2:1 (Figure 3). The third catalytic cocktail combined the photocatalytic Tf-Acr COF with a homogeneous nickel 4,4'-di-*tert*-butyl-2,2'-dipyridyl (dtbbpy) complex. Under identical conditions (3 h at 440 nm), the bifunctional material produced the desired coupling molecule in almost quantitative yield, whereas both diffusion limited catalytic processes only resulted in modest conversion.

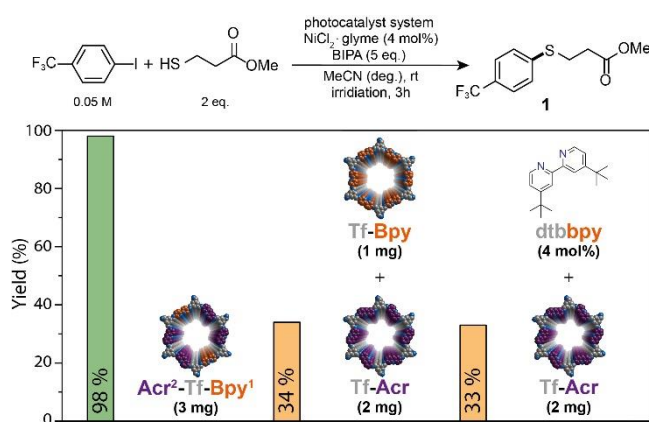


Figure 3. Comparison of the activities between multivalent COF (left), physical mixture of respective COFs (middle) and semi-heterogeneous catalysis (right).

Finally, we studied the recyclability of the bifunctional material using blue (440 nm) light in the thioetherification (Figure 4a). The first experiment was carried through *in situ* catalyst formation using the conditions reported in Figure 2a. ICP-analysis revealed that this material has a nickel content of 13.9 mg g⁻¹, corresponding to an occupation of 20.0% of bipyridine functionalities. The difference in nickel loading compared to the *ex situ* prepared material described above can be attributed to the disruption of the π - π stacking interactions by treating

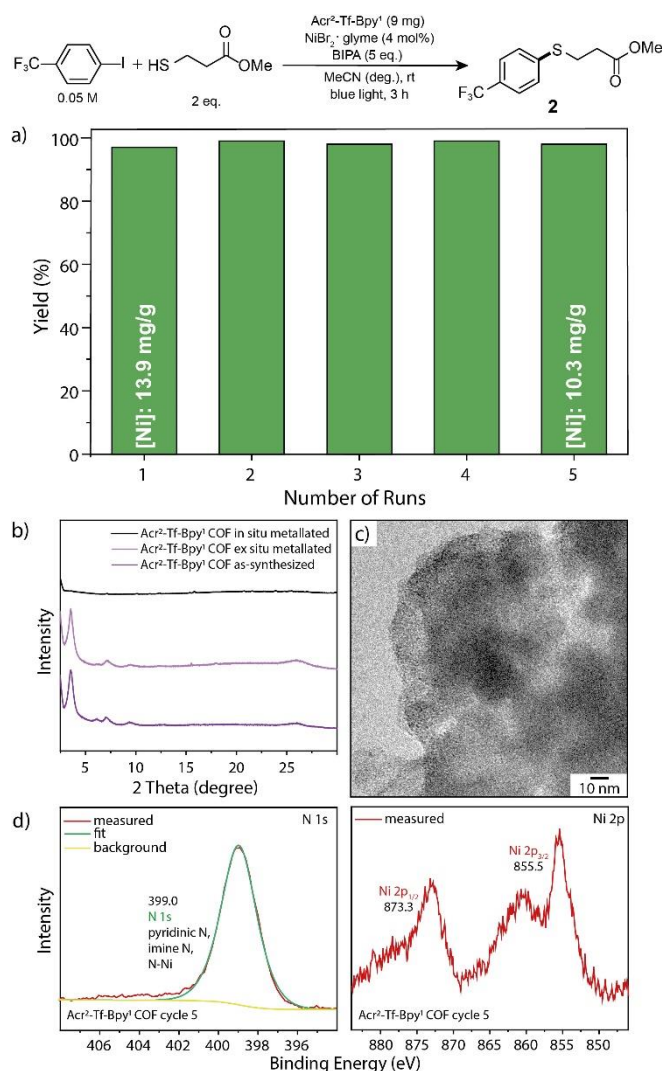


Figure 4. (a) Recyclability studies of $\text{Acr}^2\text{-Tf-Bpy}^1$ for the C–S between 4-iodobenzotrifluoride and 3-mercaptopropionate (NMR yields determined by $^1\text{H-NMR}$ using 1,3,5-trimethoxybenzene as internal standard). (b) PXRD analysis of $\text{Acr}^2\text{-Tf-Bpy}^1$ before before and after photocatalysis (in situ metallation), and ex situ metallation. (c) TEM analyses of $\text{Acr}^2\text{-Tf-Bpy}^1$ after photocatalysis. (d) N 1s and Ni 2p XPS core level spectra of the $\text{Acr}^2\text{-Tf-Bpy}^1$ COF after 5 recycling cycles of photocatalytic dual nickel C–S cross-coupling.

the material with light.^[37,51] This leads to loss of crystallinity using *in situ* metallation, enabling a larger amount of nickel to be immobilized (Figure 4b), due to the diminished long-range order. However, after the respective reaction time, the heterogeneous catalyst was separated, washed and reused without adding additional $\text{Acr}^2\text{-Tf-[Bpy]}^1$ or nickel(II) salt. The bifunctional, nickel charged COF could be recycled five times without significant loss in catalytic activity, suggesting that the nickel atoms strongly coordinate to the bipyridine linkers in the COF. After the last cycle, a nickel loading of 10.3 mg g^{-1} showed that most of the nickel atoms present after the first cycle are still immobilized. FT-IR

spectroscopy confirmed the intact chemical structure of the COF after the reaction (Figure S32), which proves that the short-range order of the material is preserved, although the long-range periodicity is lost under photocatalytic conditions. Additionally, the morphology of the material was analyzed by TEM and did not alter during the recycling study (Figure 4c and S33). XPS spectra after 5 reaction cycles showed that both the N 1s and Ni 2p signal remained unchanged after the photocatalytic cross-coupling reactions (Figure 4d). This confirms the formation of a fully heterogeneous nickel complex embedded into a stable COF matrix. Moreover, UV-vis spectroscopy showed no change in optical properties after the reaction (Figure S35).

Conclusion

In summary a series of multivariate COFs containing a bipyridine and acridine linker were prepared using different three-connected nodes and their application as catalysts for light-mediated nickel catalyzed carbon–heteroatom cross-couplings was evaluated. Four different 1,3,5-triformylbenzene derivatives were selected as nodes to study the influence of β -ketoenamine to imine ratio in the frameworks on catalytic activity. Our results show that the imine-form is key for high charge-carrier mobility that transfers conduction band electrons located at the acridine photocatalyst to an active nickel center that is attached at the bipyridine moieties. In contrast, persistent charge separated species located at the acridine moiety are formed upon excitation of COFs that have β -ketoenamine connections. This was shown to be beneficial in the diffusion limited activation of homogeneous nickel complexes. A multivariate COF that hosts nickel atoms was further shown to be a recyclable heterogeneous C–S cross-coupling catalyst that can be activated with long wavelengths.

Experimental Section

Synthesis of $\text{Acr}^x\text{-L-Bpy}^y$ COFs ($x:y = 2:1$ or $1:2$ and $\text{L} = \text{Tp}$, DHTA, HTA or Tf).

A typical COF synthesis is exemplified for $\text{Acr}^2\text{-Tf-Bpy}^1$. A Pyrex tube (o.d. \times i.d. = 15×10 mm² and length 15 cm) is charged with 1,3,5-triformylbenzene (Tf) (16.2 mg, 0.1 mmol), 2,6-diaminoacridine (Acr) (20.9 mg, 0.1 mmol), 2,2'-bipyridine-5,5'-diamine (Bpy) (9.3 mg, 0.05 mmol), 1.5 mL of *n*-BuOH, 1.5 mL of anhydrous *o*-DCB and 0.5 mL of 6 M aqueous

acetic acid. This mixture was sonicated for 15 minutes in order to get a homogenous dispersion. The tube was then flash frozen at 77 K (liquid N₂ bath) and degassed by three freeze-pump-thaw cycles. The tube was sealed off and then heated at 120 °C for 3 days. A dark red colored precipitate was collected by filtration and washed with acetone, methanol and cyclohexane. The powder collected was dried at 120 °C to give a dark red colored powder.

General experimental procedure for photocatalytic experiments.

An oven dried vial (19 x 100 mm) equipped with a stir bar was charged with NiCl₂·glyme (4-12 μmol), Acr^x-L-Bpy^y COF, 4-halobenzotrifluoride and nucleophile. The solvent (anhydrous) was added and the vessel was sealed with a septum and Parafilm. The mixture was stirred for 1 minute at high speed, followed by sonication for 5 minutes and degassing by bubbling argon for 10 minutes. The reaction mixture was stirred at 800 rpm and irradiated with 440 nm, 535 nm or 666 nm LED lamps. After the respective reaction time, 1,3,5-trimethoxybenzene (1 eq.) was added as internal standard to the reaction vessel, the mixture was shaken and an aliquot (200 μL) was removed, filtered, diluted with DMSO-d₆ and analyzed by ¹H NMR.

References

- [1] S. Martínez, L. Veth, B. Lainer, P. Dydio, *ACS Catal.* **2021**, *11*, 3891–3915.
- [2] J. Twilton, C. C. Le, P. Zhang, M. H. Shaw, R. W. Evans, D. W. C. MacMillan, *Nat. Rev. Chem.* **2017**, *1*, 0052.
- [3] J. A. Milligan, J. P. Phelan, S. O. Badir, G. A. Molander, *Angew. Chem. Int. Ed.* **2019**, *58*, 6152–6163.
- [4] C. Zhu, H. Yue, J. Jia, M. Rueping, *Angew. Chem. Int. Ed.* **2021**, *60*, 17810–17831.
- [5] A. Y. Chan, I. B. Perry, N. B. Bissonnette, B. F. Buksh, G. A. Edwards, L. I. Frye, O. L. Garry, M. N. Lavagnino, B. X. Li, Y. Liang, E. Mao, A. Millet, J. V. Oakley, N. L. Reed, H. A. Sakai, C. P. Seath, D. W. C. MacMillan, *Chem. Rev.* **2022**, *122*, 1485–1542.
- [6] D. M. Arias-Rotondo, J. K. McCusker, *Chem. Soc. Rev.* **2016**, *45*, 5803–5820.
- [7] M. A. Bryden, E. Zysman-Colman, *Chem. Soc. Rev.* **2021**, *50*, 7587–7680.
- [8] S. Gisbertz, B. Pieber, *ChemPhotoChem* **2020**, *4*, 456–475.
- [9] Y. Y. Zhu, G. Lan, Y. Fan, S. S. Veroneau, Y. Song, D. Micheroni, W. Lin, *Angew. Chem. Int. Ed.* **2018**, *57*, 14090–14094.
- [10] G. Lan, Y. Quan, M. Wang, G. T. Nash, E. You, Y. Song, S. S. Veroneau, X. Jiang, W. Lin, *J. Am. Chem. Soc.* **2019**, *141*, 15767–15772.
- [11] A. López-Magano, B. Ortín-Rubio, I. Imaz, D. MasPOCH, J. Alemán, R. Mas-Ballesté, *ACS Catal.* **2021**, *11*, 12344–12354.
- [12] A. Jati, K. Dey, M. Nurhuda, M. A. Addicoat, R. Banerjee, B. Maji, *J. Am. Chem. Soc.* **2022**, *144*, 7822–7833.
- [13] Y. Pan, N. Zhang, C. H. Liu, S. Fan, S. Guo, Z. M. Zhang, Y. Y. Zhu, *ACS Catal.* **2020**, *10*, 11758–11767.
- [14] Y. Quan, G. Lan, Y. Fan, W. Shi, E. You, W. Lin, *J. Am. Chem. Soc.* **2020**, *142*, 1746–1751.
- [15] Y. Quan, Y. Song, W. Shi, Z. Xu, J. S. Chen, X. Jiang, C. Wang, W. Lin, *J. Am. Chem. Soc.* **2020**, *142*, 8602–8607.
- [16] S. Reischauer, V. Strauss, B. Pieber, *ACS Catal.* **2020**, *10*, 13269–13274.
- [17] Z. Zhao, S. Reischauer, B. Pieber, M. Delbianco, *Green Chem.* **2021**, *23*, 4524–4530.
- [18] X. Zhao, C. Deng, D. Meng, H. Ji, C. Chen, W. Song, J. Zhao, *ACS Catal.* **2020**, *10*, 15178–15185.

- [19] A. Vijeta, C. Casadevall, S. Roy, E. Reisner, *Angew. Chem. Int. Ed.* **2021**, *60*, 8494–8499.
- [20] A. Vijeta, C. Casadevall, E. Reisner, *Angew. Chem. Int. Ed.* **2022**, *61*, e202203176.
- [21] M. Kwak, J. Bok, B. H. Lee, J. Kim, Y. Seo, S. Kim, H. Choi, W. Ko, W. Hooch Antink, C. W. Lee, G. H. Yim, H. Seung, C. Park, K. S. Lee, D. H. Kim, T. Hyeon, D. Yoo, *Chem. Sci.* **2022**, *13*, 8536–8542.
- [22] C. Cavedon, S. Gisbertz, S. Reischauer, S. Vogl, E. Sperlich, J. H. Burke, R. F. Wallick, S. Schrottke, W.-H. Hsu, L. Anghileri, Y. Pfeifer, N. Richter, C. Teutloff, H. Müller-Werkmeister, D. Cambié, P. H. Seeberger, J. Vura-Weis, R. M. van der Veen, A. Thomas, B. Pieber, *Angew. Chem. Int. Ed.* **2022**, e202211433.
- [23] W.-H. Hsu, S. Reischauer, P. H. Seeberger, B. Pieber, D. Cambié, *Beilstein J. Org. Chem.* **2022**, *18*, 1123–1130.
- [24] C. S. Diercks, O. M. Yaghi, *Science* **2017**, *355*, eaal1585.
- [25] F. Haase, B. V. Lotsch, *Chem. Soc. Rev.* **2020**, *49*, 8469–8500.
- [26] T. Zhang, G. Xing, W. Chen, L. Chen, *Mater. Chem. Front.* **2020**, *4*, 332–353.
- [27] X. Zhao, P. Pachfule, A. Thomas, *Chem. Soc. Rev.* **2021**, *50*, 6871–6913.
- [28] A. M. Evans, M. J. Strauss, A. R. Corcos, Z. Hirani, W. Ji, L. S. Hamachi, X. Aguilar-Enriquez, A. D. Chavez, B. J. Smith, W. R. Dichtel, *Chem. Rev.* **2022**, *122*, 442–564.
- [29] A. Nagai, Z. Guo, X. Feng, S. Jin, X. Chen, X. Ding, D. Jiang, *Nat. Commun.* **2011**, *2*, 536.
- [30] N. Huang, L. Zhai, D. E. Coupry, M. A. Addicoat, K. Okushita, K. Nishimura, T. Heine, D. Jiang, *Nat. Commun.* **2016**, *7*, 12325.
- [31] Z. F. Pang, S. Q. Xu, T. Y. Zhou, R. R. Liang, T. G. Zhan, X. Zhao, *J. Am. Chem. Soc.* **2016**, *138*, 4710–4713.
- [32] L. Feng, K. Y. Wang, G. S. Day, H. C. Zhou, *Chem. Soc. Rev.* **2019**, *48*, 4823–4853.
- [33] T. Zhou, X. Huang, Z. Mi, Y. Zhu, R. Wang, C. Wang, J. Guo, *Polym. Chem.* **2021**, *12*, 3250–3256.
- [34] Y. Xie, T. Pan, Q. Lei, C. Chen, X. Dong, Y. Yuan, J. Shen, Y. Cai, C. Zhou, I. Pinnau, Y. Han, *Angew. Chem. Int. Ed.* **2021**, *60*, 22432–22440.
- [35] V. S. Vyas, V. W. H. Lau, B. V. Lotsch, *Chem. Mater.* **2016**, *28*, 5191–5204.
- [36] V. S. Vyas, F. Haase, L. Stegbauer, G. Savasci, F. Podjaski, C. Ochsenfeld, B. V. Lotsch, *Nat. Commun.* **2015**, *6*, 8508.

- [37] P. Pachfule, A. Acharjya, J. Roeser, T. Langenhahn, M. Schwarze, R. Schomäcker, A. Thomas, J. Schmidt, *J. Am. Chem. Soc.* **2018**, *140*, 1423–1427.
- [38] H. Wang, H. Wang, Z. Wang, L. Tang, G. Zeng, P. Xu, M. Chen, T. Xiong, C. Zhou, X. Li, D. Huang, Y. Zhu, Z. Wang, J. Tang, *Chem. Soc. Rev.* **2020**, *49*, 4135–4165.
- [39] M. Traxler, S. Gisbertz, P. Pachfule, J. Schmidt, J. Roeser, S. Reischauer, J. Rabeah, B. Pieber, A. Thomas, *Angew. Chem. Int. Ed.* **2022**, *61*, e202117738.
- [40] H. Wang, C. Qian, J. Liu, Y. Zeng, D. Wang, W. Zhou, L. Gu, H. Wu, G. Liu, Y. Zhao, *J. Am. Chem. Soc.* **2020**, *142*, 4862–4871.
- [41] F. Liu, Y. He, X. Liu, Z. Wang, H.-L. Liu, X. Zhu, C.-C. Hou, Y. Weng, Q. Zhang, Y. Chen, *ACS Catal.* **2022**, *49*, 9494–9502.
- [42] C. Zhu, H. Yue, J. Jia, M. Rueping, *Angew. Chem. Int. Ed.* **2021**, *60*, 17810–17831.
- [43] W. Dong, Y. Yang, Y. Xiang, S. Wang, P. Wang, J. Hu, L. Rao, H. Chen, *Green Chem.* **2021**, *23*, 5797–5805.
- [44] K. Wang, H. Jiang, H. Liu, H. Chen, F. Zhang, *ACS Catal.* **2022**, *12*, 6068–6080.
- [45] S. Kandambeth, A. Mallick, B. Lukose, M. V. Mane, T. Heine, R. Banerjee, *J. Am. Chem. Soc.* **2012**, *134*, 19524–19527.
- [46] H. B. Aiyappa, J. Thote, D. B. Shinde, R. Banerjee, S. Kurungot, *Chem. Mater.* **2016**, *28*, 4375–4379.
- [47] X. Zhao, P. Pachfule, S. Li, T. Langenhahn, M. Ye, C. Schlesiger, S. Praetz, J. Schmidt, A. Thomas, *J. Am. Chem. Soc.* **2019**, *141*, 6623–6630.
- [48] B. D. Ravetz, N. E. S. Tay, C. L. Joe, M. Sezen-Edmonds, M. A. Schmidt, Y. Tan, J. M. Janey, M. D. Eastgate, T. Rovis, *ACS Cent. Sci.* **2020**, *6*, 2053–2059.
- [49] B. D. Ravetz, A. B. Pun, E. M. Churchill, D. N. Congreve, T. Rovis, L. M. Campos, *Nature* **2019**, *565*, 343–346.
- [50] S. Gisbertz, S. Reischauer, B. Pieber, *Nat. Catal.* **2020**, *3*, 611–620.
- [51] L. Stegbauer, K. Schwinghammer, B. V. Lotsch, *Chem. Sci.* **2014**, *5*, 2789–2793.

Chapter 6:

Summary and Outlook

The aim of this thesis was to investigate different porous polymeric materials for their targeted use in different fields of catalysis based on the unique properties of each material class. On the one hand, a microporous polymer network was constructed that is used for continuous-flow dehydrogenation at elevated temperatures. On the other hand, the first usage of an acridine based linker for the synthesis of porous and crystalline covalent organic frameworks has been developed. Subsequently, these framework materials were demonstrated to be efficient catalysts for metallaphotocatalytic cross-coupling reactions.

In Chapter 3, a microporous polymer network was constructed as single-site catalyst for the dehydrogenation of cyclohexane. The synthesis protocol of the material involved two post-synthetic modification steps to introduce bromoalkyl chains as anchoring sites within the pores of the polymer network. Additionally, a modified iridium (I) pincer complex was synthesized, which had a potassium phenolate moiety for the anchoring installed. Subsequently, the metal-organic catalyst was immobilized in a third post-synthetic modification to afford the heterogenization of the homogeneous iridium pincer catalyst. In contrast to previous reports from our group the linkage of the catalyst is constructed via the ligand sphere. With this, the catalyst showed activity in the dehydrogenation reaction at elevated temperatures, which was tested in continuous-flow experiments. Here the catalyst demonstrated a long-time stability, which exceeds six days on stream. Additionally, the catalytic activity was not affected by co-feeding water, which highlights the use of the hydrophobic nature of the constructed material.

The development and use of a novel linker for the construction of a series of covalent organic frameworks is described in Chapter 4. The introduction of acridine, a parent moiety of organic dyes, into the backbone of the framework structure resulted in the formation of porous and crystalline materials, that absorb broadly throughout the visible light spectrum. With these properties, the materials were tested for the metallaphotocatalytic C–N cross-coupling reaction. Among the synthesized materials the β -ketoenamine linked COF Tp-Acr showed the highest activity in the organic transformation, originating from the highest generation of electron-hole pairs under illumination, which was proven using electron

paramagnetic resonance spectroscopy. The framework was moreover able to perform the reaction for differently substituted aryl halides and could drive the reaction even using lower energy green light irradiation. Upon recycling, it was found that the photocatalyst maintains the activity for at least five reaction cycles. However, the nickel co-catalyst was not reusable and had to be added at each cycle.

With the findings of Chapter 4 showing that the nickel catalyst is not recyclable, the goal was set to develop a fully heterogeneous all-in-one metallaphotocatalyst based on covalent organic frameworks, which is described in Chapter 5. In order to do that, the concept of multivariate COFs was used, where more than the topologically necessary building blocks are applied to construct the framework. In this case the acridine linker was used as photosensitizing moiety in combination with a bipyridine linker that shows the capability to act as a linker for the complexation of the nickel salt. These two moieties were linked together by a series of four tritopic trialdehyde linkers that show a different number of additional aldehyde moieties. Testing these materials for C–N and C–S cross-couplings revealed that the activity of the COFs can be influenced by the choice of the linking aldehyde moiety. Here it can be seen that using a fully β -ketoenamine-linked COF results in persistent, localized charge separated species, which are beneficial for the semiheterogeneous C–N coupling reaction. In contrast to that, testing the multivariate COFs for C–S coupling reactions showed an inverse trend. Here the fully imine-linked COFs showed the highest activities. For this reaction the development of high charge carrier mobility between acridine and immobilized nickel is crucial to catalytic efficiency. It was also shown that for the C–S coupling this catalyst is fully recyclable and even catalyzes the cross-coupling reaction under red light irradiation.

In recent years the field of microporous polymer networks has evolved significantly. However, the application of this class of materials as support material for the introduction of catalytic moieties remains underexplored. Besides the covalent attachment of molecular catalysts, which was demonstrated within this thesis, charged porous polymers would offer the possibility to introduce ionic catalysts within the pores of the material. This approach is especially compelling, since the immobilization of the catalyst would involve a simple ion exchange protocol. But the scope of the immobilization of catalytic centers is not limited to metal-organic catalysts. Currently, a porous polymer network is developed in our group that can anchor oligopeptides as catalysts for asymmetric transformations. The broad possibility

for the introduction of catalytic units in combination with the hydrophobic nature of the polymer backbone shows moreover the potential of MPNs as suitable support material for the development of tandem catalysis systems.

In the first nearly two decades the focus in the field of covalent organic frameworks was focused on the synthesis of novel materials based on new linkers or linkages. Nowadays, the field is transforming towards a more functional-led design of framework structures. Here, the development of the multivariate COF approach opens avenues for the combination of functional moieties in a defined structure on the nanometer scale. Owing to its easily adaptable protocol, further examples in cooperative catalysis can be expected based on the combination of functionalities using this synthetic approach. Moreover, the means of reticular chemistry allow to tune the distances between the functional moieties based on the nodes used for the COF synthesis. This spatial control gives the opportunity to enable structure-activity relationship investigations, where the understanding on the length scale offers a rationale for the development of novel dual-catalytic systems.

In summary, the versatility of porous polymeric materials has been demonstrated on different catalytic transformations. The diversity of the reactions tackled with novel materials developed within this thesis ranges from single-site heterogenized homogenous catalysts for gas phase continuous-flow reactions to metallaphotocatalytic organic cross-coupling reactions. Moreover, the design of a dual-functional multivariate COF protocol was developed which allowed for cooperative catalysis within a fully heterogeneous system.

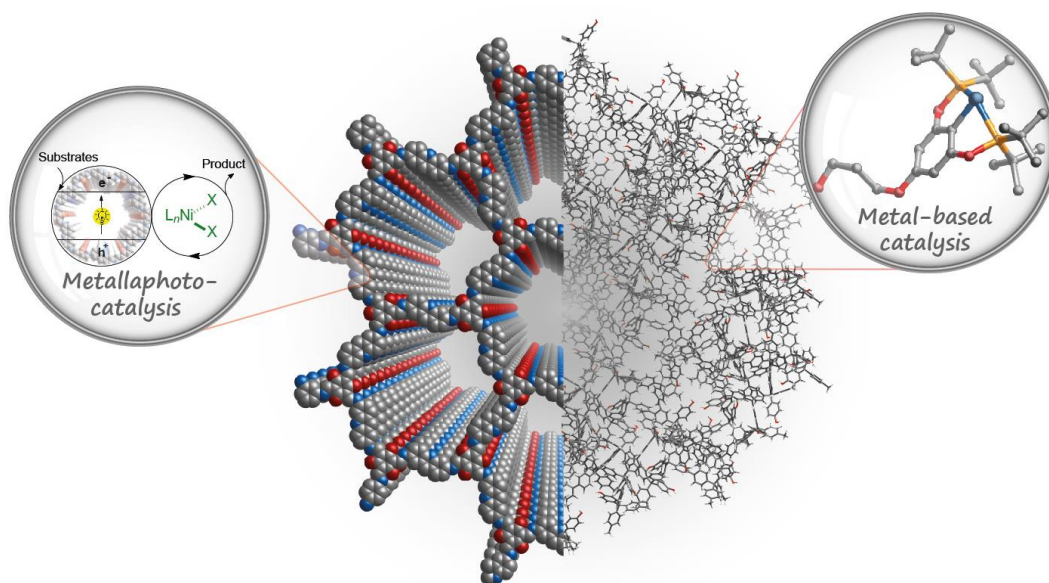


Figure 1. Graphical summary of this thesis.

APPENDIX

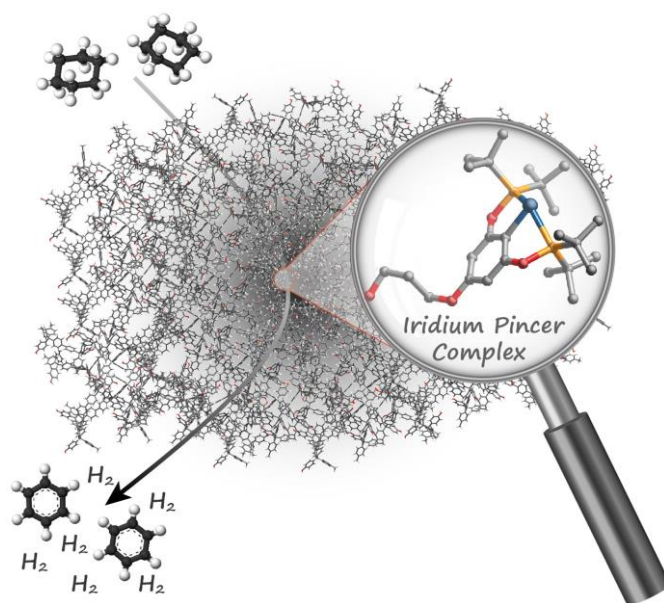
Article I:

Anchoring an Iridium Pincer Complex in a Hydrophobic Microporous Polymer for Application in Continuous-Flow Alkane Dehydrogenation

M. Traxler, M. König, M. A. Rudolph, J. Schmidt, H. Küçükkeçeci, R. Schomäcker, A. Thomas

ChemCatChem **2022**, *14*, e202200811.

Published manuscript, DOI: <https://doi.org/10.1002/cctc.202200811>



An Iridium pincer complex was anchored in a multi-step post-synthetically modified microporous polymer with a highly hydrophobic character. The immobilized catalyst was applied in continuous-flow dehydrogenation of cyclohexane.

Anchoring an Iridium Pincer Complex in a Hydrophobic Microporous Polymer for Application in Continuous-Flow Alkane Dehydrogenation

Michaela König,^[a] Michael Traxler,^[a] Maik Alexander Rudolph,^[b] Johannes Schmidt,^[a] Hüseyin Küçükkeçeci,^[a] Reinhard Schomäcker,^[b] and Arne Thomas^{*[a]}

An iridium pincer complex $\{p\text{-KO-C}_6\text{H}_4\text{-2,6-[OP(t-Bu)}_2\text{]}_2\text{Ir(C}_2\text{H}_4)\}$ is immobilized in a propyl bromide-functionalized microporous polymer network using the concepts of surface organometallic chemistry. The support material enables the formation of isolated active metal sites embedded in a chemically robust and highly hydrophobic environment. The catalyst maintained high

porosity and – without prior activation – exhibited high activity in the continuous-flow dehydrogenation of cyclohexane at elevated temperatures. The catalyst shows a stable performance for at least 7 days, even when additional H_2O was co-fed, owing to its hydrophobic nature.

Introduction

Alkanes can be extracted from various sources, including natural gas, mineral oil, coal, and biomass. Some of these alkanes (C9–C19) are utilized as fuels, but abundant leftover alkanes have poor application. In comparison, low molecular-weight alkenes and aromatic compounds are essential key intermediates in the synthesis of a multitude of fine chemicals or polymers on an industrial scale. Therefore, the conversion of alkanes to high-value alkenes or arenes is of great commercial interest.^[1] Dehydrogenation reactions are realized industrially on a large scale at high temperatures (400–600 °C) utilizing solid metal catalysts, however with low product selectivities as well as little energy efficacy.^[2] Since their discovery, molecular catalysts featuring tridentate pincer ligands are widely explored and are applied for versatile reactions, such as hydrogenation, coupling, hydrogen transfer, aldol and Michael reactions as well as dehydrogenation or even tandem reactions involving alkane dehydrogenation.^[3–12] In the field of alkane dehydrogenation iridium pincer complexes have received great interest due to

their high activity as well as regioselectivity for the formation of terminal olefins, enabled by the relatively mild reaction temperature of around 240 °C compared to currently applied industrial processes.^[13]

Combining homogeneous and heterogeneous catalysis by immobilizing a molecular catalyst onto suitable supports has been investigated widely in recent years. Thereby, the advantages of homogeneous as well as heterogeneous catalysis are combined and well-defined materials with uniform active sites of equal activity towards the reactants can be made accessible for new catalytic applications.^[14,15] Molecular pincer catalysts have been immobilized on different supports, mainly on silica and metal oxides^[2,13,16–23] as well as metal-organic frameworks^[24–28] or even microporous polymer networks,^[29] but the resulting materials were mostly investigated for stoichiometric transformation,^[30] coupled with metathesis^[31] or transfer dehydrogenations,^[2,32] whereas direct dehydrogenations remain underexplored.^[13,22] Besides the high porosity and chemical robustness, the advantage of using a microporous polymer network (MPN) as support material is the tunable environment of the catalyst, as the polymer backbone can be versatilely functionalized.

Herein, the immobilization of an organometallic iridium pincer complex on a post-modified high-surface-area MPN is presented (Scheme 1), as well as its application in a catalytic continuous-flow dehydrogenation reaction. The novel MPN provides an inert environment with isolated anchor points for the immobilization of the metal-organic complex, ensuring the formation of a single-site catalyst.

We and others have recently shown the immobilization of iridium pincer complexes.^[23,29] In these examples the complex has been conveniently anchored via the Ir center to OH-functional groups present on the surface of the support, yielding immobilized Ir(III) pincer complexes, which showed high activity in the hydrogenation of alkenes. However, such catalysts will not be active in the, industrially more important back reaction, i. e. the endothermic dehydrogenation of alkanes.

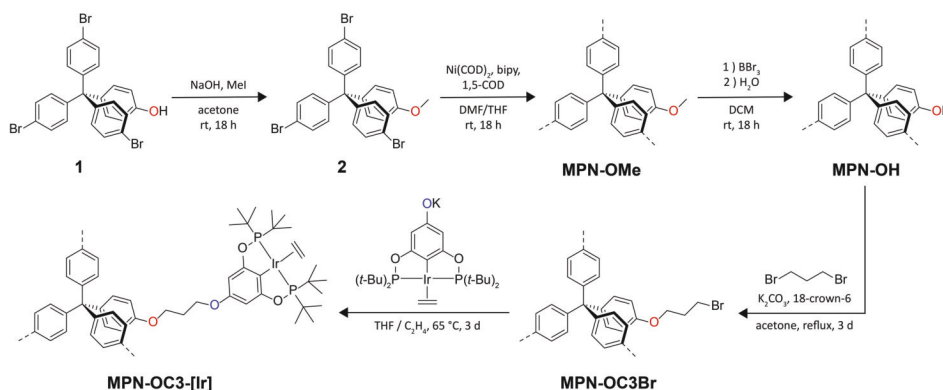
[a] M. König,^{*} M. Traxler,^{*} Dr. J. Schmidt, H. Küçükkeçeci, Prof. A. Thomas
 Institut für Chemie
 Technische Universität Berlin
 Hardenbergstrasse 40
 10623 Berlin (Germany)
 E-mail: arne.thomas@tu-berlin.de
 Homepage: <https://www.funktionsmaterialien.tu-berlin.de>

[b] M. A. Rudolph, Prof. R. Schomäcker
 Institut für Chemie
 Technische Universität Berlin
 Straße des 17. Juni 124
 10623 Berlin (Germany)

[*] These authors contributed equally.

Supporting information for this article is available on the WWW under <https://doi.org/10.1002/cctc.202200811>

© 2022 The Authors. ChemCatChem published by Wiley-VCH GmbH. This is an open access article under the terms of the Creative Commons Attribution License, which permits use, distribution and reproduction in any medium, provided the original work is properly cited.



Scheme 1. Synthesis of methoxytetraphenylmethane polymer MPN-OMe, post-synthetic modification towards hydroxy functionalized MPN-OH and alkylated MPN-OC3Br and subsequent immobilization of iridium pincer complex $\{p\text{-KO-C}_6\text{H}_4\text{-2,6-[OP(t-Bu)}_2\text{)]}_2\text{Ir(C}_2\text{H}_5)_2\}$ yielding MPN-OC3-[Ir].

For the latter reaction, the central iridium atom of the pincer catalyst cannot be anchored directly to the support material, as for an effective dehydrogenation reaction an Ir(I) catalyst is required to ensure an Ir(I)–Ir(III) couple.^[13] Therefore, the pincer complex has to be anchored to the support via the organic ligand.^[2] In this study, a synthesis route for the immobilization of a potassium phenolate substituted pincer catalyst onto a propyl bromide-functionalized MPN is presented (Scheme 1). Notably, the catalyst synthesis includes three post-synthetic modification steps on the pre-formed MPN, but can be carried out with high efficiency.

Results and Discussion

In our previous work, we developed a synthetic route to provide a highly porous polymer network with isolated, reactive hydroxy functionalities as anchor points for further post-synthetic modifications.^[29] To create such an OH-functionalized network, tris(4-bromophenyl)methanol^[33] was synthesized and converted into 4-hydroxyphenyl-tris(4-bromophenyl)methane 1. To avoid possible interactions with the utilized metal species during polymerization, the hydroxy group was protected by methylation to yield 4-methoxyphenyl-tris(4-bromophenyl)methane 2. Subsequently, the protected monomer (2) was successfully converted to a methoxy functionalized microporous polymer network MPN-OMe with a S_{BET} of $1014 \text{ m}^2 \text{ g}^{-1}$ using nickel-mediated Yamamoto polymerization.^[34] To recover the hydroxy group the methylated polymer MPN-OMe was quantitatively deprotected by successive treatment with BBr_3 and H_2O to yield a microporous polymer MPN-OH with a S_{BET} of $911 \text{ m}^2 \text{ g}^{-1}$ (Figure 1a).

As an anchoring point of an iridium pincer complex via its ligand, a small chain alkyl bromide needed to be introduced to the microporous polymer network. In order to find out a suitable chain length, which reacts efficiently with the phenolic OH groups of the polymer, but is sufficiently short not to block

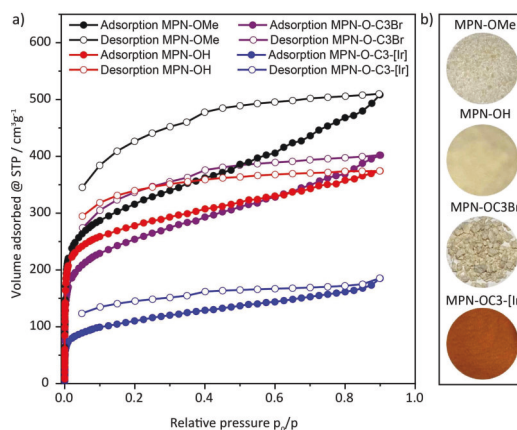


Figure 1. a) Ar sorption analysis at 87 K of MPN-OMe (black), MPN-OH (red), MPN-OC3Br (purple) and MPN-OC3-[Ir] (blue). b) Optical images of MPN-OMe, MPN-OH, MPN-OC3Br and MPN-OC3-[Ir].

the pores of the polymer network, 1,2-dibromoethane, 1,3-dibromopropane and 1,4-dibromobutane were tested in the reaction with the model compound 4-tritylphenol using different reaction protocols. Low yields and slow conversion were obtained when introducing the bromoethyl chain. On the contrary, a reaction protocol using potassium carbonate and 18-crown-6 gave high conversion rates for the respective bromopropyl and bromobutyl ethers after reflux in acetone, respectively. Therefore, the same reaction protocol was applied for the post-synthetic modification of the MPN-OH polymer. For both chain lengths, a nearly quantitative conversion of the hydroxy groups of the microporous polymer was obtained, yielding in the formation of MPN-OC3Br and MPN-OC4Br. ^{13}C CP/MAS-NMR spectroscopy confirmed the successful attachment of the bromoalkyl chains since new signals in the region between 27 and 32 ppm could be identified as the signals for the aliphatic carbons of the alkyl chains. Furthermore, a low-

field shift of the $C_{Ar}-O$ signal from 154 to 157 ppm is observed, which also proves the assumed conversion of hydroxy to ether groups (Figure 2a [MPN-OC3Br]; Figure S1 [MPN-OC4Br]). Additionally, the complete conversion of the OH group to the respective bromoalkyl ether was confirmed by FT-IR, where the characteristic band around 3500 cm^{-1} , corresponding to O-H stretching, disappeared (Figure S4). Both functionalized polymer networks maintained their microporous characteristics and exhibit a SA_{BET} determined from Ar sorption experiments of $796\text{ m}^2\text{ g}^{-1}$ for MPN-OC3Br (Figure 1a) and $781\text{ m}^2\text{ g}^{-1}$ for MPN-OC4Br (Figure S5). Such a decrease of the SA_{BET} is expected due to the increase in molecular weight of the repeating units, plus the partial pore blockage of dangling bromoalkyl chains. As both chain lengths yield comparable results, further post-modification steps were carried out on MPN-OC3Br.

For anchoring the pincer complex onto the support, a potassium phenolate substituted pincer catalyst was prepared in the next step. The tridentate iridium pincer complex $\{p\text{-KO-C}_6\text{H}_2\text{-2,6-[OP(t-Bu)}_2\text{]}_2\}\text{Ir}(\text{C}_2\text{H}_4)$ was synthesized according to the literature (Scheme S2).^[2]

Then, $\{p\text{-KO-C}_6\text{H}_2\text{-2,6-[OP(t-Bu)}_2\text{]}_2\}\text{Ir}(\text{C}_2\text{H}_4)$ was added to a suspension of MPN-OC3Br in THF under inert conditions. While stirring for 3 days under C_2H_4 atmosphere the polymer swelled and its color turned from beige to red (Figure 1b). Filtration,

extensive washing and drying in vacuum yielded the immobilized iridium pincer complex MPN-OC3-[Ir] (Scheme 1). To explore the binding situation of the immobilized pincer complex on the MPN support, a model compound featuring the repeating unit of the porous polymer was synthesized and analyzed by ^1H and ^{13}C liquid state NMR as well (supporting information).

The successful immobilization of the iridium pincer complex was again confirmed by solid-state NMR spectroscopy (Figure 2a). In the ^{13}C CP/MAS-NMR spectrum additional peaks in the aromatic region at 168, 160, and 92 ppm are observed attributed to the aromatic backbone of the pincer ligand. In addition, the signal at 28 ppm can be assigned to the methyl groups of the *tert*-butyl moiety and the signal at 41 ppm can be assigned to the quaternary *tert*-butyl carbon atom. The signal at 35 ppm can be equally assigned to the center aliphatic carbon of the C3-alkyl chain and the coordinated C_2H_4 molecules. When compared to the model compound, the signal at 67 ppm can be assigned to oxygen-connected aliphatic carbons of the alkyl chain. The peak broadening of the aromatic signal at 131 ppm is presumably due to an overlap with the spinning sideband of the signal of the *tert*-butyl methyl groups at 28 ppm. Small amounts of residual THF can be assumed due to the relatively sharp signals at 25 and 67 ppm. The ^{31}P MAS-NMR spectrum further confirms that the pincer ligand stays intact after immobilization as its chemical shift of 179 ppm closely resembles the value of the molecular complex and the designed model compound (Figure 2b).

After immobilization of the iridium pincer catalyst, the porosity of MPN-OC3-[Ir] was evaluated by low-pressure argon sorption studies. The material exhibits still a microporous character and the SA_{BET} was determined to be $360\text{ m}^2\text{ g}^{-1}$. A decrease of SA_{BET} was expected due to the addition of the iridium complex with its bulky functional groups, which increases the weight of the repeating units and occupies the free volume of the MPN. Also, the apparent pore size calculated from the adsorption isotherm decreased after catalyst immobilization from 0.65 for MPN-OC3Br to 0.58 nm for MPN-OC3-[Ir] (Figure S7).

X-ray photoelectron spectroscopy (XPS) analysis of the iridium pincer complex, $\{p\text{-KO-C}_6\text{H}_2\text{-2,6-[OP(t-Bu)}_2\text{]}_2\}\text{Ir}(\text{C}_2\text{H}_4)$, and the immobilized iridium pincer complex, MPN-OC3-[Ir], were conducted to provide further evidence for the anchoring of the catalyst onto the polymer. The molecular metal-organic complex shows two peaks in the O 1s core-level spectrum at 532.0 and 533.3 eV, which both are in the binding energy range of organic oxygen compounds (Figure 3a). Additionally, the characteristic doublet at 131.6 eV in the P 2p spectrum can be assigned to the P-O species. In the Ir 4f spectrum, two different species with characteristic doublets at 60.6 and 63.7 eV, as well as 61.9 and 65.0 eV, can be detected. The set of lower binding energy can be attributed to the unchanged Ir(I) complex, while the peaks for higher binding energy are in the range of Ir(III) species.^[29] This oxidation is most likely resulting from the transfer of the catalyst sample to the XPS measurement chamber and is limited to the outer surface of the material. In

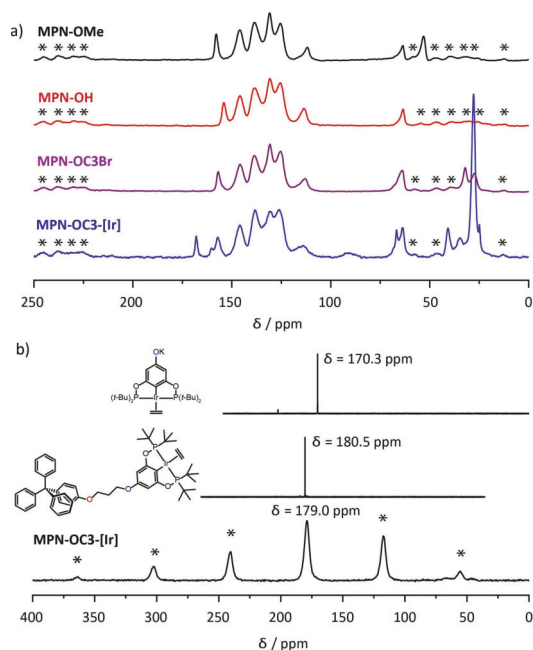


Figure 2. a) Demethylation, post-synthetic modification and immobilization of Ir pincer complex monitored by ^{13}C CP/MAS-NMR spectroscopy: MPN-OMe (black), MPN-OH (red), MPN-OC3Br (purple) and immobilized Ir pincer complex MPN-OC3-[Ir] (blue). b) ^{31}P MAS-NMR spectroscopy of pincer complex $\{p\text{-KO-C}_6\text{H}_2\text{-2,6-[OP(t-Bu)}_2\text{]}_2\}\text{Ir}(\text{C}_2\text{H}_4)$ (top), molecular model compound (middle) and immobilized iridium pincer complex MPN-OC3-[Ir] (bottom). Asterisks denote spinning sidebands.

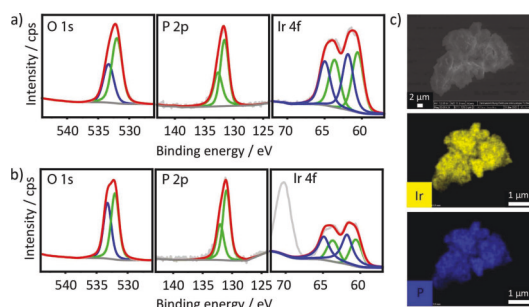


Figure 3. a) O 1s, P 2p and Ir 4f XPS spectra of $[p\text{-KO-C}_6\text{H}_4\text{-2,6-[OP(t-Bu)]}_2\text{]}_2\text{Ir(C}_2\text{H}_5)_2$. b) O 1s, P 2p and Ir 4f XPS spectra of immobilized iridium pincer complex **MPN-OC3-Ir**. (Light grey – measured spectra; red line – fitted spectra; green and blue lines – fitted signals). c) Scanning electron microscopy and energy dispersive X-ray spectroscopic elemental mapping of **MPN-OC3-Ir**. Yellow belongs to iridium, blue belongs to phosphorus.

addition, the elemental ratio between iridium and phosphorus was determined as 2:1.

After the anchoring of the catalyst onto the surface of the microporous polymer network, the O 1s signals slightly shifted to 531.5 and 532.8 eV (Figure 3b). With the absence of a metal-oxygen species at lower binding energies it can be concluded, that the pincer complex is bound via the organic phenyl group rather than the iridium metal center. The P 2p spectrum and Ir 4f spectrum stay nearly identical to that of the molecular pincer catalyst. The extra peak at around 70 eV in the Ir 4f spectrum can be assigned to the Br 3d signal originating from KBr which is the side product of the substitution reaction of the anchoring. Finally, the elemental ratio for iridium and phosphorus in the porous polymer catalyst **MPN-OC3-Ir** stays 2:1, which confirms again the successful anchoring of the intact iridium pincer complex onto the porous polymer. In addition, the immobilization of the iridium pincer catalyst on the bromoalkyl modified model compound resulted in identical binding energies in the O 1s, P 2p and Ir 4f spectra **MPN-OC3-Ir** (Figure S11).

The iridium content was determined by inductively coupled plasma optical emission spectroscopy (ICP-OES) with a value of 7.9 wt%, indicating a functionalization degree of 41%. A spherical morphology of the MPN is seen by scanning electron microscopy (SEM). Elemental mapping shows the homogeneous distribution of iridium and phosphorus within **MPN-OC3-Ir** (Figure 3c). Following the results from solid-state NMR, XPS and SEM, it can be concluded, that the molecular iridium pincer complex has been successfully immobilized onto the microporous polymer support.

The immobilized iridium pincer complex was tested in the catalytic dehydrogenation of cyclohexane to benzene. Gaseous cyclohexane was used in a continuously operated experimental setup to enable simultaneous convenient temporal resolution with adequate experiment duration. To increase the bed height and to avoid potential hot spots, the porous polymer was mixed with SiC as inert material in a 1:9 mass ratio.

Two measurements with different temperature programs were conducted. The initial temperature ramp experiment was designed to find a suitable reaction temperature for the following isothermal stability test. In the first experiment, the catalyst was initially heated to 200 °C with a temperature ramp of 20 K min⁻¹. Subsequently, the activity of the catalyst was determined by holding at this temperature for 15 min. Then, with 4 K min⁻¹ heating ramps followed by holding the temperature for 15 min, the temperature was increased in steps of 20 °C within the stability window of **MPN-OC3-Ir** to 340 °C (Figure 4a). The second measurement, using fresh catalyst material, consisted of heating with 5 K/min to 300 °C and holding for more than seven days (Figure 4b). An induction period is observed within the first 30 hours in which the activity of the catalysts is continuously rising. This might be due to an expansion of the highly cross-linked network during time, increasing the accessibility of active sites.

During both measurements, leakage (i.e. N₂, H₂O, O₂), combustion (CO_x), and partial dehydrogenation (cyclohexene) were not detected in a significant amount in comparison to the reference baselines. Consequently, total benzene selectivity is perceived. The feed consisting of argon, hydrogen, and cyclohexane was subject to minor fluctuations, but without impact on the formation of benzene. The co-feeding of hydrogen ensures a sufficient H₂ partial pressure for activating the catalyst to a dihydride complex in a plausible associative

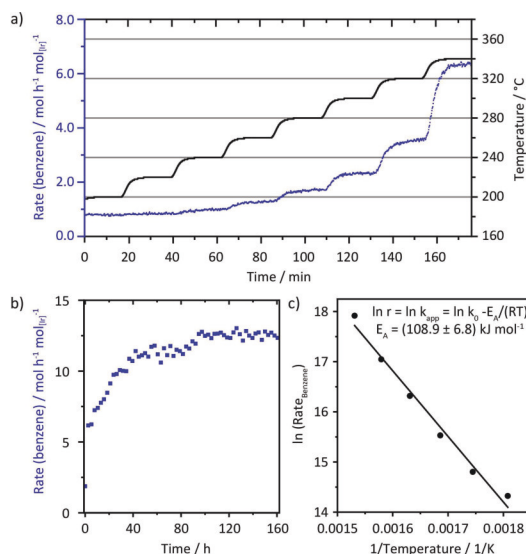


Figure 4. a) Catalytic dehydrogenation of cyclohexane. Temperature ramp measurement: Benzene formation rate depending on the catalyst bed temperature, heating with 4 K/min and holding for 15 min between 200 °C and 340 °C in steps of 20 °C. b) Isothermal stability measurement: Benzene formation rate at 300 °C for 168 h (figure neglects heating with 5 K/min to 300 °C). c) The rates of benzene formation during the steady regimes of each temperature step between 280 and 380 °C (except 380 °C in cycle 1) were averaged for each temperature. The temperature-rate pairs were used in an Arrhenius plot to determine the apparent activation energy of the dehydrogenation of cyclohexane to benzene of $(108.9 \pm 6.8) \text{ kJ mol}^{-1}$.

reaction mechanism, when performing temperature screening experiments starting with zero conversion.^[35] Additionally, the hydrogen feed could also prevent possible C–H bond activation of the support by the iridium pincer complex. Furthermore, no benzene or other organic products could be detected in a reference reaction without the feed of cyclohexane, excluding that products are detected due to a decomposition of the polymer network or ligand.

The temperature ramping dehydrogenation of the **MPN–OC3–[Ir]** catalyst showed an increased formation of benzene, which is elevating with increasing temperature (Figure 4a). At 200 °C the yield of benzene in the dehydrogenation reaction was low. With increasing temperature the conversion of cyclohexane raised stepwise to a steady-state with a turnover frequency (TOF) of $6.3 \text{ mol h}^{-1} \text{ mol}_{\text{Ir}}^{-1}$ at 340 °C. It is noteworthy that these temperatures are not accessible with unsupported molecular dehydrogenation catalysts, since the highest temperatures for those is considered 200–240 °C due to thermal instability.^[36] Ramping the catalyst to temperatures beyond the stability window of the microporous dehydrogenation catalyst up to 400 °C led to a further increase in activity, with the highest benzene formation rates peaking as high as $99.5 \text{ mol h}^{-1} \text{ mol}_{\text{Ir}}^{-1}$ at a cyclohexane conversion of more than 50%. However, the initial rates at those temperatures are declining already within the 15 min holding phase (Figure S12). These results are in full agreement with findings from Sheludko et al. that the thermal decomposition product of the supported catalyst is retaining activity, even though at lower conversion rates.^[13] Notably, the catalytic activity of the iridium pincer species is not affected by a co-feed of water (Figure S12, last cycle). This can be explained by the highly hydrophobic environment, which is provided by the microporous polymer network. This renders a further advantage of MPNs compared to other conventional, hydrophilic supports such as silica. The analysis of the temperature dependence of the reaction rates results in an apparent activation energy of $(108.9 \pm 6.8) \text{ kJ mol}^{-1}$ (Figure 4c and supporting information), which is in accordance to simulations on Pt(111) surfaces.^[37–39] The additionally performed Eyring plot confirms the activation enthalpy to be slightly higher than 100 kJ mol^{-1} and revealed a positive activation entropy of $(55.0 \pm 2.4) \text{ kJ mol}^{-1} \text{ K}^{-1}$ (Figure S14).

The following isothermal long time catalyst test showed – after an induction period of 24 h – a stable dehydrogenation of cyclohexane to benzene at a rate of $11.4 \text{ mol h}^{-1} \text{ mol}_{\text{Ir}}^{-1}$ (Figure 4b), which relates to a conversion of 4.4 % of the theoretical maximum conversion based on thermodynamic simulations (Figure S15). This activity is comparable to reported silica-supported metal nanoparticle catalysts for the dehydrogenation of cyclohexane.^[40–42] Additionally, the catalyst showed long-term stability with a turnover number higher than 1600. It should be noted, that the catalyst activity was stable for more than 7 days and no decrease in reaction rate was detected. The catalyst was analyzed after the long-term experiment using SEM and EDX analysis. The elemental mapping revealed, that both iridium and phosphorus are still distributed throughout the catalyst material (Figure S16).

Conclusion

In summary, herein we present a multi-step post-synthetically modified MPN as catalyst for the continuous flow dehydrogenation of cyclohexane to benzene. An iridium pincer complex was immobilized on an alkylated microporous polymer network with a resulting Ir content of 7.9 wt%. The successful immobilization of the intact pincer catalyst could be confirmed by solid-state ^{13}C and ^{31}P NMR spectroscopy. X-ray photoelectron spectroscopy validated the presence of the expected oxygen, phosphorus, and iridium species. Homogeneous distribution of iridium and phosphorus was confirmed by scanning electron microscopy. After immobilization, the S_{ABET} decreased from 796 to $360 \text{ m}^2 \text{ g}^{-1}$ due to the increased specific weight but without loss of the microporous characteristics. The catalytic performance was demonstrated in the continuous flow dehydrogenation of cyclohexane, where the material showed high long-term stability at a TOF of $11.4 \text{ mol h}^{-1} \text{ mol}_{\text{Ir}}^{-1}$, which – to our knowledge – was not yet reported for the catalytic dehydrogenation of cyclohexane using an anchored metal organic catalyst. We believe that this highly tunable class of materials ensures the formation of single-site catalytically active species inside a chemically robust, inert, and hydrophobic polymer, offering ample opportunity for the field of surface organometallic chemistry due to the ability of the formation of tuned environments for the catalyst.

Experimental Section

Materials and methods. All chemicals were of reagent grade and used as received, and all experiments were carried out under Ar atmosphere if stated in the procedure. ^{11}B MAS, $^{13}\text{C}\{^1\text{H}\}$ CP/MAS and ^{31}P MAS measurements were carried out using a Bruker range Avance 400 MHz solid state spectrometer operating at a spinning rate of 10 kHz. Physisorption measurements were conducted at 87 K and Argon as sorption agent at relative pressures up to $p/p_0 = 0.9$ using an Autosorb-iQ-MP from Quantachrome. X-ray photoelectron spectra were measured on a K-Alpha™ + X-ray Photoelectron Spectrometer System (Thermo Scientific). Scanning electron microscopy images were recorded via ZEISS Gemini SEM 500 using NanoVP mode operating at 15 kV. For the energy dispersive spectroscopy, Bruker Quantax XFlash 6|60 detector was used.

Catalyst preparation. Hydroxytetraphenylmethane polymer **MPN–OH** was synthesized in accordance with a reported procedure.^[29]

MPN–OC3Br. Polymer **MPN–OH** (525 mg, 1.58 mmol), K_2CO_3 (294 mg, 2.13 mmol) and a few crumbs of 18-crown-6 were suspended in acetone (60 mL). 1,3-Dibromopropane (0.98 mL, 9.62 mmol) was added via syringe and the reaction stirred at reflux for 3 days. After cooling down to room temperature the mixture was filtered off and the off-white precipitate washed with abundant amounts of water, acetone, THF and methanol. The product was purified via Soxhlet extraction from methanol overnight and dried at 80 °C in vacuum for 6 h to yield **MPN–OC3Br** as off-white powder. Yield, 620 mg (1.37 mmol repeating units, 87 %). $^{13}\text{C}\{^1\text{H}\}$ CP/MAS-NMR (100 MHz): $\delta = 157, 146, 138, 131, 125, 113, 64, 32, 27 \text{ ppm}$.

The potassium phenolate substituted pincer catalyst $\{p\text{-KO-C}_6\text{H}_4\text{-}2,6\text{-[OP(t-Bu)}_2\text{]}_2\text{Ir(C}_2\text{H}_4\text{)}\}$ was prepared according to the literature.^[2]

MPN-OC3-[Ir]. Polymer MPN-OC3Br (225 mg, 0.50 mmol) was added to a Schlenk flask and evacuated overnight. Under Ar atmosphere pincer catalyst $\{p\text{-KO-C}_6\text{H}_4\text{-2,6-[OP(t-Bu)]}_2\}_2\text{Ir(C}_2\text{H}_4\text{)}$ (400 mg, 0.60 mmol) and THF (80 mL) were added. The THF suspension was degassed by three freeze-pump-thaw cycles. The flask was refilled with ethylene gas at -78°C . The reaction stirred at 65°C for 3 days. After cooling down to room temperature the solvent was removed via filtration under Ar atmosphere and the orange solid was washed with THF ($6 \times 20\text{ mL}$) to remove the excess of metal precursor. The volatiles were removed under high vacuum (10^{-3} mbar), and the orange solid was dried under high vacuum (10^{-3} mbar) overnight. Drying in vacuum overnight (14 h) yielded the product as a red powder. $^{13}\text{C}\{^1\text{H}\}$ CP/MAS-NMR (100 MHz): $\delta = 168, 160, 157, 146, 138, 131, 126, 114, 92, 67, 64, 41, 35, 28, 25\text{ ppm}$. $^{31}\text{P}\{^1\text{H}\}$ CP/MAS-NMR (162 MHz): $\delta = 179\text{ ppm}$.

The model compound Tritylphenolate Pincer Complex (10) was synthesized similar to MPN-OC3-[Ir] but using 4-(3-bromopropoxy)tetraphenylmethane (9) as a representative unit of the polymer MPN-OC3Br (see SI).

Procedure for the dehydrogenation of cyclohexane using MPN-OC3-[Ir]. The catalytic performance was examined in a tubular fixed bed reactor (tapered quartz tube with a 4 mm inner diameter) with Swagelok Ultra-Torr fittings and Quick-Connects ensuring gas tightness against atmospheric oxygen and moisture. The reactor was placed vertically in a programmable oven (HTM Reetz). The feed of Argon (29 mL/min, 99.999%, Air Liquide) and hydrogen (1 mL/min, 99.999%, Air Liquide) was controlled by mass flow controllers (MFCs, Bronkhorst EL-FLOW) which were calibrated by a flow meter (Analyt-MTC). Argon was bubbled into a doubled walled gas-washing bottle (length 24 cm, frit VitraPOR filter plate with porosity 3) filled with cyclohexane (99.5%, Roth) which was held at 15°C by a thermostat (Lauda Eco RE620). Argon, hydrogen and cyclohexane were used without further purification. The calibration of the cyclohexane feed was conducted measuring the evaporated volume of cyclohexane depending on the time. The decrease in cyclohexane volume in the gas-washing bottle or the difference in residence time of the Argon bubbles within the gas-washing bottle is neglectable. To ensure a stationary feed composition, the MFCs were run one hour in advance of the actual measurement. The feed composition was analysed by a mass spectrometer (GAM 200, InProcess Instruments) with a time resolution of 0.95 measurements of all the 11 channels per second detecting minimal fluctuations. The gas species and their respective channels (mass per charge ratio, m/z) are listed in Table S1. Cyclohexane and cyclohexene were measured via two channels due to overlapping molecular fractions. To calibrate the signals, a reference measurement excluding MPN-OC3-[Ir] was conducted at room temperature receiving the signal intensities correlated to zero cyclohexane conversion. The catalyst material (15.5 mg of MPN-OC3-[Ir] diluted with SiC (1:9 mass related, VWR, $100\text{--}500\text{ }\mu\text{m}$) was mixed and placed on quartz wool (Roth) which was stabilized on the taper under inert conditions. With a bed height of 0.5 cm and a tube diameter of 4 mm, the residence time was 0.5 s.

Acknowledgments

M.K. and M.T. contributed equally to this work and either has the right to list themselves first in bibliographic documents. The authors thank Christina Eichenauer for surface area and TGA measurements. This work was funded by the Deutsche Forschungsgemeinschaft (DFG, German Research Foundation) under Germany's Excellence Strategy – EXC 2008 – 390540038 – UniSysCat. M.T.

thanks the Einstein Center for Catalysis/Berlin International Graduate School for Natural Science and Engineering for funding. Open Access funding enabled and organized by Projekt DEAL.

Conflict of Interest

The authors declare no conflict of interest.

Data Availability Statement

The data that support the findings of this study are available from the corresponding author upon reasonable request.

Keywords: catalysis · dehydrogenation · microporous polymer network · pincer

- [1] K. Das, A. Kumar, *Adv. Organomet. Chem.* **2019**, *72*, 1–57.
- [2] Z. Huang, M. Brookhart, A. S. Goldman, S. Kundu, A. Ray, S. L. Scott, B. C. Vicente, *Adv. Synth. Catal.* **2009**, *351*, 188–206.
- [3] J. T. Singleton, *Tetrahedron* **2003**, *59*, 1837–1857.
- [4] Y. Wang, Z. Huang, X. Leng, H. Zhu, G. Liu, Z. Huang, *J. Am. Chem. Soc.* **2018**, *140*, 4417–4429.
- [5] M. E. van der Boom, D. Milstein, *Chem. Rev.* **2003**, *103*, 1759–1792.
- [6] N. Selander, K. J. Szabó, *Chem. Rev.* **2011**, *111*, 2048–2076.
- [7] J. Choi, A. H. R. MacArthur, M. Brookhart, A. S. Goldman, *Chem. Rev.* **2011**, *111*, 1761–1779.
- [8] A. Kumar, T. M. Bhatti, A. S. Goldman, *Chem. Rev.* **2017**, *117*, 12357–12384.
- [9] L. Maser, L. Vondung, R. Langer, *Polyhedron* **2018**, *143*, 28–42.
- [10] M. A. W. Lawrence, K.-A. Green, P. N. Nelson, S. C. Lorraine, *Polyhedron* **2018**, *143*, 11–27.
- [11] E. Peris, R. H. Crabtree, *Chem. Soc. Rev.* **2018**, *47*, 1959–1968.
- [12] X. Zhou, S. Malakar, T. Dugan, K. Wang, A. Sattler, D. O. Marler, T. J. Emge, K. Krogh-Jespersen, A. S. Goldman, *ACS Catal.* **2021**, *11*, 14194–14209.
- [13] B. Sheludko, M. T. Cunningham, A. S. Goldman, F. E. Celik, *ACS Catal.* **2018**, *8*, 7828–7841.
- [14] C. Copéret, M. Chabanas, R. Petroff Saint-Arroman, J.-M. Basset, *Angew. Chem. Int. Ed.* **2003**, *42*, 156–181; *Angew. Chem.* **2003**, *115*, 164–191.
- [15] M. D. Korzyński, C. Copéret, *Trends Chem.* **2021**, *3*, 850–862.
- [16] C. del Pozo, A. Corma, M. Iglesias, F. Sánchez, *Organometallics* **2010**, *29*, 4491–4498.
- [17] M. Rimoldi, A. Mezzetti, *Inorg. Chem.* **2014**, *53*, 11974–11984.
- [18] E. K. Huang, W.-M. Cheung, K.-W. Chan, F. L.-Y. Lam, X. Hu, Q.-F. Zhang, I. D. Williams, W.-H. Leung, *Eur. J. Inorg. Chem.* **2013**, 2893–2899.
- [19] J. Ternel, L. Delevoye, F. Agbossou-Niedercorn, T. Roisnel, R. M. Gauvin, C. M. Thomas, *Dalton Trans.* **2010**, 39, 3802.
- [20] M. Rimoldi, A. Mezzetti, *Helv. Chim. Acta* **2016**, *99*, 908–915.
- [21] M. Rimoldi, D. Fodor, J. A. van Bokhoven, A. Mezzetti, *Catal. Sci. Technol.* **2015**, *5*, 4575–4586.
- [22] B. Sheludko, C. F. Castro, A. S. Goldman, F. E. Celik, *ACS Catal.* **2020**, *10*, 12425–12436.
- [23] M. Rimoldi, D. Fodor, J. A. van Bokhoven, A. Mezzetti, *Chem. Commun.* **2013**, 49, 11314–11316.
- [24] S. A. Burgess, A. Kassie, S. A. Baranowski, K. J. Fritzsche, K. Schmidt-Rohr, C. M. Brown, C. R. Wade, *J. Am. Chem. Soc.* **2016**, *138*, 1780–1783.
- [25] M. Rimoldi, A. Nakamura, N. A. Vermeulen, J. J. Henkelis, A. K. Blackburn, J. T. Hupp, J. F. Stoddart, O. K. Farha, *Chem. Sci.* **2016**, *7*, 4980–4984.
- [26] A. M. Rasero-Almansa, A. Corma, M. Iglesias, F. Sánchez, *ChemCatChem* **2013**, *5*, 3092–3100.
- [27] Y. Zhang, J. Li, X. Yang, P. Zhang, J. Pang, B. Li, H.-C. Zhou, *Chem. Commun.* **2019**, 55, 2023–2026.
- [28] B. R. Reiner, N. T. Mucha, A. Rothstein, J. S. Temme, P. Duan, K. Schmidt-Rohr, B. M. Foxman, C. R. Wade, *Inorg. Chem.* **2018**, *57*, 2663–2672.
- [29] M. König, M. Rigo, N. Chaoui, T. Tran Ngoc, J. D. Epping, J. Schmidt, P. Pachfule, M. Ye, M. Trunk, J. F. Teichert, M. Drieß, A. Thomas, *Angew.*

- Chem. Int. Ed.* **2020**, *59*, 19830–19834; *Angew. Chem.* **2020**, *132*, 20002–20006.
- [30] Z. H. Syed, D. M. Kaphan, F. A. Perras, M. Pruski, M. S. Ferrandon, E. C. Wegener, G. Celik, J. Wen, C. Liu, F. Dogan, K. I. Goldberg, M. Delferro, *J. Am. Chem. Soc.* **2019**, *141*, 6325–6337.
- [31] Z. Huang, E. Rolfe, E. C. Carson, M. Brookhart, A. S. Goldman, S. H. El-Khalafy, A. H. Roy MacArthur, *Adv. Synth. Catal.* **2010**, *352*, 125–135.
- [32] B. Sheludko, C. F. Castro, C. A. Khalap, T. J. Emge, A. S. Goldman, F. E. Celik, *ChemCatChem* **2021**, *13*, 407–415.
- [33] K. Nikitin, E. Lestini, M. Lazzari, S. Altobello, D. Fitzmaurice, *Langmuir* **2007**, *23*, 12147–12153.
- [34] J. Schmidt, M. Werner, A. Thomas, *Macromolecules* **2009**, *42*, 4426–4429.
- [35] K. Krogh-Jespersen, M. Czerw, N. Summa, K. B. Renkema, P. D. Achord, A. S. Goldman, *J. Am. Chem. Soc.* **2002**, *124*, 11404–11416.
- [36] G. E. Dobereiner, R. H. Crabtree, *Chem. Rev.* **2010**, *110*, 681–703.
- [37] B. E. Koel, D. A. Blank, E. A. Carter, *J. Mol. Catal. A* **1998**, *131*, 39–53.
- [38] M. Saeys, M. F. Reyniers, M. Neurock, G. B. Marin, *J. Phys. Chem. B* **2005**, *109*, 2064–2073.
- [39] M. K. Sabbe, G. Canduela-Rodriguez, M. F. Reyniers, G. B. Marin, *J. Catal.* **2015**, *330*, 406–422.
- [40] Z. Xia, H. Lu, H. Liu, Z. Zhang, Y. Chen, *Catal. Commun.* **2017**, *90*, 39–42.
- [41] Z. Xia, H. Liu, H. Lu, Z. Zhang, Y. Chen, *Catal. Lett.* **2017**, *147*, 1295–1302.
- [42] Z. Xia, H. Liu, H. Lu, Z. Zhang, Y. Chen, *Appl. Surf. Sci.* **2017**, *422*, 905–912.

Manuscript received: June 27, 2022

Revised manuscript received: July 17, 2022

Accepted manuscript online: July 21, 2022

Version of record online: August 18, 2022

ChemCatChem

Supporting Information

Anchoring an Iridium Pincer Complex in a Hydrophobic Microporous Polymer for Application in Continuous-Flow Alkane Dehydrogenation

Michaela König[†], Michael Traxler[†], Maik Alexander Rudolph, Johannes Schmidt, Hüseyin Küçükkeçeci, Reinhard Schomäcker, and Arne Thomas*

SUPPORTING INFORMATION

Table of Contents

Experimental Procedures	2
General	2
Syntheses	3
MAS-NMR spectroscopy	7
FT IR spectroscopy	8
Physisorption measurements	8
Thermogravimetric analysis	10
Catalytic continuous-flow dehydrogenation of cyclohexane	12
Determination of thermodynamic values	13
Scanning electron microscopy after catalysis	14
References	14
Author Contributions	14

SUPPORTING INFORMATION

Experimental Procedures

General

All inert reactions and manipulations were carried out in an argon atmosphere using standard Schlenk techniques or in an MBraun type MB 120 BG inert atmosphere drybox containing an atmosphere of argon. CDCl_3 was degassed and dried over molecular sieves for air sensitive reactions. Sodium hydride and potassium hydride were washed with hexane prior to use under argon atmosphere.

Materials

All chemicals were used as received unless otherwise noted. Anhydrous benzene (99.8 %), anhydrous diethyl ether (>99.8 %), 1,4-dibromobenzene (98 %), 1,5-cyclooctadiene (99 %), ethyl 4-bromobenzoate (98 %), boron tribromide (1 M in dichloromethane), *n*-butyllithium (2.5 M in hexane), 9-iodo-9-borabicyclo[3.3.1]nonane (1.0 M in hexanes), sodium hydride (60 % in mineral oil), potassium hydride (30 % in mineral oil), methyl iodide (>99.0 %) and 4-tritylphenol (97 %) were purchased from Sigma-Aldrich. 2,2'-bipyridine (99 %), di-*tert*-butylchlorophosphine (96 %), 5-methoxyresorcinol (95 %), 1,4-dibromobutane (99 %) and phenol (>99 %) were purchased from Alfa Aesar. Bis(1,5-cyclooctadiene)nickel(0) (98 %) and potassium carbonate (99 %) were purchased from ABCR. Anhydrous tetrahydrofuran (99.5 %), anhydrous dimethylformamide (>99.8 %), anhydrous dichloromethane (99.9 %), anhydrous hexane (97 %), anhydrous pentane (>99 %), 18-crown-6 (99 %) and tetrahydrofuran (>99.5 %) were purchased from Acros Organics. Acetone (>99.9 %), cyclohexane (>99.5 %), ethyl acetate (>99.5 %), methanol (>99 %), sulfuric acid (98 %) and THF- d_8 (99.5 % d) were purchased from Carl Roth. Diethyl ether (99.5 %) was purchased from Fisher Scientific. Sodium hydroxide (99.5 %) was purchased from Chemsolute. 1,3-dibromopropane (>98 %) and chloro(1,5-cyclooctadiene)iridium(I) dimer (>93 %) were purchased from TCI. Ethene (99.9 Vol%) was purchased from Air Liquide. CDCl_3 (99.8 % d) was purchased by Eurisotop.

NMR measurements

^1H NMR, ^{13}C NMR, and ^{31}P NMR were recorded on a Bruker Avance II 200 and Bruker Avance 400 MHz spectrometer in the given solvent.

^{11}B MAS, $^{13}\text{C}\{^1\text{H}\}$ CP/MAS and ^{31}P MAS measurements were carried out using a Bruker range Avance 400 MHz Solid State spectrometer operating at 128.3 MHz for ^{11}B , 100.6 MHz for ^{13}C , 161.9 MHz for ^{31}P and a Bruker 4 mm double resonance probe-head operating at a spinning rate of 10 kHz.

Physiosorption measurements

Argon sorption analyses were conducted at 87 K at relative pressures up to $p/p_0 = 0.9$ using an Autosorb-iQ-MP from Quantachrome. The pore size distributions were calculated from the adsorption branch of the Ar sorption isotherms by quenched solid density functional theory (QSDFT) using the slit pore model for carbon adsorbents. Before analysis, samples were degassed at 80 °C for 12 h. BET surface areas were determined over a 0.05-0.1 p/p_0 range.

Thermogravimetric analysis

TGA measurements were carried out under air on a Mettler Toledo TGA 1 Stare thermal instrument with a heating rate of 5 K min^{-1} .

ICP/OES

The iridium content of the sample was determined by inductively coupled plasma optical emission spectroscopy (ICP-OES) carried out on an ICP Horiba Ultima 2 spectrometer. Prior to the measurement 5 mL of conc. nitric acid and 2 mL of hydrofluoric acid were added to 5.1 mg of the sample with subsequent autoclave treatment at 200 °C for 5 h. The mixture was diluted with distilled water to 50 mL. Standard solutions containing 2, 4, 6 and 8 ppm iridium were used for calibration.

X-ray photoelectron spectroscopy

X-ray photoelectron spectra were measured on a K-AlphaTM + X-ray Photoelectron Spectrometer System (Thermo Scientific) with Hemispheric 180 ° dual-focus analyzer with 128-channel detector. The X-ray monochromator used micro focused Al-K α radiation.

Scanning electron microscopy

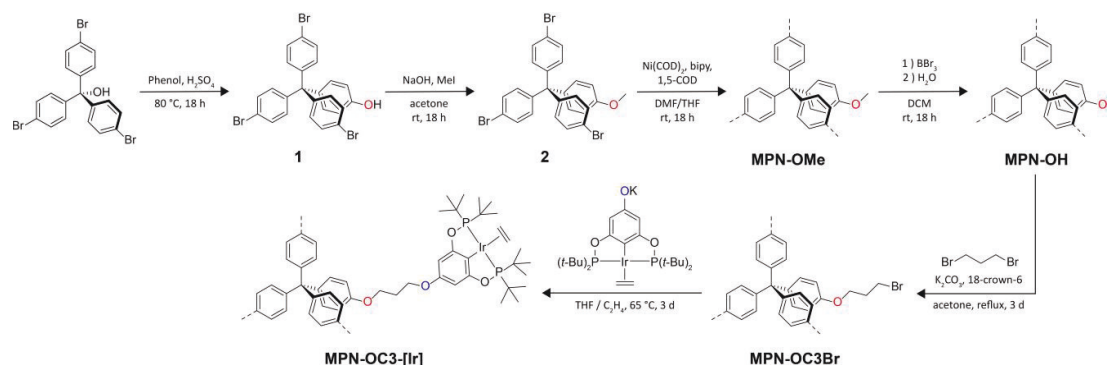
Scanning electron microscopy images were recorded via ZEISS Gemini SEM 500 using NanoVP mode operating at 15 kV. Samples were mounted on conductive carbon tape and the sample preparation was done in the glove box prior to the measurement. For the energy dispersive spectroscopy, Bruker Quantax XFlash 6|60 detector was used.

SUPPORTING INFORMATION

FT IR spectroscopy

The samples were diluted with KBr, grinded and pressed into pellets. FT IR spectra (4000–400 cm^{-1}) were recorded on a Nicolet Magna-IR 750 FT-IR spectrometer from ThermoFisherScientific. The spectra were acquired in transmission and normalized to the band at 810 cm^{-1} .

Syntheses



Scheme S1. Syntheses of the methoxytetraphenylmethane polymer network **MPN-OMe**, post-synthetic modification towards hydroxyl functionalized **MPN-OH** and alkylated **MPN-OC3Br** and immobilization of Ir pincer catalyst $\{p\text{-KO-C}_6\text{H}_4\text{-2,6-[OP(t-Bu)}_2\text{]}_2\}\text{Ir(C}_2\text{H}_4\text{)}$ yielding **MPN-OC3-[Ir]**.

Syntheses of Monomers

Synthesis of Tris(4-bromophenyl)methanol^[1]

1,4-Dibromobenzene (9.46 g, 40.1 mmol, 3.00 eq) was added to a Schlenk flask under argon atmosphere and dissolved in anhydrous THF/Et₂O (50 mL each). The mixture was cooled to -78 °C, and *n*-butyllithium (16 mL of 2.5 M in hexane, 40.0 mmol) was added dropwise during 30 min. After stirring for 1 h at -78 °C ethyl 4-bromobenzoate (2.2 mL, 13.3 mmol, 1.00 eq) was added dropwise to the mixture. The mixture was stirred for 1 h at -78 °C, then allowed to warm to 0 °C and stirred again for 1 h. To the yellowish solution, water (50 mL) and aqueous hydrogen chloride solution (1 M, 50 mL) were added and the aqueous phase was extracted with Et₂O (3 x 30 mL). The organic phase was washed with water and brine and dried over MgSO_4 . The solvent was removed under reduced pressure to yield the crude product as a yellowish oil which was adsorbed onto silica gel and purified via column chromatography from cyclohexane/ethyl acetate (95:5). The obtained solid was recrystallized from ethanol yielding the product as a white solid (4.83 g, 9.77 mmol, 73 %).

¹H NMR (200 MHz, CDCl_3): δ = 7.45 (d, J = 8.8 Hz, 6H), 7.12 (d, J = 8.7 Hz, 6H) ppm

¹³C{H} NMR (50 MHz, CDCl_3): δ = 145.1, 131.5, 129.6, 122.1, 81.3 ppm

Synthesis of 4-hydroxyphenyl-tris(4-bromophenyl)methane (1)^[2]

Tris(4-bromophenyl)methanol (4.85 g, 9.77 mmol, 1.00 eq) was dissolved in phenol (9.19 g, 97.7 mmol, 10 eq) at 80 °C. The melted phenol served as solvent and no other solvent was added. Sulfuric acid (10 drops, 98 %) was added and the colorless solution turned brown and the mixture was stirred for 18 h at 80 °C. After cooling down to room temperature, an aqueous solution of NaOH (9.1 wt. %, 60 mL) was added while a formation of a white precipitate was observed. The precipitate was filtered and washed with water. The crude product was dissolved in ethyl acetate, adsorbed onto silica gel and purified via column chromatography from cyclohexane/ethyl acetate (95:5). The obtained solid was recrystallized from ethanol yielding the product as a white solid (4.59 g, 8.01 mmol, 82 %).

¹H NMR (500 MHz, CDCl_3): δ = 7.38 (d, J = 8.7 Hz, 6H), 7.02 (d, J = 8.7 Hz, 6H), 6.97 (d, J = 8.8 Hz, 2H), 6.72 (d, J = 8.8 Hz, 2H) ppm

¹³C{H} NMR (125 MHz, CDCl_3): δ = 154.2, 145.3, 137.7, 132.6, 132.2, 131.0, 120.7, 114.9, 63.4 ppm

Synthesis of 4-methoxyphenyl-tris(4-bromophenyl)methane (2)

1 (2.00 g, 3.50 mmol, 1.00 eq) and NaOH (211 mg, 5.29 mmol, 1.51 eq) were added to acetone (20 mL) and the mixture stirred for 10 min at room temperature. To the clear solution methyl iodide (0.26 mL, 4.18 mmol, 1.20 eq) was added dropwise and the mixture was stirred for 24 h at room temperature, resulting in a suspension. The white precipitate was filtered, dissolved in ethyl acetate, adsorbed onto silica gel and purified via column chromatography from cyclohexane/ethyl acetate (95:5). The obtained solid was recrystallized from ethanol yielding the product as a white solid (1.42 g, 2.42 mmol, 69 %).

¹H NMR (500 MHz, CDCl_3): δ = 7.38 (d, J = 8.7 Hz, 6H), 7.05–6.99 (m, 8H), 6.79 (d, J = 8.9 Hz, 2H), 3.79 (s, 3H) ppm

¹³C{H} NMR (125 MHz, CDCl_3): δ = 158.1, 145.4, 137.5, 132.7, 132.0, 131.0, 120.6, 113.4, 63.5, 55.4 ppm

SUPPORTING INFORMATION

Syntheses of Polymers

Synthesis of Methoxytetraphenylmethane Polymer (MPN-OMe)^[3]

The polymerization was performed according to standard room temperature Yamamoto reaction procedure. Inside the glovebox, bis(1,5-cyclooctadiene)nickel(0) (1642 mg, 5.97 mmol, 3.50 eq), 2,2'-bipyridine (933 mg, 5.97 mmol, 3.50 eq), and 1,5-cyclooctadiene (0.73 mL, 5.97 mmol, 3.50 eq) were dissolved in anhydrous DMF/THF (160 mL each) and stirred for 15 min while the color of the mixture turned into deep purple. 4-(tris(4-bromophenyl)methyl)anisole **3** (1001 mg, 1.71 mmol, 1.00 eq) was added and the mixture stirred at room temperature for 18 h. The mixture was cooled to 0 °C, aqueous hydrogen chloride solution (10 %, 60 mL) was added dropwise and the mixture stirred at 0 °C for 1 h. The mixture was allowed to warm to room temperature, and stirred for 30 min upon which it turned light blue with a precipitate. The mixture was filtered off and the colorless precipitate washed with abundant amounts of water, THF and methanol. The product was purified *via* Soxhlet extraction from methanol overnight and dried at 80 °C in vacuum for 6 h to yield **MPN-OMe** as a white powder. Yield, 595 mg (1.71 mmol repeating units, 100 %).

¹³C{¹H} CP/MAS-NMR (100 MHz): δ = 158, 146, 138, 131, 125, 112, 64, 53 ppm

Synthesis of Hydroxytetraphenylmethane Polymer (MPN-OH)^[4]

Methoxytetraphenylmethane polymer **MPN-OMe** (479 mg, 1.38 mmol, 1.00 eq) and anhydrous DCM (50 mL) were added to a Schlenk finger under argon atmosphere. After dropwise addition of BBr₃ solution (1M in DCM, 6.90 mL, 6.90 mmol, 5.00 eq) the mixture was stirred at room temperature for 18 h while the color of the mixture turned into green. Strong gas evolution was observed during dropwise addition of water (50 mL). The mixture was stirred at room temperature for 3 h, filtered off and the off-white precipitate washed with abundant amounts of water, THF and methanol. The product was purified *via* Soxhlet extraction from methanol overnight and dried at 80 °C in vacuum for 6 h to yield **MPN-OH** as off-white powder. Yield, 430 mg (1.29 mmol repeating units, 94 %).

¹³C{¹H} CP/MAS-NMR (100 MHz): δ = 154, 146, 138, 131, 125, 114, 63 ppm

Synthesis of 4-(3-bromopropoxy)tetraphenylmethane Polymer (MPN-OC3Br)

Hydroxytetraphenylmethane polymer **MPN-OH** (525 mg, 1.58 mmol), K₂CO₃ (294 mg, 2.13 mmol) and a few crumbs of 18-crown-6 were suspended in acetone (60 mL). 1,3-Dibromopropane (0.98 mL, 9.62 mmol) was added *via* syringe and the reaction stirred at reflux for 3 days. After cooling down to room temperature the mixture was filtered off and the off-white precipitate washed with abundant amounts of water, acetone, THF and methanol. The product was purified *via* Soxhlet extraction from methanol overnight and dried at 80 °C in vacuum for 6 h to yield **MPN-OC3Br** as off-white powder. Yield, 620 mg (1.37 mmol repeating units, 87 %).

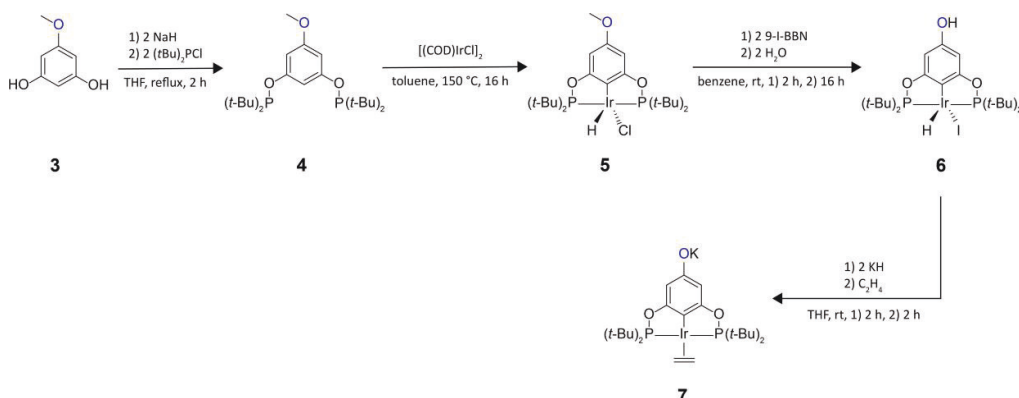
¹³C{¹H} CP/MAS-NMR (100 MHz): δ = 157, 146, 138, 131, 125, 113, 64, 32, 27 ppm

Synthesis of 4-(4-bromobutyloxy)tetraphenylmethane Polymer (MPN-OC4Br)

Hydroxytetraphenylmethane polymer **MPN-OH** (81.6 mg, 0.25 mmol), K₂CO₃ (44 mg, 0.32 mmol) and a few crumbs of 18-crown-6 were suspended in acetone (12 mL). 1,4-Dibromobutane (0.17 mL, 1.45 mmol) was added *via* syringe and the reaction stirred at reflux for 3 days. After cooling down to room temperature the mixture was filtered off and the off-white precipitate washed with abundant amounts of water, acetone, THF and methanol. The product was purified *via* Soxhlet extraction from methanol overnight and dried at 80 °C in vacuum for 6 h to yield **MPN-OC4Br** as off-white powder. Yield, 83.4 mg (0.18 mmol repeating units, 73 %).

¹³C{¹H} CP/MAS-NMR (100 MHz): δ = 157, 146, 139, 131, 125, 113, 66, 64, 29 ppm

Syntheses of Pincer Catalysts



Scheme S2. Syntheses of {*p*-KO-C₆H₂-2,6-[OP(t-Bu)₂]₂}Ir(C₂H₄) (**7**).

SUPPORTING INFORMATION

Synthesis of 5-MeOPCP (4)^[5]

To a suspension of NaH (389 mg, 14.7 mmol) in 15 mL of THF was a solution of 5-methoxyresorcinol (**3**) (984 mg, 7.02 mmol) in 15 mL of THF slowly added *via* syringe (caution: hydrogen evolution) at 0 °C. The mixture was heated to reflux for 2 h and subsequently cooled to 0 °C when di-*tert*-butyl-chlorophosphine (2.8 mL, 14.8 mmol) was added *via* syringe. The mixture was heated to reflux for another 2 h, at which point the solvent was evaporated under vacuum. The residue was extracted with 3x20 mL of hexane, and the extract was cannula transferred and filtered to give a light-yellow clear solution. After removal of hexane under vacuum, the flask was heated to 65 °C for 2 h under high vacuum which removed residual amounts of di-*tert*-butyl-chlorophosphine. The crude product was obtained as 2.28 g (5.32 mmol, 76 %) of a colorless viscous oil which solidified upon standing. The product exhibited ca. 95 % purity by NMR and was used without further purification.

¹H NMR (200 MHz, CDCl₃): δ = 6.61 (m, 1H, 2-H), 6.37 (m, 2H, 4- and 6-H), 3.75 (s, 3H, OCH₃), 1.15 (d, ³J_{P-H} = 11.8 Hz, 36H, 4x *t*-Bu) ppm

¹³C{¹H} NMR (50 MHz, CDCl₃): δ = 161.5 (C_q, d, ²J_{P-C} = 10.2 Hz), 161.1 (C_q, s), 101.6 (CH, t, ³J_{P-C} = 10.5 Hz), 97.8 (CH, d, ³J_{P-C} = 11.7 Hz), 55.5 (s, OCH₃), 35.8 (C_q, d, ¹J_{P-C} = 25.7 Hz), 27.5 (CH₃, d, ²J_{P-C} = 15.5 Hz) ppm

³¹P{¹H} NMR (81 MHz, CDCl₃): δ = 152.7 ppm

Synthesis of {*p*-OMe-C₆H₂-2,6-[OP(*t*-Bu)₂]₂}IrHCl (5**)^[5]**

Under Ar atmosphere a solution of 5-MeOPCP (**4**) (641 mg, 1.49 mmol) in 10 mL of toluene was slowly added *via* syringe to bis-(1,5-cyclooctadiene)diiridium(I)dichloride (456 mg, 0.68 mmol). The mixture was heated to 150 °C for 16 h. After cooling down to room temperature, the solvent was removed at 40 °C under high vacuum (10⁻³ mbar, 1 h) in order to remove free 1,5-cyclooctadiene. The residue was extracted with 20 mL of pentane prior to filtering and washing under air and drying at high vacuum (10⁻³ mbar, 1 h). The product was obtained as 728 mg 1.11 mmol, 82 %) of a red solid and was used without further purification.

¹H NMR (200 MHz, CDCl₃): δ = 6.27 (s, 2H, 3- and 5-H), 3.77 (s, 3H, OCH₃), 1.35 (m, 36H, 4x *t*-Bu), -41.86 (t, ²J_{P-H} = 13.3 Hz, 1H, IrH) ppm

¹³C{¹H} NMR (50 MHz, CDCl₃): δ = 167.5 (C_q, virtual triplet, apparent *J* = 6.0 Hz), 159.8 (C_q, s), 92.1 (CH, virtual triplet, apparent *J* = 5.7 Hz), 55.6 (s, OCH₃), 43.2 (C_q, virtual triplet, apparent *J* = 11.3 Hz), 39.6 (C_q, virtual triplet, apparent *J* = 12.6 Hz), 27.8 (CH₃, doublet of virtual triplets, ²J_{P-C} = 10.6 Hz, apparent *J* = 3.1 Hz) ppm

³¹P{¹H} NMR (81 MHz, CDCl₃): δ = 177.0 ppm

Synthesis of {*p*-OH-C₆H₂-2,6-[OP(*t*-Bu)₂]₂}IrH (6**)^[6]**

{*p*-OMe-C₆H₂-2,6-[OP(*t*-Bu)₂]₂}IrHCl (**5**) (667 mg, 1.02 mmol) was dissolved in benzene (30 mL) in a flame-dried Schlenk flask and put under a flow of argon. 9-I-BBN (1M in hexanes, 2.1 mL) was added, and the solution was stirred for 2 h at room temperature. The solvent was removed at room temperature under high vacuum (10⁻³ mbar) and then the by-product 9-Cl-BBN and the extra 9-I-BBN were removed at 80 °C under high vacuum (10⁻³ mbar). A mixture of benzene (20 mL) and degassed water (34 mL) was added to the residue, and the solution was stirred at room temperature overnight. Volatiles were removed under high vacuum (10⁻³ mbar). The residue was washed with pentane (30 mL) and dried under high vacuum (10⁻³ mbar) for 3 h. The product was obtained as 503 mg 0.69 mmol, 68 %) of a red solid and was used without further purification.

¹H NMR (200 MHz, CDCl₃): δ = 6.20 (s, 2H, 3- and 5-H), 4.49 (s, 1H, OH), 1.38 (virtual triplet, apparent *J* = 7.3 Hz, 36H, 4x *t*-Bu), -42.09 (t, ²J_{P-H} = 13.0 Hz, 1H, IrH) ppm

¹³C{¹H} NMR (126 MHz, CDCl₃): δ = 167.0 (C_q, virtual triplet, apparent *J* = 6.1 Hz), 155.4 (C_q, s), 117.0 (C_q, m br), 93.5 (CH, virtual triplet, apparent *J* = 5.7 Hz), 43.5 (C_q, virtual triplet, apparent *J* = 11.5 Hz), 40.3 (C_q, virtual triplet, apparent *J* = 12.7 Hz), 28.3 (CH₃, virtual triplet, apparent *J* = 2.7 Hz), 28.1 (CH₃, virtual triplet, apparent *J* = 2.9 Hz) ppm

³¹P{¹H} NMR (203 MHz, CDCl₃): δ = 181.3 ppm

Synthesis of {*p*-OK-C₆H₂-2,6-[OP(*t*-Bu)₂]₂}Ir(C₂H₄) (7**)^[6]**

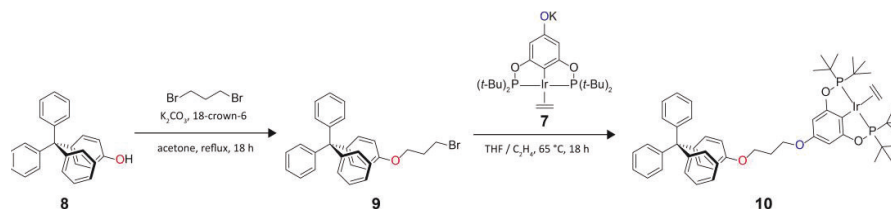
{*p*-OMe-C₆H₂-2,6-[OP(*t*-Bu)₂]₂}IrH (**6**) (600 mg, 0.82 mmol) and KH (105 mg, 2.63 mmol) were weighed into a flame-dried Schlenk flask and put under a flow of argon. THF (25 mL) was added to the flask *via* syringe and the resulting suspension was stirred for 2 h at room temperature. The solution was filtered into a Schlenk flask through a cannula filter. Ethylene was bubbled through the solution for 2 h. Volatiles were removed under high vacuum (10⁻³ mbar), and the orange solid was dried under high vacuum (10⁻³ mbar) for 3 h. The product was obtained as 494 mg (0.68 mmol, 82 %) of an orange solid and was used without further purification.

¹H NMR (200 MHz, THF-*d*₈): δ = 5.67 (s, 2H, 3- and 5-H), 2.64 (t, *J* = 3.0 Hz, 4H, C₂H₄), 1.26 (virtual triplet, apparent *J* = 6.4 Hz, 36H, 4x *t*-Bu) ppm

¹³C{¹H} NMR (50 MHz, THF-*d*₈): δ = 177.3, (C_q, s), 171.7 (C_q, s), 93.9 (CH, s), 41.4 (C_q, virtual triplet, apparent *J* = 10.7 Hz), 31.6 (CH, s, C₂H₄), 29.4 (CH₃, virtual triplet, apparent *J* = 3.3 Hz) ppm

³¹P{¹H} NMR (81 MHz, THF-*d*₈): δ = 170.4 ppm

SUPPORTING INFORMATION

Synthesis of Model compounds

Scheme S3. Synthesis of molecular model compound 10.

Synthesis of 4-(3-bromopropoxy)tetraphenylmethane (9)^[6]

4-Tritylphenol (**8**) (200 mg, 0.59 mmol), K_2CO_3 (111 mg, 0.80 mmol) and a small amount of 18-crown-6 were suspended in acetone (30 mL). 1,3-Dibromopropane (0.37 mL, 3.62 mmol) was added *via* syringe and the reaction stirred at reflux overnight. After cooling down to room temperature the mixture was dissolved in Et_2O and the organic phase was washed with H_2O and brine. The organic phase was dried over $MgSO_4$ and the solvent was removed under reduced pressure to yield the crude product which was purified from excess of 1,3-dibromopropane *via* addition of cyclohexane (3 x 10 mL) and subsequently centrifugation and removal of solvent. The product was obtained as 136 mg (0.30 mmol, 50 %) of a white solid.

1H NMR (500 MHz, $CDCl_3$): δ = 7.26 – 7.16 (m, 15H, CH_{Ar}), 7.10 (d, J = 8.8 Hz, 2H, CH_{Ar}), 6.78 (d, J = 8.8 Hz, 2H, CH_{Ar}), 4.07 (t, J = 5.8 Hz, 2H, O- CH_2), 3.59 (t, J = 6.4 Hz, 2H, CH_2 -Br), 2.30 (p, J = 6.1 Hz, 2H, C- CH_2 -C) ppm

$^{13}C\{H\}$ NMR (126 MHz, $CDCl_3$): δ = 156.8 (C_{q-O}), 147.2 (C_q), 139.4 (C_q), 132.4 (CH), 131.3 (CH), 127.6 (CH), 126.0 (CH), 113.4 (CH), 65.3 (O- CH_2), 64.5 (C_q), 32.6 (C- CH_2 -C), 30.2 (CH_2 -Br) ppm

Synthesis of the model compound Tritylphenolate Pincer Complex (10)

Under Ar atmosphere complex **7** (40 mg, 0.06 mmol), 4-(3-bromopropoxy)tetraphenylmethane (**9**) (27 mg, 0.06 mmol), and THF (10 mL) were added to a Schlenk flask. The THF solution was degassed by three freeze-pump-thaw cycles. The flask was refilled with ethylene gas at $-78^\circ C$. The mixture was heated at $65^\circ C$ overnight. After cooling down to room temperature volatiles were removed under high vacuum (10^{-3} mbar), and the orange solid was dried under high vacuum (10^{-3} mbar) for 3 h. The product was obtained as an orange solid (~80 % of the catalyst reacted to the model compound, residual 20 % of (**7**) and (**9**) still present in the reaction mixture).

1H NMR (700 MHz, $THF-d_8$): δ = 7.24 – 7.10 (m, 15H, CH_{Ar}), 7.06 (d, J = 9.0 Hz, 2H, CH_{Ar}), 6.80 (d, J = 8.9 Hz, 2H, CH_{Ar}), 4.12 (t, J = 6.2 Hz, 2H, O- CH_2), 4.09 (t, J = 6.2 Hz, 2H, O- CH_2), 2.98 (t, J = 2.6 Hz, 4H, C_2H_4), 2.18 (p, J = 6.1 Hz, 2H, C- CH_2 -C), 1.26 (virtual triplet, apparent J = 6.6 Hz, 36H, 4x *t*-Bu) ppm

$^{13}C\{H\}$ NMR (176 MHz, $THF-d_8$): δ = 169.4 (C_q), 161.5 (C_q), 158.3 (C_q), 148.3 (C_q), 139.8 (C_q), 133.1 (CH), 132.2 (CH), 128.3 (CH), 126.8 (CH), 114.1 (CH), 91.2 (CH), 65.4 (C_q), 65.4 (CH_2), 65.3 (CH_2), 42.3 (C_q , virtual triplet, apparent J = 10.7 Hz), 36.3 (CH, s, C_2H_4), 30.9 (CH_2), 29.16 (CH_3 , virtual triplet, apparent J = 2.9 Hz) ppm

$^{31}P\{H\}$ NMR (202 MHz, $THF-d_8$): δ = 180.5 ppm

Synthesis of immobilized catalyst MPN-OC3-[Ir]**Immobilization of {*p*-OK-C₆H₂-2,6-[OP(*t*-Bu)₂]₂Ir(C₂H₄) (**7**) on Polymer MPN-OC3Br for synthesizing MPN-OC3-[Ir]**

Polymer **MPN-OC3Br** (225 mg, 0.50 mmol) was added to a Schlenk flask and evacuated overnight. Under Ar atmosphere complex **7** (400 mg, 0.60 mmol) and THF (80 mL) were added. The THF suspension was degassed by three freeze-pump-thaw cycles. The flask was refilled with ethylene gas at $-78^\circ C$. The reaction stirred at $65^\circ C$ for 3 days. After cooling down to room temperature the solvent was removed *via* filtration under Ar atmosphere and the orange solid was washed with THF (6 x 20 mL) to remove the excess of metal precursor. The volatiles were removed under high vacuum (10^{-3} mbar), and the orange solid was dried under high vacuum (10^{-3} mbar) overnight. Drying in vacuum overnight (14 h) yielded the product as a red powder.

$^{13}C\{^1H\}$ CP/MAS-NMR (100 MHz): δ = 168, 160, 157, 146, 138, 131, 126, 114, 92, 67, 64, 41, 35, 28, 25 ppm

$^{31}P\{H\}$ CP/MAS-NMR (162 MHz): δ = 179 ppm

SUPPORTING INFORMATION

MAS-NMR spectroscopy

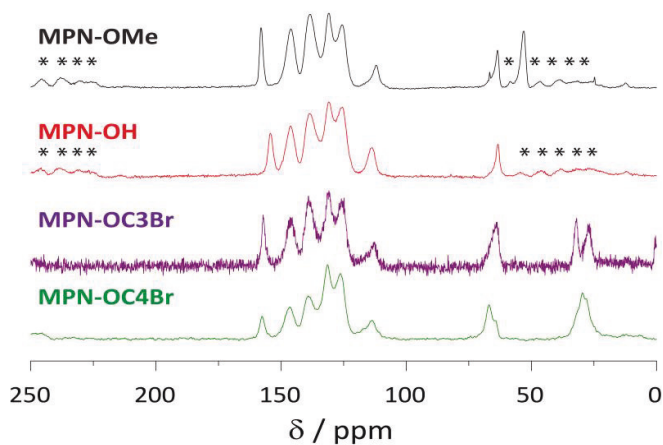


Figure S1. ^{13}C CP/MAS-NMR spectroscopy of **MPN-OMe** (black), **MPN-OH** (red), **MPN-O-C3Br** (purple) and **MPN-O-C4Br** (green). Asterisks denote spinning sidebands.

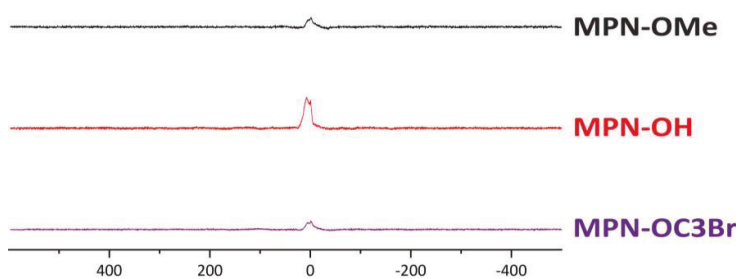


Figure S2. ^{11}B MAS-NMR spectroscopy of **MPN-OMe**, **MPN-OH** and **MPN-OC3Br**.

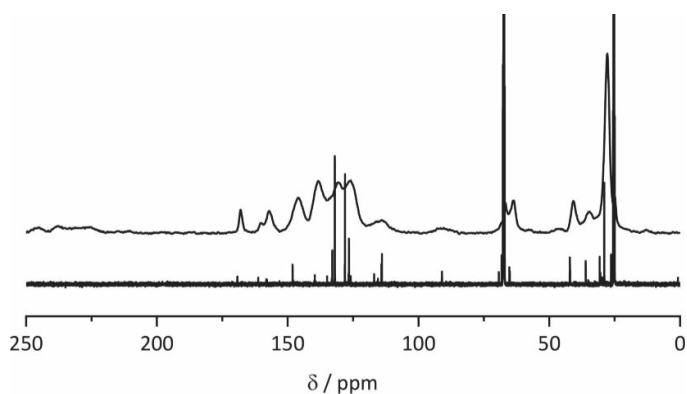


Figure S3. ^{13}C CP/MAS-NMR spectroscopy of **MPN-OC3-[Ir]** (top) and molecular model compound **10** (bottom).

SUPPORTING INFORMATION

FT IR spectroscopy

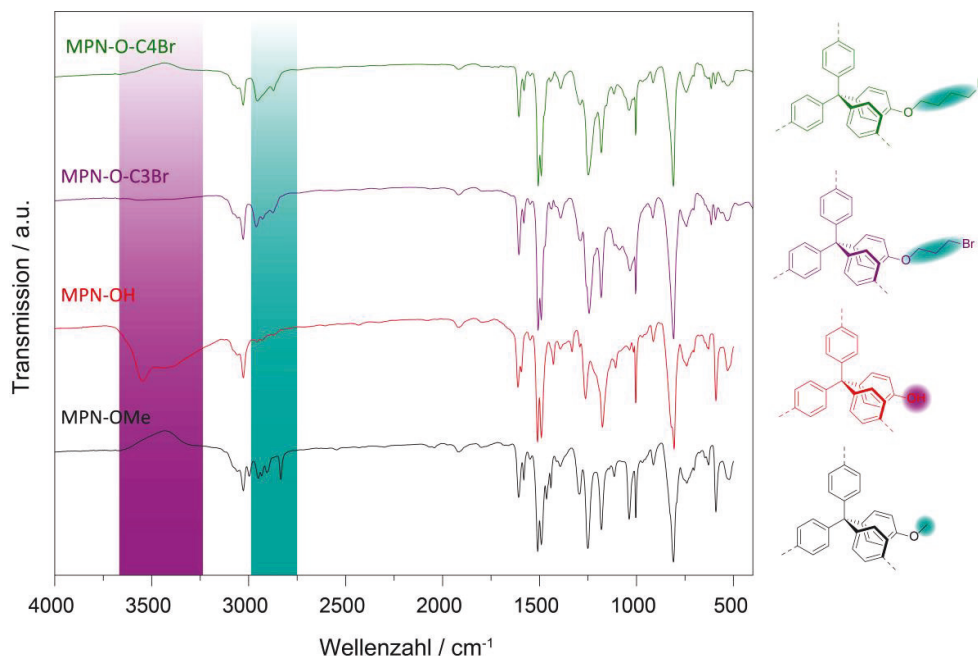


Figure S4. FT IR spectra of **MPN-OMe** (black), **MPN-OH** (red), **MPN-OC3Br** (purple) and **MPN-OC4Br**.

A successful demethylation of **MPN-OMe** towards **MPN-OH** can be confirmed by the absence of the bands between 2993 and 2831 cm^{-1} which corresponds to the valance band of the aliphatic C—H bond of the methyl group. Furthermore, the intense band between 3660 and 3240 cm^{-1} confirms the presence of O—H bond inside the polymer **MPN-OH**. After functionalization of **MPN-OH** towards **MPN-OC3Br** and **MPN-OC4Br**, the broad band between 3660 and 3240 cm^{-1} disappeared as expected and bands between 2960 and 2870 cm^{-1} could be detected as the valance bands of the aliphatic C—H bonds of the alkyl chains.

Physisorption measurements

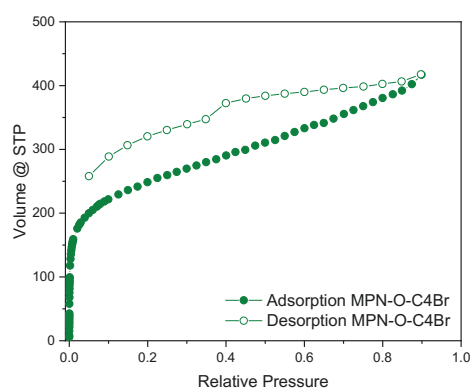


Figure S5. Ar physisorption measurement of **MPN-OC4Br** at 87 K.

SUPPORTING INFORMATION

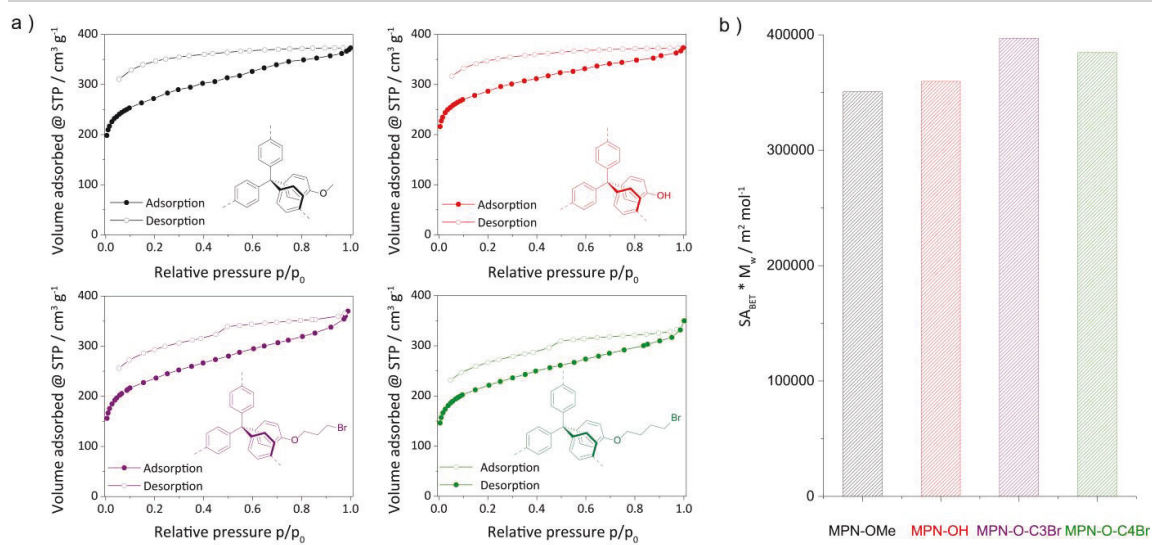


Figure S6. a) N₂ physisorption measurements of **MPN-OMe** (black), **MPN-OH** (red), **MPN-OC3Br** (purple) and **MPN-OC4Br** (green). b) Normalized surface area SA_{BET} * M_w of **MPN-OMe** (black), **MPN-OH** (red), **MPN-OC3Br** (purple) and **MPN-OC4Br** (green).

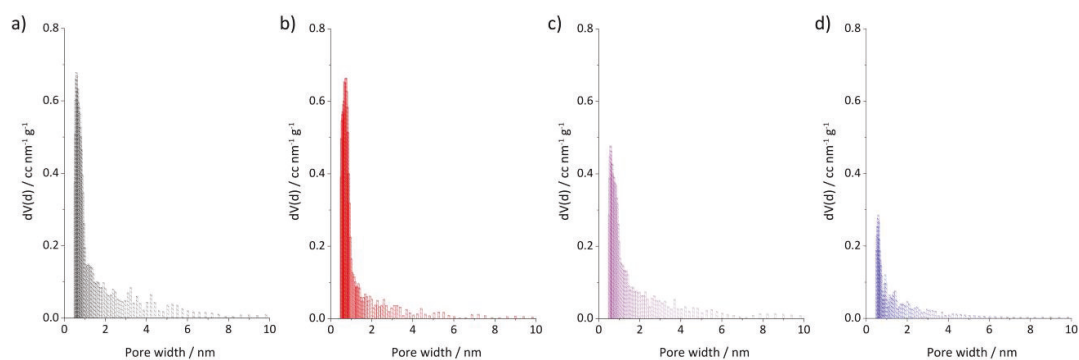


Figure S7. Pore size distribution profile calculated from Ar sorption isotherm for a) **MPN-OMe**, b) **MPN-OH**, c) **MPN-OC3Br** and d) **MPN-OC3-[Ir]**.

SUPPORTING INFORMATION

Thermogravimetric analysis

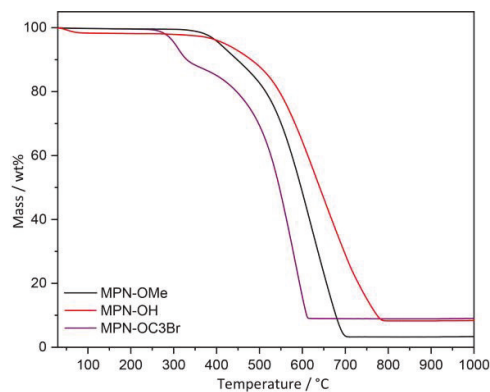


Figure S8. Thermogravimetric analysis of **MPN-OMe** (black), **MPN-OH** (red) and **MPN-OC3Br** (purple) under air with 5 K min⁻¹.

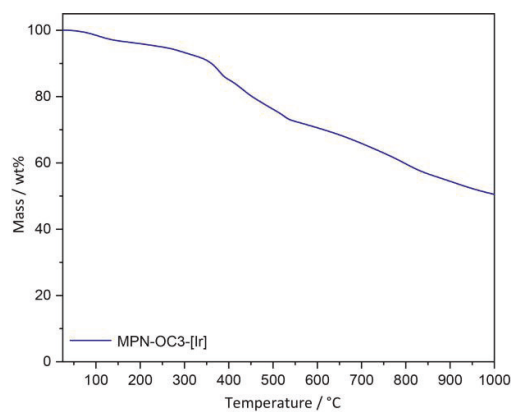


Figure S9. Thermogravimetric analysis of **MPN-OC3-[Ir]** under N₂ with 2 K min⁻¹.

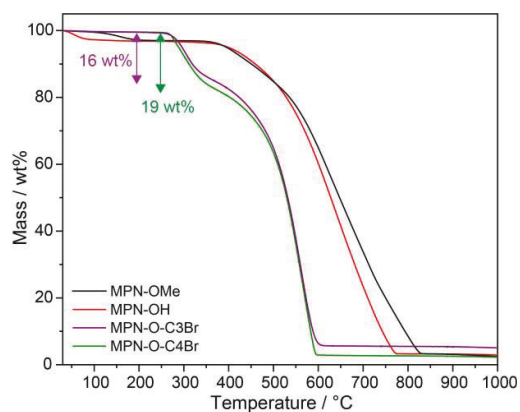


Figure S10. Thermogravimetric analysis of **MPN-OMe** (black), **MPN-OH** (red), **MPN-OC3Br** (purple) and **MPN-OC4Br** under air with 5 K min⁻¹.

SUPPORTING INFORMATION

X-ray photoelectron spectroscopy

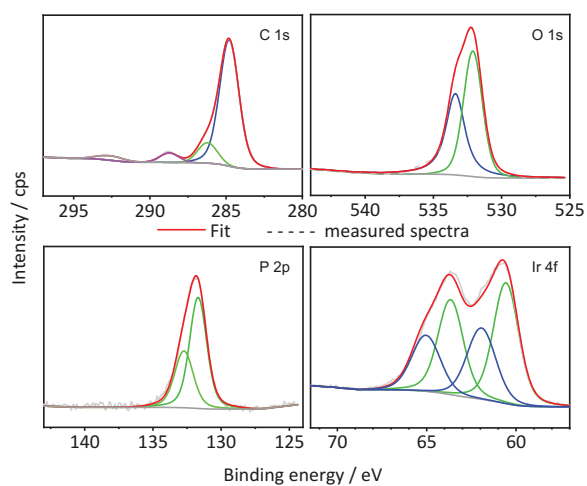


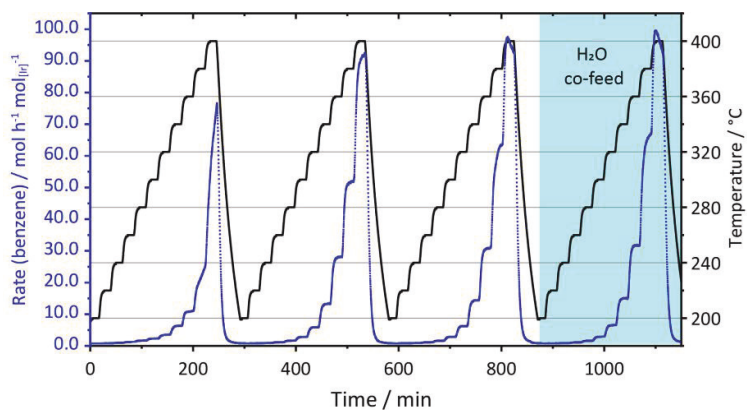
Figure S11. C 1s, O 1s, P 2p and Ir 4f XPS spectra of molecular model compound tritylphenolate pincer complex (**10**).

SUPPORTING INFORMATION

Catalytic continuous-flow dehydrogenation of cyclohexane

Table S1. Gas species and their respective mass per charge ratios (m/z).

Species	Mass per charge ratio (m/z)
Ar	40
H ₂	2
Cyclohexane	56, 84
Cyclohexene	67, 54
Benzene	78
CO ₂	44
N ₂ /CO	28
O ₂	32
H ₂ O	18

**Figure S12.** Catalytic dehydrogenation of cyclohexane. Temperature ramp measurement: Benzene formation rate depending on the catalyst bed temperature, four cycles of heating with 4 K/min and holding for 15 min between 200 °C and 400 °C in steps of 20 °C. For the last temperature ramping cycle water was co-fed to the gas flow.

SUPPORTING INFORMATION

Determination of thermodynamic values

$$\ln r = \ln k_{\text{app}} = \ln k_0 - E_A / (RT)$$

Linear Fit:

$$\ln (\text{Rate}_{\text{benzene}}) = (37.774 \pm 1.353) - (13097.300 \pm 812.305) / K * 1/\text{Temperature}$$

$$E_A = (108.9 \pm 6.8) \text{ kJ mol}^{-1}$$

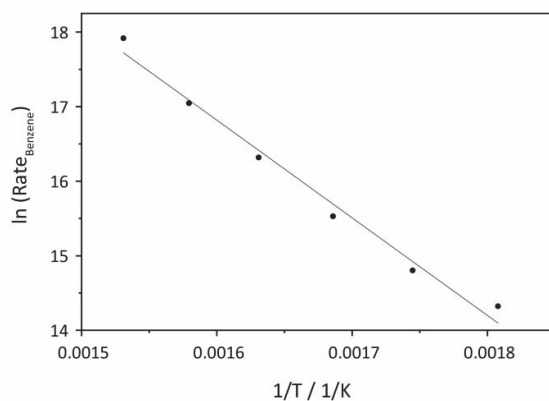


Figure S13. The rates of benzene formation during the steady regimes of each temperature step between 280 and 380 °C (except 380 °C in cycle 1) were averaged for each temperature. The temperature-rate pairs were used in an Arrhenius plot to determine the apparent activation energy of the dehydrogenation of cyclohexane to benzene of $(108.9 \pm 6.8) \text{ kJ mol}^{-1}$.

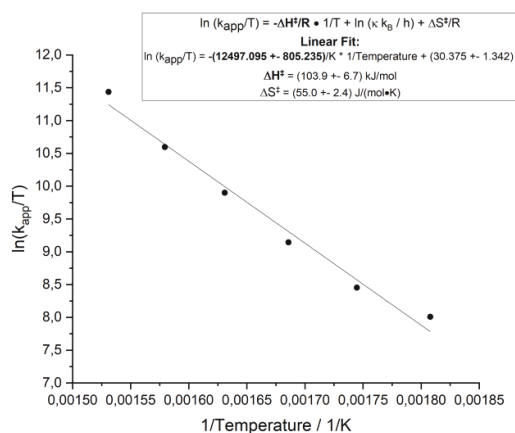


Figure S14. The rates of benzene formation during the steady regimes of each temperature step between 280 and 380 °C (except 380 °C in cycle 1) were averaged for each temperature. The temperature-rate pairs were used in an Eyring plot to determine the enthalpy and entropy of activation of the dehydrogenation of cyclohexane to benzene. The activation enthalpy was calculated as $(103.9 \pm 6.7) \text{ kJ mol}^{-1}$ and the activation entropy as $(55.0 \pm 2.4) \text{ kJ mol}^{-1} \text{ K}^{-1}$.

SUPPORTING INFORMATION

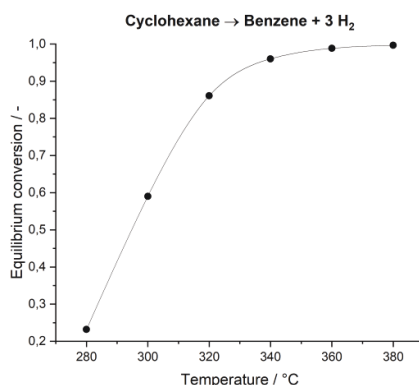


Figure S15. Equilibrium conversion of cyclohexane to benzene as a function of temperature, using standard formation enthalpies and entropies of cyclohexane, benzene and hydrogen.

Scanning electron microscopy after catalysis

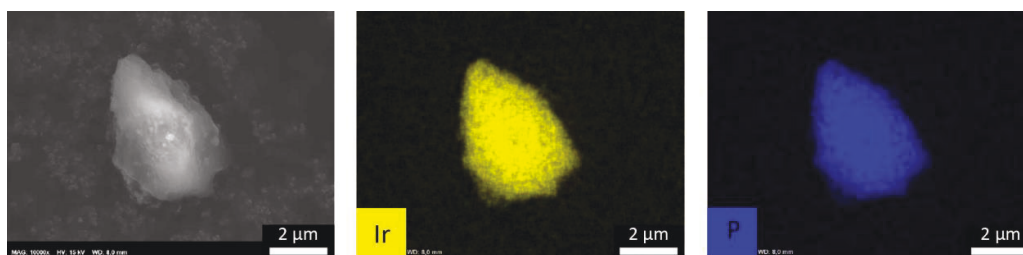


Figure S16. Scanning electron microscopy and energy dispersive X-ray spectroscopic elemental mapping of **MPN-OC3-[Ir]** after isothermal dehydrogenation experiment at 300 °C for 168 h. Yellow belongs to iridium, blue belongs to phosphorus.

References

- [1] K. Nikitin, E. Lestini, M. Lazzari, S. Altobello, D. Fitzmaurice, *Langmuir* **2007**, 23, 12147–12153.
- [2] M. E. Gallina, B. Baytekin, C. Schalley, P. Ceroni, *Chem. - A Eur. J.* **2012**, 18, 1528–1535.
- [3] W. Lu, D. Yuan, J. Sculley, D. Zhao, R. Krishna, H.-C. Zhou, *J. Am. Chem. Soc.* **2011**, 133, 18126–18129.
- [4] T. M. Kosak, H. A. Conrad, A. L. Korich, R. L. Lord, *European J. Org. Chem.* **2015**, 2015, 7460–7467.
- [5] I. Göttker-Schnetmann, P. White, M. Brookhart, *J. Am. Chem. Soc.* **2004**, 126, 1804–1811.
- [6] Z. Huang, M. Brookhart, A. S. Goldman, S. Kundu, A. Ray, S. L. Scott, B. C. Vicente, *Adv. Synth. Catal.* **2009**, 351, 188–206.

Author Contributions

All authors contributed extensively to the work presented in this paper. M.K. and A.T. conceived the research project. M.K. conducted the synthesis of monomers as well as polymers, and performed the characterizations. M.K. and M.T. synthesized the pincer complexes, model compound and performed the immobilization onto the polymer. M.T. and M.A.R. designed the dehydrogenation experiments. M.A.R. performed the dehydrogenation experiments and evaluated the data. J.S. performed and evaluated the XPS analyses for all the samples. H.K. performed the SEM analyses as well as EDX experiments. The whole project was administrated by A.T, with the help from M.K. R.S. provided the valuable guidance and helped for the catalytic tests. M.K., M.T. and A.T. wrote the manuscript with the input from the other authors.

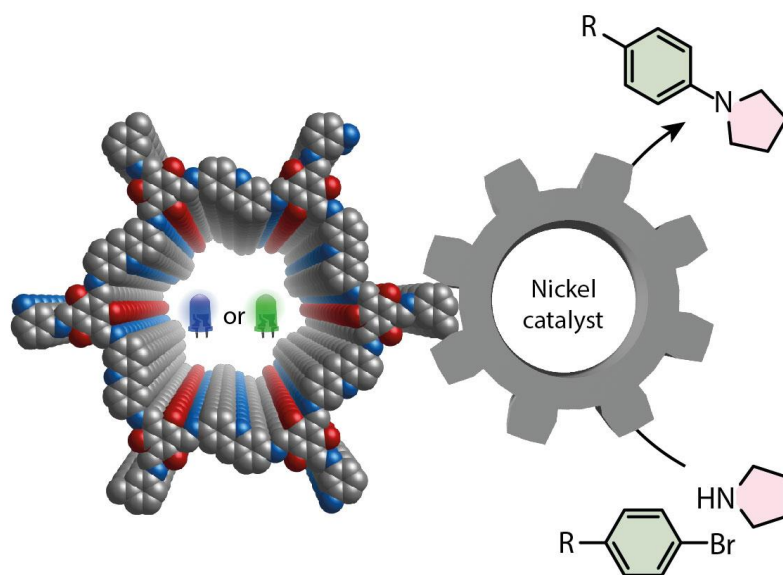
Article II:

Acridine-Functionalized Covalent Organic Frameworks (COFs) as Photocatalysts for Metallaphotocatalytic C–N Cross-Coupling

M. Traxler, S. Gisbertz, P. Pachfule, J. Schmidt, J. Roeser, S. Reischauer, B. Pieber, A. Thomas

Angew. Chem. Int. Ed. **2022**, 61, e202117738.

Published manuscript, DOI: <https://doi.org/10.1002/anie.202117738>



A new family of porous crystalline COFs bearing acridine moieties was synthesized and applied as photocatalysts in metallaphotocatalytic C–N cross-coupling. Among these materials the fully β -ketoenamine-linked COF showed the highest catalytic activity and was shown to be recyclable and even catalyzed the cross-coupling efficiently under green light irradiation.



Covalent Organic Frameworks Hot Paper

How to cite: *Angew. Chem. Int. Ed.* **2022**, *61*, e202117738

International Edition: doi.org/10.1002/anie.202117738

German Edition: doi.org/10.1002/ange.202117738

Acridine-Functionalized Covalent Organic Frameworks (COFs) as Photocatalysts for Metallaphotocatalytic C–N Cross-Coupling

Michael Traxler, Sebastian Gisbertz, Pradip Pachfule, Johannes Schmidt, Jérôme Roeser, Susanne Reischauer, Jabor Rabeah, Bartholomäus Pieber,* and Arne Thomas*

Abstract: Covalent organic frameworks (COFs) are structurally tuneable, porous and crystalline polymers constructed through the covalent attachment of small organic building blocks as elementary units. Using the myriad of such building blocks, a broad spectrum of functionalities has been applied for COF syntheses for broad applications, including heterogeneous catalysis. Herein, we report the synthesis of a new family of porous and crystalline COFs using a novel acridine linker and benzene-1,3,5-tricarbaldehyde derivatives bearing a variable number of hydroxy groups. With the broad absorption in the visible light region, the COFs were applied as photocatalysts in metallaphotocatalytic C–N cross-coupling. The fully β -ketoenamine linked COF showed the highest activity, due to the increased charge separation upon irradiation. The COF showed good to excellent yields for several aryl bromides, good recyclability and even catalyzed the organic transformation in presence of green light as energy source.

Introduction

The field of covalent organic frameworks (COFs)—crystalline and porous polymers that are solely consisting of organic building blocks reticulated via covalent bonds—has gained significant attention in the last decade.^[1–6] A variety of building units (linkers) and organic reactions have been applied for the synthesis of COFs with a broad range of functionalities, linkages and variable pore structures.^[7–13] Because these ordered structures have a permanent porosity, long-range π -conjugation, and the possibility to tune the structure of the backbone and integrate functional linkers, COFs have emerged as powerful materials for a plethora of different applications including gas storage and separation, energy storage, optoelectronics and catalysis.^[13–21] The formation of strong covalent bonds between the organic building blocks results in high chemical stability for the framework materials that can be further enhanced by introducing linkers that allow for e.g. tautomerization or hydrogen bond formation.^[22,23]

As an impact of these properties, COFs are promising candidates for heterogeneous photocatalysis using visible-light due to the long-range π -conjugation. Water splitting and CO₂ reduction dominate this application branch, and only few examples using COF photocatalysts in organic synthesis were reported.^[24] These include oxidative hydroxylation,^[25,26] C–H functionalization, cross-coupling reactions,^[27,28] oxidative N–S cyclization^[29] or tandem addition-cyclization reaction.^[30] Recently, the scope of COFs in catalyzing organic transformation has been further expanded to C–S and C–O carbon heteroatom cross-couplings through metallaphotocatalysis.^[31,32] However, COFs have not been applied in carbon-nitrogen (C–N) cross-coupling reactions, which are among the most important reactions in synthetic organic chemistry.^[33] The majority of COFs applied in photocatalysis are limited to short wavelengths (blue light radiation), which can result in deactivation of the nickel co-catalyst,^[34] and other side-reactions^[35] due to the high photon energy. These problems can be overcome using less energetic irradiation sources. Expanding the absorption of COFs in order to harvest long wavelengths requires, for example, increasing π -conjugation by extending the length of the linkers with phenyl or acetylene groups, introduction of donor–acceptor structures, post-synthetic introduction of a chromophore, or the use of organic dyes that absorb visible light as linkers.^[36–38]

The acridine motif is commonly found in organic dyes and enables efficient intersystem crossing upon excitation.

[*] M. Traxler, Dr. P. Pachfule, Dr. J. Schmidt, Dr. J. Roeser, Prof. A. Thomas

Department of Chemistry/Functional Materials,
 Technische Universität Berlin,
 Hardenbergstraße 40, 10623 Berlin (Germany)
 E-mail: arne.thomas@tu-berlin.de

S. Gisbertz, S. Reischauer, Dr. B. Pieber
 Department of Biomolecular Systems,
 Max Planck Institute of Colloids and Interfaces,
 Am Mühlenberg 1, 14476 Potsdam (Germany)
 E-mail: bartholomaeus.pieber@mpikg.mpg.de

S. Gisbertz, S. Reischauer
 Department of Chemistry and Biochemistry,
 Freie Universität Berlin,
 Takustraße 3, 14195 Berlin (Germany)

Dr. P. Pachfule
 Department of Chemical, Biological & Macro-Molecular Sciences,
 S. N. Bose National Centre for Basic Sciences,
 Kolkata-700106, India.

J. Rabeah
 Leibniz Institute for Catalysis (LIKAT Rostock),
 Universität Rostock,
 18059 Rostock (Germany)

© 2022 The Authors. Angewandte Chemie International Edition published by Wiley-VCH GmbH. This is an open access article under the terms of the Creative Commons Attribution License, which permits use, distribution and reproduction in any medium, provided the original work is properly cited.

This results in long-lived excited states that are crucial for efficient photocatalysis using low catalyst loadings.^[39,40] Recently, Stolarczyk and co-workers showed that an acridine carbon dot heterostructure can be used for photocatalytic water splitting.^[41] Homogeneous acridines have been explored in dual photocatalysis for decarboxylative *N*-alkylation, decarboxylative conjugate addition or dehydrocarboxylation of carboxylic acids.^[42–44] Further, it has been observed that acridine based small molecules and materials can harvest lower energetic light radiation compared to anthracene compounds, especially in its protonated form.^[40,41,45] However, utilization of acridine-based linkers for the synthesis of crystalline and porous materials such as COFs and MOFs have not been attempted.

Herein, we describe the synthesis of novel COFs bearing acridine moieties in reticulation with three different benzene-1,3,5-tricarbaldehyde derivatives with a variable number of hydroxy groups. The resulting materials were evaluated for their application as photocatalysts in metal-photocatalytic C–N cross-couplings. Our results indicate that not only a high surface area and crystallinity, but also a β -ketoenamine structure and high charge separation under light irradiation are the key factors for high catalytic activity.

Results and Discussion

We began our investigations by synthesizing a C2-linker bearing the acridine moiety (2,6-diaminoacridine, Acr) by a three step reaction, where 3-nitro-*N*-(4-nitrophenyl)aniline was obtained by a Buchwald–Hartwig amination.^[46] After a palladium catalyzed reduction, the linker was prepared by a Bernthsen-type acridine synthesis using formic acid [Section S3.1, in the Supporting Information].^[47] By changing the amounts of hydroxy groups, we have enabled a different β -ketoenamine to imine ratio in Tp-Acr, DHTA-Acr and HTA-Acr COFs (Figure 1a). In the special case of using the phloroglucinol based linker, the keto-enol tautomerization is irreversible towards the keto form, whereas for DHTA and HTA based COFs the tautomerization shows reversibility.^[48] Tp-Acr and DHTA-Acr COFs were prepared via an acid catalyzed Schiff base reaction, where 2,6-diaminoacridine (Acr, 31.5 mg, 0.15 mmol) was reacted with 1,3,5-triformylphloroglucinol (Tp, 21 mg, 0.1 mmol) or 2,4-dihydroxybenzene-1,3,5-tricarbaldehyde (DHTA, 19.4 mg, 0.1 mmol), respectively, using 6 M acetic acid (0.5 mL) as catalyst and a mixture of 3 mL mesitylene/dioxane (1:1) as a solvent. For the HTA-Acr COF, the solvent mixture was changed to 1:1 *n*-butanol/*o*-dichlorobenzene (3 mL) in the reaction with 2-hydroxybenzene-1,3,5-tricarbaldehyde (HTA, 17.8 mg, 0.1 mmol), while the amount of 2,6-diaminoacridine and acetic acid was kept constant (Section S3.2). All the precursor mixtures were heated for 72 h at 120 °C and the solid product washed with acetone, methanol (MeOH) and cyclohexane prior to Soxhlet extraction using MeOH to obtain the COFs as dark red solids.

Structural features and crystallinity of the synthesized COFs were determined using powder X-ray diffraction

(PXRD) analyses with a Cu K α radiation. All materials show the most intense reflections in the low angle region at 3.5 2 θ degrees for Tp-Acr as well as DHTA-Acr, and 3.6 2 θ degrees for HTA-Acr (Figure 1e–g). These can be assigned to the (100) facet of a primitive hexagonal lattice. Additional weak reflections and a broad reflection at around 26.5 2 θ degrees can be assigned to the (001) facet and confirm the crystalline π - π stacked 2D structure for all three COFs. According to the geometry of the linkers, structural models with **hcb** topology were constructed for eclipsed (AA) and staggered (AB) stacking sequences (Figure S4–S6). After geometrical optimization, the theoretical PXRD patterns of the structures were calculated and compared to the experimental diffraction pattern. All three COFs showed good agreement for the eclipsed stacking pattern, whereas the simulated staggered pattern did not fit with the measured diffractogram (Figure S7). Additionally, a full Pawley refinement was carried out to fit the final unit cell parameters, which led to acceptably low residual values and profile differences (Figure 1e–g).

All COFs were studied using ¹³C cross-polarization magic angle spinning nuclear magnetic resonance (CP-MAS NMR) analyses (Figure 2a). The pronounced carbonyl carbon (C=O) peak in the area of 180–185 ppm for Tp-Acr and DHTA-Acr indicates that these COFs exist dominantly in their keto form. In case of HTA-Acr COF, an equilibrium between the keto- and enol-form was identified via the signals at 179 and 189 ppm, respectively. Further distinctive peaks are overlapping with the broad multiple signals between 100–150 ppm due to the missing symmetry in the acridine linker. Fourier transform infrared (FT-IR) spectra of the frameworks confirmed the disappearance of characteristic signals of the precursors, while diagnostic bands of the COFs (C=O and C=C bonds at 1550–1580 cm^{−1} and for C–N bonds at around 1270 cm^{−1}) are present (Section S5.1). From the CP-MAS NMR and FTIR data, the structural integrity and formation of acridine COFs has been validated.

The permanent porosity of the acridine based COFs was confirmed using nitrogen sorption measurements at 77 K (Figure 2b). The surface areas were calculated using the Brunauer–Emmett–Teller (BET) method. Among the newly synthesized acridine COFs, Tp-Acr showed the highest BET surface area of 654 m²g^{−1}, compared to 408 m²g^{−1} for DHTA-Acr COF and 127 m²g^{−1} for the HTA-Acr COF. This shows that the number of hydroxy groups in the aldehyde linker influences the final accessible surface area of the COFs. The additional keto-/enol groups within the COF structure work as pore-directing “anchors”, improving the stacking of the layers, which results in the increase of surface area.^[49] Additional pore size evaluation revealed for all COFs a distribution close to the simulated one (Figure S11). Scanning electron microscopy (SEM) analyses revealed a rather undefined morphology from aggregated particles of Tp-Acr, DHTA-Acr and HTA-Acr, while transmission electron microscopy (TEM) confirms the presence of a sheet like structure (Figure S12). In order to investigate the chemical stability of Tp-Acr, the COF was immersed in various solvents. PXRD analyses of recovered samples

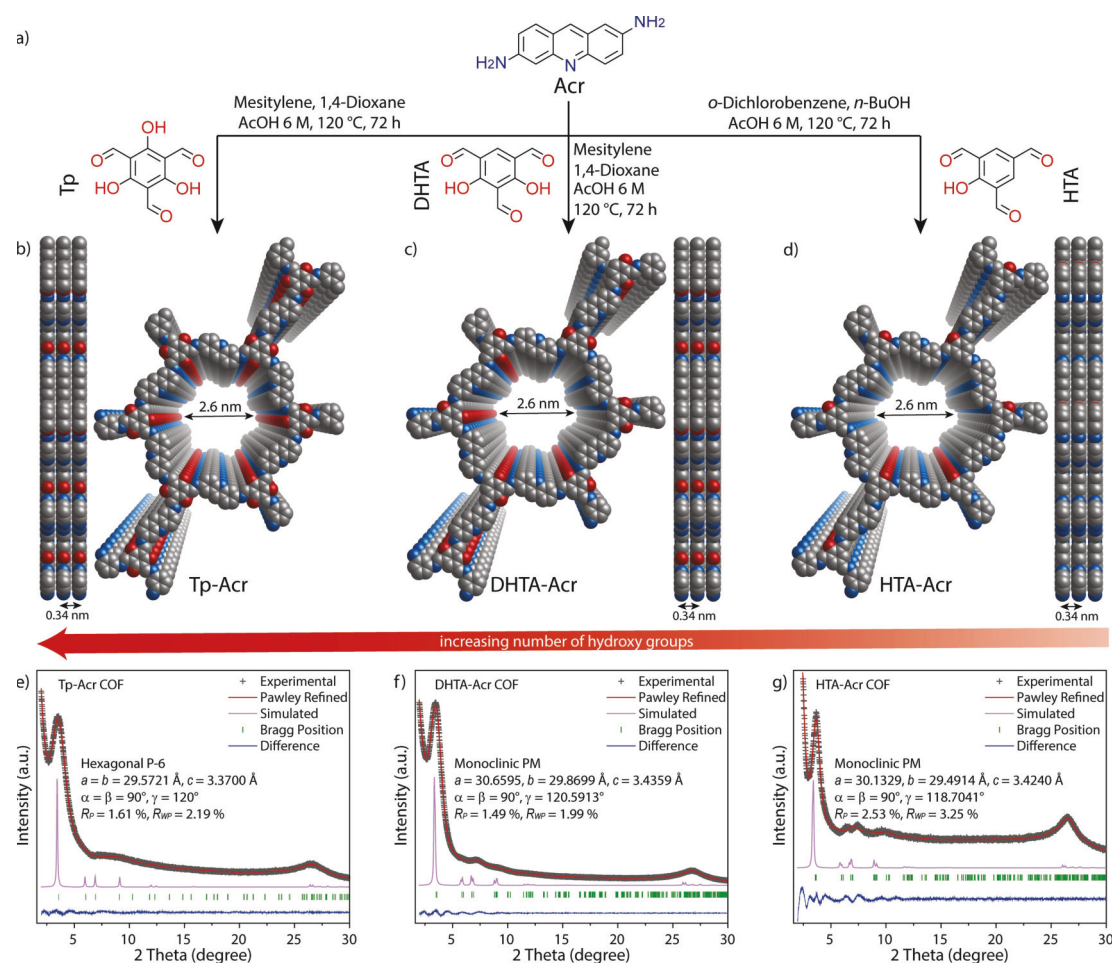


Figure 1. Synthesis and characterization of Tp-Acr, DHTA-Acr and HTA-Acr. a) Scheme of the synthesis of the COFs. b–d) Top and side views of Tp-Acr, DHTA-Acr and HTA-Acr showing the ideal eclipsed (AA) structures. e–g) Experimental, Pawley-refined and simulated powder X-ray diffraction patterns (AA stacking) and difference plot for Tp-Acr, DHTA-Acr and HTA-Acr.

confirmed, that the Tp-Acr COF retained its crystalline structure after 3 days of treatment with acetone, methanol, cyclohexane, dimethylacetamide (DMAc) or water. Moreover, the COF was stable in a basic aqueous environment (1 M NaOH) for 1 day with only a slight loss in crystallinity. No sign of decomposition or dissolution was observed, and the COF could be recovered quantitatively after the treatment (Figure S13 and S14). Additionally, the thermal stability of the COFs was tested using thermogravimetric analysis (TGA), which revealed that the frameworks are—after initial weight loss due to adsorbed solvent molecules—thermally stable up to 300 °C (Figure S15). The chemical stability of the COF in DMAc and basic medium is important as the architectural stability in polar solvents and under basic conditions renders a prerequisite for many photocatalytic reactions, particularly metallaphotocatalytic cross-couplings.^[50]

From the diffuse reflectance ultraviolet-visible (UV/Vis) spectroscopy, it was confirmed that all acridine containing COFs show a very similar absorption behavior in the visible light region. In order to distinctly investigate the effect of the acridine moiety on the optical properties, an isorecticular COF with anthracene edges (Tp-DAA, DAA: 2,6-diaminoanthracene) was synthesized for comparison (Section S6).^[51] It can be clearly seen that the absorption of Tp-DAA COF is blue shifted compared to the acridine COFs. While Tp-DAA exhibits an absorption edge at 620 nm, all acridine COFs show an absorbance over a broad range of the visible light region. The absorption edge is in all cases around 680 nm tailing up to more than 800 nm (Figure 3a). Optical band gaps calculated from Tauc plots are 1.82–1.83 eV for the acridine COFs and 1.98 eV for the anthracene analogue, confirming the impact of acridine moieties for light harvesting in the visible region (Figure 3b). The absorption of the

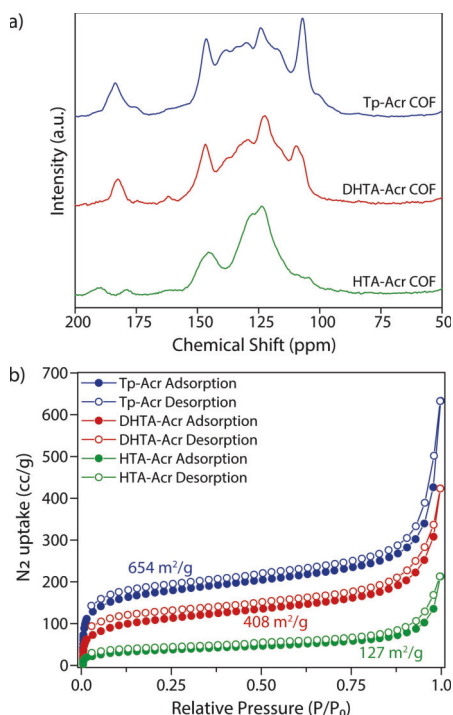


Figure 2. a) ^{13}C CP-MAS NMR spectra of Tp-Acr, DHTA-Acr and HTA-Acr. b) N_2 sorption isotherms for Tp-Acr, DHTA-Acr and HTA-Acr.

acridine moiety itself determines the photophysical properties with a peak shoulder at 610 nm that can be attributed to aggregation of the acridine units, which is red shifted to the absorption of the acridine linker itself (Figure S16). Such a phenomenon, the formation of so-called “J-aggregates”, was previously reported for porphyrin COFs.^[52] Moreover photoluminescence measurements and steady-state time-resolved fluorescence life-time measurements were performed (Section S5.6). The measurements reveal for individ-

ual decay components, that Tp-Acr shows the highest lifetime compared to other acridine based COFs.

The conduction band electrons of the acridine COF species were monitored by electron paramagnetic resonance (EPR) spectroscopy. To visualize the charge separation and transfer properties, EPR spectra of the COFs have been recorded in the dark and under photocatalytic reaction conditions. All three acridine based COFs show a singlet signal with Lorentzian line shape at $g=2.007$, which can be attributed to unpaired electrons in the conduction band.^[53] The signal intensities increased upon irradiation with light, since more electrons are excited from the valence band to the conduction band, indicating the formation of electron hole pairs in the COF semiconductors (Figure 3c).^[36,54] A clear trend in signal intensity can be found for the COF materials. The Tp-Acr COF shows by far the highest signal intensity, which suggests that the charge separation efficiency is largely improved in the fully β -keto tautomericized COF material. For DHTA-Acr and HTA-Acr the tautomerization between keto and enol form is likely to result in a decreased stability of the conduction band electrons. Compared to the structurally identical Tp-Acr, the anthracene containing Tp-DAA ($g=2.007$) COF shows a decreased efficiency in charge separation (Figure S18), highlighting the benefit of introducing the acridine moiety into the framework structure.

After confirming the porosity as well as the presence of acridine functionalities in the COF backbones and determining the enhanced light absorption in visible light region as well as the charge separation properties, we sought to study if acridine COFs are suitable photocatalysts for semi-heterogeneous dual nickel/photocatalytic C–N cross-coupling.^[50] Our investigations started by optimizing the amination of 4-bromobenzotrifluoride with pyrrolidine using the Tp-Acr COF as photocatalyst and 440 nm LEDs as light source. Nearly quantitative formation (91 %) of the desired alkyl aryl amine (**1**) was obtained within 16 h when Tp-Acr COF (2 mg mL^{-1}), $\text{NiBr}_2 \cdot 3\text{H}_2\text{O}$ (5 mol %) and three equivalents of the amine coupling partner were used in DMAc (Figure 4, Entry 1). Similarly, DHTA-Acr and HTA-Acr showed full conversion of the substrate with slightly lower

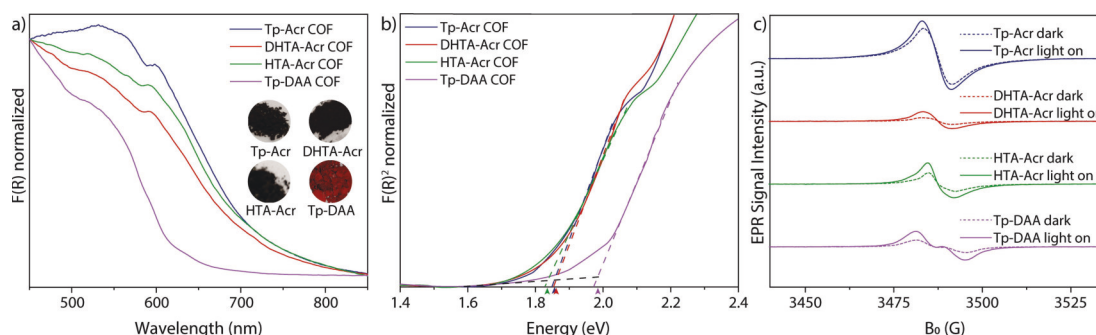


Figure 3. a) UV/Vis diffuse reflectance spectra for Tp-Acr, DHTA-Acr, HTA-Acr and Tp-DAA. The inset shows optical images of the COF powders. b) Tauc plots for Tp-Acr, DHTA-Acr, HTA-Acr and Tp-DAA. c) EPR conduction band e-signals of Tp-Acr, DHTA-Acr, HTA-Acr and Tp-DAA under dark condition (dotted lines) and during visible light irradiation (> 420 nm).

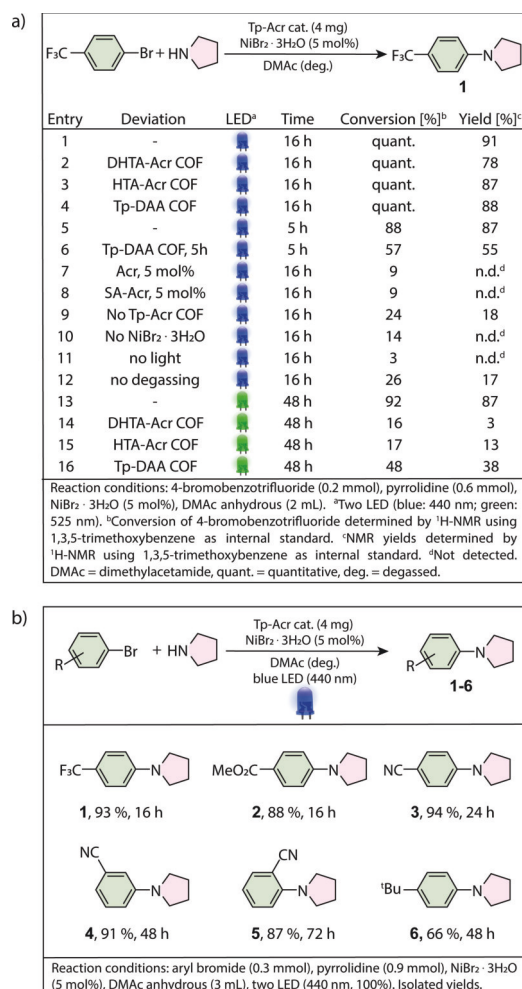


Figure 4. a) Optimized conditions and control experiments using blue and green light. b) Scope of the semi-heterogeneous amination of pyrrolidine and aryl bromides.

selectivity towards the coupling product (Entries 2 and 3). Interestingly, the isorecticular Tp-DAA COF also gave almost quantitative formation of the desired product under these conditions (Entry 4). Shorter reaction times were investigated to better compare the activity of Tp-Acr and Tp-DAA. Within five hours, the acridine COF resulted in 87 % of the desired product, while Tp-DAA gave only 55 % (Entries 5 and 6). These results highlight the advantage of using the acridine based COFs in metallaphotocatalytic C–N cross-coupling and are in full agreement with the charge separation properties found in EPR. When comparing the three acridine COFs, also the higher surface area of Tp-Acr compared to the others might accelerate the photocatalytic performance by increasing the number of accessible active sites and improving mass transfer within the material.

However, Tp-DAA shows an even higher surface area than TP-Acr from BET measurements (Figure S20), but a lower activity, thus charge carrier generation and separation seem to be the most decisive parameter for their photocatalytic performance.

Control studies using the linker 2,6-diaminoacridine (Acr) or a model compound (low molecular repeating unit of the COF structure; SA-Acr; Section S7) as photocatalyst showed no formation of the product (Entries 7 and 8), emphasizing that only after incorporation into the COF backbone, the repeating units build up their photocatalytic properties through conjugation. In case of omitting a photocatalyst, still minor product formation (18 %) was detected (Entry 9). This can be explained by photoexcitation and productive catalysis of nickel-amine complexes by the small portion of UV-light in the emission of the used light source (Figure S1).^[55] Further control studies showed that a nickel source, light and an oxygen free-environment are crucial for the desired coupling (Entry 10–12). With their extended absorption, the acridine COFs were additionally tested as photocatalyst under green light radiation (525 nm LEDs). This is important, because lower excitation energy prevents catalyst deactivation^[34] and the formation of undesired side products in case of certain substrates.^[35] Indeed, the reaction using Tp-Acr as a photocatalyst resulted in 87 % yield of **1** after 48 h (Entry 13). On the contrary, DHTA-Acr and HTA-Acr showed only minor product formation, while using Tp-DAA 38 % of the coupling product was obtained (Entries 14 and 16). These results emphasize that embedding the acridine unit into a fully keto tautomericized COF resulted in a highly efficient photocatalyst both under blue and green light irradiation. With the optimized conditions using the most efficient COF (Tp-Acr) as photocatalyst, the versatility of the semi-heterogeneous catalytic system was evaluated (Figure 4b). The reaction of pyrrolidine with electron deficient aryl bromides generally gave high yields for the corresponding aryl amines (**1–5**). An aryl bromide with electron-donating group (**6**) reacted with slightly less selectivity, which is in agreement with most dual nickel/ photocatalytic C–N coupling protocols.^[34,55–58] Nitriles (**3–5**), ester (**2**), trifluoromethyl- (**1**) as well as a bulky aliphatic residue (**6**) were tolerated in the dual catalytic amination. Substrates with an electron withdrawing meta-substituent (**4**) or ortho-substituent (**5**) did also yield the desired products in similar selectivity, although with lower efficiency than the para-substituted analogue (**3**).

A major advantage of COFs is the potential reusability of the solid photocatalyst due to easy separation from the reaction mixture. Therefore, we studied whether the Tp-Acr framework can be recycled (Figure 5). After successful C–N coupling reaction, Tp-Acr COF was recovered by centrifugation and reused for the same reaction. A first set of experiments in which the recovered material was washed with DMAc and lyophilized (Figure 5, blue bars) showed that Tp-Acr can be recycled, but a significant drop in yield of **1** was observed. We hypothesized that the loss in catalytic activity can be attributed to a collapse of the pores of the COF due to removal of DMAc. Performing a solvent exchange with MeOH and hexane prior to drying improved

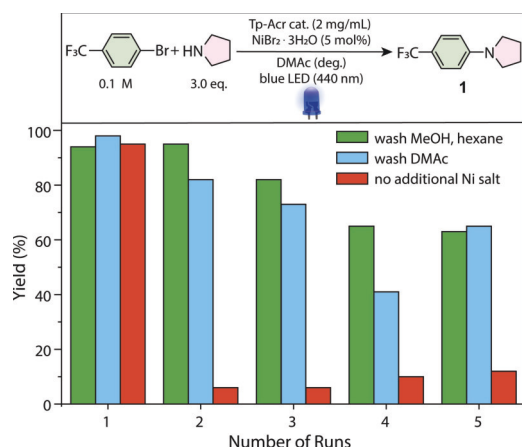


Figure 5. Reusability of Tp-Acr COF in the dual nickel/photocatalytic amination of 4-bromobenzotrifluoride and pyrrolidine (NMR yields determined by ^1H -NMR using 1,3,5-trimethoxybenzene as internal standard, DMAc anhydrous (3 mL), two blue LED [440 nm, 100%]).

the recyclability significantly (Figure 5, green bars). A catalytic activity of 60% is retained after 5 cycles of catalysis. To investigate, if the nickel salt can be reused, the recycling studies were also conducted without adding $\text{NiBr}_2 \cdot 3\text{H}_2\text{O}$ after the first run (Figure 4, red bars). A significant drop of efficiency after the first cycle was detected, meaning that addition of the nickel catalyst is needed in each cycle. Nevertheless, inductively coupled plasma optical emission spectrometry (ICP-OES) analysis revealed that 25% of the added nickel is deposited after the first reaction on the COF material that can drive the reaction in subsequent cycles with a yield of up to 10%.

In order to get an understanding of the nickel species adsorbed on the material, the Tp-Acr COF was analyzed by X-ray photoelectron spectroscopy (XPS) after the first and fifth cycle. Ni 2p core-level spectra (Figure S25d-e) of the recycled material confirmed the presence of nickel(II) species with a doublet at 856 eV and 874 eV after the catalysis. Although the crystallinity of the COF is lost due to the intense light irradiation, N 1s XPS core-level spectra show that both the aminic and pyridinic nitrogen species from the COF backbone remain unchanged during the catalysis (Figure S25a-c; S26). The structural integrity of the COF after the cross-coupling reaction was further confirmed by IR spectroscopy (Figure S27). From additional TEM analyses it is clear that the morphology of the materials stays intact throughout the catalysis (Figure S28).

Conclusion

In summary, we report the first successful preparation of crystalline and porous acridine-based COFs by following an acid-catalyzed Schiff base synthesis route using three different 1,3,5-triformylbenzene based linkers. The acridine-based conjugated COFs show light absorption over a broad range

of the visible light spectrum. Owing to these properties, the acridine-based COFs were applied for the first time in semi-heterogeneous metallaphotocatalytic C–N cross-couplings. Among the novel COFs, the fully β -ketoenamine tautomerized COF, Tp-Acr, showed a high catalytic activity both under blue and green light radiation for several aryl bromides, which is attributed to higher charge carrier separation efficiency as well as surface area. In addition, it was demonstrated that the COF could be recycled with a small drop in catalytic activity. To the best of our knowledge, this is the first example of a heterogenization of acridine photocatalysts via formation of crystalline organic frameworks.

Acknowledgements

Funded by the Deutsche Forschungsgemeinschaft (DFG, German Research Foundation) under Germany's Excellence Strategy—EXC 2008-390540038—UniSysCat and the German Ministry of Education and Research (BMBF) within the scope of the project PRODIGY (FKZ: 033RC024). The authors thank Christina Eichenauer for surface area measurements, Hüseyin Küçükkeçeci for the SEM analyses and Yasmine Ziouani for the TEM analyses. M.T. thanks the Einstein Center for Catalysis/Berlin International Graduate School for Natural Science and Engineering for funding. S.G., S.R. and B.P. gratefully acknowledge the Max-Planck Society and the International Max Planck Research School on Multiscale Bio-Systems for generous financial support. S.R. and B.P. acknowledge financial support by a Liebig Fellowship of the German Chemical Industry Fund (Fonds der Chemischen Industrie, FCI). Open Access funding enabled and organized by Projekt DEAL.

Conflict of Interest

The authors declare no conflicts.

Data Availability Statement

The data that support the findings of this study are available from the corresponding author upon reasonable request.

Keywords: Acridine • C–N Cross-Coupling • Catalysis • Covalent Organic Frameworks • Photoredox

- [1] X. Feng, X. Ding, D. Jiang, *Chem. Soc. Rev.* **2012**, *41*, 6010–6022.
- [2] J. W. Colson, W. R. Dichtel, *Nat. Chem.* **2013**, *5*, 453–465.
- [3] C. S. Diercks, O. M. Yaghi, *Science* **2017**, *355*, eaal1585.
- [4] S. Kandambeth, K. Dey, R. Banerjee, *J. Am. Chem. Soc.* **2019**, *141*, 1807–1822.
- [5] K. Geng, T. He, R. Liu, K. T. Tan, Z. Li, S. Tao, Y. Gong, Q. Jiang, D. Jiang, *Chem. Rev.* **2020**, *120*, 8814–8933.
- [6] Y. Jin, Y. Hu, M. Ortiz, S. Huang, Y. Ge, W. Zhang, *Chem. Soc. Rev.* **2020**, *49*, 4637–4666.

- [7] S. Y. Ding, W. Wang, *Chem. Soc. Rev.* **2013**, 42, 548–568.
- [8] P. J. Waller, F. Gándara, O. M. Yaghi, *Acc. Chem. Res.* **2015**, 48, 3053–3063.
- [9] S. Karak, S. Kandambeth, B. P. Biswal, H. S. Sasmal, S. Kumar, P. Pachfule, R. Banerjee, *J. Am. Chem. Soc.* **2017**, 139, 1856–1862.
- [10] Y. Jin, Y. Hu, W. Zhang, *Nat. Chem. Rev.* **2017**, 1, 0056.
- [11] O. Yahiaoui, A. N. Fitch, F. Hoffmann, M. Fröba, A. Thomas, J. Roeser, *J. Am. Chem. Soc.* **2018**, 140, 5330–5333.
- [12] A. Acharjya, P. Pachfule, J. Roeser, F. J. Schmitt, A. Thomas, *Angew. Chem. Int. Ed.* **2019**, 58, 14865–14870; *Angew. Chem.* **2019**, 131, 15007–15012.
- [13] F. Haase, B. V. Lotsch, *Chem. Soc. Rev.* **2020**, 49, 8469–8500.
- [14] S. S. Han, H. Furukawa, O. M. Yaghi, W. A. Goddard, *J. Am. Chem. Soc.* **2008**, 130, 11580–11581.
- [15] Z. Wang, S. Zhang, Y. Chen, Z. Zhang, S. Ma, *Chem. Soc. Rev.* **2020**, 49, 708–735.
- [16] D. D. Medina, T. Sick, T. Bein, *Adv. Energy Mater.* **2017**, 7, 1700387.
- [17] J. Guo, D. Jiang, *ACS Cent. Sci.* **2020**, 6, 869–879.
- [18] Y. Hu, L. J. Wayment, C. Haslam, X. Yang, S. Lee, Y. Jin, W. Zhang, *EnergyChem* **2021**, 3, 100048.
- [19] X. Zhao, P. Pachfule, A. Thomas, *Chem. Soc. Rev.* **2021**, 50, 6871.
- [20] M. S. Lohse, T. Bein, *Adv. Funct. Mater.* **2018**, 28, 1705553.
- [21] B. Liu, H. Sun, J. W. Lee, J. Yang, J. Wang, Y. Li, B. Li, M. Xu, Q. Liao, W. Zhang, D. Han, L. Niu, H. Meng, B. J. Kim, X. Guo, *Energy Environ. Sci.* **2021**, 14, 4499–4507.
- [22] N. Huang, P. Wang, D. Jiang, *Nat. Rev. Mater.* **2016**, 1, 16068.
- [23] S. Kandambeth, A. Mallick, B. Lukose, M. V. Mane, T. Heine, R. Banerjee, *J. Am. Chem. Soc.* **2012**, 134, 19524–19527.
- [24] S. Gisbertz, B. Pieber, *ChemPhotoChem* **2020**, 4, 456–475.
- [25] P. F. Wei, M. Z. Qi, Z. P. Wang, S. Y. Ding, W. Yu, Q. Liu, L. K. Wang, H. Z. Wang, W. K. An, W. Wang, *J. Am. Chem. Soc.* **2018**, 140, 4623–4631.
- [26] Y. Nailwal, A. D. D. Wananke, M. A. Addicoat, S. K. Pal, *Macromolecules* **2021**, 54, 6595–6604.
- [27] Y. Zhi, Z. Li, X. Feng, H. Xia, Y. Zhang, Z. Shi, Y. Mu, X. Liu, *J. Mater. Chem. A* **2017**, 5, 22933–22938.
- [28] W. Liu, Q. Su, P. Ju, B. Guo, H. Zhou, G. Li, Q. Wu, *ChemSusChem* **2017**, 10, 664–669.
- [29] J. Yuan, Q. Xia, W. Zhu, C. Wu, B. Wang, B. Liu, X. Yang, Y. Xu, H. Xu, *ChemPhotoChem* **2020**, 4, 445–450.
- [30] S. Liu, W. Pan, S. Wu, X. Bu, S. Xin, J. Yu, H. Xu, X. Yang, *Green Chem.* **2019**, 21, 2905–2910.
- [31] H. Chen, W. Liu, A. Laemont, C. Krishnaraj, X. Feng, F. Rohman, M. Meledina, Q. Zhang, R. Van Deun, K. Leus, P. Van Der Voort, *Angew. Chem.* **2021**, 133, 10915–10922.
- [32] W. Dong, Y. Yang, Y. Xiang, S. Wang, P. Wang, J. Hu, L. Rao, H. Chen, *Green Chem.* **2021**, 23, 5797–5805.
- [33] D. G. Brown, J. Boström, *J. Med. Chem.* **2016**, 59, 4443–4458.
- [34] S. Gisbertz, S. Reischauer, B. Pieber, *Nat. Catal.* **2020**, 3, 611–620.
- [35] S. Reischauer, V. Strauss, B. Pieber, *ACS Catal.* **2020**, 10, 13269–13274.
- [36] P. Pachfule, A. Acharjya, J. Roeser, R. P. Sivasankaran, M. Y. Ye, A. Brückner, J. Schmidt, A. Thomas, *Chem. Sci.* **2019**, 10, 8316–8322.
- [37] S. Lin, C. S. Diercks, Y. B. Zhang, N. Kornienko, E. M. Nichols, Y. Zhao, A. R. Paris, D. Kim, P. Yang, O. M. Yaghi, C. J. Chang, *Science* **2015**, 349, 1208–1213.
- [38] D. Bessinger, L. Ascherl, F. Auras, T. Bein, *J. Am. Chem. Soc.* **2017**, 139, 12035–12042.
- [39] W. E. Ford, M. A. J. Rodgers, *J. Photochem. Photobiol. A* **1991**, 59, 73–80.
- [40] T. T. Eisenhart, J. L. Dempsey, *J. Am. Chem. Soc.* **2014**, 136, 12221–12224.
- [41] J. Fang, T. Debnath, S. Bhattacharyya, M. Döblinger, J. Feldmann, J. K. Stolarczyk, *Nat. Commun.* **2020**, 11, 5179.
- [42] V. T. Nguyen, V. D. Nguyen, G. C. Haug, H. T. Dang, S. Jin, Z. Li, C. Flores-Hansen, B. S. Benavides, H. D. Arman, O. V. Larionov, *ACS Catal.* **2019**, 9, 9485–9498.
- [43] V. T. Nguyen, V. D. Nguyen, G. C. Haug, N. T. H. Vuong, H. T. Dang, H. D. Arman, O. V. Larionov, *Angew. Chem. Int. Ed.* **2020**, 59, 7921–7927; *Angew. Chem.* **2020**, 132, 7995–8001.
- [44] H. T. Dang, G. C. Haug, V. T. Nguyen, N. T. H. Vuong, V. D. Nguyen, H. D. Arman, O. V. Larionov, *ACS Catal.* **2020**, 10, 11448–11457.
- [45] D. Rădulescu, G. Ostrogovich, *Chem. Ber.* **1931**, 64, 2233–2240.
- [46] D. H. O'Donovan, B. Kelly, E. Diez-Cecilia, M. Kitson, I. Rozas, *New J. Chem.* **2013**, 37, 2408–2418.
- [47] A. Albert, *J. Chem. Soc.* **1948**, 1225–1230.
- [48] H. Wang, C. Qian, J. Liu, Y. Zeng, D. Wang, W. Zhou, L. Gu, H. Wu, G. Liu, Y. Zhao, *J. Am. Chem. Soc.* **2020**, 142, 4862–4871.
- [49] S. T. Emmerling, R. Schuldt, S. Bette, L. Yao, R. E. Dinnebier, J. Kästner, B. V. Lotsch, *J. Am. Chem. Soc.* **2021**, 143, 15711–15722.
- [50] C. Zhu, H. Yue, J. Jia, M. Rueping, *Angew. Chem. Int. Ed.* **2021**, 60, 17810–17831; *Angew. Chem.* **2021**, 133, 17954–17975.
- [51] M. A. Khayum, S. Kandambeth, S. Mitra, S. B. Nair, A. Das, S. S. Nagane, R. Mukherjee, R. Banerjee, *Angew. Chem. Int. Ed.* **2016**, 55, 15604–15608; *Angew. Chem.* **2016**, 128, 15833–15837.
- [52] N. Keller, M. Calik, D. Sharapa, H. R. Soni, P. M. Zehetmaier, S. Rager, F. Auras, A. C. Jakowetz, A. Görling, T. Clark, T. Bein, *J. Am. Chem. Soc.* **2018**, 140, 16544–16552.
- [53] J. Zhang, G. Zhang, X. Chen, S. Lin, L. Möhlmann, G. Doléga, G. Lipner, M. Antonietti, S. Blechert, X. Wang, *Angew. Chem. Int. Ed.* **2012**, 51, 3183–3187; *Angew. Chem.* **2012**, 124, 3237–3241.
- [54] D. Hollmann, M. Karnahl, S. Tschierlei, K. Kailasam, M. Schneider, J. Radnik, K. Grabow, U. Bentrup, H. Junge, M. Beller, S. Lochbrunner, A. Thomas, A. Brückner, *Chem. Mater.* **2014**, 26, 1727–1733.
- [55] C. H. Lim, M. Kudisch, B. Liu, G. M. Miyake, *J. Am. Chem. Soc.* **2018**, 140, 7667–7673.
- [56] E. B. Corcoran, M. T. Pirnot, S. Lin, S. D. Dreher, D. A. Dirocco, I. W. Davies, S. L. Buchwald, D. W. C. Macmillan, *Science* **2016**, 353, 279–283.
- [57] I. Ghosh, J. Khamrai, A. Savateev, N. Shlapakov, M. Antonietti, B. König, *Science* **2019**, 365, 360–366.
- [58] Y. Y. Liu, D. Liang, L. Q. Lu, W. J. Xiao, *Chem. Commun.* **2019**, 55, 4853–4856.

Manuscript received: December 28, 2021
 Accepted manuscript online: February 21, 2022
 Version of record online: March 23, 2022



Supporting Information

Acridine-Functionalized Covalent Organic Frameworks (COFs) as Photocatalysts for Metallaphotocatalytic C–N Cross-Coupling

M. Traxler, S. Gisbertz, P. Pachfule, J. Schmidt, J. Roeser, S. Reischauer, J. Rabeah, B. Pieber, A. Thomas**

Table of Contents

Table of Contents	2
S1. General Remarks	3
S2. Setup for photochemical reactions	6
S3. Synthesis of organic linkers and COFs	8
S3.1 Synthesis of the organic linkers	8
S3.2 Synthesis of covalent organic frameworks (COFs)	12
S4. Structure modeling and atomic coordinates of COFs	13
S5. Characterization of COFs.....	20
S5.1 FT-IR results of Tp-Acr, DHTA-Acr and HTA-Acr COFs	20
S5.2 Pore size distribution for COFs.....	22
S5.3 SEM & TEM analysis of Tp-Acr, DHTA-Acr and HTA-Acr COFs.....	23
S5.4 Chemical and thermal stability of Tp-Acr, DHTA-Acr and HTA-Acr COFs	24
S5.5 UV-vis of Tp-Acr, DHTA-Acr and HTA-Acr COFs.....	25
S5.6 Photoluminescence measurements and fluorescence life-time of Tp-Acr, DHTA-Acr and HTA-Acr COFs	26
S5.7 EPR-results of Tp-Acr, DHTA-Acr and HTA-Acr COFs	27
S6. Synthesis and Characterization of Tp-DAA COF ^[6]	28
S7. Synthesis of model compound (SA-Acr)	32
S8. Photocatalytic reaction optimization.....	33
S8.1 General experimental procedure for screening experiments.....	33
S8.2 Screening of Acridine-COFs.....	34
S8.3 Control studies	34
S9. Photocatalysis - recycling studies	35
S9.1 Analysis of recycled Tp-Acr COF	38
S10. Scope and limitations	40
S11. References	45
S12. Author Contributions	46
S13. Copies of NMR spectra.....	47

S1. General Remarks

All air and moisture sensitive reactions were performed using standard Schlenk-line techniques under an atmosphere of argon. Substrates, reagents, and solvents were purchased from commercial suppliers and used without further purification. The precursors such as phloroglucinol (TCI, > 99 %), resorcinol (> 98.5 %), phenol (TCI, > 99 %), 1-chloro-3-nitrobenzene (TCI, > 99 %), 4-nitroaniline (Carl Roth, > 98.5 %), 2,6-diaminoanthraquinone (TCI, > 97 %) and salicylic aldehyde (Sigma Aldrich, 98 %) were purchased and used as received. Reactants and solvents were obtained from Sigma Aldrich ((2-biphenyl)dicyclohexylphosphine (CyJohnPhos, 97 %), 1,2-dimethoxyethane (DME, 99.5 %, anhydrous), tin (powder <150 μm , 99.5 %), mesitylene (1,3,5-trimethylbenzene, 98 %), 1,2-dichlorobenzene (*o*-DCB, 99 %, anhydrous), glycerol (99.5 %)), TCI (tris(dibenzylideneacetone)dipalladium(0) ($\text{Pd}_2(\text{dba})_3$, > 75 %), hexamethylenetetramine (HMTA, > 99 %)), ABCR (tripotassium phosphate (K_3PO_4 , 97 %), palladium (Pd/C, 10 % on activated charcoal), trifluoroacetic acid (TFA, 99.9 %), 1,4-dioxane (99.5 %)), Carl Roth (formic acid (> 98 %), hydrochloric acid (37 %), sulfuric acid (96 %)), Alphagaz (hydrogen gas (99.999 %)), Eurisotop (CDCl_3 (99.8 % $_d$), $\text{DMSO-}d_6$ (99.8 % $_d$)), Chemsolute (sodium hydroxide (NaOH, 99.5 %)), Fluka Analytical (sodium borohydride (> 99 %)) or Grüssing (1-butanol (*n*-BuOH, 99.5 %)). Powder X-ray diffraction data were collected on a Bruker D8 Advance diffractometer in reflection geometry operating with a Cu K_α anode ($\lambda = 1.54178 \text{ \AA}$) with a working voltage at 40 kV and a current of 40 mA. Samples were ground and mounted as loose powders onto a Si sample holder. PXRD patterns were collected from 2 to 60 2θ degrees with a step size of 0.02 degrees and an exposure time of 2 seconds per step. LED lamps for photocatalytic experiments were purchased from Kessil Lightning.^[1] ^1H -, ^{13}C -, and ^{19}F spectra were recorded on a Varian 400 spectrometer (400 MHz, Agilent), an AscendTM 400 spectrometer (400 MHz, cryoprobe, Bruker), a Varian 600 spectrometer (600 MHz, Agilent), a Bruker Avance II spectrometer (200 MHz, Bruker) and an Bruker Avance 400 spectrometer (400 MHz, Bruker) at 298 K, and are reported in ppm relative to the residual solvent peaks. Peaks are reported as: s = singlet, d = doublet, t = triplet, q = quartet, m = multiplet or unresolved, with coupling constants in Hz. $^{13}\text{C}\{^1\text{H}\}$ cross polarization magic angle spinning (CP/MAS) measurements were carried out using a Bruker range Avance 400 MHz Solid State spectrometer operating at 100.6 MHz and a Bruker 4 mm double resonance probe-head operating at a spinning rate of 10 kHz. Nitrogen sorption measurements were performed at 77 K using an Autosorb-iQ-MP from Quantachrome. Prior the analysis the samples were dried and

degassed at 150 °C for 12 h. Using the N₂ adsorption isotherms, the surface areas were calculated over a pressure range $0.05-0.1 = p/p_0$ using Brunauer-Emmett-Teller (BET) methods. The pore size distributions were calculated from the adsorption isotherms by Quenched Solid State Functional Theory (QSDFT) using N₂ sorption data collected at 77 K. We used the carbon cylindrical pore model for analyzing the distribution. Thermogravimetric analysis (TGA) measurements were carried out under nitrogen atmosphere on a Mettler Toledo TGA 1 Stare thermal instrument with a heating rate of 10 K min⁻¹. Solid state diffuse reflectance ultraviolet-visible spectroscopy (UV-vis) spectra have been collected on a Varian Cary 300 UV-Vis Spectrophotometer. UV-vis absorption spectra of COF suspensions were collected using a Shimadzu UV-1900. Fluorescence spectra were measured using a microplate reader (SpectraMax M5, Molecular Devices). Photoluminescence lifetime was measured using the time-correlated single photon counting technique (TCSPC, FluoTime 250, fluorescence lifetime spectrometer). The Fourier transform infrared spectroscopy (FTIR) analyses of the samples were carried on Varian 640IR spectrometer equipped with an ATR cell. The scanning electron microscope (SEM) analyses of COF samples were performed on a Zeiss Gemini SEM 500 scanning electron microscope. Transmission electron microscopy (TEM) analyses were performed on a FEI Tecnai G2 20 S-TWIN transmission electron microscope (FEI Company, Eindhoven, Netherlands) equipped with a LaB₆ source at 200 kV acceleration voltage. Images were recorded with a GATAN MS794 P CCD camera. X-Ray photoelectron spectra were measured on a K-Alpha™ + X-ray Photoelectron Spectrometer System (Thermo Scientific) with Hemispheric 180° dual-focus analyzer with 128-channel detector. The X-ray monochromator used micro focused Al-K α radiation. High resolution mass spectrometry (HR-MS) was performed on an LTQ Orbitrap XL spectrometer using electrospray ionization (ESI) or atmospheric pressure chemical ionization (APCI). Inductively coupled plasma - optical emission spectrometry (ICP-OES) was carried out using a Horiba Ultra 2 instrument equipped with a photomultiplier tube detection system. Analytical thin layer chromatography (TLC) was performed on pre-coated TLC-sheets, ALUGRAM Xtra SIL G/UV254 sheets (Macherey-Nagel) and visualized with 254 nm light or staining solutions followed by heating. Purification of final compounds was carried out by flash chromatography using Silica 60 M (0.04-0.063 mm) silica gel (Sigma Aldrich). Centrifugation was carried out using an Eppendorf 5430 centrifuge. Electron paramagnetic resonance (EPR) measurements in X-band (microwave frequency \approx 9.8 GHz) were performed at 300 K by a Bruker EMX CW-micro spectrometer equipped with an ER 4119HS-WI high-sensitivity optical resonator with a grid in the front side. The samples were illuminated by a 300 W Xe lamp with 420 nm cut-off filter (LOT Oriel). All

the samples were measured under the same conditions (microwave power: 6.99 mW, receiver gain: 1×10^4 , modulation frequency: 100 kHz, modulation amplitude: 3 G, Sweep time: 122.8 s). g values have been calculated from the resonance field B_0 and the resonance frequency ν using the resonance condition $h\nu = g\beta B_0$. The calibration of the g values was performed using DPPH (2,2-diphenyl-1-picrylhydrazyl) ($g = 2.0036 \pm 0.00004$).

S2. Setup for photochemical reactions

Photochemical experiments involving visible light irradiation were carried out using Kessil PR160L-440 (440nm, blue light) or Kessil PR160L-525 (525 nm, green light) LED lamps with the respective power settings.^[1] One or two lamps were used, depending on the required light intensity to irradiate reaction vessels located on a stirring plate (lamp-vessel distance: 4.5 cm; stirring speed: 800 rpm, Figure S2). To avoid heating of the reaction mixture, fans were used for cooling.

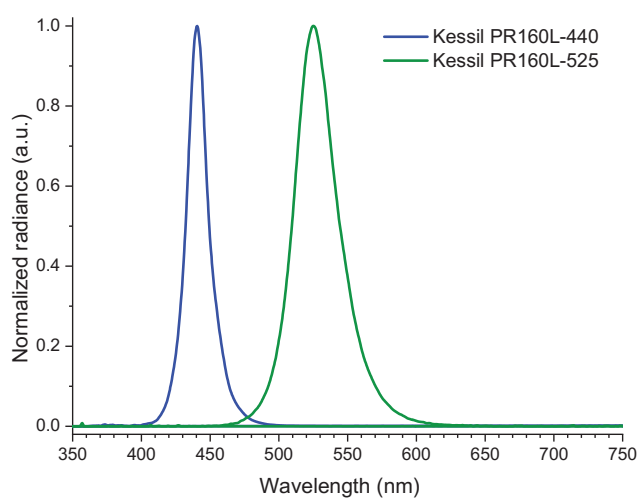


Figure S 1. Emission spectra of Kessil PR160L-400 (blue) and Kessil PR160L-525 (green).

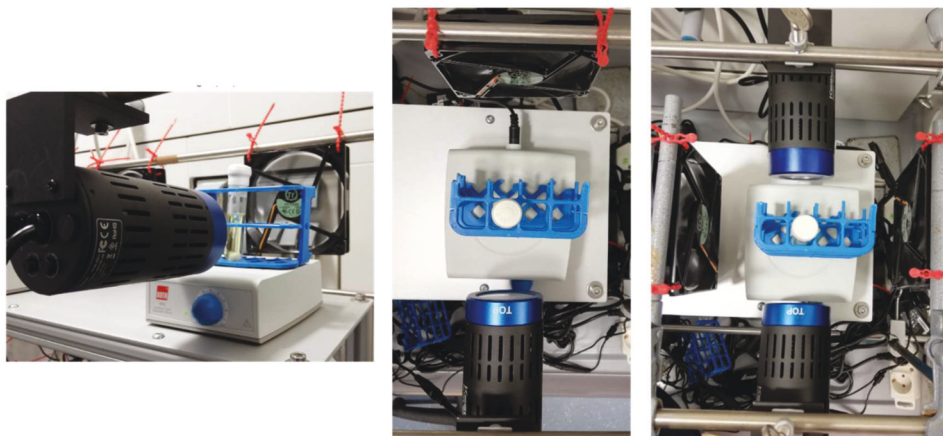


Figure S 2. Configuration of the experimental setup using one or two LED lamps.

Experiments using red light were carried out using a Kessil H160 Tuna Flora LED in “red” mode (Figure S3). Two sealed reaction vessels were placed between two lamps on a stirring plate (4.5 cm distance from each lamp). To avoid heating of the reaction mixture, a fan was used for cooling. All reactions were performed with maximum stirring speed.

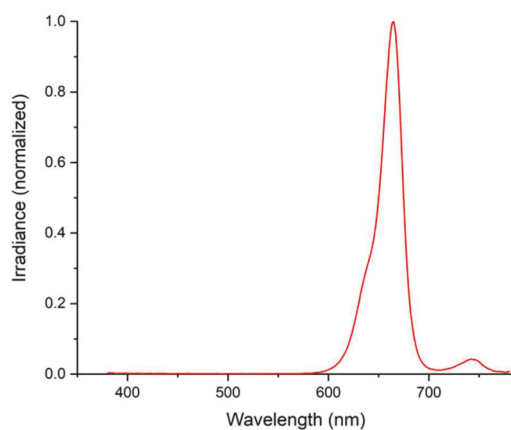
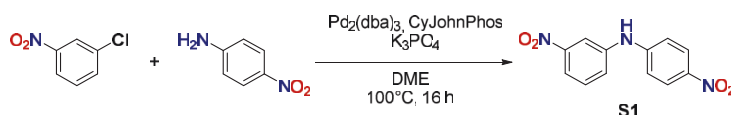


Figure S 3 . Emission spectra of the Kessil H160 Tuna Flora LED in “red” mode.

S3. Synthesis of organic linkers and COFs

S3.1 Synthesis of the organic linkers

Synthesis of 2,6-diaminoacridine:

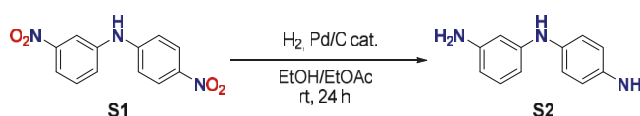


Scheme S 1. Synthesis of 3-nitro-*N*-(4-nitrophenyl)aniline (S1) via Buchwald-Hartwig coupling.

3-nitro-*N*-(4-nitrophenyl)aniline (S1): To a flame dried and three times evacuated and backfilled Schlenk flask were under argon counterflow 206 mg (0.22 mmol, 3 mol%) of $\text{Pd}_2(\text{dba})_3$ and 80 mg (2-biphenyl)dicyclohexylphosphine (CyJohnPhos, 0.22 mmol, 3 mol%) added. 15 mL of anhydrous 1,2-dimethoxyethane (DME) were added and the resulting suspension was stirred for 5 min at room temperature. Subsequently, 1.18 g (7.5 mmol, 1.0 eq.) of 1-chloro-3-nitrobenzene, 1.03 g (7.5 mmol, 1.0 eq.) of 4-nitroaniline and 2.23 g (10.5 mmol, 1.4 eq.) of K_3PO_4 were added and the mixture was heated to 100°C for 24 h while stirring was maintained. After cooling to room temperature, the suspension was diluted with 300 mL of $\text{Et}_2\text{O}/\text{EtOAc}$ (1:1), filtered through Celite and concentrated using the rotary evaporator. The crude material was purified by column chromatography on silica gel using 30 % EtOAc in cyclohexane to get the product as an orange powder (1.85 g, 95%).

^1H NMR (400 MHz, $\text{DMSO}-d_6$) δ 9.67 (s, 1H), 8.16 (d, $J = 9.2$ Hz, 2H), 7.86 (ddd, $J = 7.8, 2.2, 1.2$ Hz, 1H), 7.68 (ddd, $J = 8.1, 2.1, 1.2$ Hz, 1H), 7.63 (t, $J = 8.0$ Hz, 1H), 7.21 (d, $J = 9.3$ Hz, 2H). ^{13}C NMR (101 MHz, $\text{DMSO}-d_6$) δ 149.13, 148.66, 141.91, 139.37, 130.90, 126.10, 125.40, 116.86, 114.83, 113.41.

These data are in full agreement with those previously published in the literature.^[2]



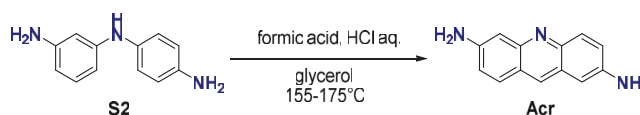
Scheme S 2. Synthesis of 3-(4-aminoanilino)aniline (S2) from 3-nitro-*N*-(4-nitrophenyl)aniline (S1).

3-(4-aminoanilino)aniline (S2): A suspension of 1.66 g (6.4 mmol) of 3-nitro-*N*-(4-nitrophenyl)aniline (S1), 332 mg (0.31 mmol, 4.9 mol%) of Pd/C (10 wt% Pd), 200 mL EtOH

and 100 mL EtOAc were degassed for 15 min using an argon purge. Subsequently, the suspension was degassed for 10 min using and H₂ purge and thereafter stirred for 24 h under hydrogen atmosphere. The catalyst was removed by filtration through Celite and the solvent was concentrated under vacuum and dried at 65 °C under high vacuum to give a dark brown solid (1.23 g, 96 %).

¹H NMR (200 MHz, DMSO-*d*₆) δ 7.11 (s, 1H), 6.83 – 6.68 (m, 3H), 6.51 (d, *J* = 8.6 Hz, 2H), 6.06 (t, *J* = 2.0 Hz, 1H), 5.99 (ddd, *J* = 7.9, 2.1, 0.8 Hz, 1H), 5.88 (ddd, *J* = 7.8, 2.0, 0.9 Hz, 1H), 4.74 (bs, 4H). ¹³C NMR (50 MHz, DMSO-*d*₆) δ 149.20, 147.28, 143.21, 132.35, 129.14, 122.39, 114.69, 104.20, 103.03, 99.56.

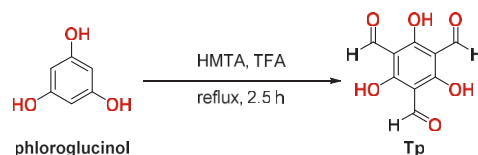
These data are in full agreement with those previously published in the literature.^[2]



Scheme S 3. Synthesis of 2,6-diaminoacridine (Acr) from 3-(4-aminoanilino)aniline (S2).

2,6-diaminoacridine (Acr): To 1.23 g (6.1 mmol, 1.0 eq.) of 3-(4-aminoanilino)aniline (S2) were 4 mL glycerol, 235 µl (6.1 mmol, 1.0 eq.) of formic acid and 660 µl (7.9 mmol, 1.3 eq.) of 37 % aqueous HCl solution added. The reaction mixture was heated to 155 °C during 30 min, kept at this temperature for 30 min before heating it to 175 °C for another 30 min. After cooling to room temperature 2.5 mL of aqueous sulfuric acid (30 %_{w/v}) were added and the reaction was heated to 95 °C for 10 min. Subsequently, the reaction was diluted to 25 mL with H₂O and the reaction mixture was kept at 0 °C for 1 h. The precipitated acid sulfate of the compound was filtered off, washed with water (40 mL) and Et₂O (60 mL). The dark red powder was boiled in 10 mL of aqueous NaOH (1 M) to precipitate the 2,6-diaminoacridine. The dark brown compound was filtered and washed with ice cold water (60 mL) and cold Et₂O (10 mL) and dried under vacuum at 65 °C (407 mg, 32 %).

¹H NMR (400 MHz, DMSO-*d*₆) δ 8.35 – 8.24 (m, 1H), 7.67 (dd, *J* = 9.0, 2.9 Hz, 2H), 7.22 (dd, *J* = 9.2, 2.3 Hz, 1H), 6.99 (dd, *J* = 9.0, 2.0 Hz, 1H), 6.84 – 6.82 (m, 1H), 6.82 – 6.80 (m, 1H), 5.83 – 5.78 (m, 1H), 5.43 – 5.39 (m, 1H). ¹³C NMR (101 MHz, DMSO-*d*₆) δ 148.54, 148.07, 144.44, 144.07, 130.64, 128.51, 128.23, 125.84, 124.52, 121.45, 120.55, 103.65, 103.48. HR-ESI-MS [*M*+H⁺] (*m/z*): 210.1028 (th.: 210.1026).

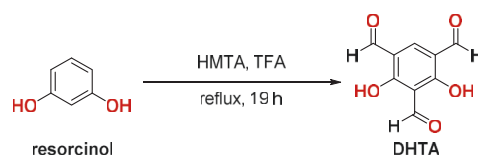
Synthesis of aldehyde linkers:

Scheme S 4. Synthesis of 1,3,5-triformylphloroglucino (Tp) from phloroglucinol.

1,3,5-triformylphloroglucino (Tp): To 10.0 g (80 mmol, 1.0 eq.) of phloroglucinol and 25.0 g (179 mmol, 2.2 eq.) of hexamethylenetetramine (HMTA) were 150 mL trifluoroacetic acid (TFA) added slowly under argon atmosphere at 0 °C. After complete addition, the suspension was heated at 100 °C for 2.5 h. The reaction mixture was cooled to around 50 °C and 240 mL of 3 M HCl were added, and the solution was heated at 100 °C for 1 h. After cooling to room temperature, the solution was filtered through Celite, extracted with 3x 200 mL dichloromethane, dried over magnesium sulfate, and filtered. Rotary evaporation of the solution afforded of an off-white powder. A pure sample was obtained by washing the solid sample with 10 mL of cold EtOH followed by sublimation under reduced pressure (2.76 g, 16 %).

^1H NMR (200 MHz, CDCl_3) δ 14.11 (s, 1H), 10.14 (s, 1H). ^{13}C NMR (50 MHz, CDCl_3) δ 192.17, 173.71, 103.05.

These data are in full agreement with those previously published in the literature.^[3]



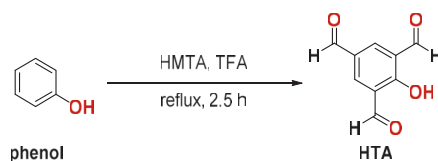
Scheme S 5. Synthesis of 2,4-dihydroxy-1,3,5-triformylcarbaldehyde (DHTA) from resorcinol.

2,4-dihydroxy-1,3,5-triformylcarbaldehyde (DHTA): To 3.6 g (33 mmol, 1.0 eq.) of resorcinol and 10.0 g (71 mmol, 2.2 eq.) of hexamethylenetetramine (HMTA) were 35 mL trifluoroacetic acid added slowly under argon atmosphere at 0 °C. After complete addition, the suspension was heated at 130 °C for 16 h and afterwards 3 h at 150 °C. The reaction mixture was cooled to around 100 °C and 55 mL of 3 M HCl were added, and the solution was heated at 105 °C for 30 min. After cooling to room temperature, the solution was filtered through Celite, extracted with 3x 50 mL dichloromethane, dried over magnesium sulfate, and filtered. Rotary evaporation of the solution afforded of an off-white powder. A pure sample was

obtained by washing the solid sample with 10 mL of cold EtOH followed by sublimation under reduced pressure (1.37 g, 21 %).

^1H NMR (400 MHz, $\text{DMSO-}d_6$) δ 10.26 (s, 1H), 10.09 (s, 2H), 8.40 (s, 1H). ^{13}C NMR (101 MHz, $\text{DMSO-}d_6$) δ 193.93, 189.97, 169.97, 140.66, 115.80, 109.95.

These data are in full agreement with those previously published in the literature.^[4]



Scheme S 6. Synthesis of 2-hydroxy-1,3,5-triformylcarbaldehyde (HTA) from phenol.

2-hydroxy-1,3,5-triformylcarbaldehyde (HTA): To 3.5 g (36.7 mmol, 1.0 eq.) of phenol and 10.1 g (71.3 mmol, 2.0 eq.) of hexamethylenetetramine (HMTA) were 50 mL trifluoroacetic acid added slowly under argon atmosphere at 0 °C. After complete addition, the suspension was heated at 120 °C for 20 h and afterwards 30 min at 150 °C. The reaction mixture was cooled to around 120 °C and 50 mL of 3 M HCl were added, and the solution was heated at 120 °C for 30 min. While cooling to room temperature a yellow precipitate was formed, which was filtered, washed with 20 mL of cold EtOH and dried under vacuo to give an off-white solid (3.64 g, 56%). Pure sample was obtained by sublimation of the crude material under reduced pressure.

^1H NMR (200 MHz, $\text{DMSO-}d_6$) δ 10.30 (s, 2H), 9.99 (s, 1H), 8.52 (s, 2H). ^1H NMR (200 MHz, CDCl_3) δ 12.16 (s, 1H), 10.32 (s, 2H), 10.01 (s, 1H), 8.51 (s, 2H). ^{13}C NMR (50 MHz, $\text{DMSO-}d_6$) δ 191.65, 190.72, 165.88, 137.31, 128.30, 124.09.

These data are in full agreement with those previously published in the literature.^[5]

S3.2 Synthesis of covalent organic frameworks (COFs)

Tp-Acr COF: A Pyrex tube (o.d. \times i.d. = 15 \times 10 mm² and length 15 cm) is charged with triformylphloroglucinol (**Tp**) (21 mg, 0.1 mmol), 2,6-diaminoacridine (**Acr**) (31.5 mg, 0.15 mmol), 1.5 mL of mesitylene, 1.5 mL of dioxane and 0.5 mL of 6 M aqueous acetic acid. This mixture was sonicated for 15 minutes in order to get a homogenous dispersion. The tube was then flash frozen at 77 K (liquid N₂ bath) and degassed by three freeze-pump-thaw cycles. The tube was sealed off and then heated at 120 °C for 3 days. A dark red colored precipitate was collected by filtration, washed with anhydrous acetone, methanol and cyclohexane before Soxhlet extraction with methanol. The powder collected was then solvent exchanged twice, with a cyclohexane and then dried at 120 °C to give a dark red colored powder (46 mg, 98 %).

DHTA-Acr COF: The synthesis of **DHTA-Acr COF** was carried out by utilizing the same protocol with a mixture of 2,4-dihydroxybenzene-1,3,5-tricarbaldehyde (**DHTA**) (19.4 mg, 0.1 mmol), 2,6-diaminoacridine (**Acr**) (31.5 mg, 0.15 mmol), 1.5 mL of mesitylene, 1.5 mL of dioxane and 0.5 mL of 6 M aqueous acetic acid. This mixture was sonicated for 15 minutes in order to get a homogenous dispersion. The tube was then flash frozen at 77 K (liquid N₂ bath) and degassed by three freeze-pump-thaw cycles. The tube was sealed off and then heated at 120 °C for 3 days. A dark red colored precipitate was collected by filtration, washed with anhydrous acetone, methanol and cyclohexane before Soxhlet extraction with methanol. The powder collected was then solvent exchanged twice, with a cyclohexane and then dried at 120 °C to give a dark red colored powder (46 mg, 99 %).

HTA-Acr COF: The synthesis of **HTA-Acr COF** was carried out by utilizing the same protocol with a mixture of 2-hydroxybenzene-1,3,5-tricarbaldehyde (**HTA**) (17.8 mg, 0.1 mmol), 2,6-diaminoacridine (**Acr**) (31.5 mg, 0.15 mmol), 1.5 mL of *n*-BuOH, 1.5 mL of anhydrous *o*-DCB and 0.5 mL of 6 M aqueous acetic acid. This mixture was sonicated for 15 minutes in order to get a homogenous dispersion. The tube was then flash frozen at 77 K (liquid N₂ bath) and degassed by three freeze-pump-thaw cycles. The tube was sealed off and then heated at 120 °C for 3 days. A dark red colored precipitate was collected by filtration, washed with anhydrous acetone, methanol and cyclohexane before Soxhlet extraction with methanol. The powder collected was then solvent exchanged twice, with a cyclohexane and then dried at 120 °C to give a dark red colored powder (37 mg, 84 %).

S4. Structure modeling and atomic coordinates of COFs

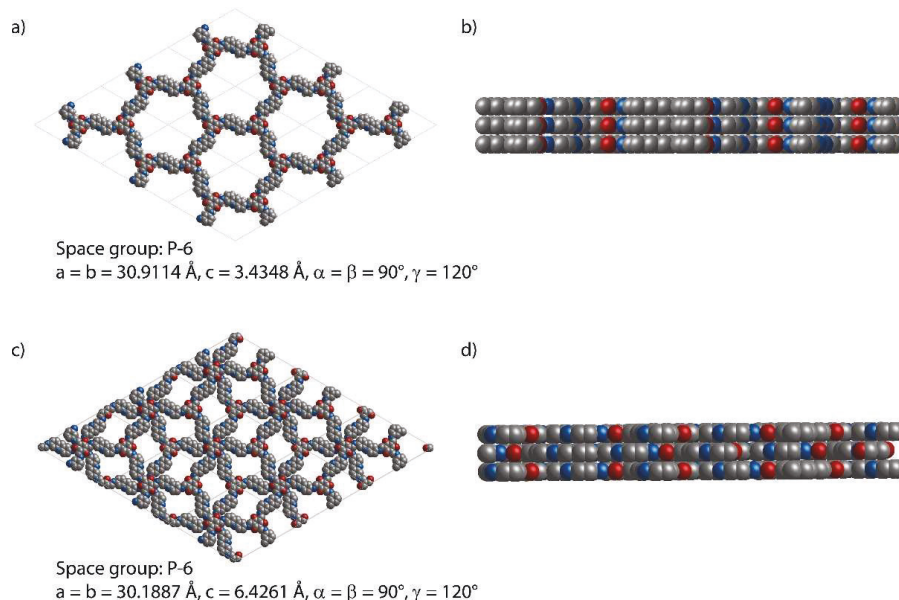


Figure S 4. Computationally determined structures of Tp-Acr. a) The theoretical structure of Tp-Acr with eclipsed (AA) stacking arrangement. b) Side view of Tp-Acr structure with eclipsed (AA) stacking arrangement. c) The theoretical structure of Tp-Acr with staggered (AB) stacking arrangement. d) Side view of Tp-Acr structure with staggered (AB) stacking arrangement.

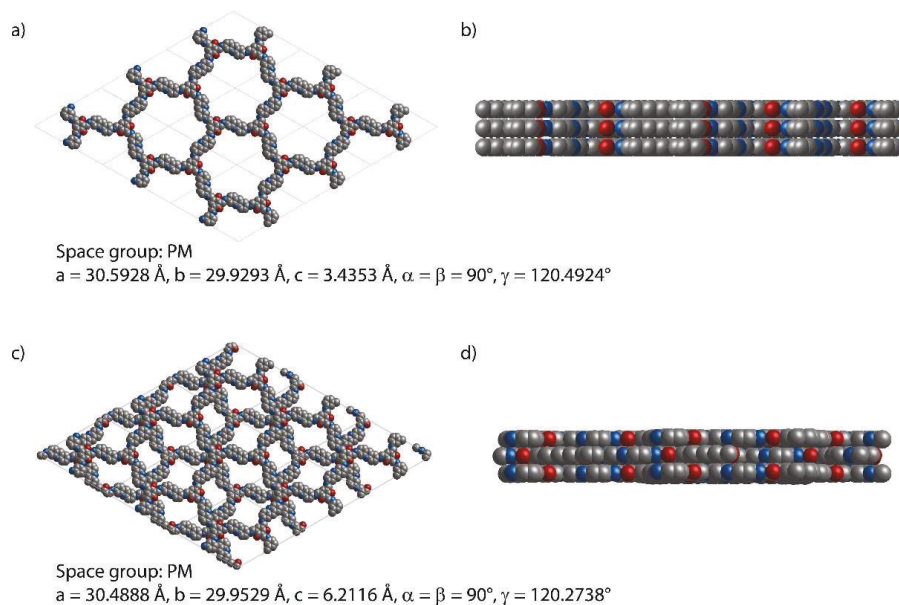


Figure S 5. Computationally determined structures of DHTA-Acr. a) The theoretical structure of DHTA-Acr with eclipsed (AA) stacking arrangement. b) Side view of DHTA-Acr structure with eclipsed (AA) stacking arrangement. c) The theoretical structure of DHTA-Acr with staggered (AB) stacking arrangement. d) Side view of DHTA-Acr structure with staggered (AB) stacking arrangement.

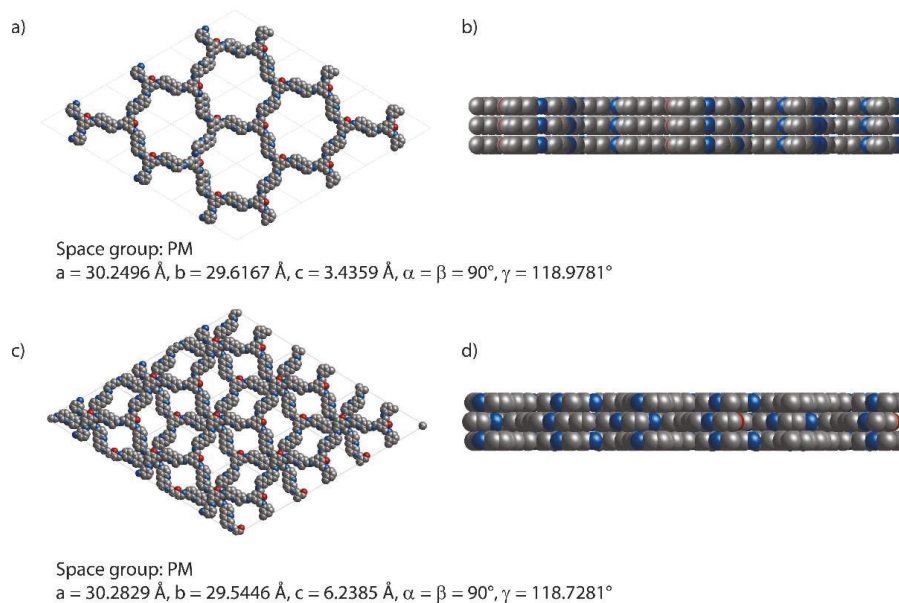


Figure S 6. Computationally determined structures of HTA-Acr. a) The theoretical structure of HTA-Acr with eclipsed (AA) stacking arrangement. b) Side view of HTA-Acr structure with eclipsed (AA) stacking arrangement. c) The theoretical structure of HTA-Acr with staggered (AB) stacking arrangement. d) Side view of HTA-Acr structure with staggered (AB) stacking arrangement.

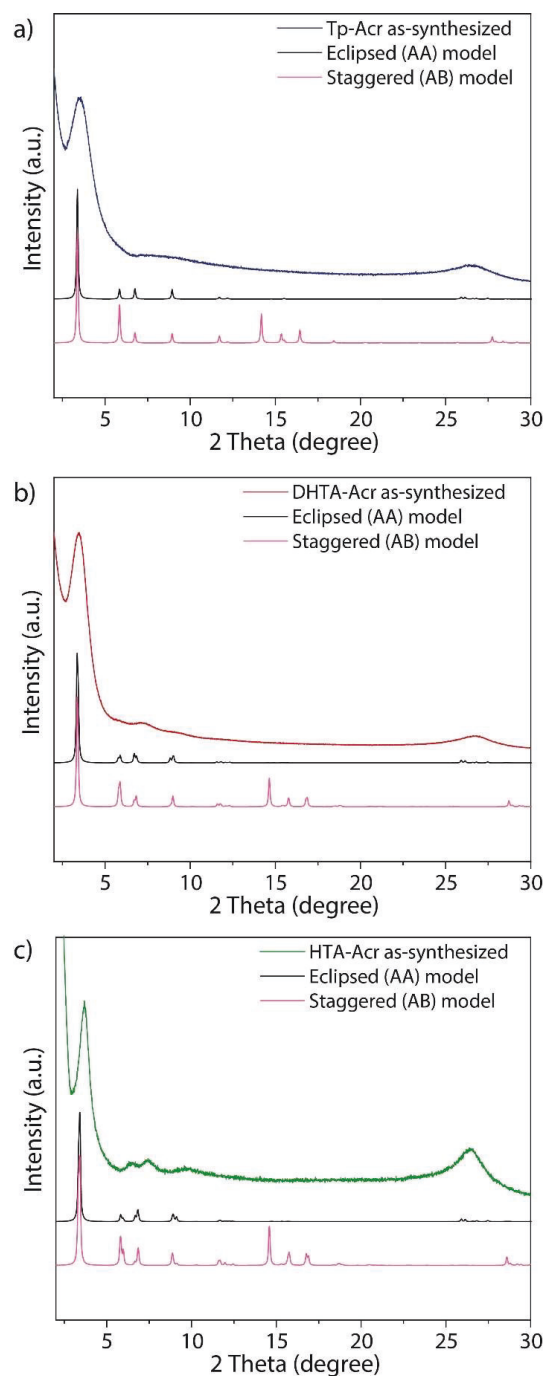


Figure S 7. Comparison between simulated and experimental PXRD patterns for a) Tp-Acr, b) DHTA-Acr and HTA-Acr COFs, showing a good match between the experimental diffractogram and the eclipsed stacking model (AA).

Table S 1. Fractional atomic coordinates for Tp-Acr COF.

Tp-Acr-COF				
Space group symmetry: P-6 (174)				
a = b = 30.9114 Å; c = 3.4348 Å				
$\alpha = \beta = 90^\circ$; $\gamma = 120^\circ$				
Atom name	Atom	x	y	z
H1	H	0.44644	0.40004	0
H2	H	0.46699	0.59166	0
H3	H	0.36561	0.40202	0
H4	H	0.32101	0.45088	0
C5	C	0.54847	0.44164	0
C6	C	0.60253	0.46881	0
C7	C	0.62804	0.52263	0
C8	C	0.6009	0.54886	0
H9	H	0.5268	0.40048	0
H10	H	0.62148	0.59027	0
H11	H	0.66942	0.54455	0
C12	C	0.44374	0.5506	0
C13	C	0.38973	0.52526	0
C14	C	0.36241	0.47142	0
C15	C	0.38778	0.44341	0
O16	O	0.27439	0.56395	0
N17	N	0.36115	0.55203	0
C18	C	0.30132	0.61027	0
C19	C	0.35822	0.63396	0
C20	C	0.38373	0.60706	0
C21	C	0.46926	0.52263	0
C22	C	0.44121	0.46874	0
N23	N	0.52124	0.5475	0
H24	H	0.42476	0.62902	0
H25	H	0.32187	0.52808	0
O26	O	0.72219	0.43631	0
N27	N	0.63293	0.44395	0
C28	C	0.69679	0.38986	0
C29	C	0.63972	0.36411	0
C30	C	0.61239	0.38919	0
C31	C	0.52111	0.46795	0
C32	C	0.54758	0.52186	0
C33	C	0.46752	0.44151	0
H34	H	0.57146	0.36585	0
H35	H	0.67198	0.46913	0

Table S 2. Fractional atomic coordinates for DHTA-Acr COF.

DHTA-Acr-COF				
Space group symmetry: PM (6)				
a = 30.5928; b = 29.9293 Å; c = 3.4353 Å				
$\alpha = \beta = 90^\circ$; $\gamma = 120.4924^\circ$				
Atom name	Atom	x	y	z
H1	H	0.44528	0.39443	0
H2	H	0.59584	0.04762	0
H3	H	0.96004	0.5596	0
H4	H	0.46471	0.58747	0
H5	H	0.36468	0.39517	0
H6	H	0.32011	0.44378	0
C7	C	0.54672	0.43811	0
C8	C	0.6004	0.46656	0
C9	C	0.62524	0.52108	0
C10	C	0.59794	0.54682	0
H11	H	0.5256	0.39633	0
H12	H	0.61804	0.5888	0
H13	H	0.66627	0.54396	0
C14	C	0.44169	0.54581	0
C15	C	0.38813	0.5196	0

C16	C	0.36118	0.46501	0
C17	C	0.38653	0.43715	0
O18	O	0.27334	0.55829	0
N19	N	0.35979	0.54633	0
C20	C	0.30106	0.60517	0
C21	C	0.35718	0.62886	0
C22	C	0.38241	0.60207	0
C23	C	0.46716	0.51805	0
C24	C	0.43958	0.46342	0
N25	N	0.5187	0.54393	0
H26	H	0.4231	0.62478	0
H27	H	0.32074	0.52207	0
O28	O	0.72453	0.4418	0
N29	N	0.63125	0.44252	0
C30	C	0.70007	0.39464	0
C31	C	0.64319	0.36637	0
C32	C	0.61315	0.39038	0
C33	C	0.51917	0.46399	0
C34	C	0.5451	0.51864	0
C35	C	0.46598	0.43647	0
H36	H	0.57265	0.36454	0
H37	H	0.66988	0.46875	0
H38	H	0.40194	0.87345	0
H39	H	0.59001	0.96127	0
H40	H	0.54012	0.86675	0
C41	C	0.55801	0.11073	0
C42	C	0.53324	0.13979	0
C43	C	0.47982	0.11263	0
C44	C	0.45189	0.05835	0
H45	H	0.5987	0.12888	0
H46	H	0.41085	0.03834	0
H47	H	0.45962	0.13364	0
C48	C	0.44269	0.89145	0
C49	C	0.467	0.86188	0
C50	C	0.52037	0.88822	0
C51	C	0.549	0.94214	0
O52	O	0.4337	0.70739	0
N53	N	0.44008	0.8058	0
C54	C	0.38769	0.68662	0
C55	C	0.36257	0.71853	0
C56	C	0.38863	0.77386	0
C57	C	0.47155	0.94584	0
C58	C	0.52485	0.97104	0
N59	N	0.44826	0.9743	0
H60	H	0.36531	0.79138	0
H61	H	0.4639	0.79072	0
H62	H	0.57559	0.29257	0
N63	N	0.56037	0.19604	0
C64	C	0.61638	0.31174	0
C65	C	0.63976	0.28168	0
C66	C	0.61202	0.22662	0
C67	C	0.53009	0.05646	0
C68	C	0.4768	0.03009	0
C69	C	0.55476	0.02804	0
H70	H	0.63436	0.20826	0
H71	H	0.53768	0.2127	0
H72	H	0.12572	0.53095	0
H73	H	0.04725	0.64078	0
H74	H	0.14005	0.68259	0
C75	C	0.89605	0.45624	0
C76	C	0.86758	0.40143	0
C77	C	0.89373	0.37401	0
C78	C	0.94653	0.39995	0
H79	H	0.87788	0.47909	0
H80	H	0.96579	0.37799	0
H81	H	0.873	0.33203	0
C82	C	0.11033	0.55629	0
C83	C	0.14131	0.61092	0
C84	C	0.11748	0.64067	0
C85	C	0.06457	0.61695	0
H86	H	0.29235	0.71675	0
N87	N	0.19627	0.63752	0

C88	C	0.30919	0.69272	0
C89	C	0.27767	0.6384	0
C90	C	0.22389	0.61323	0
C91	C	0.05753	0.5326	0
C92	C	0.03438	0.56288	0
N93	N	0.02871	0.48017	0
H94	H	0.20402	0.57162	0
H95	H	0.21443	0.67778	0
O96	O	0.71564	0.28134	0
N97	N	0.81276	0.37191	0
C98	C	0.69617	0.30807	0
C99	C	0.72796	0.36576	0
C100	C	0.77986	0.39347	0
C101	C	0.94937	0.48246	0
C102	C	0.9744	0.4539	0
C103	C	0.97836	0.53669	0
H104	H	0.79782	0.43508	0
H105	H	0.79792	0.3322	0

Table S 3. Fractional atomic coordinates for HTA-Acr COF.

HTA-Acr-COF				
Space group symmetry: PM (6)				
a = 30.2496; b = 29.6167 Å; c = 3.4359 Å				
$\alpha = \beta = 90^\circ$; $\gamma = 118.9781^\circ$				
Atom name	Atom	x	y	z
H1	H	0.45098	0.39971	0
H2	H	0.59571	0.04	0
H3	H	0.95459	0.56059	0
H4	H	0.46949	0.59409	0
H5	H	0.37111	0.4026	0
H6	H	0.32628	0.45239	0
C7	C	0.55152	0.44029	0
C8	C	0.60495	0.46675	0
C9	C	0.63017	0.52109	0
C10	C	0.60328	0.54843	0
H11	H	0.52994	0.39878	0
H12	H	0.62361	0.59022	0
H13	H	0.67106	0.5425	0
C14	C	0.44709	0.5526	0
C15	C	0.39364	0.52724	0
C16	C	0.36719	0.47292	0
C17	C	0.39268	0.44436	0
O18	O	0.27272	0.56071	0
N19	N	0.36451	0.55417	0
C20	C	0.29871	0.60746	0
C21	C	0.355	0.63263	0
C22	C	0.38396	0.60647	0
C23	C	0.47283	0.52397	0
C24	C	0.44544	0.46957	0
N25	N	0.52427	0.54853	0
H26	H	0.42446	0.63052	0
H27	H	0.32581	0.52992	0
H28	H	0.7183	0.42938	0
N29	N	0.63484	0.44053	0
C30	C	0.69738	0.38782	0
C31	C	0.644	0.36206	0
C32	C	0.61525	0.38817	0
C33	C	0.52452	0.46762	0
C34	C	0.55053	0.522	0
C35	C	0.47164	0.44156	0
H36	H	0.57486	0.36396	0
H37	H	0.67377	0.46457	0
H38	H	0.40098	0.87292	0
H39	H	0.5879	0.95154	0
H40	H	0.53624	0.85749	0
C41	C	0.55942	0.10646	0
C42	C	0.53513	0.13698	0

C43	C	0.48195	0.11177	0
C44	C	0.45366	0.05794	0
H45	H	0.59998	0.12342	0
H46	H	0.41279	0.03942	0
H47	H	0.4622	0.13401	0
C48	C	0.44144	0.88874	0
C49	C	0.46441	0.85698	0
C50	C	0.51752	0.88073	0
C51	C	0.54711	0.93434	0
H52	H	0.42223	0.70463	0
N53	N	0.4361	0.80117	0
C54	C	0.38166	0.68687	0
C55	C	0.35758	0.71758	0
C56	C	0.38464	0.77231	0
C57	C	0.47115	0.94259	0
C58	C	0.52415	0.9654	0
N59	N	0.44879	0.9728	0
H60	H	0.36233	0.79173	0
H61	H	0.45827	0.7832	0
H62	H	0.57618	0.2898	0
N63	N	0.56237	0.19289	0
C64	C	0.61681	0.3077	0
C65	C	0.64052	0.27707	0
C66	C	0.61378	0.22236	0
C67	C	0.53103	0.05243	0
C68	C	0.47793	0.02815	0
C69	C	0.55483	0.02213	0
H70	H	0.63646	0.20349	0
H71	H	0.53976	0.21042	0
H72	H	0.12359	0.53314	0
H73	H	0.04035	0.64186	0
H74	H	0.13304	0.68386	0
C75	C	0.89343	0.45747	0
C76	C	0.86667	0.40285	0
C77	C	0.89438	0.376	0
C78	C	0.94696	0.40221	0
H79	H	0.87401	0.47988	0
H80	H	0.9674	0.38066	0
H81	H	0.87503	0.33422	0
C82	C	0.1072	0.5583	0
C83	C	0.13675	0.61268	0
C84	C	0.11158	0.64212	0
C85	C	0.05872	0.61829	0
H86	H	0.28751	0.71855	0
N87	N	0.19154	0.63921	0
C88	C	0.30438	0.69375	0
C89	C	0.27358	0.6399	0
C90	C	0.22009	0.61492	0
C91	C	0.05453	0.53453	0
C92	C	0.02997	0.56443	0
N93	N	0.02722	0.48235	0
H94	H	0.20136	0.57351	0
H95	H	0.20896	0.67933	0
O96	O	0.71789	0.27792	0
N97	N	0.81212	0.37275	0
C98	C	0.69661	0.3038	0
C99	C	0.72559	0.36149	0
C100	C	0.77921	0.39193	0
C101	C	0.94661	0.48398	0
C102	C	0.97312	0.45589	0
C103	C	0.97404	0.53801	0
H104	H	0.79433	0.43324	0
H105	H	0.79884	0.33333	0

S5. Characterization of COFs

S5.1 FT-IR results of Tp-Acr, DHTA-Acr and HTA-Acr COFs

Fourier transform infrared (FT-IR) spectra show the disappearance of the vibration of the amino group of the 2,6-diaminoacridine linker at around 3400 cm^{-1} , and of the stretching vibration of C=O groups of the aldehyde linker ($1690\text{--}1640\text{ cm}^{-1}$). The bands of the newly formed C=O and C=C bonds were merged into one single peak at 1580 cm^{-1} for the Tp-Acr COF, at 1552 cm^{-1} for the DHTA-Acr COF and 1578 cm^{-1} for the HTA-Acr COF, respectively. Furthermore, the C-N stretching vibration appeared around 1270 cm^{-1} for all COFs. Distinctive spectral bands of the acridine linker at $\sim 800\text{ cm}^{-1}$ can be also found in the acridine COFs.

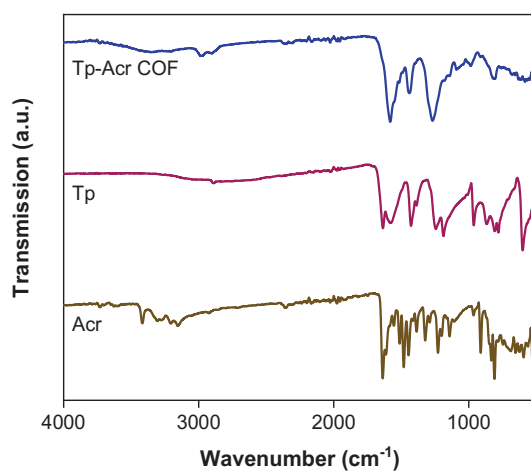


Figure S 8. FT-IR analyses of Tp-Acr COF in comparison with the corresponding aldehyde (Tp) and amine (Acr) showing the formation of the framework structure.

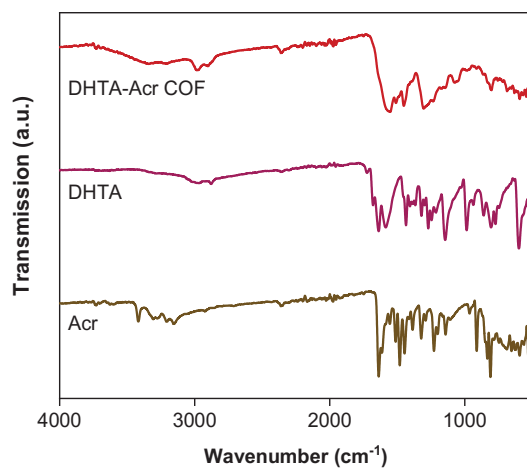


Figure S 9. FT-IR analyses of DHTA-Acr COF in comparison with the corresponding aldehyde (DHTA) and amine (Acr) showing the formation of the framework structure.

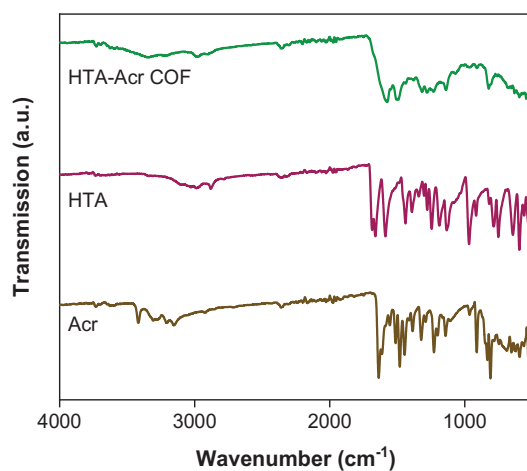


Figure S 10. FT-IR analyses of HTA-Acr COF in comparison with the corresponding aldehyde (HTA) and amine (Acr) showing the formation of the framework structure.

S5.2 Pore size distribution for COFs

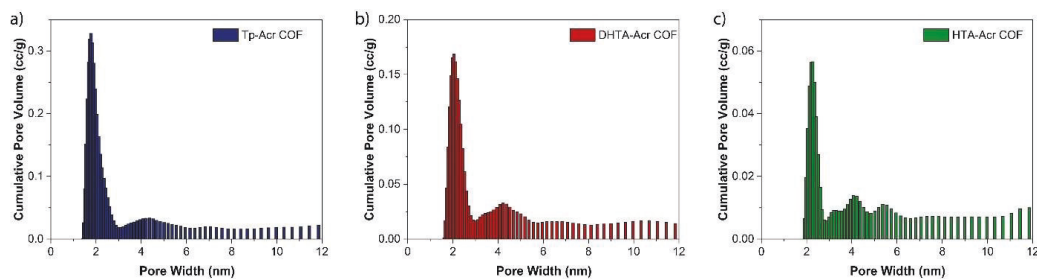


Figure S 11. Pore size distribution of (a) Tp-Acr, (b) DHTA-Acr and (c) HTA-Acr COFs, showing the pores distribution close to the ideal pore size calculated from simulated structures.

Tp-Acr COF:

Method = Quenched Solid State Functional Theory (QSDFT)

Model = N₂ at 77 K on carbon cylindrical pore (fitting error = 1.6%)

DHTA-Acr COF:

Method = Quenched Solid State Functional Theory (QSDFT)

Model = N₂ at 77 K on carbon cylindrical pore (fitting error = 3.0%)

HTA-Acr COF:

Method = Quenched Solid State Functional Theory (QSDFT)

Model = N₂ at 77 K on carbon cylindrical pore (fitting error = 3.1%)

S5.3 SEM & TEM analysis of Tp-Acr, DHTA-Acr and HTA-Acr COFs

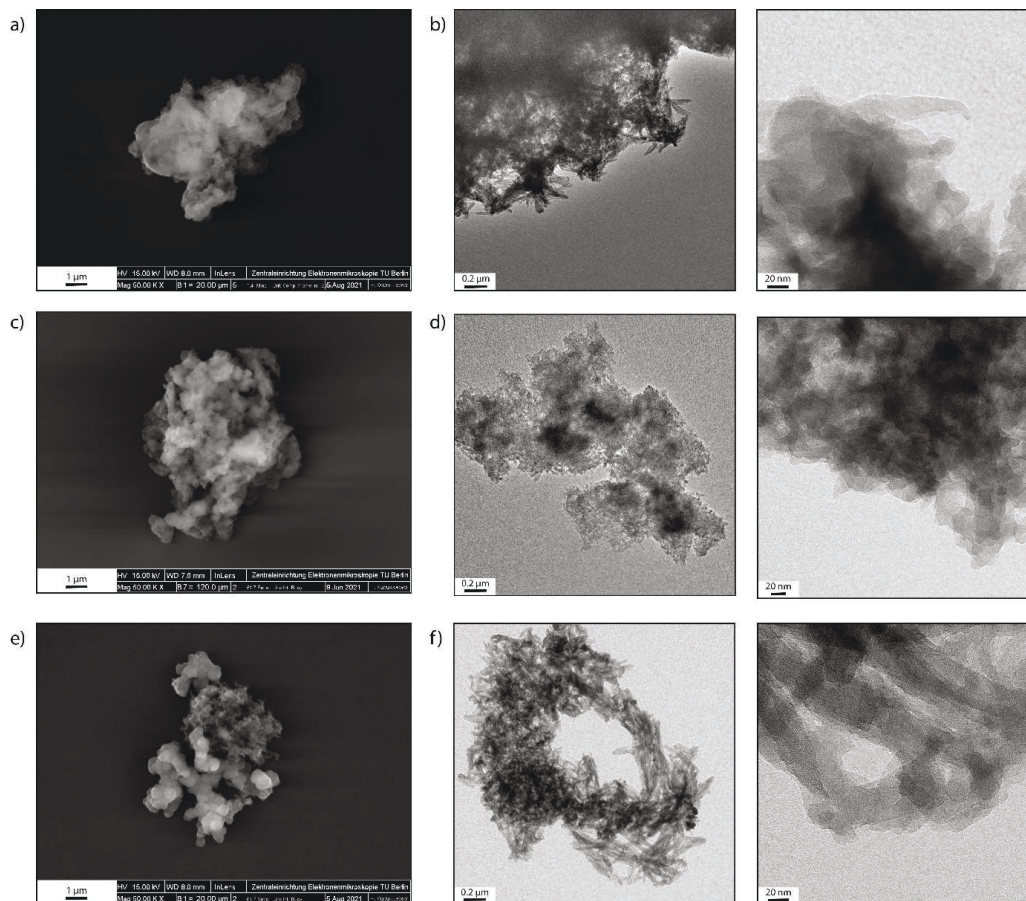


Figure S 12. SEM and TEM analyses of Tp-Acr, DHTA-Acr and HTA-Acr. (a, c, e) SEM images of Tp-Acr, DHTA-Acr and HTA-Acr COFs showing the flower like structures, respectively. (b, d, f) TEM images of Tp-Acr, DHTA-Acr and HTA-Acr COFs showing the morphology and the layered structure of the COF matrix, respectively.

S5.4 Chemical and thermal stability of Tp-Acr, DHTA-Acr and HTA-Acr COFs

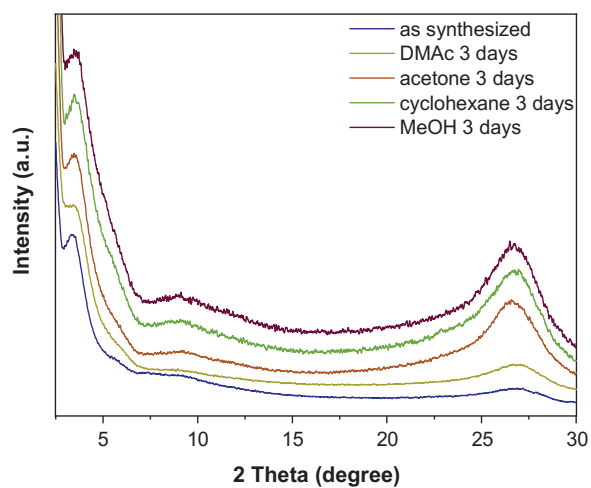


Figure S 13. Chemical stability of Tp-Acr. The PXRD profiles of the COF sample treated for 3 days in different solvents compared to the as-synthesized COF.

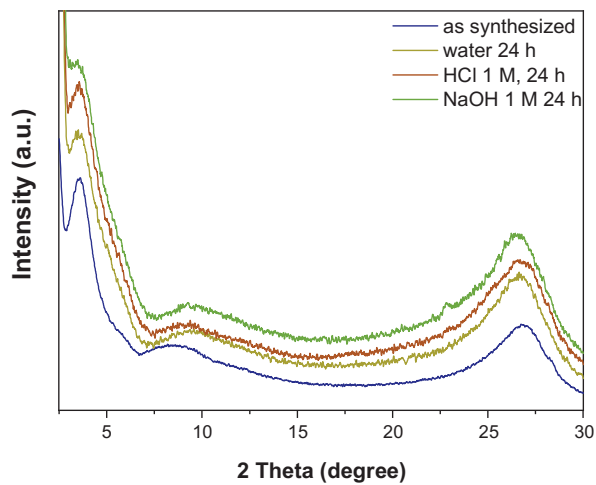


Figure S 14. Chemical stability of Tp-Acr. The PXRD profiles of the COF sample treated for 24 h in different aqueous neutral, acidic and alkaline conditions compared to the as-synthesized COF.

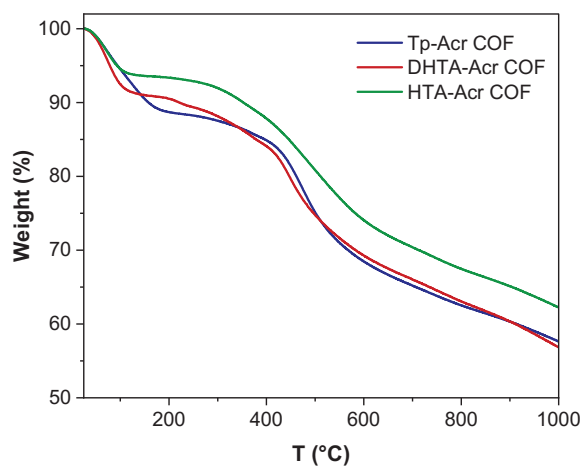


Figure S 15. Thermogravimetric analyses (TGA) for Tp-Acr, DHTA-Acr and HTA-Acr COFs, showing the thermal stability of the COFs below 300 °C, under nitrogen atmosphere.

S5.5 UV-vis of Tp-Acr, DHTA-Acr and HTA-Acr COFs

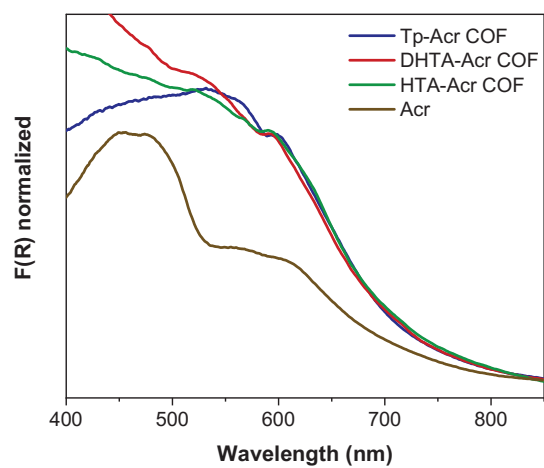


Figure S 16. UV-vis diffuse reflectance spectroscopy analysis of Tp-Acr, DHTA-Acr and HTA-Acr in comparison to 2,6-diaminoacridine (Acr).

S5.6 Photoluminescence measurements and fluorescence life-time of Tp-Acr, DHTA-Acr and HTA-Acr COFs

Preparation of the samples for luminescence studies:

0.5 mg of COF was dispersed in 10 ml dimethylacetamide by sonicating for 5 minutes at 40 °C. Prior the UV-vis and PL measurements the bigger particles were let to sediment to obtain a nearly clear solution. The clear COF dispersed solutions were used for the PL and steady-state time-resolved fluorescence decay measurements.

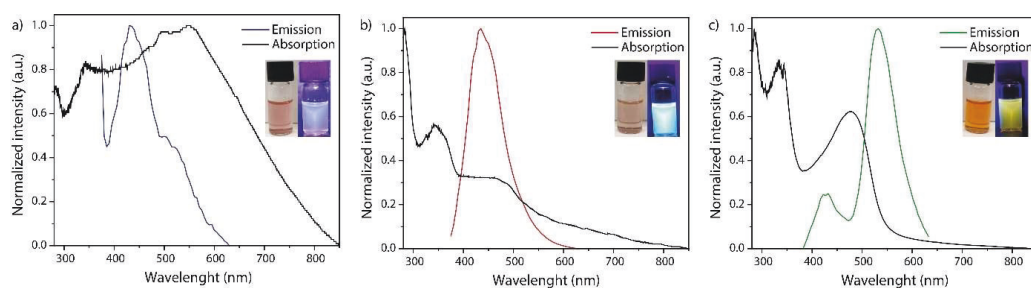


Figure S 17. Steady-state absorption and emission profiles of dispersed a) Tp-Acr, b) DHTA-Acr and c) HTA-Acr in dimethylacetamide. For the fluorescence measurements the samples were excited at a wavelength of 360 nm. Optical images at ambient light and upon excitation under a 365 nm UV-lamp is shown in every case.

Table S 4. Life-time decay components and amplified average life-time

COF	$\lambda_{exc.}$ (nm)	$\lambda_{col.}$ (nm)	a_1	τ_1 (ns)	a_2	τ_2 (ns)	τ_{av} (ns)
Tp-Acr	360	430	221	0.0212	6.02	5.26	0.16
DHTA-Acr	360	430	11.1	4.62			4.62
HTA-Acr	360	430	17.4	0.111	8.85	4.56	1.61

S5.7 EPR-results of Tp-Acr, DHTA-Acr and HTA-Acr COFs

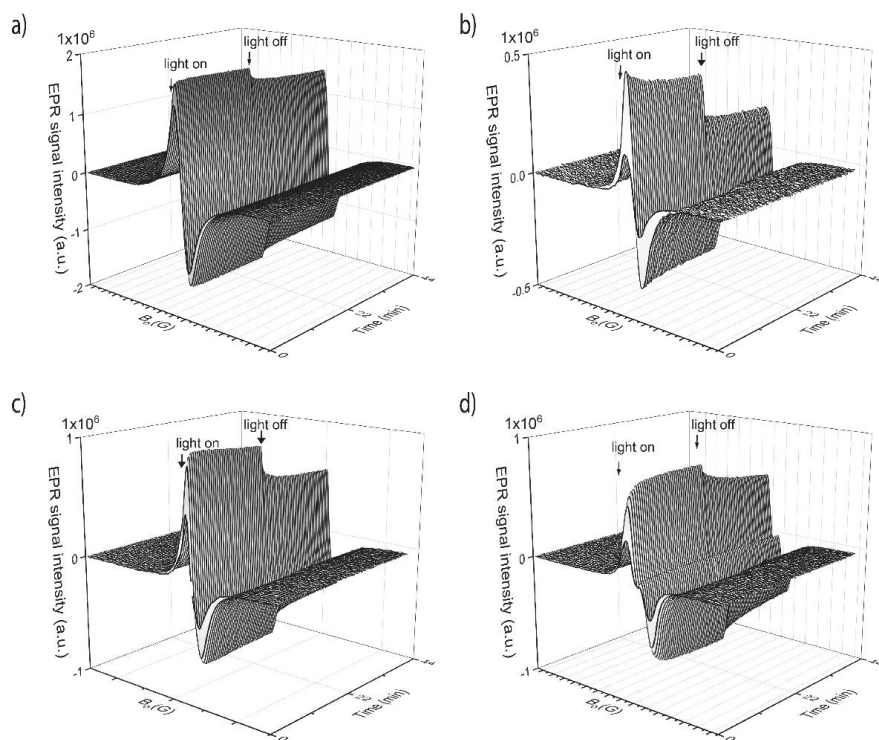
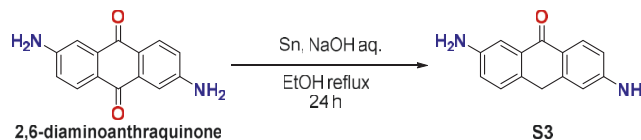


Figure S18. Time resolved EPR conduction band e^- signals of (a) Tp-Acr, (b) DHTA-Acr, (c) HTA-Acr and (d) Tp-DAA under dark condition (0 min) and during visible light irradiation (0.5-22 min) and after the light was switched off (22.5-44 min).

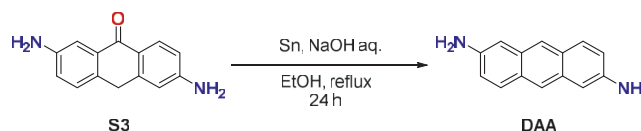
S6. Synthesis and Characterization of Tp-DAA COF^[6]

Scheme S 7. Synthesis of 2,6-diaminoanthrone (S3) from 2,6-diaminoanthraquinone.

2,6-diaminoanthrone (3): 2.50 g (10.5 mmol, 1.0 eq.) of 2,6-diaminoanthraquinone were combined with 7.47 g (63 mmol, 6.0 eq) of tin powder ($> 150\mu\text{m}$), 44 mL of 2.5 M aqueous NaOH and 50 mL of EtOH. The reaction was heated to reflux under argon atmosphere for 24 h, when the still hot reaction mixture was poured into 250 mL of H₂O and stirred for 20 min. The resulting precipitate was filtered and dried under vacuo to give the product as a yellow-brown solid (1.80g, 77 %).

¹H NMR (200 MHz, DMSO-*d*₆) δ 7.87 (d, J = 8.6 Hz, 1H), 7.33 (d, J = 2.4 Hz, 1H), 7.15 (d, J = 8.1 Hz, 1H), 6.84 (dd, J = 8.1, 2.5 Hz, 1H), 6.62 (dd, J = 8.7, 2.0 Hz, 1H), 6.53 (d, J = 1.5 Hz, 1H), 6.04 (s, 2H), 5.19 (s, 2H), 4.04 (s, 2H). ¹³C NMR (50 MHz, DMSO-*d*₆) δ 181.70, 152.91, 147.19, 143.63, 132.46, 128.90, 128.86, 127.72, 120.68, 119.06, 113.27, 110.56, 109.78, 30.97.

These data are in full agreement with those previously published in the literature.^[7]



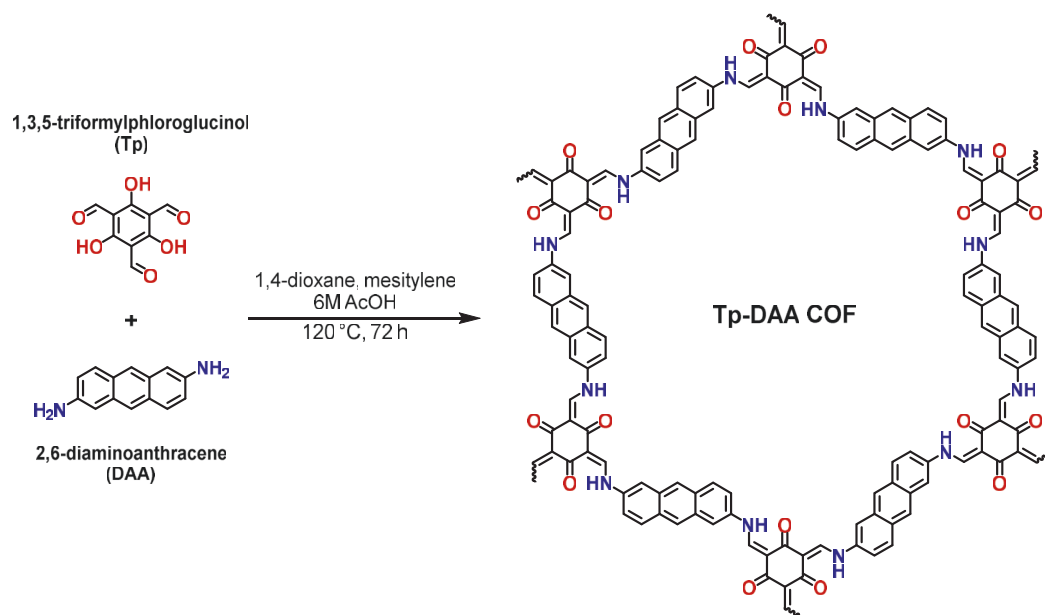
Scheme S 8. Synthesis of 2,6-diaminoanthracene from 2,6-diaminoanthrone (S3).

2,6-diaminoanthracene (DAA): 1.80 g (8 mmol, 1.0 eq.) of 2,6-diaminoanthrone (S3) were combined with 2.43 g (64 mmol, 8.0 eq.) of NaBH₄, 36 mL of 2.5 M aqueous NaOH and 40 mL of EtOH. The reaction mixture was refluxed for 6 h. The still hot reaction was poured into 280 mL of water and stirred for 15 min. The formed solid was filtered and washed with water (3x 20 mL) and EtOH (3x 20 mL). The product was dried under vacuo to give the product as a yellow-brown solid (810 mg, 48.6 %).

¹H NMR (700 MHz, DMSO-*d*₆) δ 7.82 (s, 2H), 7.63 (d, J = 8.9 Hz, 2H), 6.93 (dd, J = 8.9, 2.1 Hz, 2H), 6.79 (d, J = 1.7 Hz, 2H), 5.21 (s, 4H). ¹³C NMR (176 MHz, DMSO-*d*₆) δ 144.05, 130.65, 127.96, 127.24, 121.35, 120.46, 103.76.

These data are in full agreement with those previously published in the literature.^[8]

Tp-DAA COF: A Pyrex tube (o.d. \times i.d. = 15 \times 10 mm² and length 15 cm) is charged with triformylphloroglucinol (**Tp**) (21 mg, 0.1 mmol), 2,6-diaminoanthracene (**DAA**) (31.2 mg, 0.15 mmol), 1.5 mL of mesitylene, 1.5 mL of dioxane and 0.5 mL of 6 M aqueous acetic acid. This mixture was sonicated for 15 minutes in order to get a homogenous dispersion. The tube was then flash frozen at 77 K (liquid N₂ bath) and degassed by three freeze-pump-thaw cycles. The tube was sealed off and then heated at 120 °C for 3 days. A dark red colored precipitate was collected by filtration, washed with anhydrous acetone, methanol and cyclohexane to give a deep red colored powder (46 mg, 98 %).



Scheme S 9. Synthesis of Tp-DAA COF from 1,3,5-triformylphloroglucinol (Tp) and 2,6-diaminoanthracene (DAA) using 1,4-dioxane: mesitylene (1:1) as solvent combination and acetic acid (6M) as catalyst.

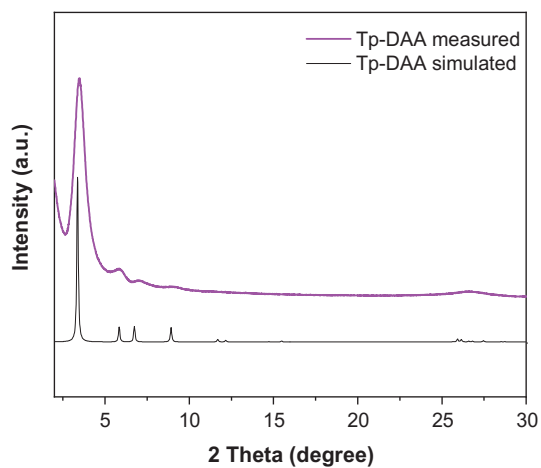


Figure S 19. Experimental and simulated powder X-ray diffraction pattern for Tp-DAA-COF (AA stacking) showing the matching of the pattern.

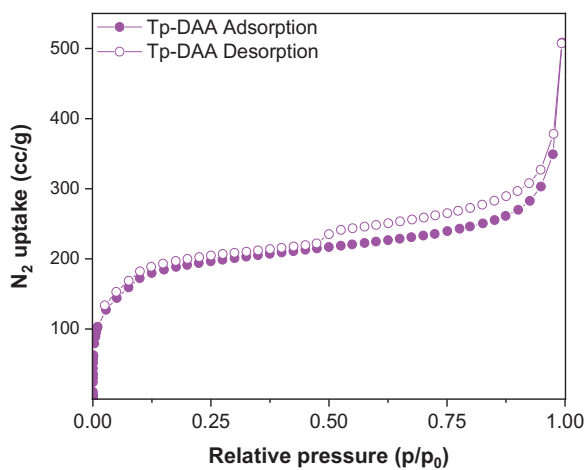


Figure S 20. N_2 sorption isotherms for Tp-DAA. Using Brunauer-Emmett-Teller (BET) analysis the surface area was calculated 716 m^2/g for Tp-DAA.

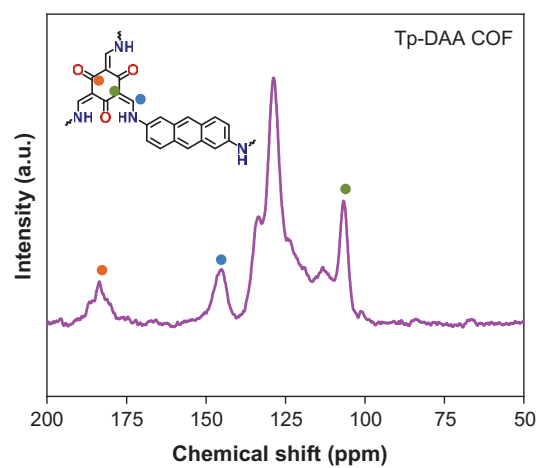


Figure S 21. ^{13}C CP-MAS solid-state NMR spectra of Tp-DAA.

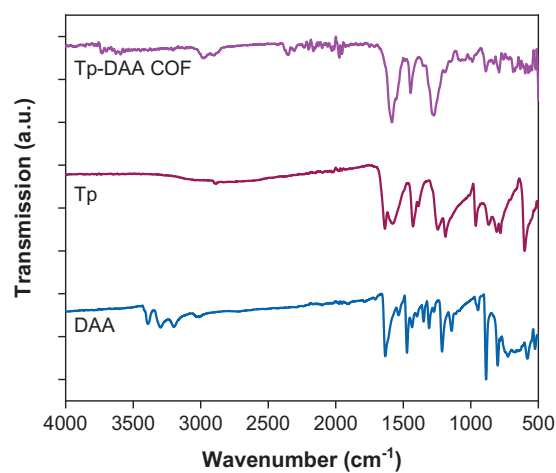
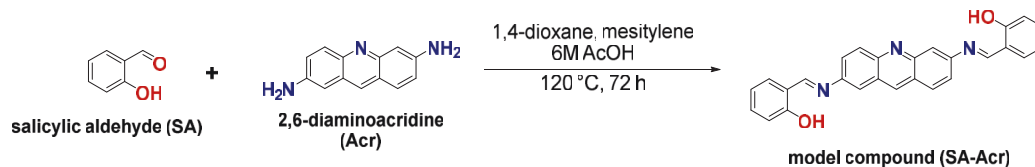


Figure S 22. FT-IR analyses of Tp-DAA COF in comparison with the corresponding aldehyde (Tp) and amine (DAA) showing the formation of the framework structure.

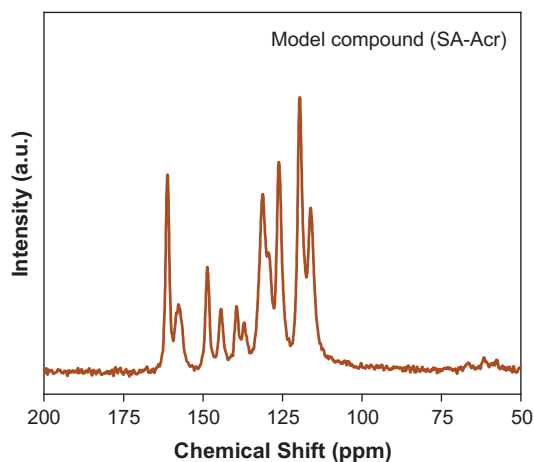
S7. Synthesis of model compound (SA-Acr)



Scheme S 10. Synthesis of the model compound SA-Acr.

Model compound (SA-Acr): To a Schlenk flask were 63 mg (0.30 mmol, 1.0 eq.) of 2,6-diaminoacridine (Acr), 68 μl (0.66 mmol, 2.2 eq.) and 5 mL of 1,4-dioxane added. To the resulting suspension 1.0 mL of 6 M aqueous acetic acid were added. The flask was closed and heated to 100 $^{\circ}\text{C}$ for 24 h while stirring the reaction mixture. After cooling to room temperature, the resulting yellow-brown suspension was filtered and washed with 10 mL acetone to remove residual starting materials. The model compound was subsequently dried under vacuo to give the desired compound as a dark brown powder (71 mg, 57%).

ESI-MS $[\text{M}+\text{H}^+]$ (m/z): 418.1549 (th.: 418.1550).

Figure S 23. ^{13}C CP-MAS solid-state NMR spectra of the model compound SA-Acr.

S8. Photocatalytic reaction optimization

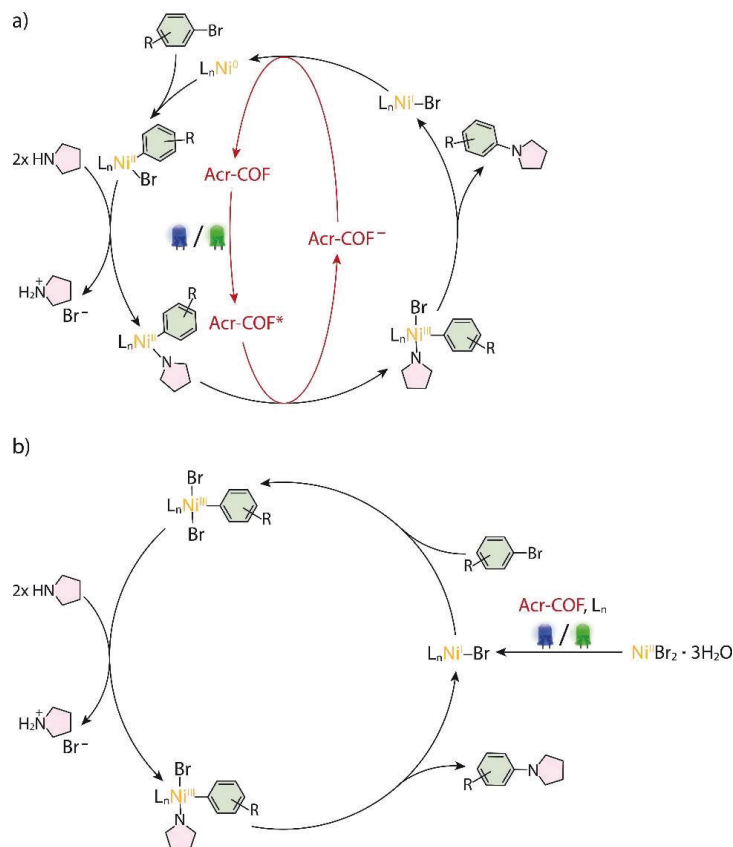


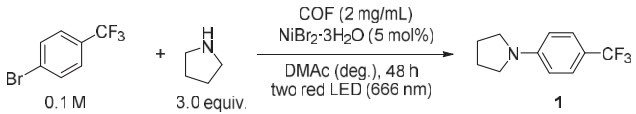
Figure S 24. Proposed mechanisms invoked in the nickel mediated metallaphotocatalytic C-N cross-coupling: a) oxidation-state modulation;^[9] b) thermally sustained $Ni^{II/III}$ cycle.^[10] L_n = pyrrolidine.

S8.1 General experimental procedure for screening experiments

An oven dried vial (16 x 100 mm) equipped with a stir bar was charged with the Ni^{II} catalyst (5-10 μ mol, 5 mol%) and the Acridine-COF (2-4 mg). Subsequently, bromobenzotrifluoride (100-200 μ mol) and pyrrolidine (300-450 μ mol, 37.0 μ L, 3.0 equiv.) and the solvent (anhydrous, 2 mL) were added and the vial was sealed with a septum and Parafilm. The reaction mixture was sonicated for 5-10 min followed by stirring for 5 min until a fine dispersion of the solids was achieved and the mixture was then degassed by bubbling N_2 for 15 min. The mixture was stirred at 800 rpm and irradiated with two LED lamps (440 nm) at full power. After the respective reaction time, one equivalent of 1,3,5-trimethoxybenzene (0.3 mmol, 50.5 mg) was added. An aliquot of the reaction mixture (~300 μ L) was filtered, diluted with DMSO- d_6 and subjected to 1H -NMR analysis.

S8.2 Screening of Acridine-COFs

Table S 5. Screening of acridine based COFs using two red LEDs.^a

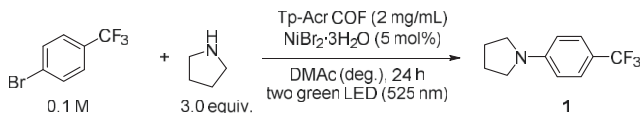


Entry	Acridine-COF	Conversion [%] ^b	1 [%] ^c
1	Tp-Acr	2	2
2	DHTA-Acr	13	n.d. ^d
3	HTA-Acr	11	1

^aReaction conditions: 4-bromobenzotrifluoride (0.2 mmol), pyrrolidine (0.6 mmol), NiBr₂·3H₂O (5 mol%), Acridine-COF (4 mg), DMac (anhydrous, 2 mL), 2 red LED (100%) for 48h. ^bConversion of 4-bromobenzotrifluoride determined by ¹H-NMR using 1,3,5-trimethoxybenzene as internal standard. ^cNMR yields determined by ¹H-NMR using 1,3,5-trimethoxybenzene as internal standard. ^dnot detected.

S8.3 Control studies

Table S 6. Control studies using two green LEDs.^a




Entry	Deviation from standard conditions	Conversion [%] ^b	1 [%] ^c
1	None	54	52
2	Tp-DAA COF	28	27
3	2,6-diaminoacridine (5-mol%) instead of COF	6	n.d. ^d
4	Model compound (SA-Acr) instead of COF	9	n.d.
5	No Tp-Acr COF	7	3

^aReaction conditions: 4-bromobenzotrifluoride (0.2 mmol), pyrrolidine (0.6 mmol), NiBr₂·3H₂O (5 mol%), Acridine-COF (4 mg), DMac (anhydrous, 2 mL), 2 green LED (100%) for 24h. ^bConversion of 4-bromobenzotrifluoride determined by ¹H-NMR using 1,3,5-trimethoxybenzene as internal standard. ^cNMR yields determined by ¹H-NMR using 1,3,5-trimethoxybenzene as internal standard. ^dnot detected.

S9. Photocatalysis - recycling studies

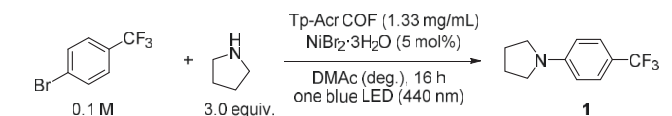
An oven dried vial (13 x 80 mm) equipped with a stir bar was charged with Acridine-COF (4 mg) and $\text{NiBr}_2 \cdot 3\text{H}_2\text{O}$ (4.1 mg, 15 μmol , 5 mol%). Subsequently, 4-bromobenzotrifluoride (67.5 mg, 42.0 μl , 0.3 mmol, 1.0 equiv.) and pyrrolidine (64.0 mg, 73.9 μl , 0.9 mmol, 3.0 equiv.) and DMAc (anhydrous, 3 mL) were added and the vial was sealed with a septum and Parafilm. The reaction mixture was sonicated for 5-10 min followed by stirring for 5 min until fine dispersion of the solids was achieved and the mixture was then degassed by bubbling N_2 for 10 min. The mixture was stirred at 800 rpm and irradiated with one or two LED lamps (440 nm) at full power. After the respective reaction time, one equivalent of 1,3,5-trimethoxybenzene (50.5 mg, 0.3 mmol) was added and the mixture was stirred for 5 min. The reaction mixture was centrifuged at 3500 rpm for 10 min and the liquid phase was carefully separated and analyzed by ^1H -NMR. The Acridine-COF was washed 2 times with DMAc (anhydrous, 3 mL, followed by centrifugation at 3500 rpm for 10 min and separation of the liquid phase), lyophilized (overnight) and reused in the next reaction. Alternatively, the Acridine-COF was washed first with methanol 3 mL (followed by centrifugation at 3000 rpm for 10 min and separation of the liquid phase) and then with hexane (followed by centrifugation at 3500 rpm for 10 min and separation of the liquid phase), dried under reduced pressure and reused in the next reaction.

Table S 7. Reusability of Tp-Acr-COF using 2 blue lamps.^a

	
Cycle	1 [%] ^b
1	98
2	82
3	73
4	41
5	65

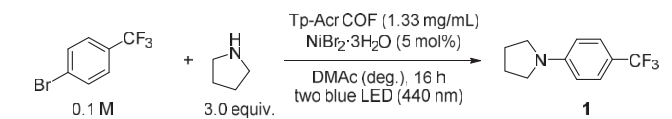
^aReaction conditions: 4-bromobenzotrifluoride (0.3 mmol), pyrrolidine (0.9 mmol), $\text{NiBr}_2 \cdot 3\text{H}_2\text{O}$ (5 mol%), Acr-COF (4 mg - reused), DMAc (anhydrous, 3 mL), 2 blue LED (100%) for 16h. ^bNMR yields determined by ^1H -NMR using 1,3,5-trimethoxybenzene as internal standard.

Table S 8. Reusability of Tp-Acr COF using 1 blue lamp.^a

	
Cycle	1 [%] ^b
1	53
2	52
3	49
4	27
5	23

^aReaction conditions: 4-bromobenzotrifluoride (0.3 mmol), pyrrolidine (0.9 mmol), NiBr₂·3H₂O (5 mol%), Acr-COF (4 mg - reused), DMAc (anhydrous, 3 mL), 1 blue LED (100%) for 16h. ^bNMR yields determined by ¹H-NMR using 1,3,5-trimethoxybenzene as internal standard.

Table S 9. Reusability of Tp-Acr COF using 2 blue lamp and adding only NiBr₂·3H₂O in the first cycle.^a

	
Cycle	1 [%] ^b
1	95
2	6
3	6
4	10
5	12

^aReaction conditions: 4-bromobenzotrifluoride (0.3 mmol), pyrrolidine (0.9 mmol), NiBr₂·3H₂O (5 mol%), Acr-COF (4 mg - reused), DMAc (anhydrous, 3 mL), 2 blue LED (100%) for 16h. ^bNMR yields determined by ¹H-NMR using 1,3,5-trimethoxybenzene as internal standard.

Table S 10. Reusability of Tp-Acr COF using two blue lamp and washing with MeOH and hexane.^a

Cycle	1 [%] ^b
1	94
2	95
3	82
4	65
5	63

^aReaction conditions: 4-bromobenzotrifluoride (0.3 mmol), pyrrolidine (0.9 mmol), NiBr₂·3H₂O (5 mol%), Acr-COF (4 mg - reused), DMAc (anhydrous, 3 mL), 2 blue LED (100%) for 16h. ^bNMR yields determined by ¹H-NMR using 1,3,5-trimethoxybenzene as internal standard.

S9.1 Analysis of recycled Tp-Acr COF

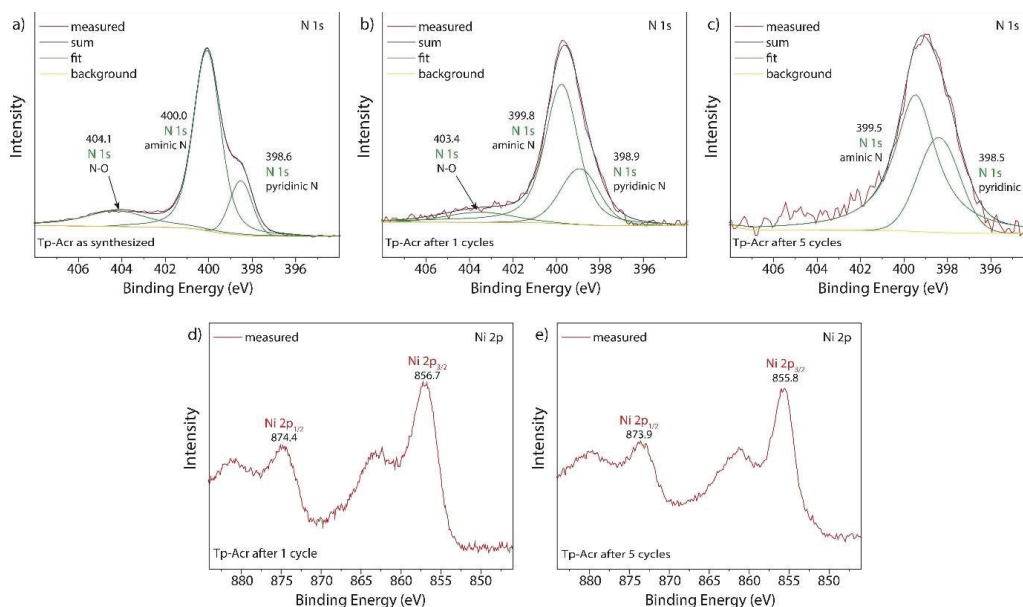


Figure S 25. (a, b, c) N 1s XPS core level spectra of the TP-Acr COF as synthesized (a), after the first reaction cycle (b) and after 5 recycling cycles (c) of photocatalytic dual nickel C-N cross coupling. (d, e) Ni 2p XPS core level spectra of the TP-Acr COF after the first reaction cycle (d) and after 5 recycling cycles (e) of photocatalytic dual nickel C-N cross coupling.

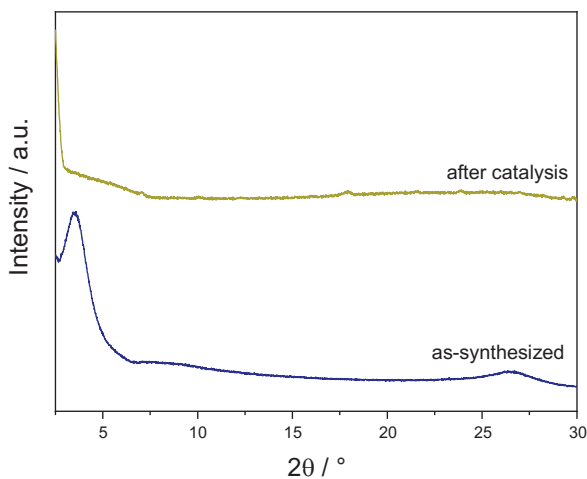


Figure S 26. FT-IR analyses of Tp-Acr COF before and after photocatalysis, showing that the framework structure loses crystallinity under photocatalysis conditions

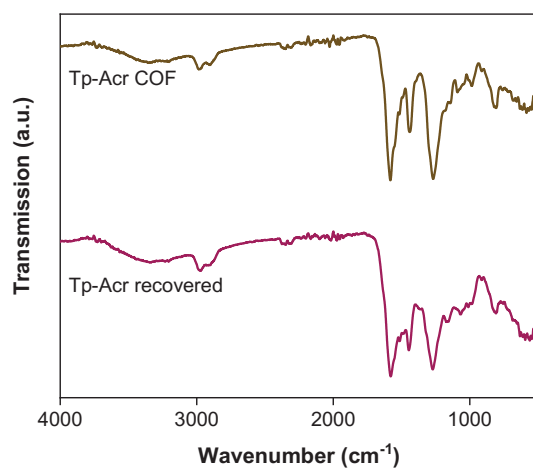


Figure S 27. FT-IR analyses of Tp-Acr COF before and after photocatalysis, showing that the framework structure remains stable under photocatalysis conditions.

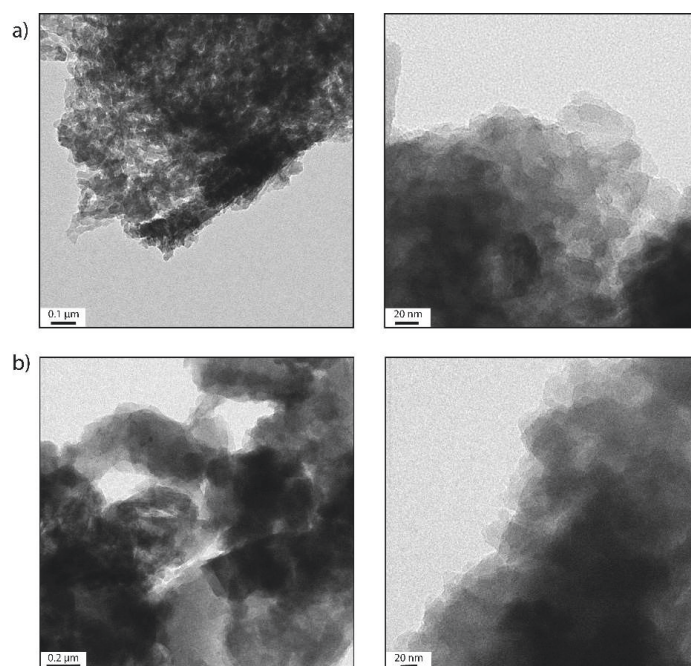
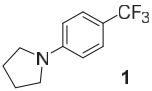
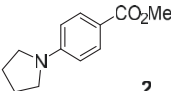
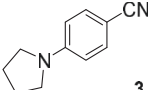
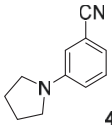
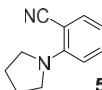
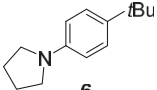


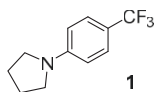
Figure S 28. TEM analyses of Tp-Acr after 1 (a) and 5 (b) cycles of photocatalysis, respectively, showing the morphology and the layered structure of the COF matrix

S10. Scope and limitations

General experimental procedure. An oven dried vial (13 x 95 mm) equipped with a stir bar was charged with $\text{NiBr}_2 \cdot 3\text{H}_2\text{O}$ (4.1 mg, 15 μmol , 5 mol%), aryl bromide (0.3 mmol, 1 equiv.) and Tp-2,6-Acr-COF (4.0 mg). Subsequently, the amine (0.9 mmol, 3 equiv.) and DMAc (anhydrous, 3 mL) were added and the vial was sealed with a septum and parafilm. The reaction mixture was sonicated for 5-10 min and the mixture was then degassed by bubbling N_2 for 10 min. The mixture was stirred at 800 rpm and irradiated with two LED lamps (440 nm) at full power. After the respective reaction time, one equivalent of 1,3,5-trimethoxybenzene (50.5 mg, 0.3 mmol, internal standard) was added. An aliquot (~300 μL) of the reaction mixture was diluted with DMSO-d_6 and subjected to $^1\text{H-NMR}$ analysis. After full consumption of the arene starting material, the liquid phase was diluted with H_2O (40 mL) and extracted with ethyl acetate (3 x 30 mL). The combined organic phases were washed with H_2O (40 mL), NaHCO_3 solution (40 mL) and brine (40 mL), dried over Na_2SO_4 and concentrated. The crude product was purified by flash column chromatography (SiO_2 , Hexane/EtOAc). The final product was characterized by $^1\text{H-NMR}$, $^{13}\text{C-NMR}$, $^{19}\text{F-NMR}$.

Table S 11. Scope of the C–N coupling reaction.^a

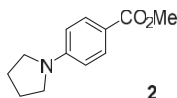
Product	Reaction time	NMR yield ^b	Isolated yield
 1	16 hours	95%	93%
 2	16 hours	90%	88%
 3	24 hours	97%	94%
 4	48 hours	94%	91%
 5	72 hours	92%	87%
 6	48 hours	68%	66%
^a Reaction conditions according to general procedure. ^b NMR yields determined by ¹ H-NMR using maleic acid as internal standard			



1-(4-(trifluoromethyl)phenyl)pyrrolidine: From pyrrolidine (64.0 mg, 73.9 μ l, 0.9 mmol, 3.0 equiv.) and 4-bromobenzotrifluoride (67.5 mg, 42.0 μ l, 0.3 mmol, 1.0 equiv.). Reaction time: 16 h. Purification with flash chromatography (3% ethyl acetate in hexane) afforded the title compound (59.8 mg, 0.28 mmol, 93%) as a white solid.

^1H NMR (400 MHz, CDCl_3) δ 7.45 (d, J = 8.6 Hz, 2H), 6.56 (d, J = 8.6 Hz, 2H), 3.45 – 3.20 (m, 4H), 2.16 – 1.94 (m, 4H). ^{13}C NMR (101 MHz, CDCl_3) δ 149.9, 126.5 (q, J = 3.7 Hz), 125.5 (q, J = 270.0 Hz), 116.7 (q, J = 32.4 Hz), 110.9, 47.6, 25.6. ^{19}F NMR (376 MHz, CDCl_3) δ -60.5 (s, 3F).

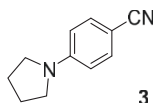
These data are in full agreement with those previously published in the literature.^[11]



1-(4-methylbenzoate)pyrrolidine: From pyrrolidine (64.0 mg, 73.9 μ l, 0.9 mmol, 3.0 equiv.) and 4-bromomethylbenzoate (64.5 mg, 0.3 mmol, 1.0 equiv.). Reaction time: 16 h. Purification with flash chromatography (5% ethyl acetate in hexane) afforded the title compound (54.3 mg, 0.26 mmol, 88%).

^1H NMR (400 MHz, CDCl_3) δ 7.89 (d, J = 8.9 Hz, 2H), 6.50 (d, J = 8.9 Hz, 2H), 3.85 (s, 3H), 3.50 – 3.19 (m, 4H), 2.13 – 1.90 (m, 4H). ^{13}C NMR (101 MHz, CDCl_3) δ 167.8, 150.9, 131.5, 116.3, 110.7, 51.5, 47.6, 25.6.

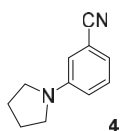
These data are in full agreement with those previously published in the literature.^[12]



1-(4-benzonitrile)pyrrolidine: From pyrrolidine (64.0 mg, 73.9 μ l, 0.9 mmol, 3.0 equiv.) and 4-bromobenzonitrile (54.6 mg, 0.3 mmol, 1.0 equiv.). Reaction time: 24 h. Purification with flash chromatography (5% ethyl acetate in hexane) afforded the title compound (48.5 mg, 0.28 mmol, 94%) as a white solid.

^1H NMR (400 MHz, CDCl_3) δ 7.43 (d, J = 8.8 Hz, 2H), 6.49 (d, J = 8.9 Hz, 2H), 3.44 – 3.19 (m, 4H), 2.16 – 1.94 (m, 4H). ^{13}C NMR (101 MHz, CDCl_3) δ = 150.1, 133.5, 121.16, 111.5, 96.6, 47.6, 25.5.

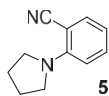
These data are in full agreement with those previously published in the literature.^[13]



1-(3-benzonitrile)pyrrolidine: From pyrrolidine (64.0 mg, 73.9 μ l, 0.9 mmol, 3.0 equiv.) and 3-bromobenzonitrile (54.6 mg, 0.3 mmol, 1.0 equiv.). Reaction time: 48 h. No internal standard (1,3,5-trimethoxybenzene was used) due to poor separation from the product during flash chromatography. Purification with flash chromatography (1. gradient 3-5% ethyl acetate in hexane; 2. Isocratic 5% ethyl acetate in hexane) afforded the title compound (47.1 mg, 0.27 mmol, 91%) as a white solid.

^1H NMR (400 MHz, CDCl_3) δ 7.33 – 7.21 (m, 1H), 6.91 (d, J = 7.5 Hz, 1H), 6.81 – 6.71 (m, 2H), 3.36 – 3.23 (m, 4H), 2.13 – 1.98 (m, 4H). ^{13}C NMR (101 MHz, CDCl_3) δ 147.7, 129.8, 120.0, 118.6, 115.9, 114.4, 112.8, 47.7, 25.5.

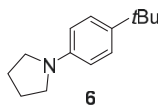
These data are in full agreement with those previously published in the literature.^[14]



1-(2-benzonitrile)pyrrolidine: From pyrrolidine (64.0 mg, 73.9 μ l, 0.9 mmol, 3.0 equiv.) and 2-bromobenzonitrile 4-bromobenzonitrile (54.6 mg, 0.3 mmol, 1.0 equiv.). Reaction time: 72 h. No internal standard (1,3,5-trimethoxybenzene was used) due to poor separation from the product during flash chromatography. Purification with flash chromatography (eluent: 1. gradient 3-5% ethyl acetate in hexane; 2. Isocratic 5% ethyl acetate in hexane) afforded the title compound (45.0 mg, 0.26 mmol, 87%) as a colorless oil.

^1H NMR (400 MHz, CDCl_3) δ 7.43 (m, 1H), 7.32 (m, 1H), 6.67 – 6.62 (m, 2H), 3.65 – 3.53 (m, 4H), 2.06 – 1.94 (m, 4H). ^{13}C NMR (101 MHz, CDCl_3) δ 150.1, 135.8, 133.5, 121.6, 116.0, 114.3, 94.4, 49.9, 25.8.

These data are in full agreement with those previously published in the literature.^[15]



1-(4-(*tert*-butyl)phenyl)pyrrolidine: From pyrrolidine (64.0 mg, 73.9 μ l, 0.9 mmol, 3.0 equiv.) and 4-bromo-*tert*-butylbenzene (63.9 mg, 52.2 μ l, 0.3 mmol, 1.0 equiv.). Reaction time: 48 h. Purification with flash chromatography (3% ethyl acetate in hexane) afforded the title compound (40.3 mg, 0.20 mmol, 66%) as a colorless oil.

^1H NMR (400 MHz, CDCl_3) δ 7.34 (d, J = 8.7 Hz, 2H), 6.61 (d, J = 8.7 Hz, 2H), 3.42 – 3.30 (m, 4H), 2.11 – 2.02 (m, 4H), 1.40 (s, 9H). ^{13}C NMR (101 MHz, CDCl_3) δ 145.9, 138.0, 126.0, 111.4, 47.8, 33.8, 31.7, 25.6.

These data are in full agreement with those previously published in the literature.^[12]

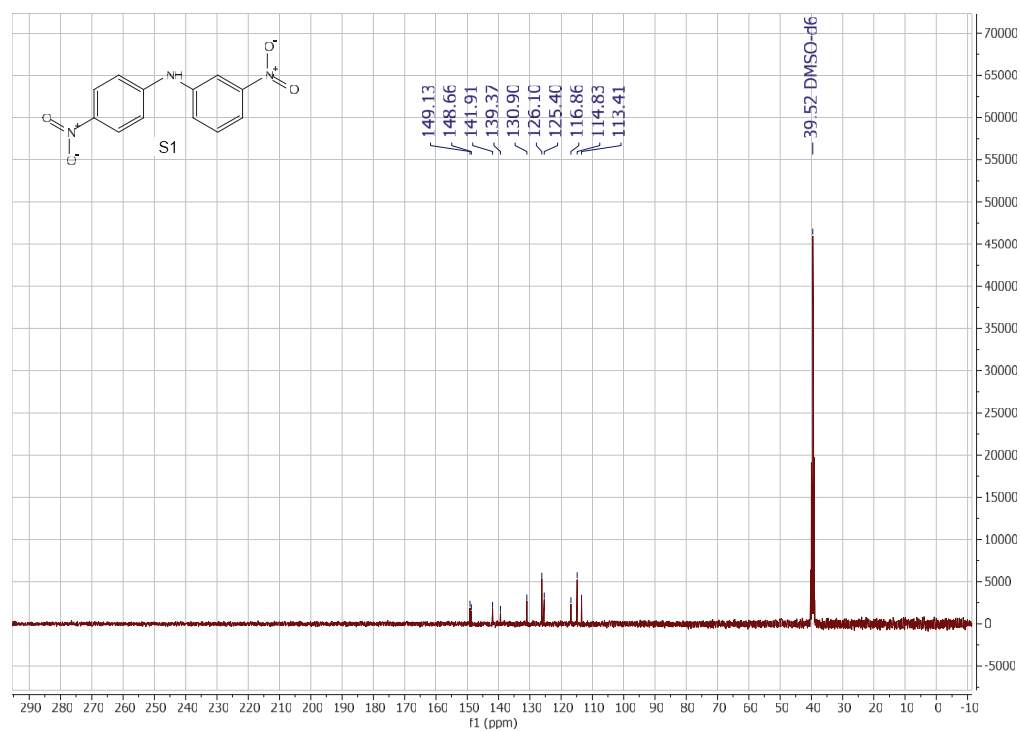
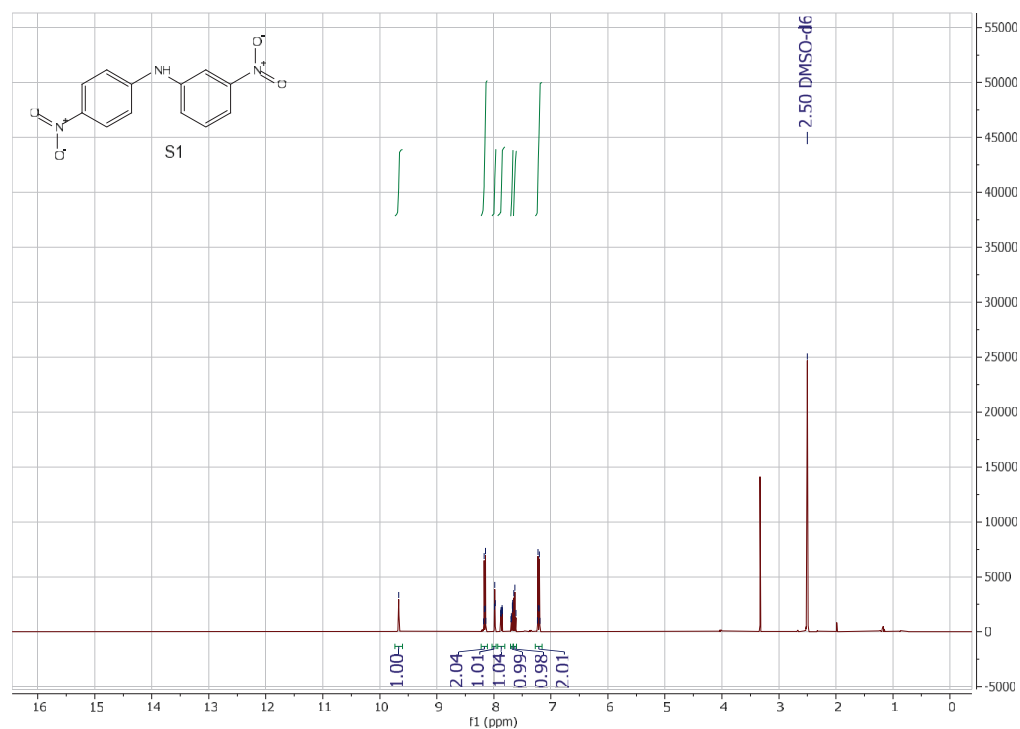
S11. References

- [1] “<https://www.kessil.com/photoreaction/PR160L.php>,” **n.d.**
- [2] D. H. O’Donovan, B. Kelly, E. Diez-Cecilia, M. Kitson, I. Rozas, *New J. Chem.* **2013**, 37, 2408–2418.
- [3] J. H. Chong, M. Sauer, B. O. Patrick, M. J. MacLachlan, *Org. Lett.* **2003**, 5, 3823–3826.
- [4] S. Haldar, D. Chakraborty, B. Roy, G. Banappanavar, K. Rinku, D. Mullangi, P. Hazra, D. Kabra, R. Vaidhyanathan, *J. Am. Chem. Soc.* **2018**, 140, 13367–13374.
- [5] A. A. Anderson, T. Goetzen, S. A. Shackelford, S. Tsank, *Synth. Commun.* **2000**, 30, 3227–3232.
- [6] M. A. Khayum, S. Kandambeth, S. Mitra, S. B. Nair, A. Das, S. S. Nagane, R. Mukherjee, R. Banerjee, *Angew. Chem. Int. Ed.* **2016**, 55, 15604–15608.
- [7] R. Kantam, R. Holland, B. P. Khanna, K. D. Revell, *Tetrahedron Lett.* **2011**, 52, 5083–5085.
- [8] I. Rose, M. Carta, R. Malpass-Evans, M. C. Ferrari, P. Bernardo, G. Clarizia, J. C. Jansen, N. B. McKeown, *ACS Macro Lett.* **2015**, 4, 912–915.
- [9] E. B. Corcoran, M. T. Pirnot, S. Lin, S. D. Dreher, D. A. DiRocco, I. W. Davies, S. L. Buchwald, D. W. C. Macmillan, *Science* **2016**, 353, 279–283.
- [10] R. Sun, Y. Qin, D. G. Nocera, *Angew. Chem. Int. Ed.* **2020**, 59, 9527–9533.
- [11] E. Brenner, R. Schneider, Y. Fort, *Tetrahedron* **1999**, 55, 12829–12842.
- [12] M. H. S. A. Hamid, C. L. Allen, G. W. Lamb, A. C. Maxwell, H. C. Maytum, A. J. A. Watson, J. M. J. Williams, *J. Am. Chem. Soc.* **2009**, 131, 1766–1774.
- [13] C. Desmarests, R. Schneider, Y. Fort, *J. Org. Chem.* **2002**, 67, 3029–3036.
- [14] J. P. Wolfe, H. Tomori, J. P. Sadighi, J. Yin, S. L. Buchwald, *J. Org. Chem.* **2000**, 65, 1158–1174.
- [15] P. Yu, B. Morandi, *Angew. Chem.* **2017**, 129, 15899–15903.

S12. Author Contributions

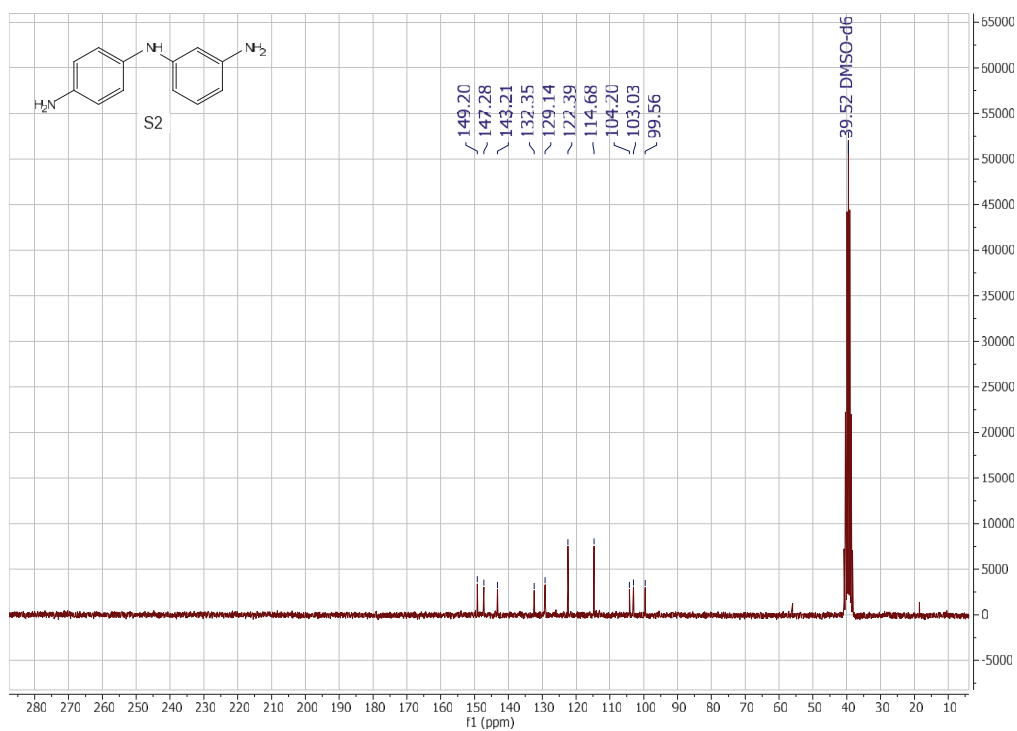
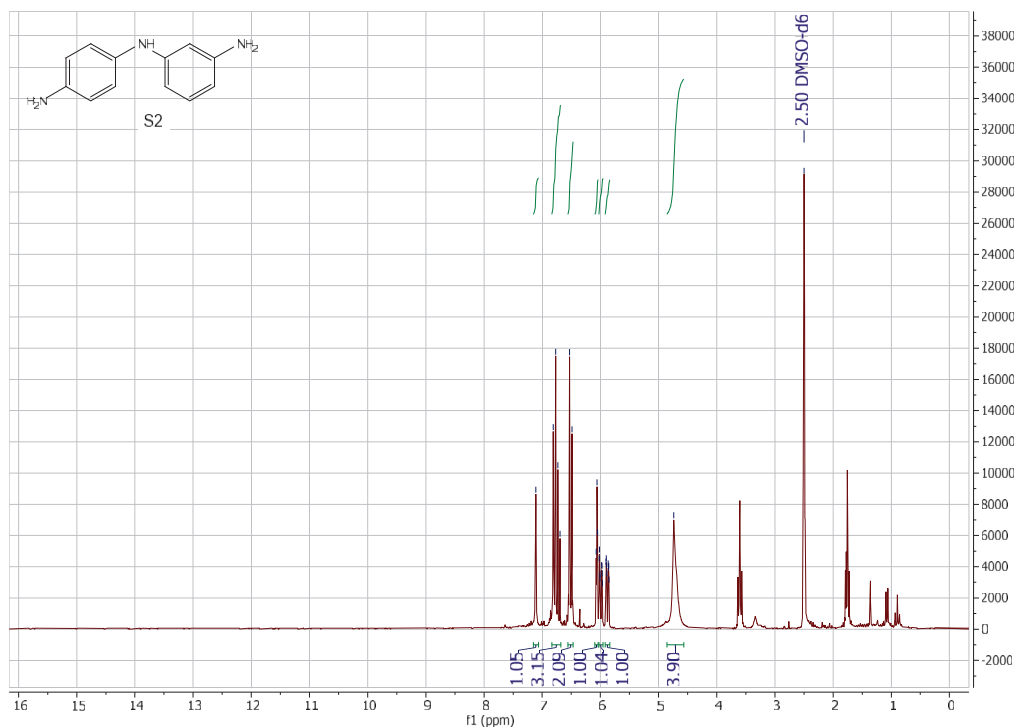
All authors contributed extensively to the work presented in this paper. M.T., P.P. and A.T. conceived the research project. M.T. conducted the synthesis of linkers as well as COFs and performed the characterizations. S.G. performed and evaluated the photocatalytic experiments. J.S. performed and evaluated the XPS analyses. J. Roeser. performed the simulations of the COFs. S.R. performed the photoluminescence measurements and photocatalytic experiments. J. Rabeah performed the EPR analyses. The whole project was directed by A.T and B.P. with the help from M.T. and P.P., M.T. wrote the manuscript with the input from the other authors.

S13. Copies of NMR spectra

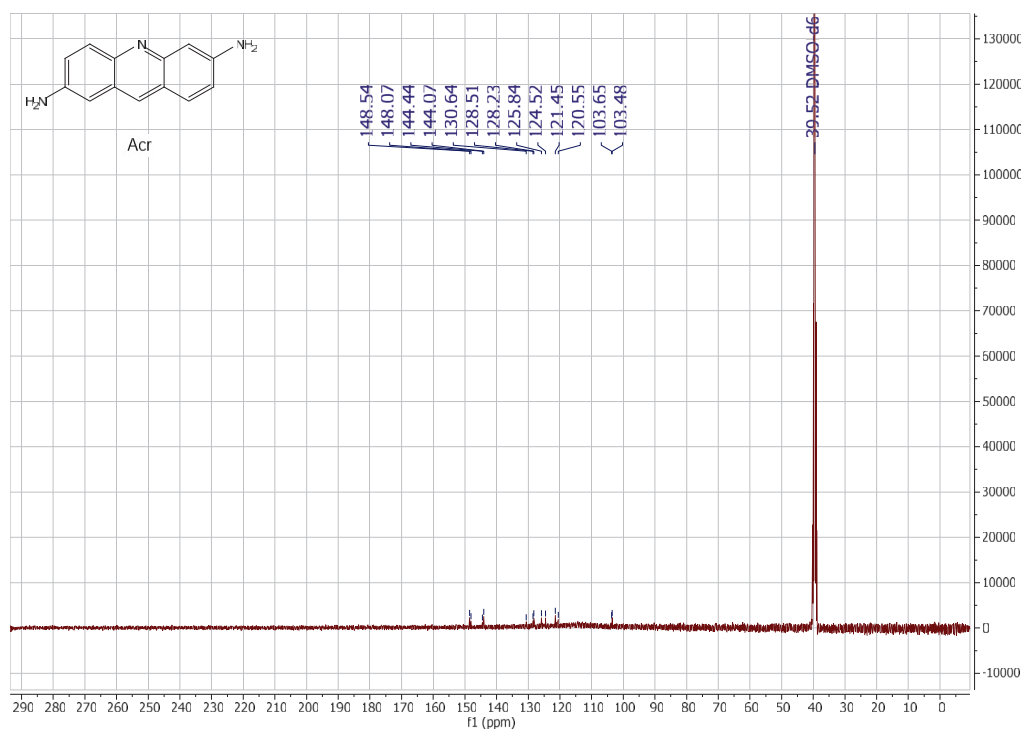
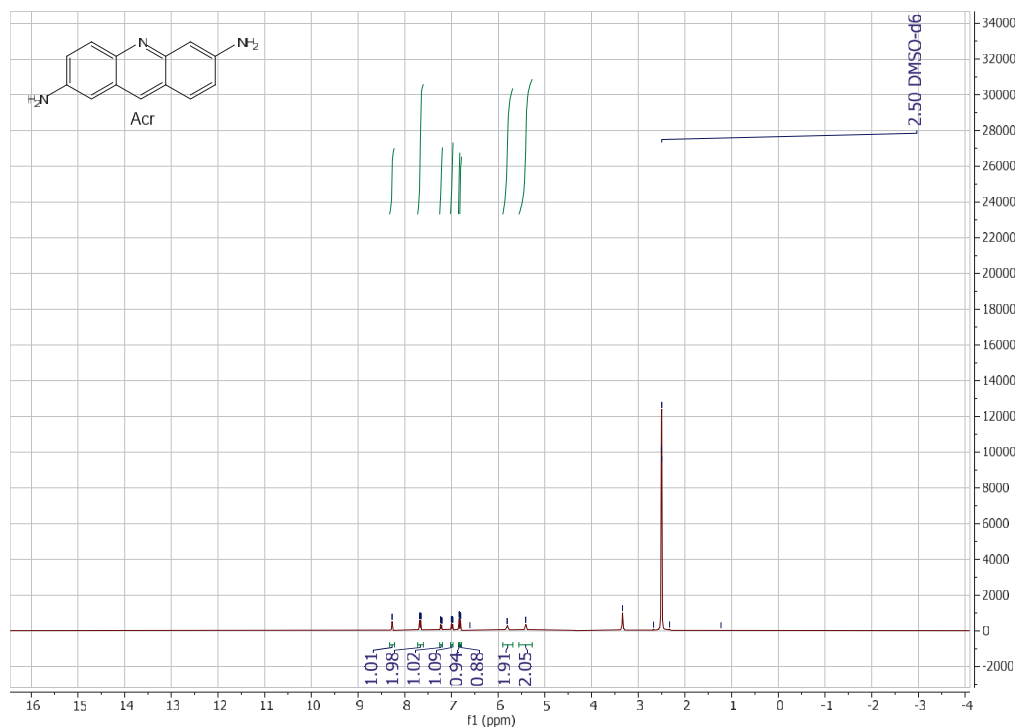


S47

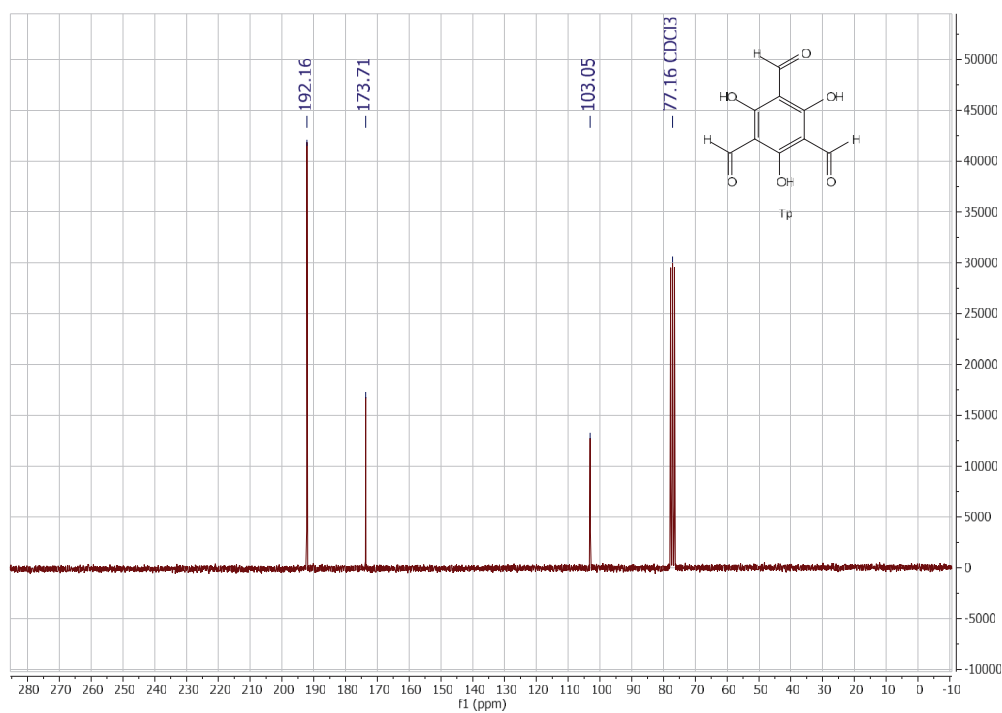
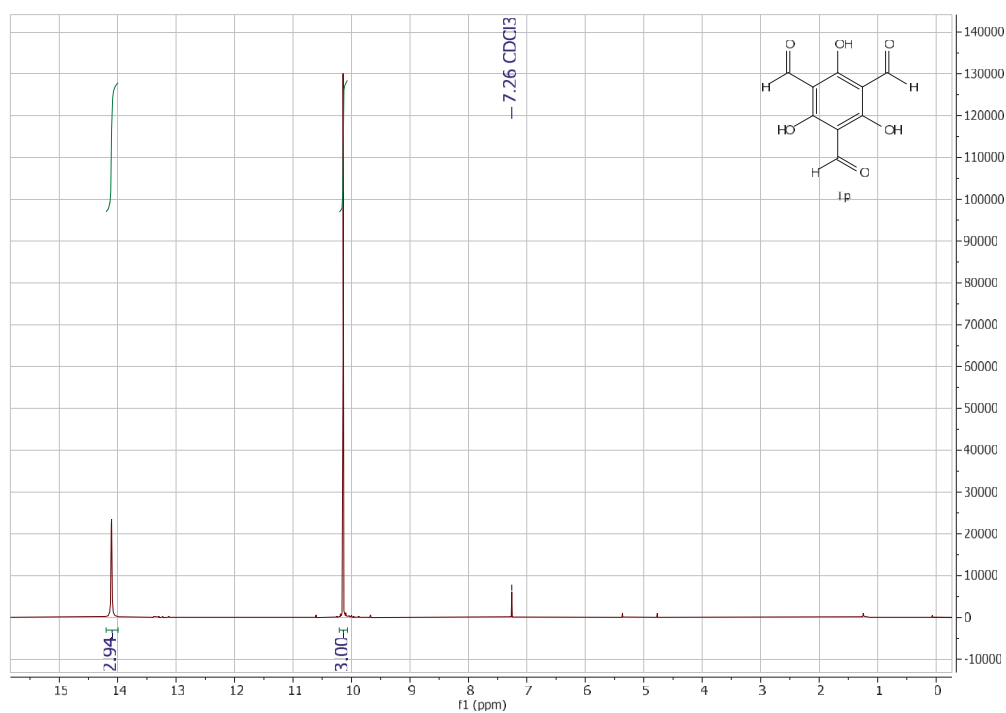
Appendix

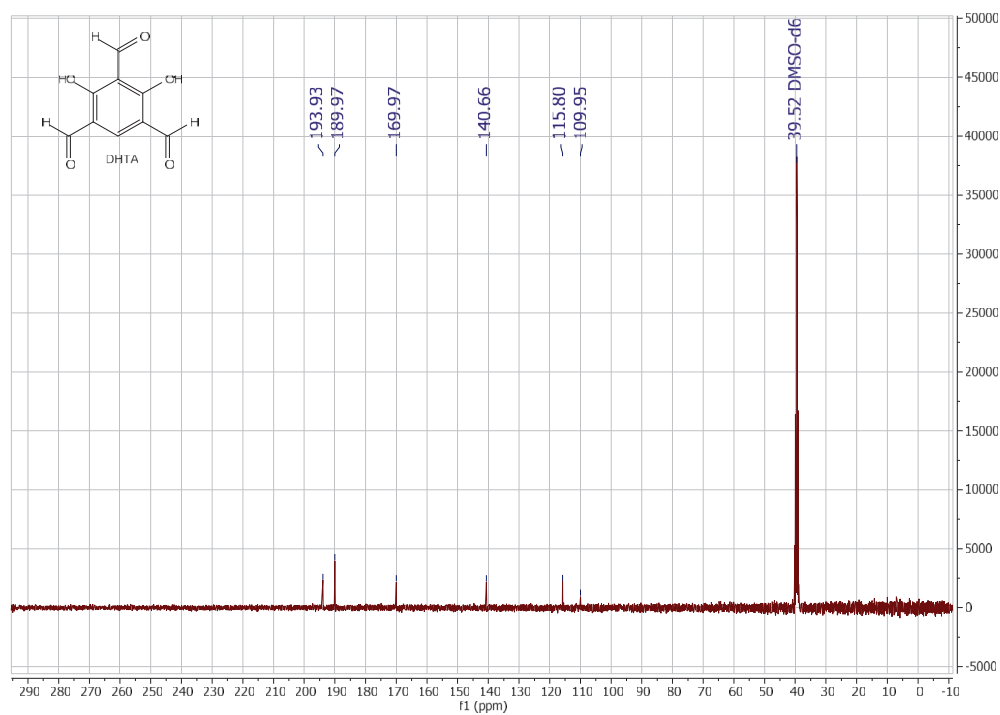
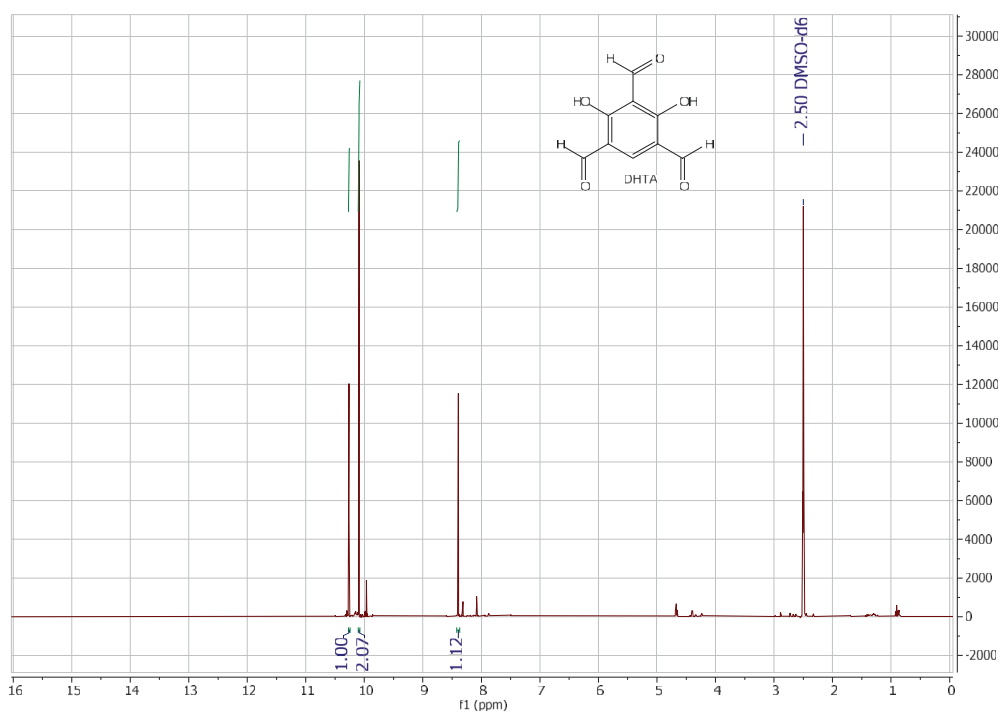


S48

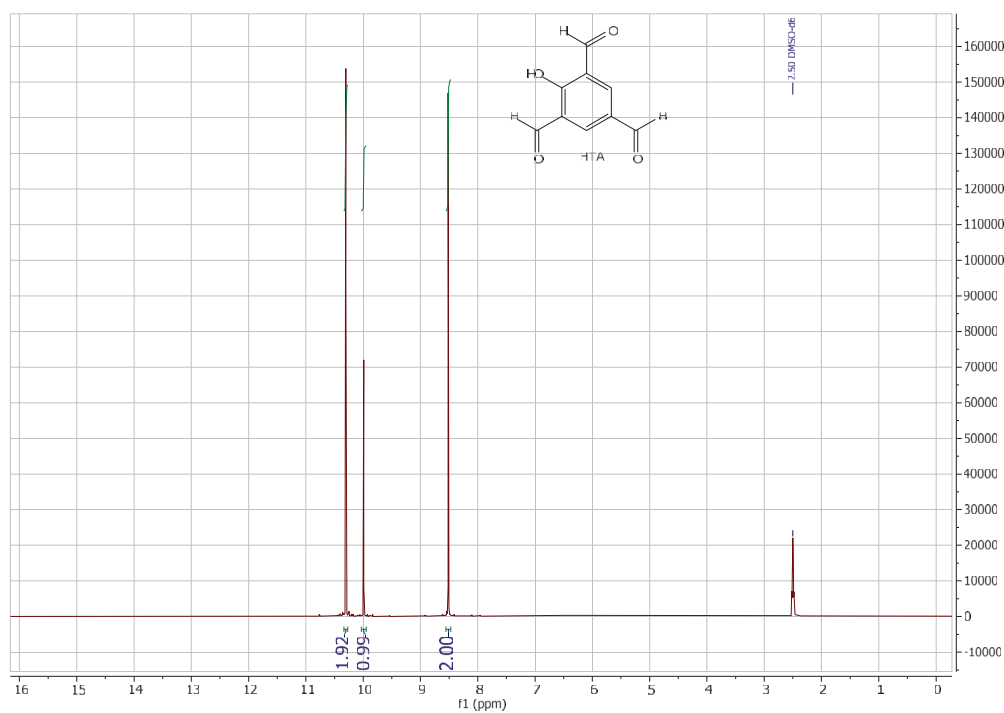
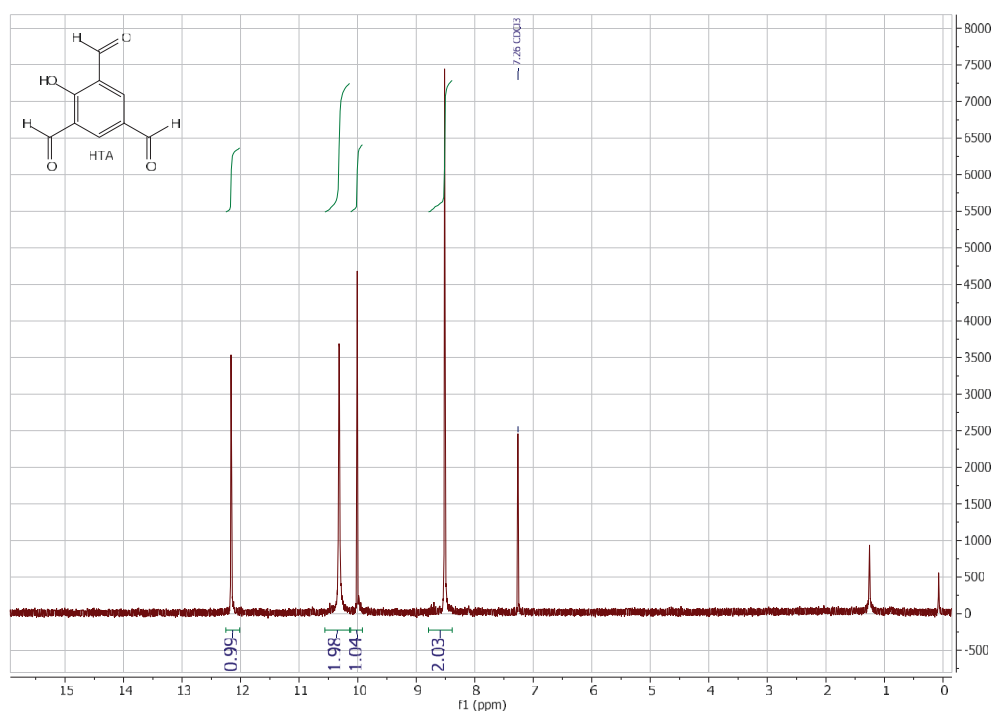


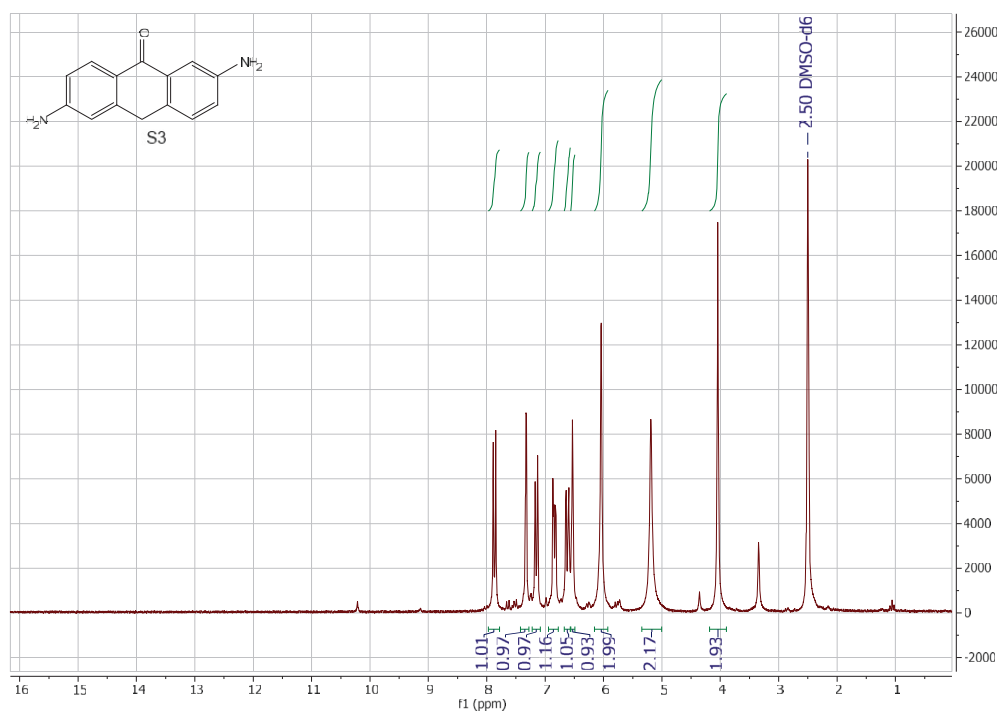
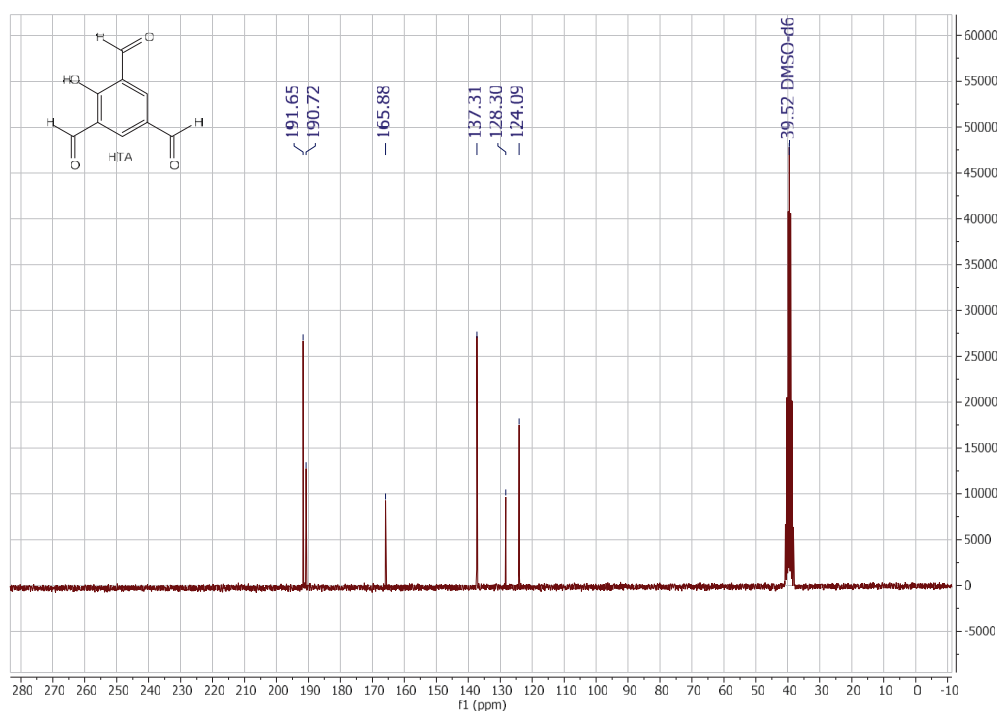
Appendix





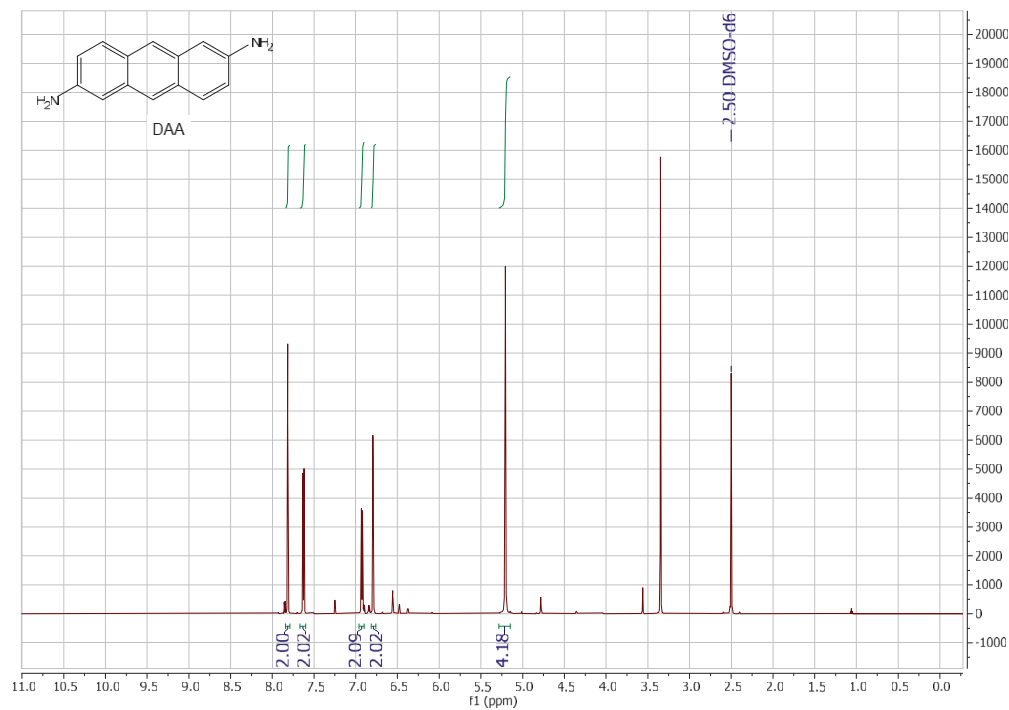
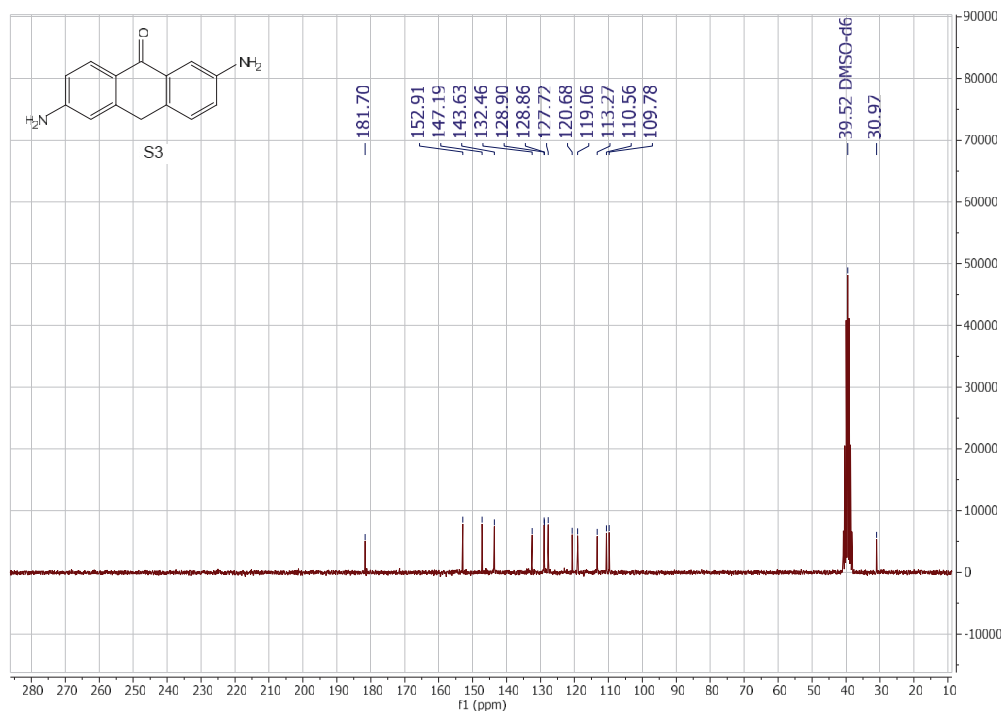
Appendix

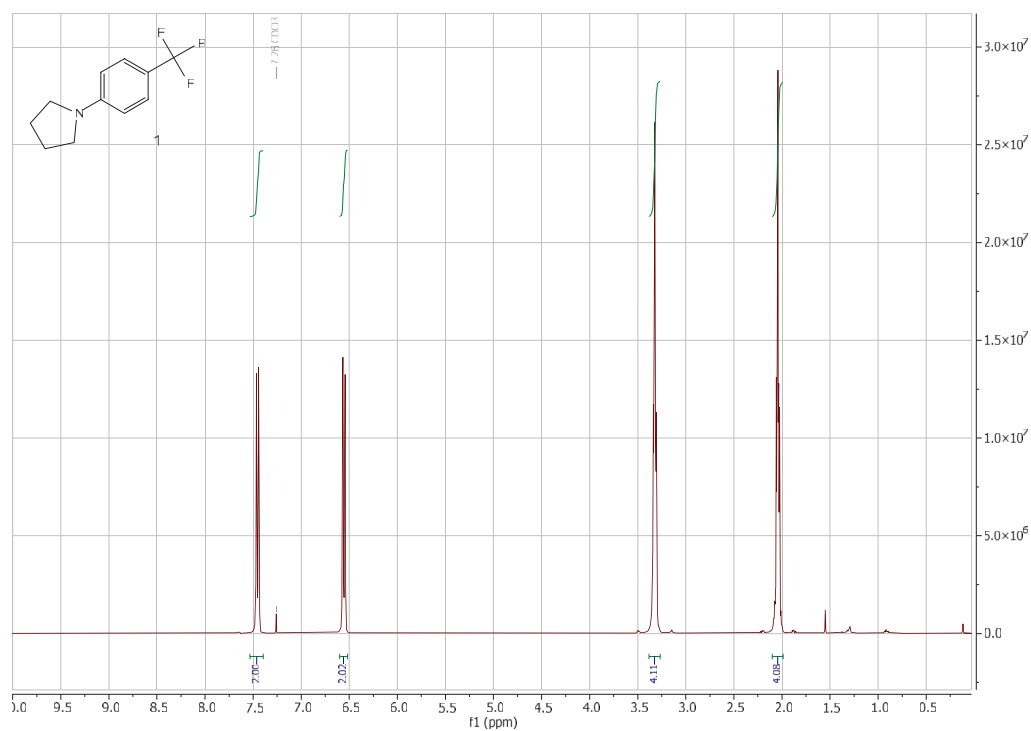
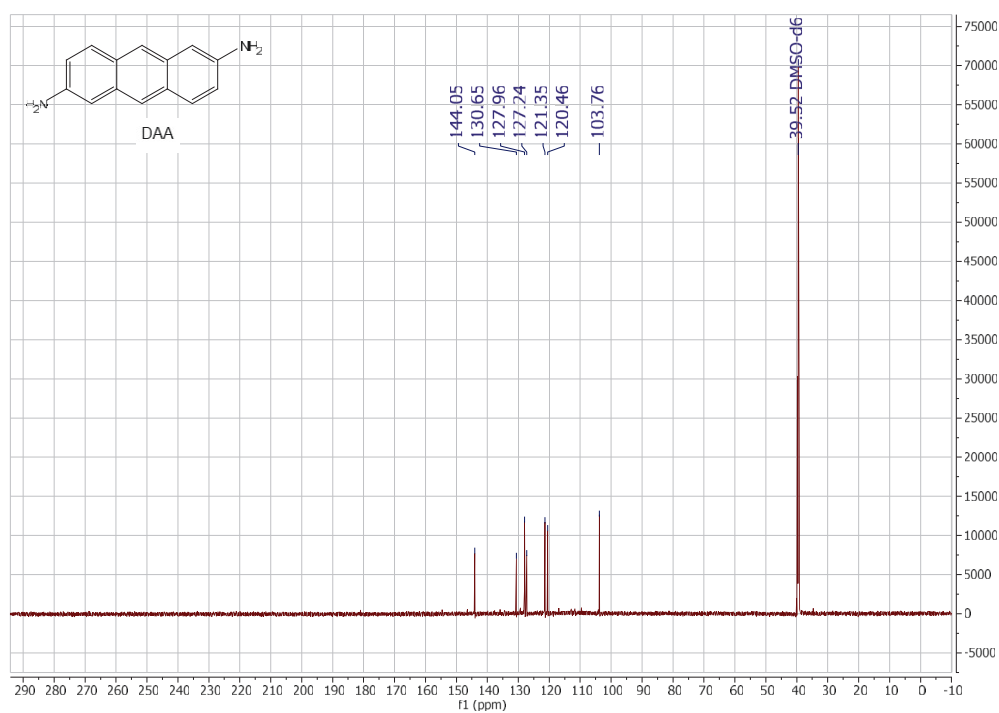




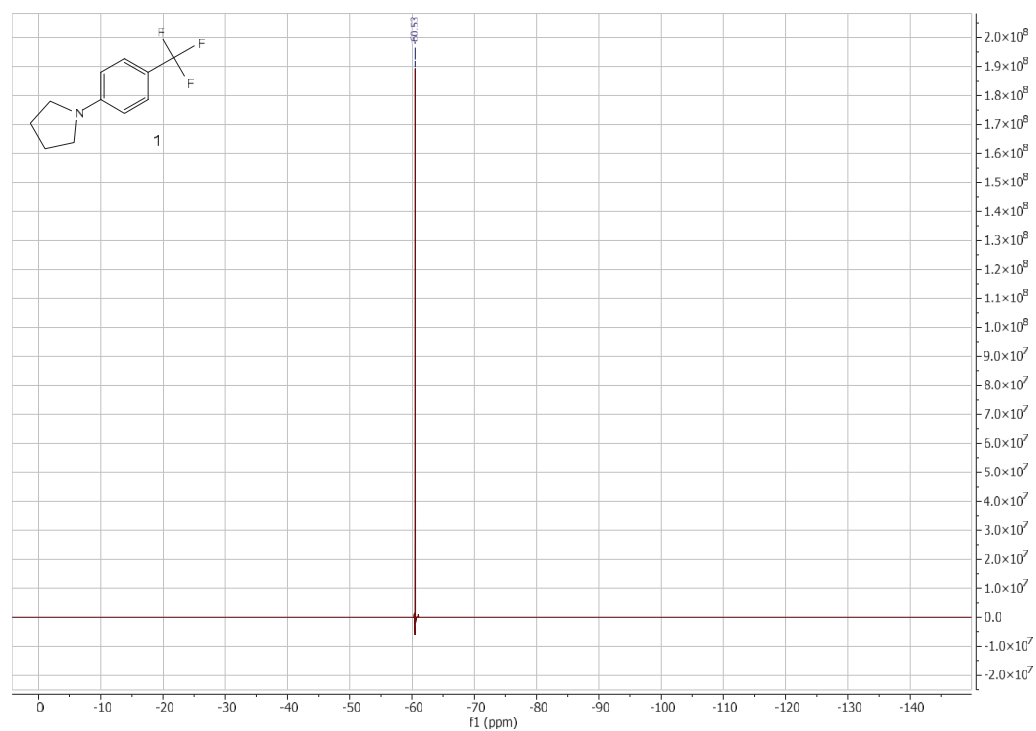
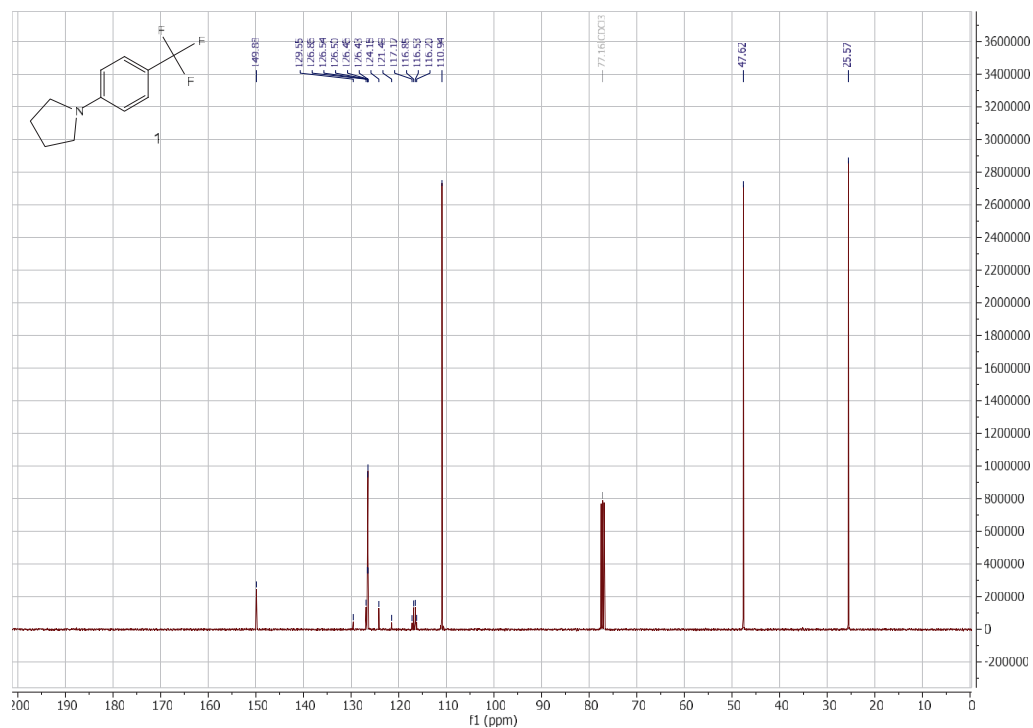
S53

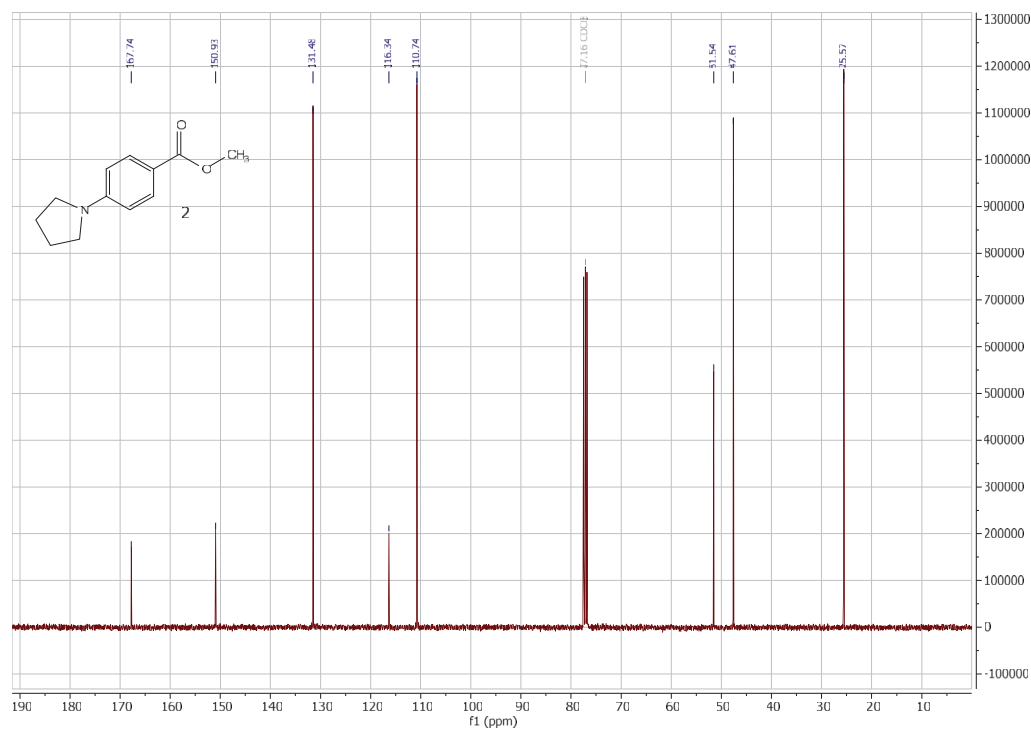
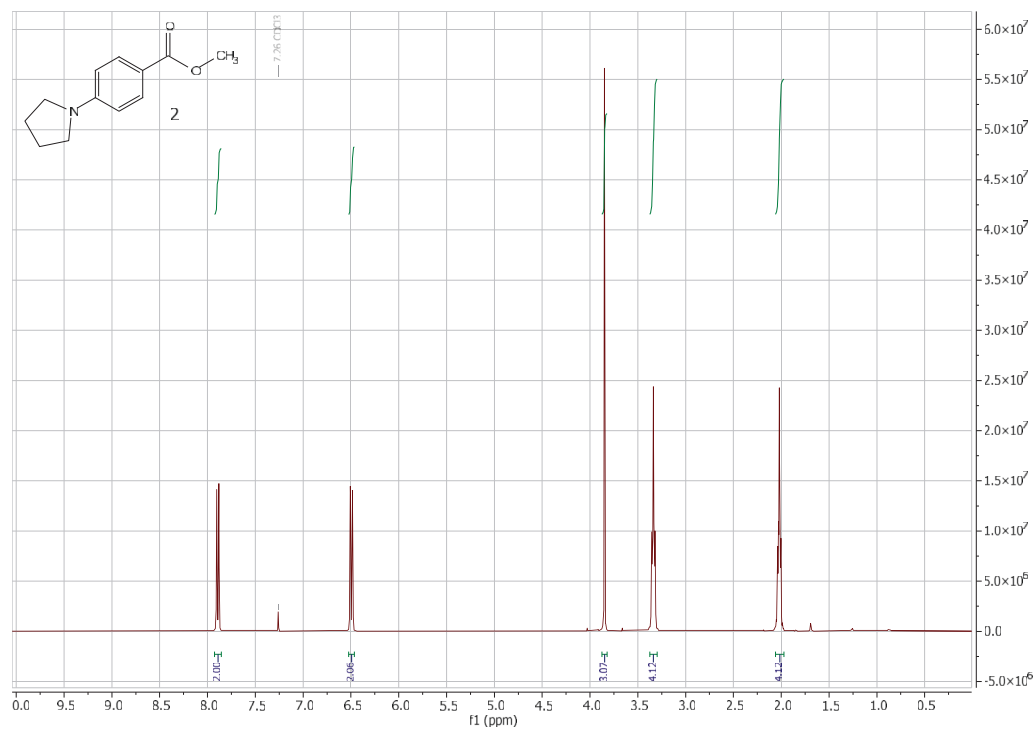
Appendix





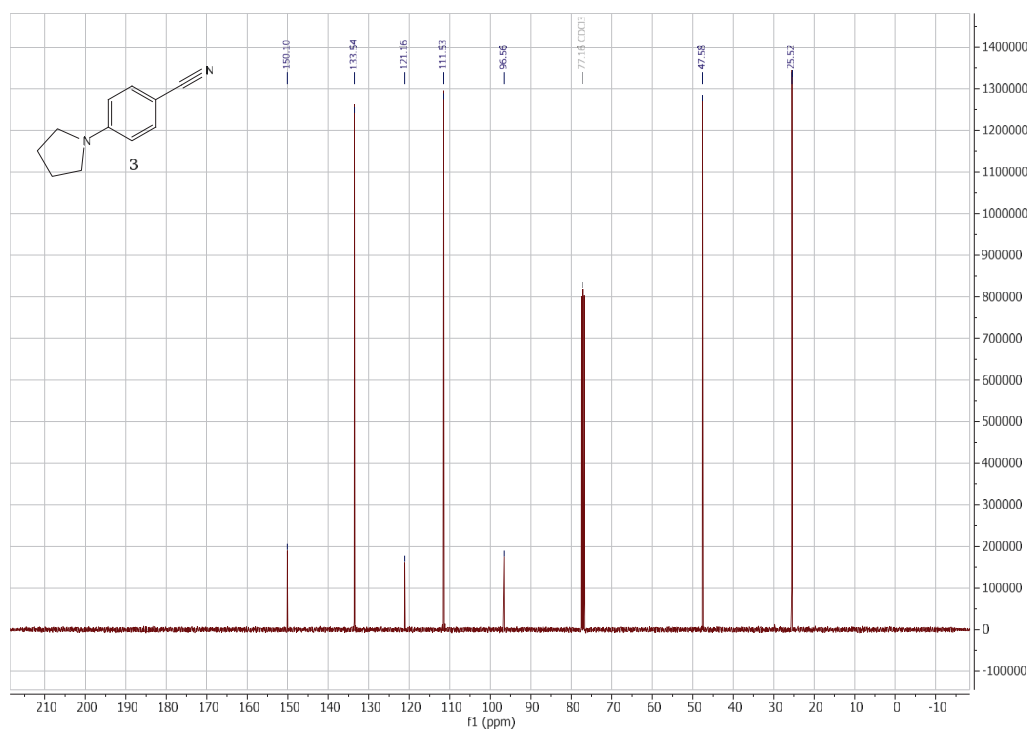
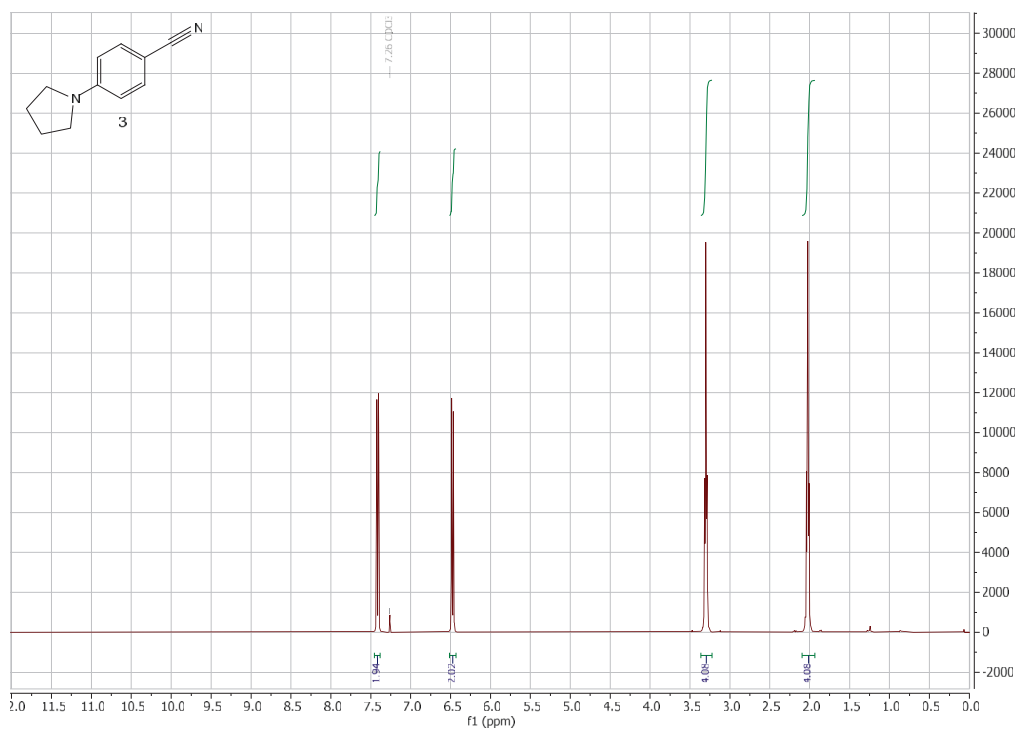
Appendix

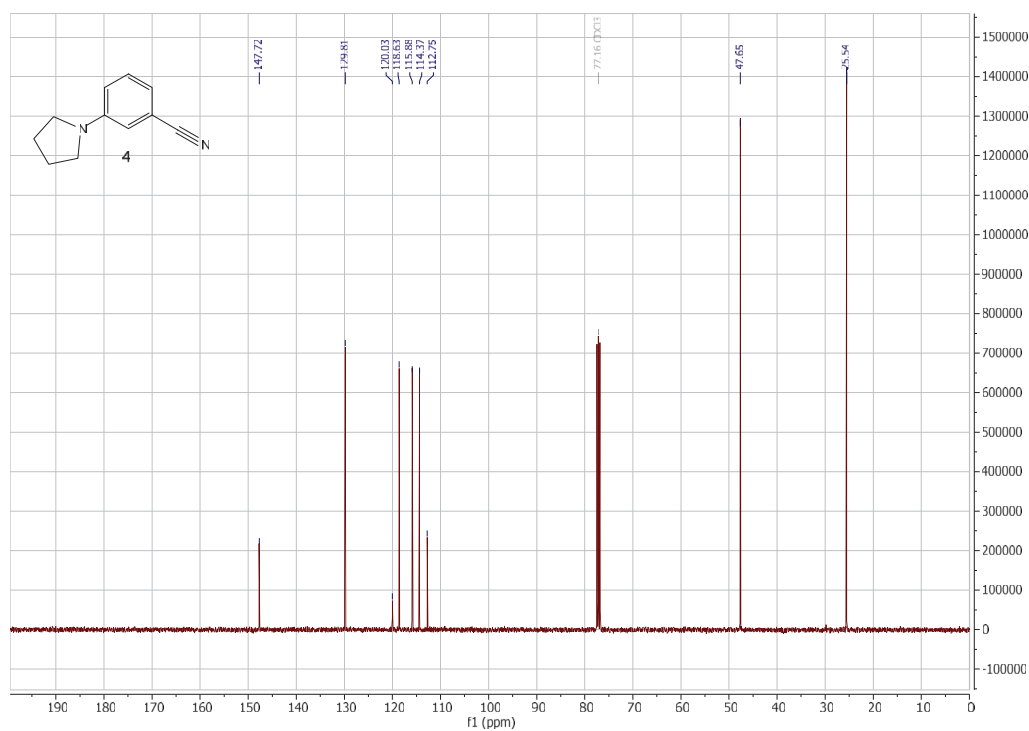
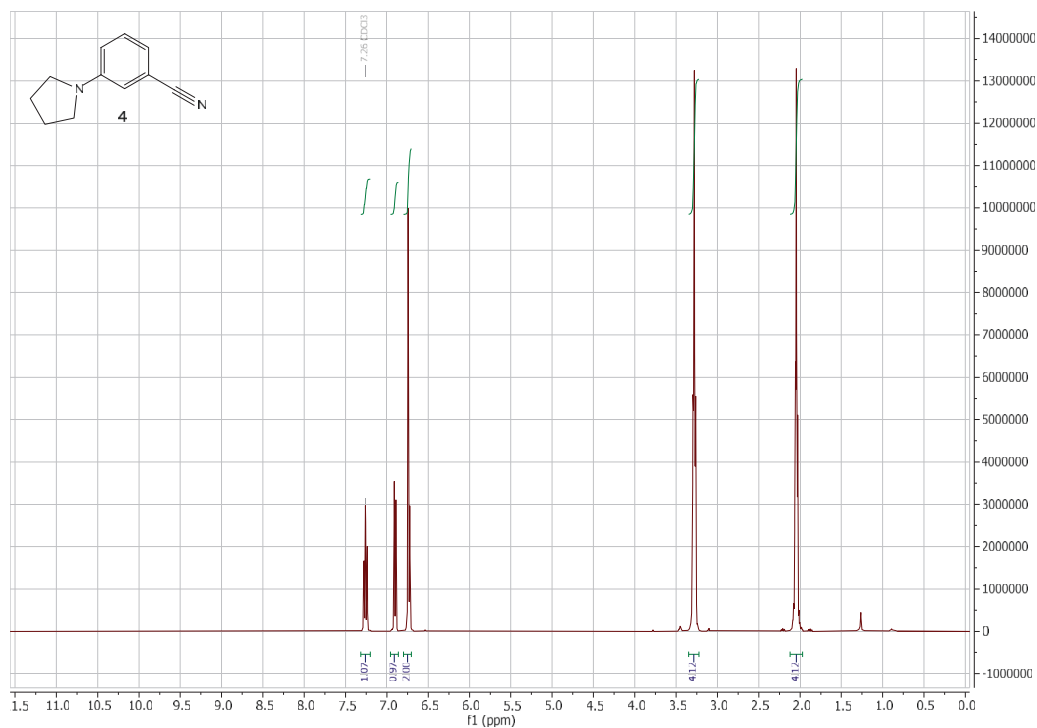


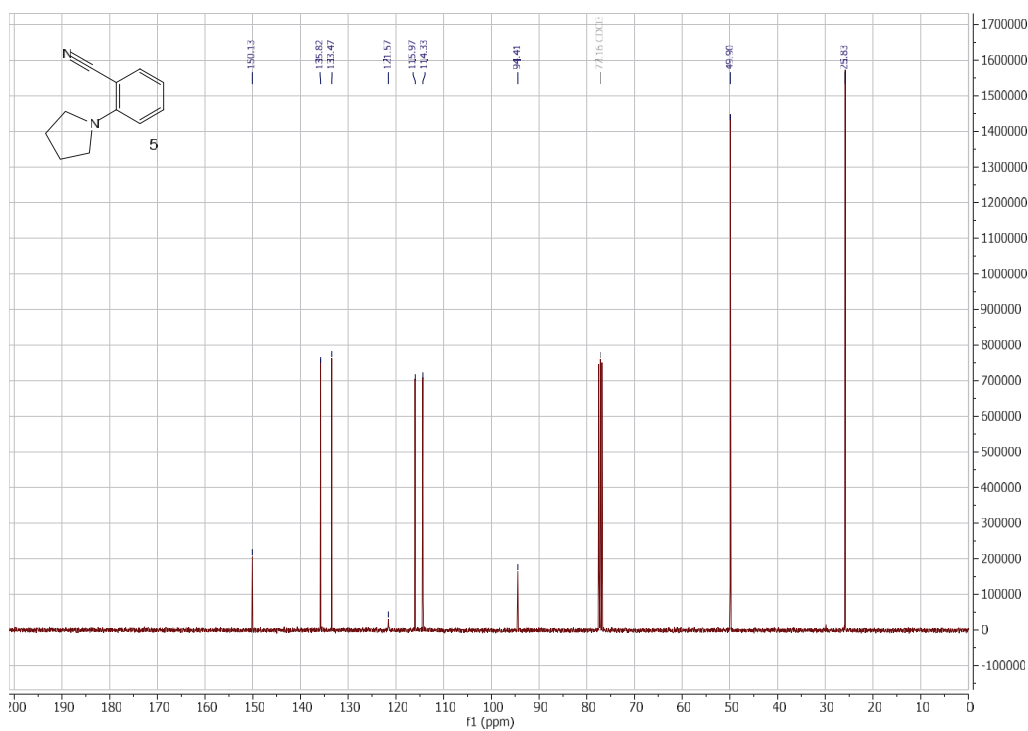
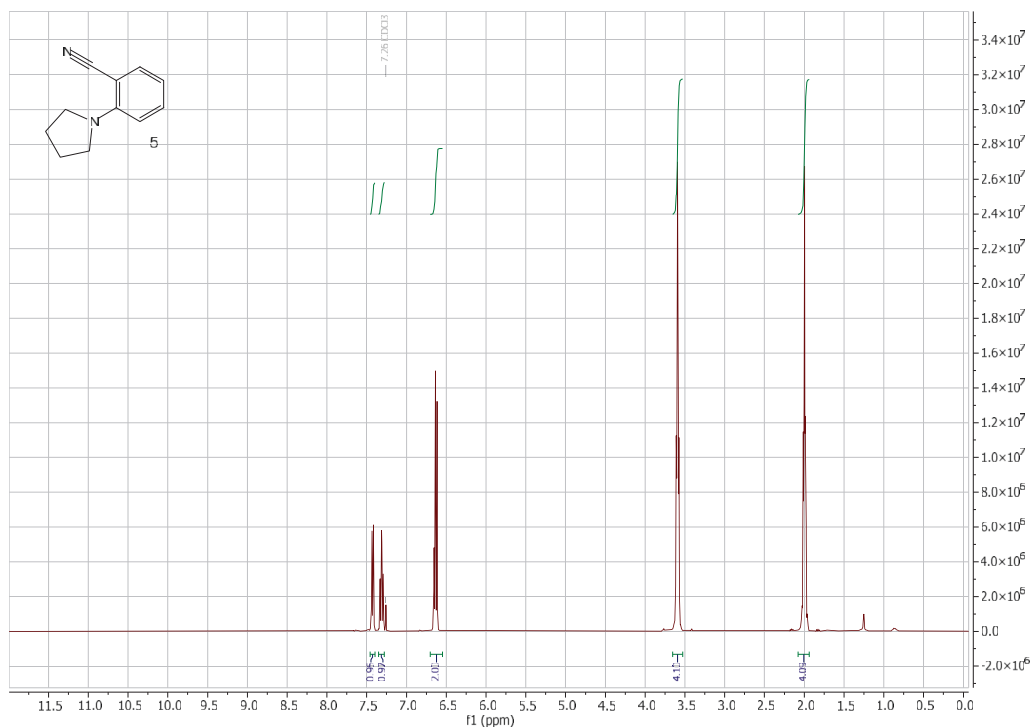


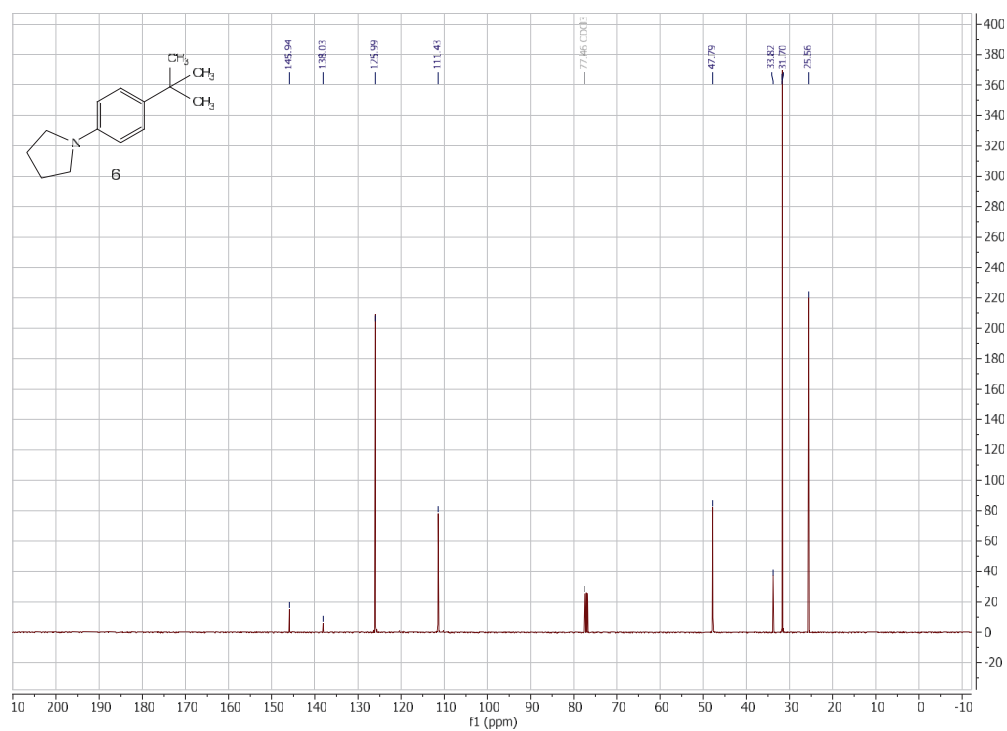
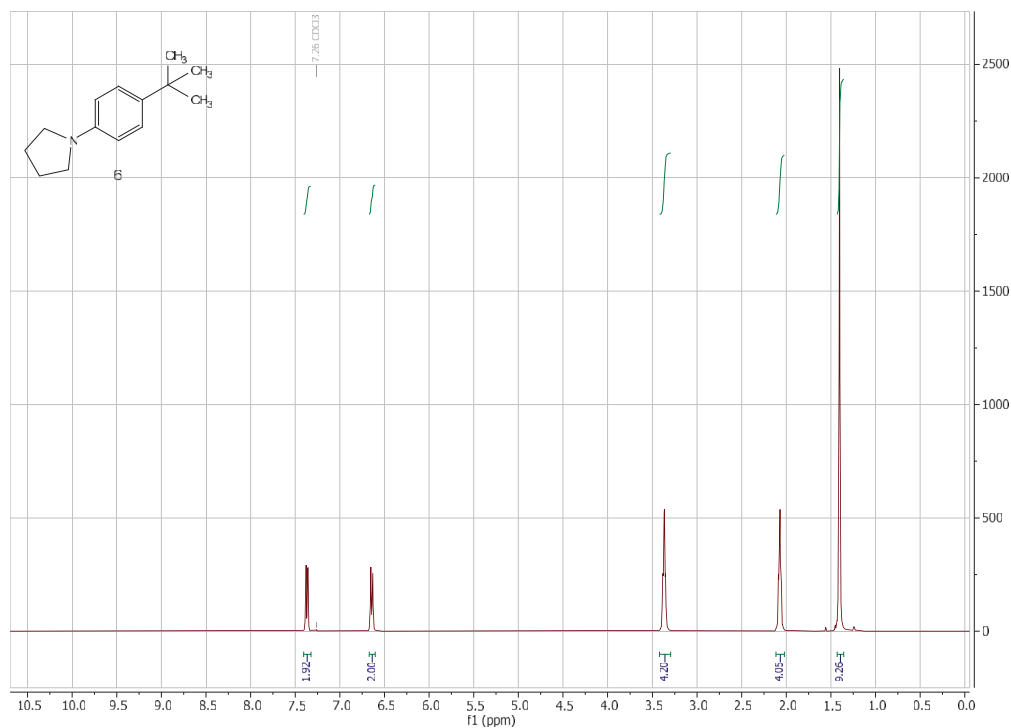
S57

Appendix









S61

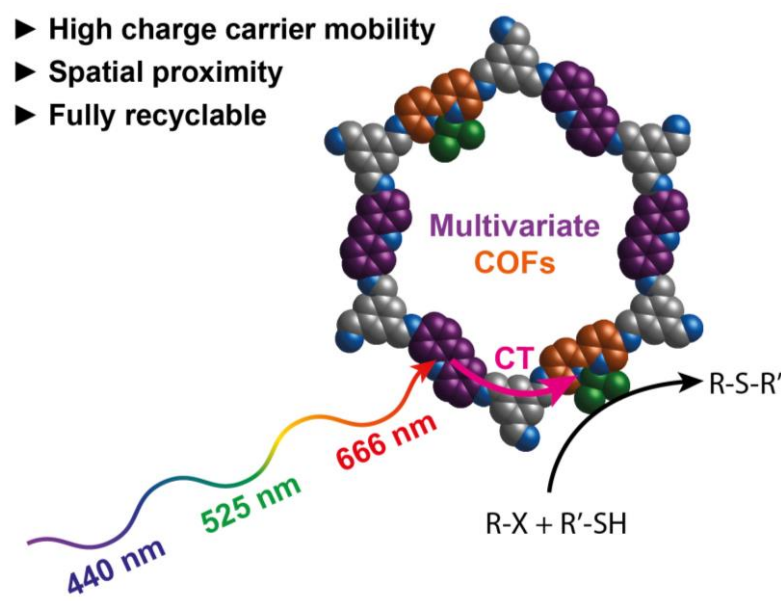
Article III:

Programmable Photocatalytic Activity of Multivariate Covalent Organic Frameworks Used as Metallaphotocatalysts

M. Traxler, S. Reischauer, S. Vogl, J. Roeser, J. Rabeah, C. Penschke, P. Saalfrank, B. Pieber, A. Thomas

Chem. Eur. J. **2022**, e202202967.

Accepted manuscript, DOI: <https://doi.org/10.1002/chem.202202967>



Various multivariate COFs bearing a moiety for photosensitization and complexation of nickel catalysts was synthesized using reticulation with different 1,3,5-triformylbenzene nodes. This enabled the switching between persistent, charge separated species or efficient charge-carrier mobility for different metallaphotocatalytic cross-coupling reactions based on the node unit. The framework showed recyclability and the possibility to drive the reactions using red light irradiation.

RESEARCH ARTICLE

Programmable Photocatalytic Activity of Multivariate Covalent Organic Frameworks Used as Metallaphotocatalysts

Michael Traxler,^{+[a]} Susanne Reischauer,^{+[b,c]} Sarah Vogl,^[a] Jérôme Roeser,^[a] Jabor Rabeah,^[c] Christopher Penschke,^[d] Peter Saalfrank,^[d] Bartholomäus Pieber,^{+[b]} Arne Thomas^{+[a]}

[a] M. Traxler,⁺ Dr. S. Vogl, Dr. J. Roeser, Prof. A. Thomas
Department of Chemistry/Functional Materials

Technische Universität Berlin
Hardenbergstraße 40, 10623 Berlin, Germany
E-mail: arne.thomas@tu-berlin.de

[b] Dr. S. Reischauer,⁺ Dr. B. Pieber
Department of Biomolecular Systems
Max Planck Institute of Colloids and Interfaces
Am Mühlenberg 1, 14476 Potsdam, Germany
E-mail: bartholomaeus.pieber@mpikg.mpg.de

[c] Dr. S. Reischauer⁺
Department of Chemistry and Biochemistry
Freie Universität Berlin
Takustraße 3, 14195 Berlin, Germany

[d] Dr. J. Rabeah
Leibniz Institute for Catalysis (LIKAT Rostock)
Universität Rostock
Albert-Einstein-Straße 29a, 18059 Rostock, Germany

[e] Dr. C. Penschke, Prof. P. Saalfrank
Institut für Chemie
Universität Potsdam
Karl-Liebknecht Straße 24-25, 14476 Potsdam, Germany

[*] These authors contributed equally.

Supporting information for this article is given via a link at the end of the document.

Abstract: The multivariate approach allows to incorporate several functionalities into a single covalent organic framework (COF) and consequently allows the construction of bifunctional materials for cooperative catalysis. The well-defined structure of such multivariate COFs is furthermore ideally suited for structure-activity relationship studies. We report a series of multivariate COFs that contain acridine- and 2,2'-bipyridine linkers connected through 1,3,5-benzenetrioldehyde derivatives. The acridine motif is responsible for broad light absorption, while the bipyridine unit enables complexation of nickel catalysts. These features enable usage of the framework materials as catalysts for light-mediated carbon–heteroatom cross-couplings. Variation of the node units shows that the catalytic activity correlates to the keto-enamine tautomer isomerism. This allows switching between high charge-carrier mobility and persistent, localized charge-separated species depending on the nodes, a tool to tailor the materials for specific reactions. Moreover, nickel-loaded COFs are recyclable and catalyze cross-couplings even using red light irradiation.

Introduction

Combining two or more catalysts that work in concert to enable the formation of a chemical bond (cooperative catalysis, dual catalysis) has recently become a powerful addition to the synthetic chemist's toolbox.^[1] In particular, the combination of nickel- and photocatalysis (metallaphotocatalysis) has led to the discovery of a number of carbon–heteroatom (C–X) and carbon–carbon (C–C) cross-coupling methods that are carried out under

mild conditions using visible-light.^[2–5] These reactions are typically carried out using a photocatalyst in combination with a molecular, homogeneous nickel catalyst. The efficacy of such complex systems depends on a multitude of parameters that are individually optimized to maximize product formation. These include irradiation wavelength, photon flux, activity/selectivity of the nickel catalyst, photoelectronic properties of photocatalysts, base, temperature, solvent and stoichiometry, among others.

The interaction between the catalysts in solution requires persistent excited state lifetimes of the photocatalyst as it must be longer than the time it takes to diffuse to the nickel complex to induce catalysis. Thus, these transformations are limited to photocatalysts that populate triplet excited states with high quantum yields, such as Ir or Ru polypyridyl complexes^[6], and organic compounds that show thermally activated delayed fluorescence.^[7] Similarly, certain semiconducting materials generate sufficiently long-lived charge-separated species.^[8]

Close spatial proximity between the two catalysts is arguably beneficial for electron (or energy) transfer events between the two catalytic species but this parameter is difficult to tune using homogeneous catalysts. Immobilizing the photo- and the nickel catalyst on a support enables controlling the distance between the individual catalysts at the nanoscale. For example, iridium polypyridyl- and nickel bipyridine complexes were integrated in metal–organic frameworks (MOFs),^[9,10] covalent organic frameworks (COFs),^[11,12] and linear polymers.^[13] Indeed, these bifunctional catalysts often showed synergistic effects in terms of higher turnover numbers and catalytic activities in C–C and C–X cross-couplings as compared to using the individual catalysts in solution. A similar trend was observed for MOFs that have

RESEARCH ARTICLE

incorporated catalysts for dual photo-/Lewis acid catalysis.^[14,15] Decoupling the interaction between the photocatalyst and the nickel catalyst from the limiting rate of diffusion was also shown to increase the arsenal of suitable photocatalysts for metallaphotocatalytic reactions.^[16,17] However, these concepts rely on the immobilization of photo- and nickel catalysts on a supporting material that potentially influences transmission of the generated charge carriers to the active metal site.

Another appealing strategy is to integrate a nickel catalyst directly into a photocatalytically active polymeric material. Seminal approaches include the incorporation of nickel atoms into carbon nitride materials^[18–21] and a conjugated microporous polymer that contains a bipyridine motif in its repeating unit that can ligate nickel atoms.^[22,23] However, these ill-defined macrostructures do not allow for detailed structure-activity relationship studies to better understand the underlying processes, which renders knowledge-guided improvement of the bifunctional materials difficult.

Covalent organic frameworks (COFs) are well-defined, crystalline, highly porous polymers with tunable structures that are prepared by covalently attaching multiconnected nodes with linear linkers, which can introduce functional groups into the backbone.^[24–28] When a three or higher connected node component is allowed to react with more than one linker unit, several functionalities can be integrated into the backbone of a single COF material (multivariate approach).^[29–34] Owing to their conjugated backbones, COF materials have been shown to serve as valuable photocatalysts.^[35–39] Using the modularity of COFs the optoelectrical properties can be influenced through, for example, the choice of the node component.^[40,41] We have shown that COFs bearing acridine linkers are promising metal-free, heterogeneous photocatalyst that can be combined with homogeneous nickel complexes for metallaphotocatalysis.^[39] Our results suggested that the β -ketoenamine to imine ratio on the node that connects the linkers is a key parameter influencing charge-carrier separation. Others have reported the integration of nickel complexes into a photocatalytically active COF structure to realize visible-light mediated cross-couplings^[42,43] or hydroxylation of aryl chlorides with water.^[44]

Inspired by these studies, we hypothesized that a multivariate COF prepared from an acridine linker, a linking unit that provides coordination sites for nickel, and benzene-1,3,5-tricarbaldehyde derivatives as 3-connected (3-c) nodes would enable detailed structure-activity relationship studies that shine light on parameters that influence the activity of such bifunctional multivariate COF metallaphotocatalysts. Here, we show that the β -ketoenamine to imine ratio significantly varies the efficacy of such COFs as catalysts for C–S and C–N cross-couplings. Our results show that the imine-form leads to high charge carrier mobility that is ideal for activating nickel sites that are ligated at the COF backbone. In contrast, β -ketoenamine tautomerized COFs have localized, persistent charge-separated species that is key for diffusion limited interaction with homogeneous nickel complexes.

Results and Discussion

Our investigations started with the synthesis of a set of eight multivariate COFs using 2,6-acridinediamine (Acr) as chromophoric linker and 2,2'-bipyridine-5,5'-diamine (Bpy) as

metal binding site (Figure 1a). Since both linkers are varying in length, an Acr/Bpy ratio of 2:1 and 1:2 was used to ensure the formation of extended structures of the expected honeycomb topology.^[30] The number of hydroxy groups on the 3-connected benzene-1,3,5-tricarbaldehyde nodes was varied within each series of Acr/Bpy COFs to investigate the influence of the β -ketoenamine to imine ratio on charge-carrier mobility. 1,3,5-triformylphloroglucinol (Tp) was used to synthesize the irreversible keto tautomeric COFs, whereas 1,3,5-triformylbenzene (Tf) carries no tautomerizable group and thus yields a fully imine linked COF (Figure 2e). 2,4-dihydroxybenzene-1,3,5-tricarbaldehyde (DHTA) and 2-hydroxybenzene-1,3,5-tricarbaldehyde (HTA) was used to prepare COF backbones that have reversible tautomeric forms.^[40] All multivariate Acr^x-L-Bpy^y COFs (where x:y = 2:1 or 1:2 and L = Tp, DHTA, HTA or Tf) were synthesized by an acid catalyzed Schiff base reaction (detailed information for the synthesis of all COFs can be found in Section S3.2 in the Supporting Information). The crystallinity of the synthesized COFs was determined by powder X-ray diffraction (PXRD) analyses using Cu K α radiation (Figure 1b and Figure S5). All materials show an intense reflection in the low angle area at around 3.5 2 θ degrees, which can be assigned to the (100) facet of a primitive hexagonal lattice. Weaker reflections in the 5–10 2 θ degree range and a broad peak at 26.5 2 θ degrees confirmed the formation of crystalline, π - π stacked two-dimensional structures for all COFs. According to the symmetry of the linkers, the structural models for the multivariate COFs were constructed by generating the expected 2D layers with **hcb** topology. The models were geometrically optimized, and their corresponding theoretical PXRD patterns were compared to the experimentally measured patterns. Theoretical diffraction patterns of models with eclipsed stacking sequences (AA) are in good agreement with the measured diffractograms (Figure S4–S5).

Nitrogen sorption measurements at 77 K confirmed the porosity of all COFs (Figure 1c and Figure S6). Based on the Brunauer-Emmett-Teller (BET) method, surface areas of the COFs were determined. Among the series of Acr²-L-Bpy¹ COFs, Acr²-HTA-Bpy¹ showed the highest specific surface area (1093 m²/g). The fully imine-based COF Acr²-Tf-Bpy¹ showed the lowest surface area of 210 m²/g. A different trend was found for Acr¹-L-Bpy² COFs, where the highest surface area was obtained using DHTA (926 m²/g) and the lowest using HTA (175 m²/g). The pore size of all Acr²-L-Bpy¹ COFs are close to theoretical values (Figure S7). Fourier transform infrared (FT-IR) spectroscopy confirmed the formation of the framework materials. Characteristic signals of the precursors disappeared, while peaks that can be assigned to C=O and C=C or C=N vibrations, respectively, are present after the COF synthesis (Figure S8–S9). Thermal stability of the multivariate COFs was investigated using thermogravimetric analysis (TGA). After an initial weight loss due to adsorbed moisture and solvent molecules, all materials were thermally stable up to 350 °C (Figure S10).

The structural integrity of frameworks was studied by ¹³C cross-polarization magic angle spinning nuclear magnetic resonance (CP-MAS NMR) analyses (Figure S11). For Acr^x-Tp-Bpy^y COFs, a distinct carbonyl carbon (C=O) peak around 180–185 ppm as well the C=C signal at 105 ppm confirm the dominant presence of the keto form.^[45] These two peaks decreased with a lower degree of tautomerization when less hydroxy groups were on the node and completely vanished for Acr^x-Tf-Bpy^y, indicative of increasing

RESEARCH ARTICLE

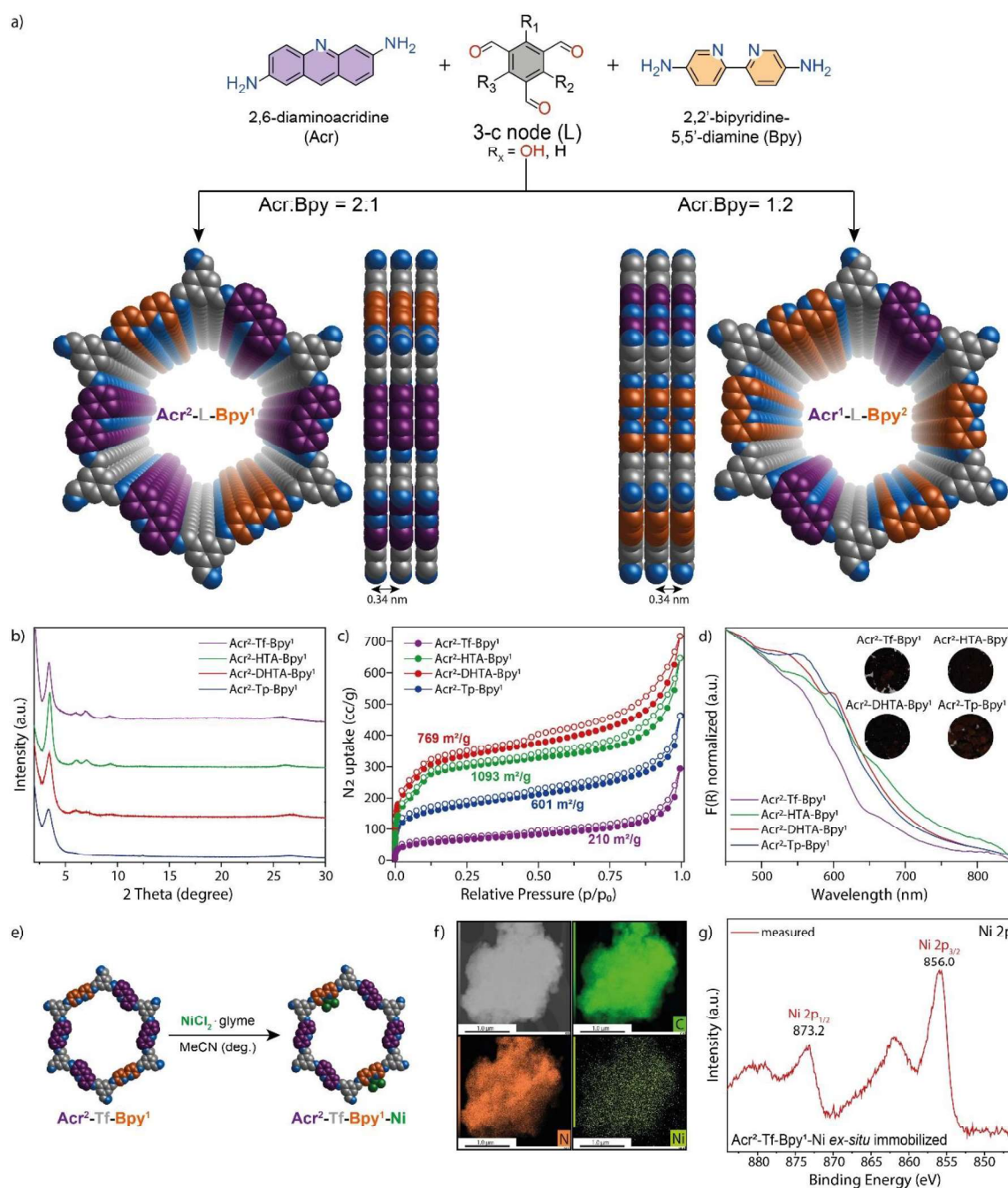


Figure 1. Synthesis and characterization of $\text{Acr}^x\text{-L-Bpy}^y$ ($x:y = 1:2$ or $2:1$; $L = \text{Tp, DHTA, HTA}$ or Tf). (a) Scheme of the synthesis of the COFs; top and side views of $\text{Acr}^x\text{-L-Bpy}^y$ COFs showing the ideal eclipsed (AA) structures. (b) Experimental X-ray diffraction patterns for $\text{Acr}^2\text{-L-Bpy}^1$ COFs, calculated BET surface areas are shown in the insets. (c) N_2 sorption isotherms for $\text{Acr}^2\text{-L-Bpy}^1$ COFs, calculated BET surface areas are shown in the insets. (d) UV-vis diffuse reflectance spectra for $\text{Acr}^2\text{-L-Bpy}^1$ COFs. The inset shows optical images of the COF powders. (e) Schematic illustration of the preparation of $\text{Acr}^2\text{-Tf-Bpy}^1\text{-[Ni]}$. (f) TEM image of $\text{Acr}^2\text{-Tf-Bpy}^1$ and the elemental mapping of carbon, nitrogen and nickel. (g) XPS Ni 2p core-level spectrum of $\text{Acr}^2\text{-Tf-Bpy}^1\text{-[Ni]}$.

RESEARCH ARTICLE

amounts of imine tautomers among the series. Signals between 115–150 ppm confirm the presence heteroaromatic linkers in all COF backbones. Diagnostic signals at 150 and 133 ppm were assigned to the bipyridine motif and confirm an increasing bipyridine:acridine ratio when higher amounts of 2,2'-bipyridine-5,5'-diamine were used for the COF synthesis (Figure S25b).^[46,47] X-ray photoelectron spectroscopy (XPS) also depicted the gradual reduction of keto-enamine tautomerization in the series of COFs. Deconvolution revealed signals in the N 1s spectrum at 400 eV that can be assigned to the secondary amine group of the keto-enamine linkage. The ratio between these signals gradually decreases with increased number of tautomerizable groups and vanishes for fully imine-based COFs Acr^x-Tp-Bpy^y (Figure S12). Aromatic nitrogen atoms of the acridine and bipyridine atoms show a signal with the binding energy of 399 eV in the N 1s spectrum. The different amounts of bipyridine units within the COF backbones can be determined qualitatively, with a more pronounced signal for Acr¹-Tp-Bpy² compared to Acr²-Tp-Bpy¹. For the other COFs this peak is overlying with the signals of the imine and enol bonded nitrogen atoms. To quantitatively determine the amount of Acr and Bpy units in the backbone of the multivalent materials, Acr^x-Tp-Bpy^y COFs were digested in a solution of 0.1 mL of 10 M NaOH in D₂O and 0.5 mL DMSO-d₆ at 120 °C and subsequently analyzed with ¹H-NMR. Integration of the peaks at 7.89 and 7.69 ppm that can be assigned to Bpy and Acr, respectively, show that the amount of substrates used in the synthesis is in agreement with the incorporated ratio of the two linkers, demonstrating no preferential reaction of the linkers (Figure S13).

Using diffuse reflectance ultraviolet-visible (UV-vis) spectroscopy we confirmed that multivariate COFs broadly absorb across the visible-light spectrum (Figure 1d, S15a). The absorption onsets of all COFs are above 700 nm. In comparison, COFs that exclusively contain bipyridine linkers (L-Bpy) absorb less broadly (Figure S24). This shows that the introduction of the acridine moiety is key for efficient solar harvesting.^[39] Using calculations on the level of density functional theory (DFT) we discovered that the introduction of a bipyridine linker into the backbone of the framework is not changing the band gap of the multivariate Acr²-L-Bpy¹ COFs (Section S4.10), confirming our experimental findings.

Before testing the materials in cross-coupling reaction as suitable catalysts, nickel complexation at Acr²-Tp-Bpy¹ was tested *ex situ* by refluxing a suspension of the COF and NiCl₂·glyme in acetonitrile (Figure 1e). After confirming the crystallinity of the material by PXRD (Figure S31), the resulting Acr²-Tp-Bpy¹-Ni was characterized by transmission electron microscopy (TEM) and shows rather undefined morphology of the particles (Figure 1f). Elemental mapping illustrates a homogeneous distribution of nickel, nitrogen and carbon within the material. XPS analysis confirmed successful coordination of Ni^{II} on the bipyridine nitrogen atoms within the COF (Figure 1g). The Ni 2p spectrum showed the presence of nickel with a doublet at 855.7 eV and 873.4 eV, assigned to 2p_{3/2} and 2p_{1/2} signals for Ni^{II} species, respectively. Inductive coupled plasma - optical emission spectroscopy (ICP-OES) was used to quantify the immobilization of the transition metal (Table S9) and showed a nickel loading of 3.59 mg g⁻¹, corresponding to an occupation of 5.1% of bipyridine functionalities.

With the fully characterized Acr^x-L-Bpy^y COFs in hand, we sought to study if these bifunctional materials are suitable as

heterogeneous metallaphotocatalysts for carbon–heteroatom cross-couplings in presence of a nickel(II) salt (*in situ* complexation). Indeed, Acr²-Tp-Bpy¹ showed high catalytic activity in the C–S coupling of 4-iodobenzotrifluoride with methyl 3-mercaptopropionate. Almost quantitative formation of the desired product (**1**) was achieved within three hours using 440 nm LEDs (Figure 2a, Entry 1). Control studies showed that only small amounts of the coupling product were formed without the Ni^{II} salt, or Acr²-Tp-Bpy¹ (Entry 2,3). No reaction occurred in the absence of a base or light (Entry 4,5). Nickel complexation can also be carried out prior to catalysis (Entry 6).

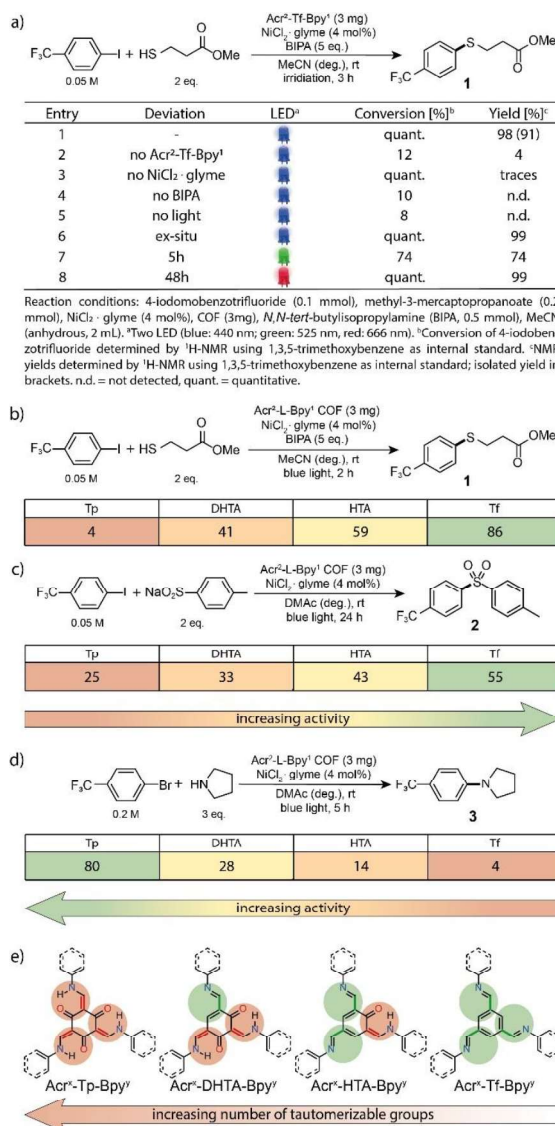


Figure 2. Optimized conditions and control experiments using blue, green and red light for the C–S between 4-iodobenzotrifluoride and 3-mercaptopropionate (a). Screening of Acr²-L-Bpy¹ COFs for the coupling of 4-iodobenzotrifluoride with 3-mercaptopropionate (b) and sodium *p*-toluenesulfonate (c); NMR yields determined by ¹H-NMR using internal standard. COFs bearing linkers with different tautomerizable groups (d).

RESEARCH ARTICLE

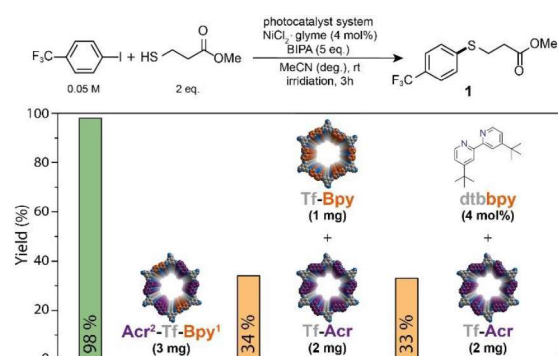


Figure 3. Comparison of the activities between multivalent COF (left), physical mixture of respective COFs (middle) and semi-heterogeneous catalysis (right).

High energy of blue light potentially causes deactivation of nickel catalysts and can lead to undesired side reactions.^[16] Longer wavelengths do not only serve as a tool to overcome such drawbacks, but also potentially provide better scalable protocols^[48] and enable irradiation through tissue^[49], which is a promising feature towards biological applications. Consequently, we were delighted to see that Acr²-Tf-Bpy¹ shows high catalytic activity using green light (Entry 7) and even results in quantitative product formation after 48 h using red LEDs (Entry 8). By comparing the series of Acr²-L-Bpy¹ COFs as catalysts, for the same cross-coupling reaction a clear trend regarding the nodes was identified (Figure 2b). Fully tautomerized Acr²-Tp-Bpy¹ showed the lowest catalytic activity with a yield of 4% after 2 h irradiation time. Decreasing the number of hydroxy groups on the node resulted in a gradual increase of the desired product under identical conditions. The same activity pattern was observed in the coupling of 4-iodobenzotrifluoride and sodium *p*-toluenesulfonate (Figure 2c), where the same overall trend was found for Acr¹-L-Bpy² and L-Bpy COFs, showing less than 45 and 36% activity per added nickel center (Table S4). However, the related C–N coupling between pyrrolidine and 4-bromobenzotrifluoride showed a reversed trend (Figure 2d). Here, the keto-tautomer Acr²-Tp-Bpy¹ gave the highest yield, while the corresponding imine-based COF showed low catalytic activity. This discrepancy can be rationalized by the different involved mechanisms. C–S couplings require coordination of Ni to a bipyridine ligand. In C–N cross-couplings, the secondary amine is added in large excess, because it simultaneously serves as substrate, base and, more importantly, ligand for the first-row transition metal.^[50] As such, this reaction is catalyzed through a homogeneous Ni(pyrrolidine)_n complex that is activated by the COF that only acts as photocatalyst. Hence, the trend in the COF activity results from the fact that the irreversible tautomer stabilizes the conduction band electrons located at the acridine motif, resulting in a persistent charge-separated species that is ideally suited for a diffusion limited dual catalytic interaction with a homogeneous nickel intermediate.^[39] In contrast, in the C–S cross-couplings nickel catalysis requires bipyridine ligation and occurs therefore directly at the COF backbone. Consequently, this transformation benefits from high charge carrier mobility governed by a fully imine-based backbone. These results are supported by electron paramagnetic resonance (EPR) spin

trapping experiments that provide evidence for enhanced formation of spin adducts when a mixture of metalated Acr²-Tf-Bpy¹-Ni, 5,5-dimethyl-1-pyrrolin-*N*-oxid (DMPO) and 4-iodobenzotrifluoride in acetonitrile is irradiated compared to the Acr²-Tp-Bpy¹-Ni (Figure S19, see Section S4.12 for details). Next, we aimed to investigate if the high spatiotemporal control that results from the close proximity of the photocatalyst (COF) and the nickel center in combination with the high charge-carrier mobility is superior to related, diffusion limited transformations. We compared the catalytic activity of *in situ* nickel loaded Acr²-Tf-Bpy¹ with two other catalytic systems in the cross-coupling of 4-iodobenzotrifluoride with methyl 3-mercaptopropionate (Figure 3). One catalytic system contained a mixture of a photocatalytic COF that only contains acridine units (Tf-Acr; Section S5.3) with a nickel containing bipyridine COF (Tf-Bpy; Section S5.1) in the ratio of 2:1 (Figure 3). The third catalytic cocktail combined the photocatalytic Tf-Acr COF with a homogeneous nickel 4,4'-di-*tert*-butyl-2,2'-dipyridyl (dtbbpy)

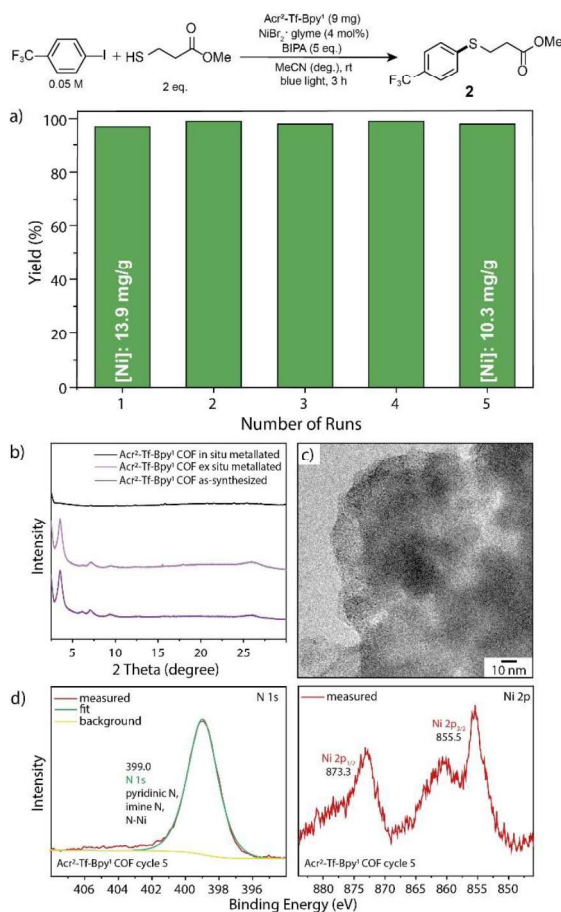


Figure 4. (a) Recyclability studies of Acr²-Tf-Bpy¹ for the C–S between 4-iodobenzotrifluoride and 3-mercaptopropionate (NMR yields determined by ¹H-NMR using 1,3,5-trimethoxybenzene as internal standard). (b) PXRD analysis of Acr²-Tf-Bpy¹ before and after photocatalysis (in situ metalation), and ex situ metalation. (c) TEM analyses of Acr²-Tf-Bpy¹ after photocatalysis. (d) N 1s and Ni 2p XPS core level spectra of the Acr²-Tf-Bpy¹ COF after 5 recycling cycles of photocatalytic dual nickel C–S cross-coupling.

RESEARCH ARTICLE

complex. Under identical conditions (3 h at 440 nm), the bifunctional material produced the desired coupling molecule in almost quantitative yield, whereas both diffusion limited catalytic processes only resulted in modest conversion.

Finally, we studied the recyclability of the bifunctional material using blue (440 nm) light in the thioetherification (Figure 4a). The first experiment was carried through *in situ* catalyst formation using the conditions reported in Figure 2a. ICP-analysis revealed that this material has a nickel content of 13.9 mg g⁻¹, corresponding to an occupation of 20.0% of bipyridine functionalities. The difference in nickel loading compared to the *ex situ* prepared material described above can be attributed to the disruption of the π - π stacking interactions by treating the material with light.^[37,51] This leads to loss of crystallinity using *in situ* metalation, enabling a larger amount of nickel to be immobilized (Figure 4b), due to the diminished long-range order. However, after the respective reaction time, the heterogeneous catalyst was separated, washed and reused without adding additional Acr²-Tf-[Bpy]¹ or nickel(II) salt. The bifunctional, nickel charged COF could be recycled five times without significant loss in catalytic activity, suggesting that the nickel atoms strongly coordinate to the bipyridine linkers in the COF. After the last cycle, a nickel loading of 10.3 mg g⁻¹ showed that most of the nickel atoms present after the first cycle are still immobilized. FT-IR spectroscopy confirmed the intact chemical structure of the COF after the reaction (Figure S32), which proves that the short-range order of the material is preserved, although the long-range periodicity is lost under photocatalytic conditions. Additionally, the morphology of the material was analyzed by TEM and did not alter during the recycling study (Figure 4c and S33). XPS spectra after 5 reaction cycles showed that both the N 1s and Ni 2p signal remained unchanged after the photocatalytic cross-coupling reactions (Figure 4d). This confirms the formation of a fully heterogeneous nickel complex embedded into a stable COF matrix. Moreover, UV-vis spectroscopy showed no change in optical properties after the reaction (Figure S35).

Conclusion

In summary a series of multivariate COFs containing a bipyridine and acridine linker were prepared using different three-connected nodes and their application as catalysts for light-mediated nickel catalyzed carbon-heteroatom cross-couplings was evaluated. Four different 1,3,5-triformylbenzene derivatives were selected as nodes to study the influence of β -ketoenamine to imine ratio in the frameworks on catalytic activity. Our results show that the imine-form is key for high charge-carrier mobility that transfers conduction band electrons located at the acridine photocatalyst to an active nickel center that is attached at the bipyridine moieties. In contrast, persistent charge separated species located at the acridine moiety are formed upon excitation of COFs that have β -ketoenamine connections. This was shown to be beneficial in the diffusion limited activation of homogeneous nickel complexes. A multivariate COF that hosts nickel atoms was further shown to be a recyclable heterogeneous C-S cross-coupling catalyst that can be activated with long wavelengths.

Experimental Section

Synthesis of Acr^x-L-Bpy^y COFs (x:y = 2:1 or 1:2 and L = Tp, DHTA, HTA or Tf). A typical COF synthesis is exemplified for Acr²-Tf-Bpy¹. A Pyrex tube (o.d. \times i.d. = 15 \times 10 mm² and length 15 cm) is charged with 1,3,5-triformylbenzene (Tf) (16.2 mg, 0.1 mmol), 2,6-diaminoacridine (Acr) (20.9 mg, 0.1 mmol), 2,2'-bipyridine-5,5'-diamine (Bpy) (9.3 mg, 0.05 mmol), 1.5 mL of *n*-BuOH, 1.5 mL of anhydrous *o*-DCB and 0.5 mL of 6 M aqueous acetic acid. This mixture was sonicated for 15 minutes in order to get a homogenous dispersion. The tube was then flash frozen at 77 K (liquid N₂ bath) and degassed by three freeze-pump-thaw cycles. The tube was sealed off and then heated at 120 °C for 3 days. A dark red colored precipitate was collected by filtration and washed with acetone, methanol and cyclohexane. The powder collected was dried at 120 °C to give a dark red colored powder.

General experimental procedure for photocatalytic experiments. An oven dried vial (19 x 100 mm) equipped with a stir bar was charged with NiCl₂·glyme (4–12 μ mol), Acr^x-L-Bpy^y COF, 4-halobenzotrifluoride and nucleophile. The solvent (anhydrous) was added and the vessel was sealed with a septum and Parafilm. The mixture was stirred for 1 minute at high speed, followed by sonication for 5 minutes and degassing by bubbling argon for 10 minutes. The reaction mixture was stirred at 800 rpm and irradiated with 440 nm, 535 nm or 666 nm LED lamps. After the respective reaction time, 1,3,5-trimethoxybenzene (1 eq.) was added as internal standard to the reaction vessel, the mixture was shaken and an aliquot (200 μ L) was removed, filtered, diluted with DMSO-d₆ and analyzed by ¹H NMR.

Acknowledgements

M.T. and S.R. contributed equally to this work and either has the right to list them self first in bibliographic documents. Funded by the Deutsche Forschungsgemeinschaft (DFG, German Research Foundation) under Germany's Excellence Strategy – EXC 2008 – 390540038 – UniSysCat. M.T. thanks the Einstein Center for Catalysis/Berlin International Graduate School for Natural Science and Engineering for funding. S.R. and B.P. thank the Max-Planck Society for generous financial support. B.P. acknowledges financial support by the Boehringer Ingelheim Foundation (Plus 3 perspectives program) and the Deutsche Forschungsgemeinschaft (DFG, German Research Foundation, BP 1635/2-19). The authors thank Christina Eichenauer for surface area measurements, Heike Runge for SEM and TEM analyses.

Conflict of Interests

The authors declare no conflicts.

Keywords: catalysis • covalent organic frameworks • cross-coupling • photoredox • tuneable activity

References

- [1] S. Martínez, L. Veth, B. Lainer, P. Dydio, *ACS Catal.* **2021**, *11*, 3891–3915.
- [2] J. Twilton, C. C. Le, P. Zhang, M. H. Shaw, R. W. Evans, D. W. C. MacMillan, *Nat. Rev. Chem.* **2017**, *1*, 0052.

RESEARCH ARTICLE

- [3] J. A. Milligan, J. P. Phelan, S. O. Badir, G. A. Molander, *Angew. Chem. Int. Ed.* **2019**, *58*, 6152–6163.
- [4] C. Zhu, H. Yue, J. Jia, M. Rueping, *Angew. Chem. Int. Ed.* **2021**, *60*, 17810–17831.
- [5] A. Y. Chan, I. B. Perry, N. B. Bissonnette, B. F. Buksh, G. A. Edwards, L. I. Frye, O. L. Garry, M. N. Lavagnino, B. X. Li, Y. Liang, E. Mao, A. Millet, J. V. Oakley, N. L. Reed, H. A. Sakai, C. P. Seath, D. W. C. MacMillan, *Chem. Rev.* **2022**, *122*, 1485–1542.
- [6] D. M. Arias-Rotondo, J. K. McCusker, *Chem. Soc. Rev.* **2016**, *45*, 5803–5820.
- [7] M. A. Bryden, E. Zyman-Colman, *Chem. Soc. Rev.* **2021**, *50*, 7587–7680.
- [8] S. Gisbertz, B. Pieber, *ChemPhotoChem* **2020**, *4*, 456–475.
- [9] Y. Y. Zhu, G. Lan, Y. Fan, S. S. Veroneau, Y. Song, D. Micheroni, W. Lin, *Angew. Chem. Int. Ed.* **2018**, *57*, 14090–14094.
- [10] G. Lan, Y. Quan, M. Wang, G. T. Nash, E. You, Y. Song, S. S. Veroneau, X. Jiang, W. Lin, *J. Am. Chem. Soc.* **2019**, *141*, 15767–15772.
- [11] A. López-Magano, B. Ortín-Rubio, I. Imaz, D. Maspoch, J. Alemán, R. Mas-Ballester, *ACS Catal.* **2021**, *11*, 12344–12354.
- [12] A. Jati, K. Dey, M. Nurhuda, M. A. Addicoat, R. Banerjee, B. Maji, *J. Am. Chem. Soc.* **2022**, *144*, 7822–7833.
- [13] Y. Pan, N. Zhang, C. H. Liu, S. Fan, S. Guo, Z. M. Zhang, Y. Y. Zhu, *ACS Catal.* **2020**, *10*, 11758–11767.
- [14] Y. Quan, G. Lan, Y. Fan, W. Shi, E. You, W. Lin, *J. Am. Chem. Soc.* **2020**, *142*, 1746–1751.
- [15] Y. Quan, Y. Song, W. Shi, Z. Xu, J. S. Chen, X. Jiang, C. Wang, W. Lin, *J. Am. Chem. Soc.* **2020**, *142*, 8602–8607.
- [16] S. Reischauer, V. Strauss, B. Pieber, *ACS Catal.* **2020**, *10*, 13269–13274.
- [17] Z. Zhao, S. Reischauer, B. Pieber, M. Delbianco, *Green Chem.* **2021**, *23*, 4524–4530.
- [18] X. Zhao, C. Deng, D. Meng, H. Ji, C. Chen, W. Song, J. Zhao, *ACS Catal.* **2020**, *10*, 15178–15185.
- [19] A. Vijeta, C. Casadevall, S. Roy, E. Reisner, *Angew. Chem. Int. Ed.* **2021**, *60*, 8494–8499.
- [20] A. Vijeta, C. Casadevall, E. Reisner, *Angew. Chem. Int. Ed.* **2022**, *61*, e202203176.
- [21] M. Kwak, J. Bok, B. H. Lee, J. Kim, Y. Seo, S. Kim, H. Choi, W. Ko, W. Hooch Antink, C. W. Lee, G. H. Yim, H. Seung, C. Park, K. S. Lee, D. H. Kim, T. Hyeon, D. Yoo, *Chem. Sci.* **2022**, *13*, 8536–8542.
- [22] C. Cavedon, S. Gisbertz, S. Reischauer, S. Vogl, E. Sperlich, J. H. Burke, R. F. Wallick, S. Schrottke, W.-H. Hsu, L. Anghileri, Y. Pfeifer, N. Richter, C. Teutloff, H. Müller-Werkmeister, D. Cambié, P. H. Seeberger, J. Vura-Weis, R. M. van der Veen, A. Thomas, B. Pieber, *Angew. Chem. Int. Ed.* **2022**, e202211433.
- [23] W.-H. Hsu, S. Reischauer, P. H. Seeberger, B. Pieber, D. Cambié, *Beilstein J. Org. Chem.* **2022**, *18*, 1123–1130.
- [24] C. S. Diercks, O. M. Yaghi, *Science* **2017**, *355*, eaal1585.
- [25] F. Haase, B. V. Lotsch, *Chem. Soc. Rev.* **2020**, *49*, 8469–8500.
- [26] T. Zhang, G. Xing, W. Chen, L. Chen, *Mater. Chem. Front.* **2020**, *4*, 332–353.
- [27] X. Zhao, P. Pachfule, A. Thomas, *Chem. Soc. Rev.* **2021**, *50*, 6871–6913.
- [28] A. M. Evans, M. J. Strauss, A. R. Corcos, Z. Hirani, W. Ji, L. S. Hamachi, X. Aguilar-Enriquez, A. D. Chavez, B. J. Smith, W. R. Dichtel, *Chem. Rev.* **2022**, *122*, 442–564.
- [29] A. Nagai, Z. Guo, X. Feng, S. Jin, X. Chen, X. Ding, D. Jiang, *Nat. Commun.* **2011**, *2*, 536.
- [30] N. Huang, L. Zhai, D. E. Coupry, M. A. Addicoat, K. Okushita, K. Nishimura, T. Heine, D. Jiang, *Nat. Commun.* **2016**, *7*, 12325.
- [31] Z. F. Pang, S. Q. Xu, T. Y. Zhou, R. R. Liang, T. G. Zhan, X. Zhao, *J. Am. Chem. Soc.* **2016**, *138*, 4710–4713.
- [32] L. Feng, K. Y. Wang, G. S. Day, H. C. Zhou, *Chem. Soc. Rev.* **2019**, *48*, 4823–4853.
- [33] T. Zhou, X. Huang, Z. Mi, Y. Zhu, R. Wang, C. Wang, J. Guo, *Polym. Chem.* **2021**, *12*, 3250–3256.
- [34] Y. Xie, T. Pan, Q. Lei, C. Chen, X. Dong, Y. Yuan, J. Shen, Y. Cai, C. Zhou, I. Pinnau, Y. Han, *Angew. Chem. Int. Ed.* **2021**, *60*, 22432–22440.
- [35] V. S. Vyas, V. W. H. Lau, B. V. Lotsch, *Chem. Mater.* **2016**, *28*, 5191–5204.
- [36] V. S. Vyas, F. Haase, L. Stegbauer, G. Savasci, F. Podjaski, C. Ochsenfeld, B. V. Lotsch, *Nat. Commun.* **2015**, *6*, 8508.
- [37] P. Pachfule, A. Acharjya, J. Roeser, T. Langenhahn, M. Schwarze, R. Schomäcker, A. Thomas, J. Schmidt, *J. Am. Chem. Soc.* **2018**, *140*, 1423–1427.
- [38] H. Wang, H. Wang, Z. Wang, L. Tang, G. Zeng, P. Xu, M. Chen, T. Xiong, C. Zhou, X. Li, D. Huang, Y. Zhu, Z. Wang, J. Tang, *Chem. Soc. Rev.* **2020**, *49*, 4135–4165.
- [39] M. Traxler, S. Gisbertz, P. Pachfule, J. Schmidt, J. Roeser, S. Reischauer, J. Rabeah, B. Pieber, A. Thomas, *Angew. Chem. Int. Ed.* **2022**, *61*, e202117738.
- [40] H. Wang, C. Qian, J. Liu, Y. Zeng, D. Wang, W. Zhou, L. Gu, H. Wu, G. Liu, Y. Zhao, *J. Am. Chem. Soc.* **2020**, *142*, 4862–4871.
- [41] F. Liu, Y. He, X. Liu, Z. Wang, H.-L. Liu, X. Zhu, C.-C. Hou, Y. Weng, Q. Zhang, Y. Chen, *ACS Catal.* **2022**, *49*, 9494–9502.
- [42] C. Zhu, H. Yue, J. Jia, M. Rueping, *Angew. Chem. Int. Ed.* **2021**, *60*, 17810–17831.
- [43] W. Dong, Y. Yang, Y. Xiang, S. Wang, P. Wang, J. Hu, L. Rao, H. Chen, *Green Chem.* **2021**, *23*, 5797–5805.
- [44] K. Wang, H. Jiang, H. Liu, H. Chen, F. Zhang, *ACS Catal.* **2022**, *12*, 6068–6080.
- [45] S. Kandambeth, A. Mallick, B. Lukose, M. V. Mane, T. Heine, R. Banerjee, *J. Am. Chem. Soc.* **2012**, *134*, 19524–19527.
- [46] H. B. Aiyappa, J. Thote, D. B. Shinde, R. Banerjee, S. Kurungot, *Chem. Mater.* **2016**, *28*, 4375–4379.
- [47] X. Zhao, P. Pachfule, S. Li, T. Langenhahn, M. Ye, C. Schlesiger, S. Praetz, J. Schmidt, A. Thomas, *J. Am. Chem. Soc.* **2019**, *141*, 6623–6630.
- [48] B. D. Ravetz, N. E. S. Tay, C. L. Joe, M. Sezen-Edmonds, M. A. Schmidt, Y. Tan, J. M. Janey, M. D. Eastgate, T. Rovis, *ACS Cent. Sci.* **2020**, *6*, 2053–2059.
- [49] B. D. Ravetz, A. B. Pun, E. M. Churchill, D. N. Congreve, T. Rovis, L. M. Campos, *Nature* **2019**, *565*, 343–346.
- [50] S. Gisbertz, S. Reischauer, B. Pieber, *Nat. Catal.* **2020**, *3*, 611–620.
- [51] L. Stegbauer, K. Schwinghammer, B. V. Lotsch, *Chem. Sci.* **2014**, *5*, 2789–2793.

Table of Contents

Table of Contents	2
S1. General Remarks	4
S2. Setup for photochemical reactions	6
S3. Synthesis of organic linkers and COFs	8
S3.1 Synthesis of the organic linkers	8
S3.2 Synthesis of multivariate covalent organic frameworks (COFs)	12
S4. Characterization multivariate COFs	15
S4.1 PXRD analysis of $\text{Acr}^x\text{-L-Bpy}^y$ COFs ($x:y = 2:1$ or $1:2$; $L = \text{Tp, DHTA, HTA, Tf}$) ..	15
S4.2 Nitrogen sorption experiments for $\text{Acr}^1\text{-L-Bpy}^2$ multiple-component COFs	16
S4.3 Pore size distribution for $\text{Acr}^2\text{-L-Bpy}^1$ multiple-component COFs	16
S4.4 FT-IR results of $\text{Acr}^x\text{-L-Bpy}^y$ COFs	17
S4.5 Thermogravimetric analyses of $\text{Acr}^x\text{-L-Bpy}^y$ COFs	19
S4.6 Solid-state NMR	19
S4.7 X-ray photoelectron spectroscopy (XPS) analysis of $\text{Acr}^x\text{-L-Bpy}^y$ COFs	20
S4.8 COF digestion of $\text{Acr}^x\text{-Tp-Bpy}^y$	20
S4.9 UV-vis of $\text{Acr}^x\text{-L-Bpy}^x$ COFs	21
S4.10 Comparison of theoretical and experimental excitation energies and band gaps	22
S4.11 Photoluminescence measurements of $\text{Acr}^2\text{-L-Bpy}^1$ multiple-component COFs	25
S4.12 Fluorescence quenching studies of $\text{Acr}^2\text{-Tf-Bpy}^1$ multiple-component COF	26
S4.13 Electron paramagnetic resonance (EPR) spin trap experiments of $\text{Acr}^2\text{-Tf-[Ni]}^1$ and $\text{Acr}^2\text{-Tp-[Ni]}^1$ multiple-component COFs	26
S5. Synthesis and characterization of reference COFs	29
S5.1 Synthesis of bipyridine COFs	29
S5.2 Characterization of bipyridine COFs	30
S5.3 Synthesis of Tf-Acr COF	33
S5.4 Characterization of Tf-Acr COF	33
S6. Synthesis and characterization of model compounds	34
S6.1 Synthesis of acridine model compound (SA-Acr)	34
S6.2 Synthesis of bipyridine model compounds (BA-Bpy)	35
S7. Photocatalytic reaction optimization	36
S7.1 General experimental procedure for screening experiments	36
S7.2 Initial screening experiments using sodium <i>p</i> -toluenesulfonate	36
S7.3 Screening experiments for different COFs	37
S7.4 Screening different COFs for cross-coupling of aryl halides and nucleophiles	38
S7.5 Control studies	39
S8. Photocatalysis - recycling studies	41

Appendix

S8.1 Reaction procedure	41
S8.2 Analysis of recycled Tp-Acr COF	42
S10. References	46
S11. Author Contributions	47
S12. Copies of NMR spectra.....	48

S1. General Remarks

All air and moisture sensitive reactions were performed using standard Schlenk-line techniques under an atmosphere of argon. Substrates, reagents, and solvents were purchased from commercial suppliers and used without further purification. The precursors such as phloroglucinol (TCI, > 99 %), resorcinol (> 98.5 %), phenol (TCI, > 99 %), 1,3,5-triformylbenzene (TCI, > 98 %), 2,2'-bipyridine-5,5'-diamine (BLDpharm, 97 %), 1-chloro-3-nitrobenzene (TCI, > 99 %), 4-nitroaniline (Carl Roth, > 98.5 %), 2,6-diaminoanthraquinone (TCI, > 97 %) and salicylic aldehyde (Sigma Aldrich, 98 %) were purchased and used as received. Reactants and solvents were obtained from Sigma Aldrich ((2-biphenyl)dicyclohexylphosphine (CyJohnPhos, 97 %), 1,2-dimethoxyethane (DME, 99.5 %, anhydrous), tin (powder <150 μm , 99.5 %), mesitylene (1,3,5-trimethylbenzene, 98 %), 1,2-dichlorobenzene (*o*-DCB, 99 %, anhydrous), glycerol (99.5 %)), TCI (tris(dibenzylideneacetone)dipalladium(0) ($\text{Pd}_2(\text{dba})_3$, > 75 %), hexamethylenetetramine (HMTA, > 99 %)), ABCR (tripotassium phosphate (K_3PO_4 , 97 %), palladium (Pd/C, 10 % on activated charcoal), trifluoroacetic acid (TFA, 99.9 %), 1,4-dioxane (99.5 %)), Carl Roth (formic acid (> 98 %), hydrochloric acid (37 %), sulfuric acid (96 %)), Alphagaz (hydrogen gas (99.999 %)), Eurisotop (CDCl_3 (99.8 % $_d$), $\text{DMSO-}d_6$ (99.8 % $_d$)), Chemsolute (sodium hydroxide (NaOH, 99.5 %)), Fluka Analytical (sodium borohydride (> 99 %)) or Grüssing (1-butanol (*n*-BuOH, 99.5 %)). Powder X-ray diffraction data were collected on a Bruker D8 Advance diffractometer in reflection geometry operating with a Cu K_α anode ($\lambda = 1.54178 \text{ \AA}$) with a working voltage at 40 kV and a current of 40 mA. Samples were ground and mounted as loose powders onto a Si sample holder. PXRD patterns were collected from 2 to 60 2θ degrees with a step size of 0.02 degrees and an exposure time of 2 seconds per step. LED lamps for photocatalytic experiments were purchased from Kessil Lightning.^[1] ^1H -, ^{13}C -, and ^{19}F spectra were recorded on a Varian 400 spectrometer (400 MHz, Agilent), an Ascend™ 400 spectrometer (400 MHz, cryoprobe, Bruker), a Varian 600 spectrometer (600 MHz, Agilent), a Bruker Avance II spectrometer (200 MHz, Bruker) or an Bruker Avance 400 spectrometer (400 MHz, Bruker) at 298 K, and are reported in ppm relative to the residual solvent peaks. Peaks are reported as: s = singlet, d = doublet, t = triplet, q = quartet, m = multiplet or unresolved, with coupling constants in Hz. $^{13}\text{C}\{^1\text{H}\}$ cross polarization magic angle spinning (CP/MAS) measurements were carried out using a Bruker range Avance 400 MHz Solid State spectrometer operating at 100.6 MHz and a Bruker 4 mm double resonance probe-head operating at a spinning rate of 10 kHz. Nitrogen sorption measurements were performed at 77 K using an

Autosorb-iQ-MP or QuadraSorb from Quantachrome. Prior the analysis the samples were dried and degassed at 150 °C for 12 h. Using the N₂ adsorption isotherms, the surface areas were calculated over a pressure range $0.05-0.1 = p/p_0$ using Brunauer-Emmett-Teller (BET) methods. The pore size distributions were calculated from the adsorption isotherms by Quenched Solid State Functional Theory (QSDFT) using N₂ sorption data collected at 77 K. We used the carbon cylindrical pore model for analyzing the distribution. Thermogravimetric analysis (TGA) measurements were carried out under nitrogen atmosphere on a Mettler Toledo TGA 1 Stare thermal instrument with a heating rate of 10 K min⁻¹. Solid state diffuse reflectance ultraviolet-visible spectroscopy (UV-vis) spectra have been collected on a Varian Cary 300 UV-Vis Spectrophotometer. UV-vis absorption spectra of COF suspensions were collected using a Shimadzu UV-1900. Fluorescence spectra were measured using a microplate reader (SpectraMax M5, Molecular Devices) or FluoroMax-2 (ISA Instruments S.A., Inc.). The Fourier transform infrared spectroscopy (FTIR) analyses of the samples were carried on Varian 640IR spectrometer equipped with an ATR cell. The TEM images were acquired using a Jeol TEM-F200, for the investigation, the acceleration voltage was set to 80 kV, the emission was put to 115,8 μ A and a condenser aperture with a diameter of 200 μ m was used. The specimens were prepared by dissolving a powder sample of the material in ethanol, sonicating the solution for 15 minutes and finally dropping a few drops onto a copper TEM grid coated with holey carbon film. Once the solution had dried off, the specimens were investigated. Scanning electron microscopy (SEM) images were obtained on a LEO 1550-Gemini microscope. Energy-dispersive X-ray (EDX) investigations were conducted on a Link ISIS-300 system (Oxford Microanalysis Group) equipped with a Si(Li) detector and an energy resolution of 133 eV. X-Ray photoelectron spectra were measured on a K-AlphaTM + X-ray Photoelectron Spectrometer System (Thermo Scientific) with Hemispheric 180° dual-focus analyzer with 128-channel detector. The X-ray monochromator used micro focused Al-K α radiation. High resolution mass spectrometry (HR-MS) was performed on an LTQ Orbitrap XL spectrometer using electrospray ionization (ESI) or atmospheric pressure chemical ionization (APCI). Inductively coupled plasma - optical emission spectrometry (ICP-OES) was carried out using a Horiba Ultra 2 instrument equipped with a photomultiplier tube detection system. Analytical thin layer chromatography (TLC) was performed on pre-coated TLC-sheets, ALUGRAM Xtra SIL G/UV254 sheets (Macherey-Nagel) and visualized with 254 nm light or staining solutions followed by heating. Purification of final compounds was carried out by flash chromatography using a Biotage Isolera automatic column system with pre-packed silica columns. Centrifugation was carried out using an Eppendorf 5430 centrifuge.

S2. Setup for photochemical reactions

Photochemical experiments involving visible light irradiation were carried out using Kessil PR160L-440 (440nm, blue light) or Kessil PR160L-525 (525 nm, green light) LED lamps with the respective power settings.^[1] One or two lamps were used, depending on the required light intensity to irradiate reaction vessels located on a stirring plate (lamp-vessel distance: 4.5 cm; stirring speed: 800 rpm, Figure S2). To avoid heating of the reaction mixture, fans were used for cooling.

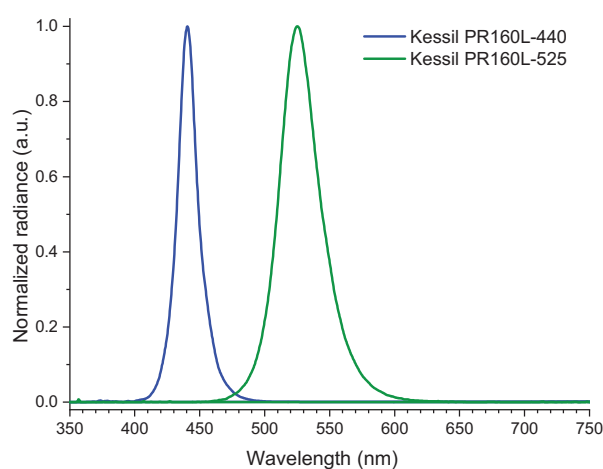


Figure S 1. Emission spectra of Kessil PR160L-440 (blue) and Kessil PR160L-525 (green).

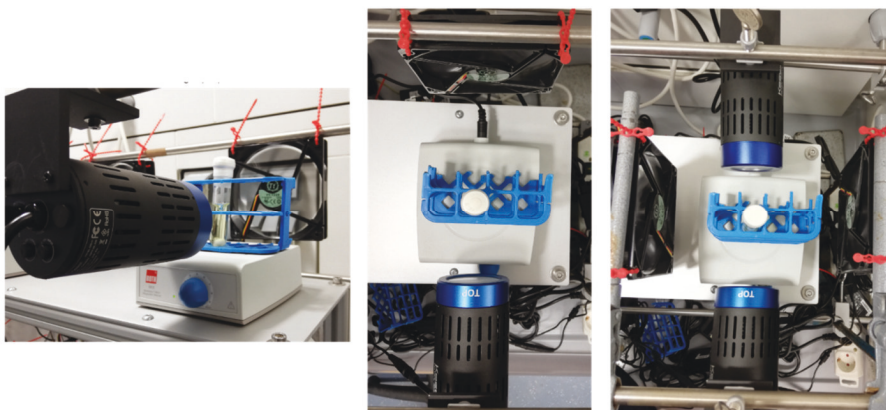


Figure S 2. Configuration of the experimental setup using one or two LED lamps.

Experiments using red light were carried out using a Kessil H160 Tuna Flora LED in “red” mode (Figure S3). Two sealed reaction vessels were placed between two lamps on a stirring plate (4.5 cm distance from each lamp). To avoid heating of the reaction mixture, a fan was used for cooling. All reactions were performed with maximum stirring speed.

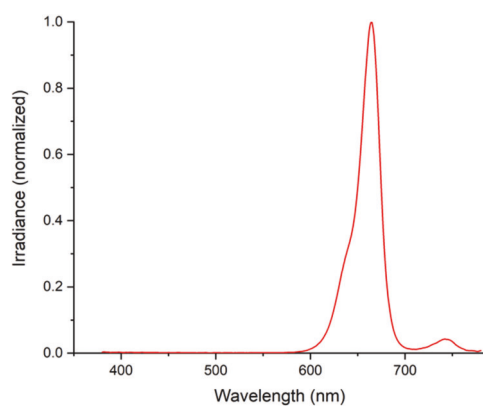
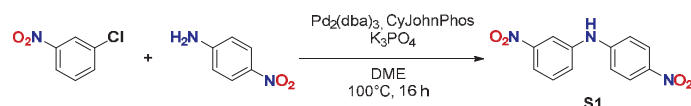


Figure S 3 . Emission spectra of the Kessil H160 Tuna Flora LED in “red” mode.

S3. Synthesis of organic linkers and COFs

S3.1 Synthesis of the organic linkers

Synthesis of 2,6-diaminoacridine:

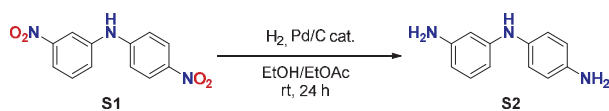


Scheme S 1. Synthesis of 3-nitro-*N*-(4-nitrophenyl)aniline (S1) via Buchwald-Hartwig coupling.

3-nitro-*N*-(4-nitrophenyl)aniline (S1): To a flame dried and three times evacuated and backfilled Schlenk flask were under argon counterflow 206 mg (0.22 mmol, 3 mol%) of $\text{Pd}_2(\text{dba})_3$ and 80 mg (2-biphenyl)dicyclohexylphosphine (CyJohnPhos, 0.22 mmol, 3 mol%) added. 15 mL of anhydrous 1,2-dimethoxyethane (DME) were added and the resulting suspension was stirred for 5 min at room temperature. Subsequently, 1.18 g (7.5 mmol, 1.0 eq.) of 1-chloro-3-nitrobenzene, 1.03 g (7.5 mmol, 1.0 eq.) of 4-nitroaniline and 2.23 g (10.5 mmol, 1.4 eq.) of K_3PO_4 were added and the mixture was heated to 100 °C for 24 h while stirring was maintained. After cooling to room temperature, the suspension was diluted with 300 mL of $\text{Et}_2\text{O}/\text{EtOAc}$ (1:1), filtered through Celite and concentrated using the rotary evaporator. The crude material was purified by column chromatography on silica gel using 30 % EtOAc in cyclohexane to get the product as an orange powder (1.85 g, 95%).

^1H NMR (400 MHz, $\text{DMSO}-d_6$) δ 9.67 (s, 1H), 8.16 (d, $J = 9.2$ Hz, 2H), 7.86 (ddd, $J = 7.8, 2.2, 1.2$ Hz, 1H), 7.68 (ddd, $J = 8.1, 2.1, 1.2$ Hz, 1H), 7.63 (t, $J = 8.0$ Hz, 1H), 7.21 (d, $J = 9.3$ Hz, 2H). ^{13}C NMR (101 MHz, $\text{DMSO}-d_6$) δ 149.13, 148.66, 141.91, 139.37, 130.90, 126.10, 125.40, 116.86, 114.83, 113.41.

These data are in full agreement with those previously published in the literature.^[2]



Scheme S 2. Synthesis of 3-(4-aminoanilino)aniline (S2) from 3-nitro-*N*-(4-nitrophenyl)aniline (S1).

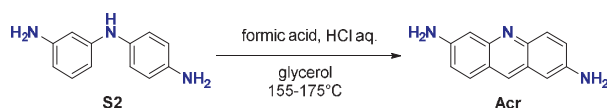
3-(4-aminoanilino)aniline (S2): A suspension of 1.66 g (6.4 mmol) of 3-nitro-*N*-(4-nitrophenyl)aniline (S1), 332 mg (0.31 mmol, 4.9 mol%) of Pd/C (10 wt% Pd), 200 mL EtOH

S8

and 100 mL EtOAc were degassed for 15 min using an argon purge. Subsequently, the suspension was degassed for 10 min using and H₂ purge and thereafter stirred for 24 h under hydrogen atmosphere. The catalyst was removed by filtration through Celite and the solvent was concentrated under vacuum and dried at 65 °C under high vacuum to give a dark brown solid (1.23 g, 96 %).

¹H NMR (200 MHz, DMSO-*d*₆) δ 7.11 (s, 1H), 6.83 – 6.68 (m, 3H), 6.51 (d, *J* = 8.6 Hz, 2H), 6.06 (t, *J* = 2.0 Hz, 1H), 5.99 (ddd, *J* = 7.9, 2.1, 0.8 Hz, 1H), 5.88 (ddd, *J* = 7.8, 2.0, 0.9 Hz, 1H), 4.74 (bs, 4H). ¹³C NMR (50 MHz, DMSO-*d*₆) δ 149.20, 147.28, 143.21, 132.35, 129.14, 122.39, 114.69, 104.20, 103.03, 99.56.

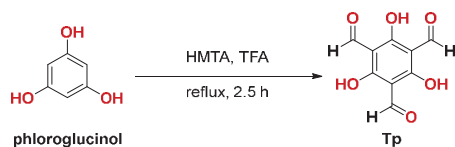
These data are in full agreement with those previously published in the literature.^[2]



Scheme S 3. Synthesis of 2,6-diaminoacridine (Acr) from 3-(4-aminoanilino)aniline (S2).

2,6-diaminoacridine (Acr): To 1.23 g (6.1 mmol, 1.0 eq.) of 3-(4-aminoanilino)aniline (S2) were 4 mL glycerol, 235 µl (6.1 mmol, 1.0 eq.) of formic acid and 660 µl (7.9 mmol, 1.3 eq.) of 37 % aqueous HCl solution added. The reaction mixture was heated to 155 °C during 30 min, kept at this temperature for 30 min before heating it to 175 °C for another 30 min. After cooling to room temperature 2.5 mL of aqueous sulfuric acid (30 %_{w/v}) were added and the reaction was heated to 95 °C for 10 min. Subsequently, the reaction was diluted to 25 mL with H₂O and the reaction mixture was kept at 0 °C for 1 h. The precipitated acid sulfate of the compound was filtered off, washed with water (40 mL) and Et₂O (60 mL). The dark red powder was boiled in 10 mL of aqueous NaOH (1 M) to precipitate the 2,6-diaminoacridine. The dark brown compound was filtered and washed with ice cold water (60 mL) and cold Et₂O (10 mL) and dried under vacuum at 65 °C (407 mg, 32 %).

¹H NMR (400 MHz, DMSO-*d*₆) δ 8.35 – 8.24 (m, 1H), 7.67 (dd, *J* = 9.0, 2.9 Hz, 2H), 7.22 (dd, *J* = 9.2, 2.3 Hz, 1H), 6.99 (dd, *J* = 9.0, 2.0 Hz, 1H), 6.84 – 6.82 (m, 1H), 6.82 – 6.80 (m, 1H), 5.83 – 5.78 (m, 1H), 5.43 – 5.39 (m, 1H). ¹³C NMR (101 MHz, DMSO-*d*₆) δ 148.54, 148.07, 144.44, 144.07, 130.64, 128.51, 128.23, 125.84, 124.52, 121.45, 120.55, 103.65, 103.48. HR-ESI-MS [*M*+H⁺] (*m/z*): 210.1028 (th.: 210.1026).

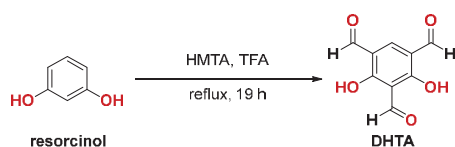
Synthesis of aldehyde linkers:

Scheme S 4. Synthesis of 1,3,5-triformylphloroglucino (Tp) from phloroglucinol.

1,3,5-triformylphloroglucino (Tp): To 10.0 g (80 mmol, 1.0 eq.) of phloroglucinol and 25.0 g (179 mmol, 2.2 eq.) of hexamethylenetetramine (HMTA) were 150 mL trifluoroacetic acid (TFA) added slowly under argon atmosphere at 0 °C. After complete addition, the suspension was heated at 100 °C for 2.5 h. The reaction mixture was cooled to around 50 °C and 240 mL of 3 M HCl were added, and the solution was heated at 100 °C for 1 h. After cooling to room temperature, the solution was filtered through Celite, extracted with 3x 200 mL dichloromethane, dried over magnesium sulfate, and filtered. Rotary evaporation of the solution afforded of an off-white powder. A pure sample was obtained by washing the solid sample with 10 mL of cold EtOH followed by sublimation under reduced pressure (2.76 g, 16 %).

^1H NMR (200 MHz, CDCl_3) δ 14.11 (s, 1H), 10.14 (s, 1H). ^{13}C NMR (50 MHz, CDCl_3) δ 192.17, 173.71, 103.05.

These data are in full agreement with those previously published in the literature.^[3]



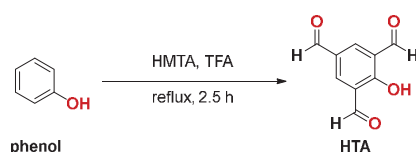
Scheme S 5. Synthesis of 2,4-dihydroxybenzene-1,3,5-tricarbaldehyde (DHTA) from resorcinol.

2,4-dihydroxybenzene-1,3,5-tricarbaldehyde (DHTA): To 3.6 g (33 mmol, 1.0 eq.) of resorcinol and 10.0 g (71 mmol, 2.2 eq.) of hexamethylenetetramine (HMTA) were 35 mL trifluoroacetic acid added slowly under argon atmosphere at 0 °C. After complete addition, the suspension was heated at 130 °C for 16 h and afterwards 3 h at 150 °C. The reaction mixture was cooled to around 100 °C and 55 mL of 3 M HCl were added, and the solution was heated at 105 °C for 30 min. After cooling to room temperature, the solution was filtered through Celite, extracted with 3x 50 mL dichloromethane, dried over magnesium sulfate, and filtered. Rotary evaporation of the solution afforded of an off-white powder. A pure sample was

obtained by washing the solid sample with 10 mL of cold EtOH followed by sublimation under reduced pressure (1.37 g, 21 %).

^1H NMR (400 MHz, $\text{DMSO-}d_6$) δ 10.26 (s, 1H), 10.09 (s, 2H), 8.40 (s, 1H). ^{13}C NMR (101 MHz, $\text{DMSO-}d_6$) δ 193.93, 189.97, 169.97, 140.66, 115.80, 109.95.

These data are in full agreement with those previously published in the literature.^[4]



Scheme S 6. Synthesis of 2-hydroxybenzene-1,3,5-tricarbaldehyde (HTA) from phenol.

2-hydroxybenzene-1,3,5-tricarbaldehyde (HTA): To 3.5 g (36.7 mmol, 1.0 eq.) of phenol and 10.1 g (71.3 mmol, 2.0 eq.) of hexamethylenetetramine (HMTA) were 50 mL trifluoroacetic acid added slowly under argon atmosphere at 0 °C. After complete addition, the suspension was heated at 120 °C for 20 h and afterwards 30 min at 150 °C. The reaction mixture was cooled to around 120 °C and 50 mL of 3 M HCl were added, and the solution was heated at 120 °C for 30 min. While cooling to room temperature a yellow precipitate was formed, which was filtered, washed with 20 mL of cold EtOH and dried under vacuo to give an off-white solid (3.64 g, 56%). Pure sample was obtained by sublimation of the crude material under reduced pressure.

^1H NMR (200 MHz, $\text{DMSO-}d_6$) δ 10.30 (s, 2H), 9.99 (s, 1H), 8.52 (s, 2H). ^1H NMR (200 MHz, CDCl_3) δ 12.16 (s, 1H), 10.32 (s, 2H), 10.01 (s, 1H), 8.51 (s, 2H). ^{13}C NMR (50 MHz, $\text{DMSO-}d_6$) δ 191.65, 190.72, 165.88, 137.31, 128.30, 124.09.

These data are in full agreement with those previously published in the literature.^[5]

S3.2 Synthesis of multivariate covalent organic frameworks (COFs)

Acr²-Tp-Bpy¹ COF: A Pyrex tube (o.d. \times i.d. = 15 \times 10 mm² and length 15 cm) is charged with triformylphloroglucinol (**Tp**) (21 mg, 0.1 mmol), 2,6-diaminoacridine (**Acr**) (20.9 mg, 0.1 mmol), 2,2'-bipyridine-5,5'-diamine (**Bpy**) (9.3 mg, 0.05 mmol), 1.5 mL of *n*-BuOH, 1.5 mL of anhydrous *o*-DCB and 0.5 mL of 6 M aqueous acetic acid. This mixture was sonicated for 15 minutes in order to get a homogenous dispersion. The tube was then flash frozen at 77 K (liquid N₂ bath) and degassed by three freeze-pump-thaw cycles. The tube was sealed off and then heated at 120 °C for 3 days. A dark red colored precipitate was collected by filtration and washed with acetone, methanol and cyclohexane. The powder collected was dried at 120 °C to give a dark red colored powder (44 mg, 96 %).

Acr¹-Tp-Bpy² COF: A Pyrex tube (o.d. \times i.d. = 15 \times 10 mm² and length 15 cm) is charged with triformylphloroglucinol (**Tp**) (21 mg, 0.1 mmol), 2,6-diaminoacridine (**Acr**) (10.4 mg, 0.05 mmol), 2,2'-bipyridine-5,5'-diamine (**Bpy**) (18.6 mg, 0.1 mmol), 1.5 mL of *n*-BuOH, 1.5 mL of anhydrous *o*-DCB and 0.5 mL of 6 M aqueous acetic acid. This mixture was sonicated for 15 minutes in order to get a homogenous dispersion. The tube was then flash frozen at 77 K (liquid N₂ bath) and degassed by three freeze-pump-thaw cycles. The tube was sealed off and then heated at 120 °C for 3 days. A dark red colored precipitate was collected by filtration and washed with acetone, methanol and cyclohexane. The powder collected was dried at 120 °C to give a dark red colored powder (38 mg, 86 %).

Acr²-DHTA-Bpy¹ COF: A Pyrex tube (o.d. \times i.d. = 15 \times 10 mm² and length 15 cm) is charged with 2,4-dihydroxybenzene-1,3,5-tricarbaldehyde (**DHTA**) (19.4 mg, 0.1 mmol), 2,6-diaminoacridine (**Acr**) (20.9 mg, 0.1 mmol), 2,2'-bipyridine-5,5'-diamine (**Bpy**) (9.3 mg, 0.05 mmol), 1.5 mL of *n*-BuOH, 1.5 mL of anhydrous *o*-DCB and 0.5 mL of 6 M aqueous acetic acid. This mixture was sonicated for 15 minutes in order to get a homogenous dispersion. The tube was then flash frozen at 77 K (liquid N₂ bath) and degassed by three freeze-pump-thaw cycles. The tube was sealed off and then heated at 120 °C for 3 days. A dark red colored precipitate was collected by filtration and washed with acetone, methanol and cyclohexane. The powder collected was dried at 120 °C to give a dark red colored powder (43 mg, 98 %).

Acr¹-DHTA-Bpy² COF: A Pyrex tube (o.d. \times i.d. = 15 \times 10 mm² and length 15 cm) is charged with 2,4-dihydroxybenzene-1,3,5-tricarbaldehyde (**DHTA**) (19.4 mg, 0.1 mmol), 2,6-diaminoacridine (**Acr**) (10.4 mg, 0.05 mmol), 2,2'-bipyridine-5,5'-diamine (**Bpy**) (18.6 mg, 0.1 mmol), 1.5 mL of *n*-BuOH, 1.5 mL of anhydrous *o*-DCB and 0.5 mL of 6 M aqueous acetic acid. This mixture was sonicated for 15 minutes in order to get a homogenous dispersion. The tube was then flash frozen at 77 K (liquid N₂ bath) and degassed by three freeze-pump-thaw cycles. The tube was sealed off and then heated at 120 °C for 3 days. A dark red colored precipitate was collected by filtration and washed with acetone, methanol and cyclohexane. The powder collected was dried at 120 °C to give a dark red colored powder (38 mg, 89 %).

Acr²-HTA-Bpy¹ COF: A Pyrex tube (o.d. \times i.d. = 15 \times 10 mm² and length 15 cm) is charged with 2-hydroxybenzene-1,3,5-tricarbaldehyde (**HTA**) (17.8 mg, 0.1 mmol), 2,6-diaminoacridine (**Acr**) (20.9 mg, 0.1 mmol), 2,2'-bipyridine-5,5'-diamine (**Bpy**) (9.3 mg, 0.05 mmol), 1.5 mL of *n*-BuOH, 1.5 mL of anhydrous *o*-DCB and 0.5 mL of 6 M aqueous acetic acid. This mixture was sonicated for 15 minutes in order to get a homogenous dispersion. The tube was then flash frozen at 77 K (liquid N₂ bath) and degassed by three freeze-pump-thaw cycles. The tube was sealed off and then heated at 120 °C for 3 days. A dark red colored precipitate was collected by filtration and washed with acetone, methanol and cyclohexane. The powder collected was dried at 120 °C to give a dark red colored powder (41 mg, 97 %).

Acr¹-HTA-Bpy² COF: A Pyrex tube (o.d. \times i.d. = 15 \times 10 mm² and length 15 cm) is charged with 2-hydroxybenzene-1,3,5-tricarbaldehyde (**HTA**) (17.8 mg, 0.1 mmol), 2,6-diaminoacridine (**Acr**) (10.4 mg, 0.05 mmol), 2,2'-bipyridine-5,5'-diamine (**Bpy**) (18.6 mg, 0.1 mmol), 1.5 mL of *n*-BuOH, 1.5 mL of anhydrous *o*-DCB and 0.5 mL of 6 M aqueous acetic acid. This mixture was sonicated for 15 minutes in order to get a homogenous dispersion. The tube was then flash frozen at 77 K (liquid N₂ bath) and degassed by three freeze-pump-thaw cycles. The tube was sealed off and then heated at 120 °C for 3 days. A dark red colored precipitate was collected by filtration and washed with acetone, methanol and cyclohexane. The powder collected was dried at 120 °C to give a dark red colored powder (34 mg, 89 %).

Acr²-Tf-Bpy¹ COF: A Pyrex tube (o.d. \times i.d. = 15 \times 10 mm² and length 15 cm) is charged with 1,3,5-triformylbenzene (**Tf**) (16.2 mg, 0.1 mmol), 2,6-diaminoacridine (**Acr**) (20.9 mg, 0.1 mmol), 2,2'-bipyridine-5,5'-diamine (**Bpy**) (9.3 mg, 0.05 mmol), 1.5 mL of *n*-BuOH, 1.5 mL of anhydrous *o*-DCB and 0.5 mL of 6 M aqueous acetic acid. This mixture was sonicated for 15 minutes in order to get a homogenous dispersion. The tube was then flash frozen at 77 K (liquid N₂ bath) and degassed by three freeze-pump-thaw cycles. The tube was sealed off and then heated at 120 °C for 3 days. A dark red colored precipitate was collected by filtration and washed with acetone, methanol and cyclohexane. The powder collected was dried at 120 °C to give a dark red colored powder (37 mg, 91 %).

Acr¹-Tf-Bpy² COF: A Pyrex tube (o.d. \times i.d. = 15 \times 10 mm² and length 15 cm) is charged with 1,3,5-triformylbenzene (**Tf**) (16.2 mg, 0.1 mmol), 2,6-diaminoacridine (**Acr**) (10.4 mg, 0.05 mmol), 2,2'-bipyridine-5,5'-diamine (**Bpy**) (18.6 mg, 0.1 mmol), 1.5 mL of *n*-BuOH, 1.5 mL of anhydrous *o*-DCB and 0.5 mL of 6 M aqueous acetic acid. This mixture was sonicated for 15 minutes in order to get a homogenous dispersion. The tube was then flash frozen at 77 K (liquid N₂ bath) and degassed by three freeze-pump-thaw cycles. The tube was sealed off and then heated at 120 °C for 3 days. A dark red colored precipitate was collected by filtration and washed with acetone, methanol and cyclohexane. The powder collected was dried at 120 °C to give a dark red colored powder (33 mg, 81 %).

S4. Characterization multivariate COFs

S4.1 PXRD analysis of $\text{Acr}^x\text{-L-Bpy}^y$ COFs ($x:y = 2:1$ or $1:2$; L = Tp, DHTA, HTA, Tf)

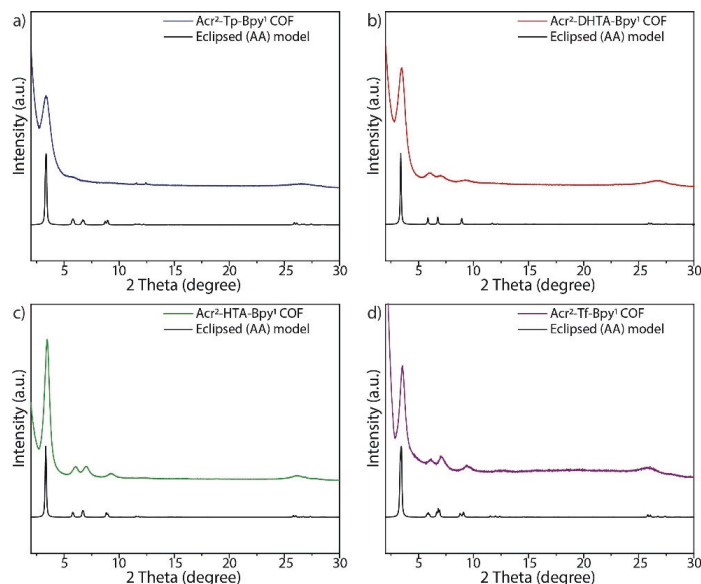


Figure S 4. Comparison between simulated and experimental PXRD patterns for a) $\text{Acr}^2\text{-Tp-Bpy}^1$, b) $\text{Acr}^2\text{-DHTA-Bpy}^1$, c) $\text{Acr}^2\text{-HTA-Bpy}^1$ and d) $\text{Acr}^2\text{-Tf-Bpy}^1$ COFs, showing excellent agreement between the experimental diffractogram and the eclipsed stacking model (AA).

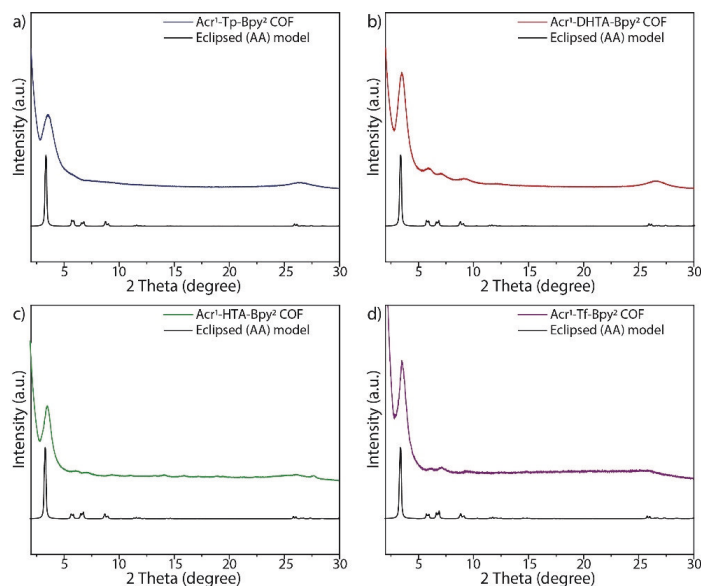


Figure S 5. Comparison between simulated and experimental PXRD patterns for a) $\text{Acr}^1\text{-Tp-Bpy}^2$, b) $\text{Acr}^1\text{-DHTA-Bpy}^2$, c) $\text{Acr}^1\text{-HTA-Bpy}^2$ and d) $\text{Acr}^1\text{-Tf-Bpy}^2$ COFs, showing excellent agreement between the experimental diffractogram and the eclipsed stacking model (AA).

S4.2 Nitrogen sorption experiments for Acr¹-L-Bpy² multiple-component COFs

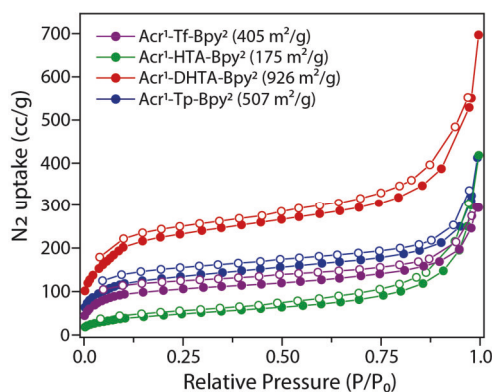


Figure S 6. N₂ sorption isotherms for Acr¹-Tp-Bpy², Acr¹-DHTA-Bpy², Acr¹-HTA-Bpy² and Acr¹-Tf-Bpy² COFs, calculated BET surface areas are shown in brackets.

S4.3 Pore size distribution for Acr²-L-Bpy¹ multiple-component COFs

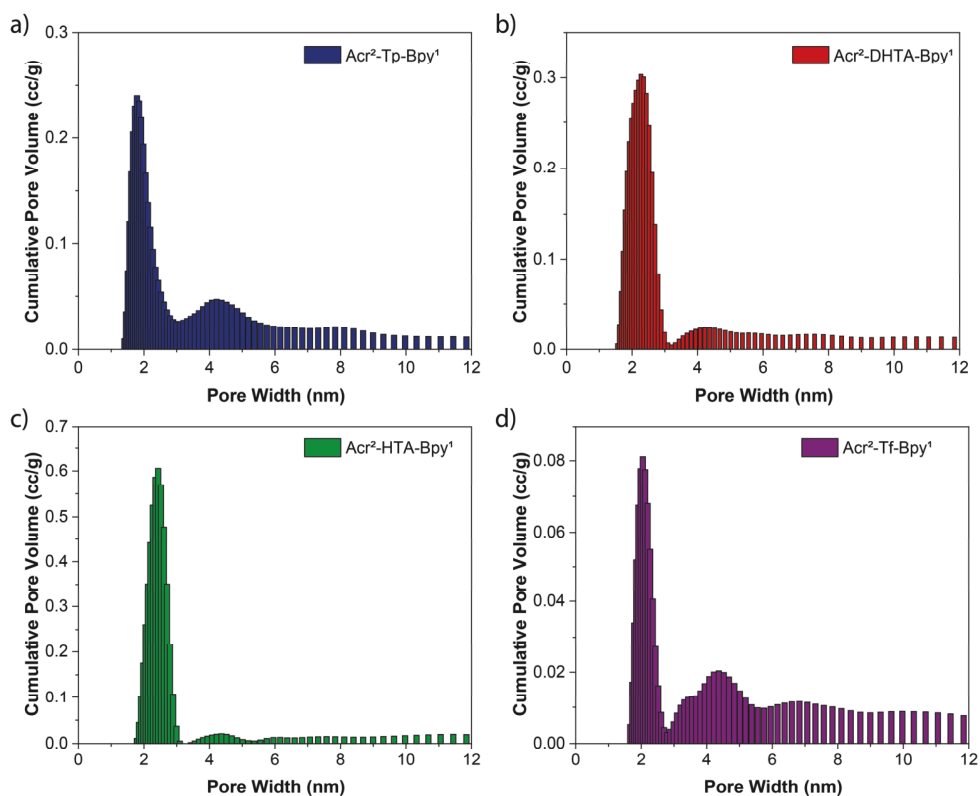


Figure S 7. Pore size distribution of a) Acr²-Tp-Bpy¹, b) Acr²-DHTA-Bpy¹, c) Acr²-HTA-Bpy¹ and d) Acr²-Tf-Bpy¹ COFs, showing the pores distribution close to the ideal pore size calculated from simulated structures.

Acr²-Tp-Bpy¹ COF:

Method = Quenched Solid State Functional Theory (QSDFT)

Model = N₂ at 77 K on carbon cylindrical pore (fitting error = 1.1%)

Acr²-DHTA-Bpy¹ COF:

Method = Quenched Solid State Functional Theory (QSDFT)

Model = N₂ at 77 K on carbon cylindrical pore (fitting error = 1.3%)

Acr²-HTA-Bpy¹ COF:

Method = Quenched Solid State Functional Theory (QSDFT)

Model = N₂ at 77 K on carbon cylindrical pore (fitting error = 2.1%)

Acr²-Tf-Bpy¹ COF:

Method = Quenched Solid State Functional Theory (QSDFT)

Model = N₂ at 77 K on carbon cylindrical pore (fitting error = 1.6%)

S4.4 FT-IR results of of Acr^x-L-Bpy^y COFs

Fourier transform infrared (FT-IR) spectra show the disappearance of the vibration of the amino group of the 2,6-diaminoacridine (**Acr**) and 2,2'-bipyridine-5,5'-diamine (**Bpy**) linker at around 3400 cm⁻¹, and of the stretching vibration of C=O groups of the aldehyde linker (1690-1640 cm⁻¹). The bands of the newly formed C=O and C=C and C=N bonds, respectively were merged into a peak in the range of 1630 cm⁻¹ to 1560 cm⁻¹ for the COFs, where the peak is at higher wavenumber for imine-based COFs. Distinctive spectral bands of the acridine linker at ~800 cm⁻¹ and for the bipyridine unit at ~1250 cm⁻¹ can be also found in the acridine COFs.

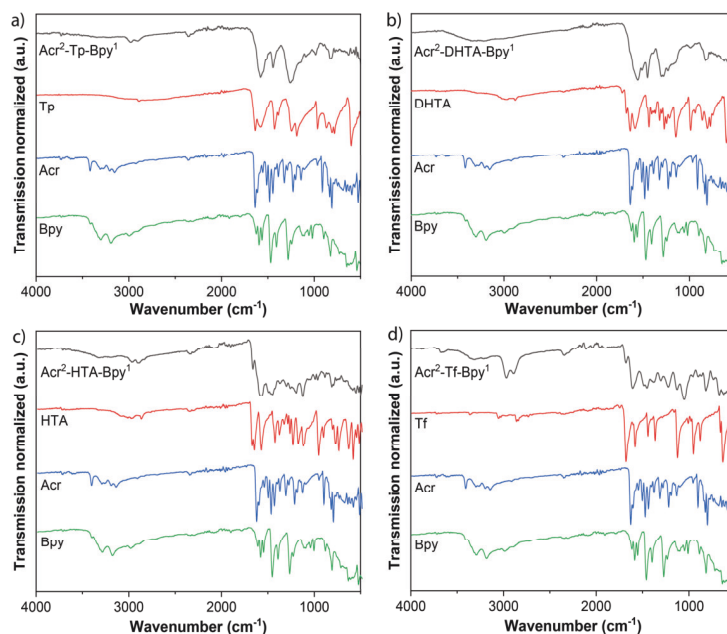


Figure S 8. FT-IR analyses of $\text{Acr}^2\text{-L-Bpy}^1$ COFs [L = Tp (a), DHTA (b), HTA (c), Tf (d)] in comparison with the corresponding aldehydes and amines (Acr, Bpy) showing the formation of the framework structure.

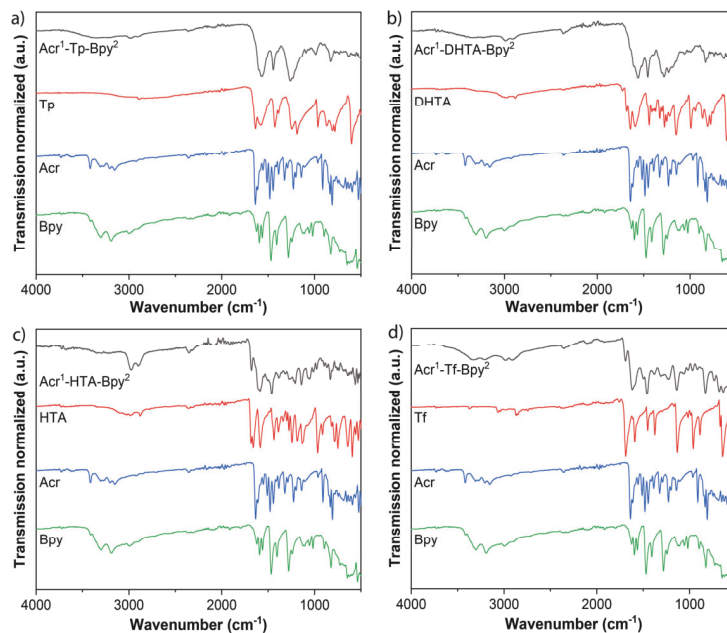


Figure S 9. FT-IR analyses of $\text{Acr}^1\text{-L-Bpy}^2$ COFs [L = Tp (a), DHTA (b), HTA (c), Tf (d)] in comparison with the corresponding aldehydes and amines (Acr, Bpy) showing the formation of the framework structure.

S18

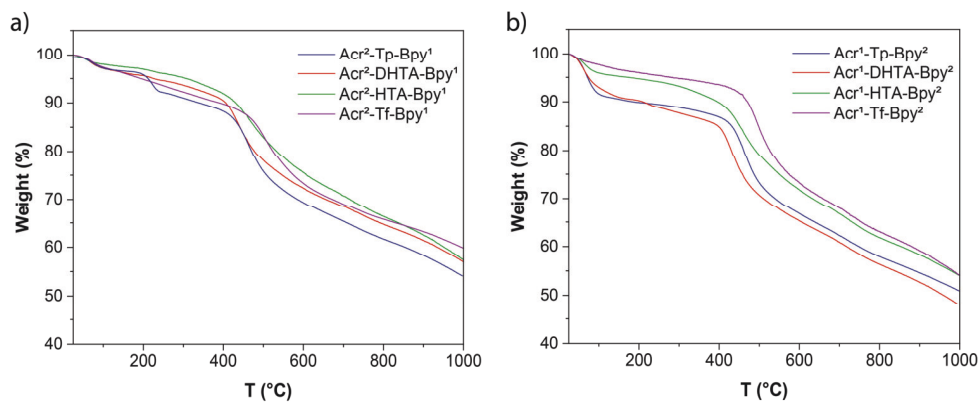
S4.5 Thermogravimetric analyses of $\text{Acr}^x\text{-L-Bpy}^y$ COFs

Figure S10. Thermogravimetric analyses (TGA) for a) $\text{Acr}^2\text{-L-Bpy}^1$ and b) $\text{Acr}^1\text{-L-Bpy}^2$ COFs, showing the thermal stability of the COFs up to 350 °C, under nitrogen atmosphere.

S4.6 Solid-state NMR

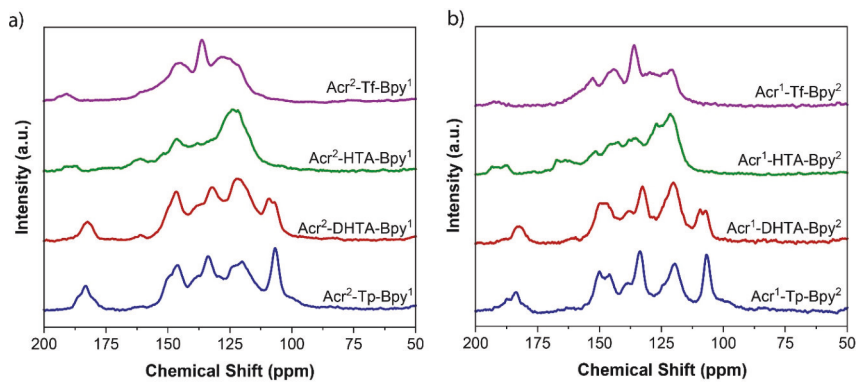


Figure S11. ^{13}C CP-MAS NMR spectra of a) $\text{Acr}^2\text{-L-Bpy}^1$ and b) $\text{Acr}^1\text{-L-Bpy}^2$ COFs.

S4.7 X-ray photoelectron spectroscopy (XPS) analysis of $\text{Acr}^x\text{-L-Bpy}^y$ COFs

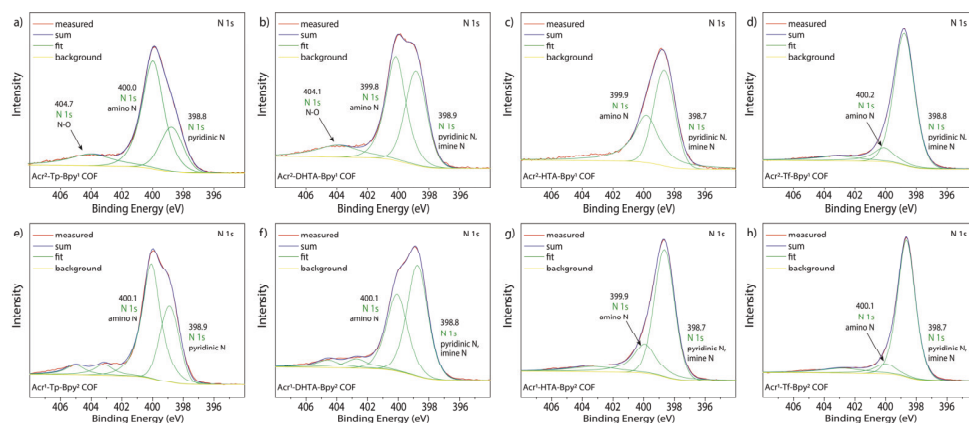


Figure S 12. (a, b, c, d) N 1s XPS core-level spectra of the $\text{Acr}^2\text{-L-Bpy}^1$ multi-component COFs [L= Tp (a), DHTA (b), HTA (c), Tf (d)]. (e, f, g, h) N 1s XPS core-level spectra of the $\text{Acr}^1\text{-L-Bpy}^2$ COFs [L= Tp (e), DHTA (f), HTA (g), Tf (h)].

S4.8 COF digestion of $\text{Acr}^x\text{-Tp-Bpy}^y$

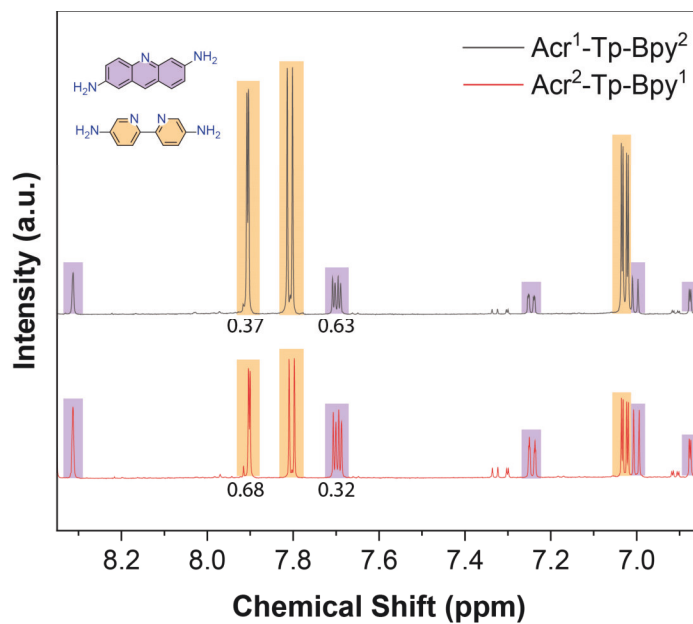
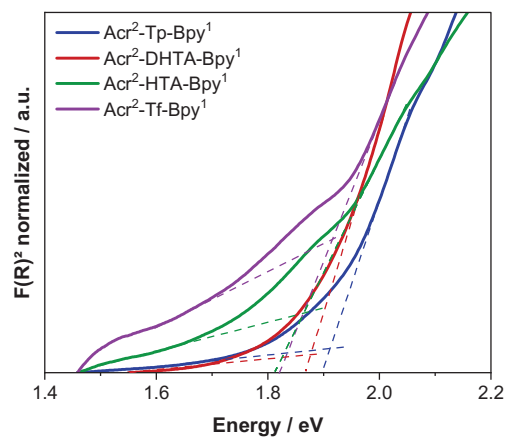
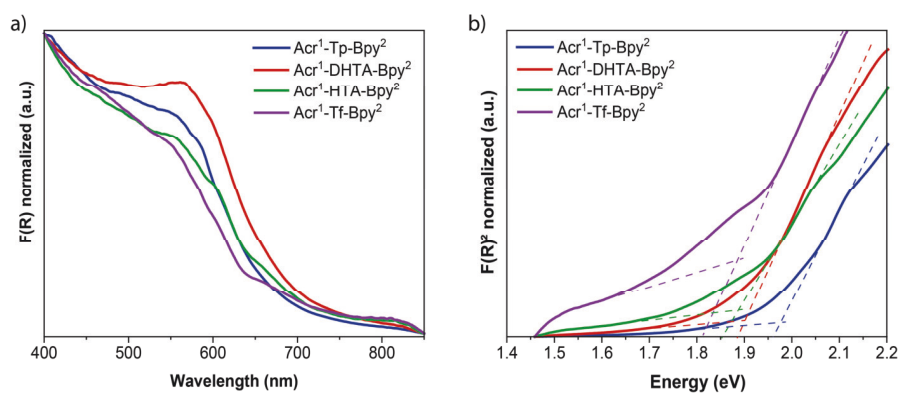


Figure S 13. Partial ^1H NMR spectra (DMSO- d_6 , 700 MHz, 298K) of digested $\text{Acr}^x\text{-Tp-Bpy}^y$ COFs. Each material sample was digested in a solution of 0.1 mL of 10 M NaOH in D_2O and 0.5 mL DMSO- d_6 at 120 $^\circ\text{C}$ for 3 h.

S4.9 UV-vis of $\text{Acr}^x\text{-L-Bpy}^x$ COFsFigure S 14. Tauc plots for $\text{Acr}^2\text{-L-Bpy}^1$ COFs.Figure S 15. a) UV-vis diffuse reflectance spectroscopy analysis of $\text{Acr}^1\text{-L-Bpy}^2$ COFs. b) Tauc plots for $\text{Acr}^1\text{-L-Bpy}^2$ COFs.

S4.10 Comparison of theoretical and experimental excitation energies and band gaps

Density functional theory using gradient corrected or hybrid functionals with dispersion corrections were used to compare experimental and theoretical excitation energies and band gaps (see “Computational details” below), as well as the stability of keto and enol forms, and effects of metalation. Both periodic calculations and cluster models were used, the former giving band gaps, the latter, via linear response time-dependent DFT (TD-DFT) in addition excitation energies and oscillator strengths.

Periodic calculations were performed on AA-stacked COF periodic models for L-Acr, Acr²-L-Bpy¹ and Acr²-L-Bpy¹-Ni for single-layer models (L = Tp, DHTA, HTA, Tf). Relative energies of keto and enol tautomers at the PBE+D3 level show a strong preference (around 0.4 to 1.1 eV per unit cell) for keto-Tp and keto-DHTA, while enol HTA COFs are slightly more stable (by less than 0.1 eV) than keto HTA COFs. Band gaps between keto and enol tautomers typically differ by up to 0.2 eV at the PBE level (see Table S1, below), indicating a strong influence of keto-enol tautomerism on the electronic structure. Cluster models consisting of one complete pore were built from the PBE+D3 optimized planar bulk structures and reoptimized using PBE+D3. The results reported here all use a cluster model with amine groups capping the structure to ensure fully hydrogen-bonded keto groups if applicable (Figure S16).

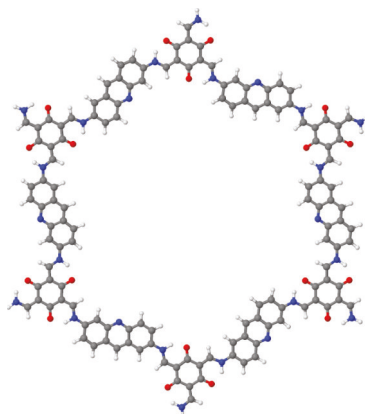


Figure S 16. Cluster models of Tp-Acr. The model is cut to keep the hydrogen-bonded amine groups.

Table S 1. Indirect band gaps in eV for planar periodic models; HOMO-LUMO gaps, E_g , and excitation energies (1st “bright” transition), E_{ex} , in eV for cluster models (in parentheses: enol tautomers).

	experimental UV-vis DRS	Periodic models		Cluster models		
		PBE planar, one layer	HSE PBE opt. one layer	PBE E_g	CAM-B3LYP E_g	E_{ex}
Tp-Acr	1.83 ^a	1.38	2.07	1.48	4.82	3.03
DHTA- Acr	1.83 ^a	1.19	1.84	1.07	4.31	2.71
HTA-Acr	1.82 ^a	0.94	1.54	0.82 (1.35)	4.08 (4.80)	2.59 (3.16)
Tf-Acr	1.87	1.66	2.35	1.68	5.04	3.23
Acr ² -Tp-Bpy ¹	1.92	1.41	2.11	1.53	4.89	3.03
Acr ² -DHTA-Bpy ¹	1.87	1.30	1.96	1.21	4.48	2.75
Acr ² -HTA-Bpy ¹	1.84	0.98	1.59	0.83 (1.33)	4.09 (4.75)	2.64 (3.22)
Acr ² -Tf-Bpy ¹	1.90	1.66	2.36	1.68	5.04	3.23
Acr ² -Tp-Bpy ¹ -Ni		1.01	1.94	1.09	4.63	2.92
Acr ² -DHTA-Bpy ¹ -Ni		1.07	1.65	0.73	3.97	2.69
Acr ² -HTA-Bpy ¹ -Ni		0.77	1.43	0.66 (0.81)	3.85 (4.37)	2.58 (2.95)
Acr ² -Tf-Bpy ¹ -Ni	1.92 ^b	0.88	2.06	0.85	4.59	3.15

^a Values obtained from literature.^[6] ^b Degree of metalation 19.4%

In Table S1 we compare indirect band gaps calculated from periodic models and HOMO-LUMO gaps and lowest bright transition energies for L-Acr, Acr²-L-Bpy¹ and Acr²-L-Bpy¹-Ni to the onset of measured UV-vis DRS spectra. Values for L-Acr have been obtained from literature.^[6] The exchange of an acridine unit with a bipyridine moiety is not having a significant impact on the optical properties, which can be confirmed with the theoretical calculations. Metalation of this bipyridine unit is in experimental spectra not resulting in a change of the band gap, while calculations would suggest a red shift. This is most likely because of incomplete metalation of the COF. Calculations suggest that the removal of additional hydroxy groups from Tp to DHTA and HTA results in a gradual decrease in band gap, while Tf linked COFs are not following this trend and have again larger band gaps. However, this trend is not observed for acridine containing COFs, while purely bipyridine linked COFs are following this trend (Figure S24). This suggests an insufficient representation of the acridine chromophore in the calculations. The absolute values for all calculated band gaps on the PBE level of theory differ significantly from the ones derived from UV-vis measurements. This is not unexpected, since PBE gives smaller gaps and excitation energies compared to functionals containing exact exchange (HSE and CAM-B3LYP). Further, in the cluster models only a single hexagonal pore was used for the calculations, and no defects/imperfections were considered. In fact, periodic models (on the PBE level of theory) provide a smaller gap when compared to cluster models. In passing we note that calculations indicate buckled/twisted structures being more stable than plana ones, which may also have an effect on the optoelectronic properties of the materials.

Computational details: Calculations on periodic models were performed with VASP^[7,8], version 5.4.4. Atomic positions and cell parameters were optimized using the PBE functional^[9] with the D3 dispersion correction^[10] with Becke-Johnson damping.^[11] Projector augmented-wave^[12,13] pseudopotentials were used, which included the semi-core s and p states for Ni (resulting in 18 explicitly treated electrons). The kinetic energy cutoff was set to 600 eV and a $2\times 2\times 4$ k point grid was used. SCF and force convergence criteria were set to 10^{-6} eV and 10^{-2} eV/Å, respectively. Single-layer models employ a cell vector perpendicular to the layer of 20 Å, resulting in a vacuum space of at least 16 Å for the twisted COFs. HSE^[14,15] single-point calculations were performed on the PBE-optimized single-layer models.

Cluster calculations were performed using ORCA,^[16] version 4.0.0.2. The cluster models were based on the periodic models and reoptimized using the PBE functional^[9] with the D3 dispersion correction^[10] with Becke-Johnson damping.^[11] A def2-TZVP basis set^[17] was employed together with an auxiliary def2 basis set for the RI approximation. CAM-B3LYP^[18–21] calculations were performed using the def2-SVP basis set.^[17] Time-dependent density functional theory (TD-DFT)^[22] was used to calculate excitation energies and oscillator strengths.

S4.11 Photoluminescence measurements of $\text{Acr}^2\text{-L-Bpy}^1$ multiple-component COFs

Preparation of the samples for luminescence studies: 0.5 mg of COF was dispersed in 10 ml acetonitrile by sonicating for 5 minutes at 40 °C. Prior the UV-vis and PL measurements the bigger particles were let to sediment to obtain a nearly clear solution. The clear COF dispersed solutions were used for the PL measurements.

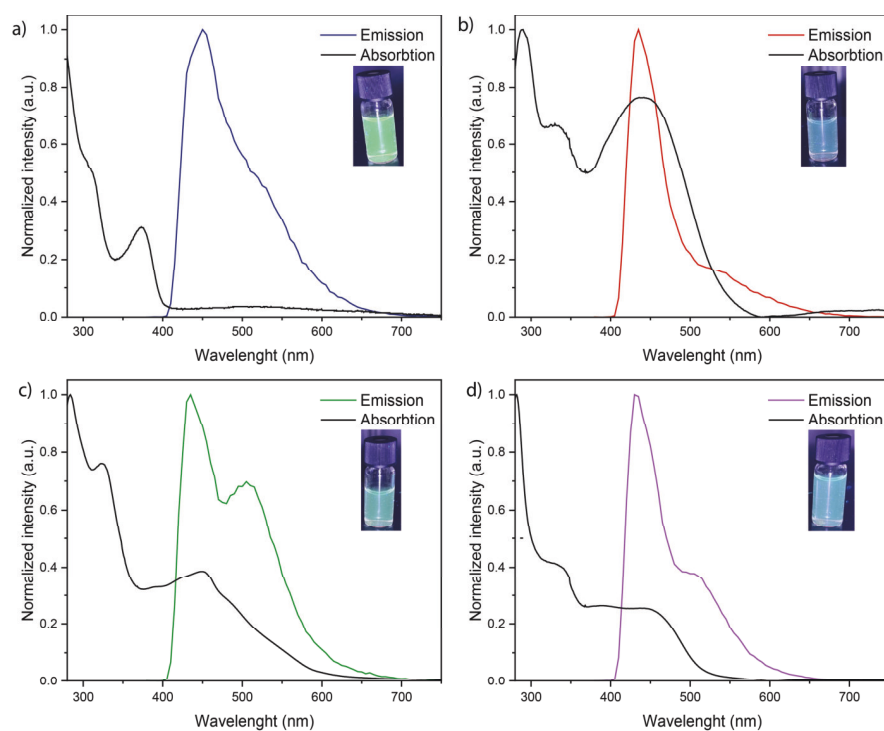


Figure S 17. Steady-state absorption and emission profiles of dispersed a) $\text{Acr}^2\text{-Tp-Bpy}^1$, b) $\text{Acr}^2\text{-DHTA-Bpy}^1$, c) $\text{Acr}^2\text{-HTA-Bpy}^1$ and d) HTA-Acr in acetonitrile. For the fluorescence measurements the samples were excited at a wavelength of 360 nm. Optical images at ambient light and upon excitation under a 365 nm UV-lamp is shown in every case.

S4.12 Fluorescence quenching studies of Acr²-Tf-Bpy¹ multiple-component COF

Preparation of the samples for luminescence studies:

0.5 mg of COF was dispersed in 10 ml DMSO by sonicating for 10 minutes. Prior the fluorescence measurements the bigger particles were let to sediment to obtain a nearly clear solution.

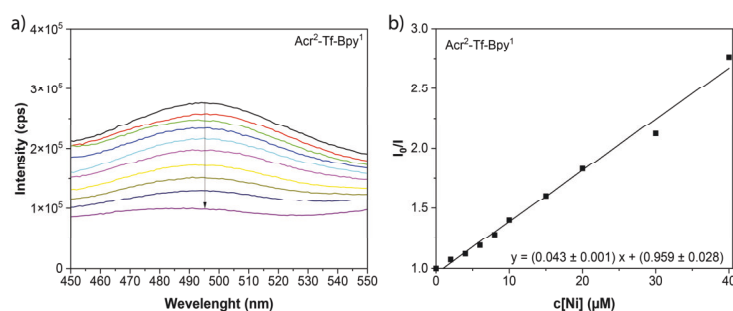


Figure S 18. a) Fluorescence quenching experiments of Acr²-Tf-Bpy¹ COF in presence of NiCl₂·glyme. b) Stern-Volmer quenching plot.

S4.13 Electron paramagnetic resonance (EPR) spin trap experiments of Acr²-Tf-[Ni]¹ and Acr²-Tp-[Ni]¹ multiple-component COFs

Acr²-Tf-[Ni]¹ and Acr²-Tp-[Ni]¹ COFs were prepared by ex-situ metalation of the respective multivalent frameworks in acetonitrile with an excess of NiCl₂·glyme at 40 °C for 3 h while stirring the suspension. The material was filtered and washed with H₂O dist., MeOH and cyclohexane before drying under vacuum. Electron paramagnetic resonance (EPR) spectra were recorded on a X-band Bruker EMX CW-micro EPR spectrometer equipped with an ER4119HS high-sensitivity resonator using modulation frequency of 100 kHz and modulation amplitude up to 1G. The experimental spectrum was simulated with EasySpin program. In-situ EPR spectrum was recorded at 20 °C during irradiating a home-made EPR quartz flat-cell (ID 0.5 mm) filled under Ar with a suspension of COF catalysts (5 mg COF + 20 μL 4-iodobenzotrifluoride + 5,5-dimethyl-1-pyrrolin-N-oxid (DMPO) solution prepared by dissolving of 10 μl DMPO in 0.5 MeCN). In situ EPR spectra were recorded before and after irradiation the sample with a 300 W Xe-arc lamp (LOT Oriel GmbH, Germany) using a cut-off filter GG420.

To gain more knowledge about the reason for different catalytic activity behaviors, in situ EPR investigations were conducted in the presence of DMPO as spin trap reagent to detect the

possible formation of organic radical during the catalytic reaction. Photoirradiation of $\text{Acr}^2\text{-Tf-[Ni]}^1$ in the presence of 4-iodobenzotrifluoride caused appearing of multiple-lines EPR signal at $g = 2.007$ and its intensity increased with irradiation time (Figure S18a). This signal can be simulated assuming the coupling of electron spin half center ($S = 1/2$) interacting with two nonequivalent nitrogen nuclei ($I = 1$; $A_{\text{N1}} = 13.23$ G and $A_{\text{N2}} = 1.27$ G) and one hydrogen nucleus ($I = 1/2$; $A_{\text{H}} = 8.94$ G) suggesting the formation of DMPO-N spin adduct (Figure S18b, red line). This indicates the formation of N centered radical during the irradiation of the $\text{Acr}^2\text{-Tf-[Ni]}^1$ catalyst. The EPR spectrum also showed the appearing of an additional weak signal with time. The origin of this signal is not clear since it is very weak and only its outer lines were resolved (indicated by a star in Figure S18b, black line). In comparison to the $\text{Acr}^2\text{-Tf-[Ni]}^1$ COF, very weak signal was observed for the $\text{Acr}^2\text{-Tp-[Ni]}^1$ (Figure S19, blue line) revealing the low photocatalytic activity of the keto-enamine linked COF compared to the fully imine multivalent framework.

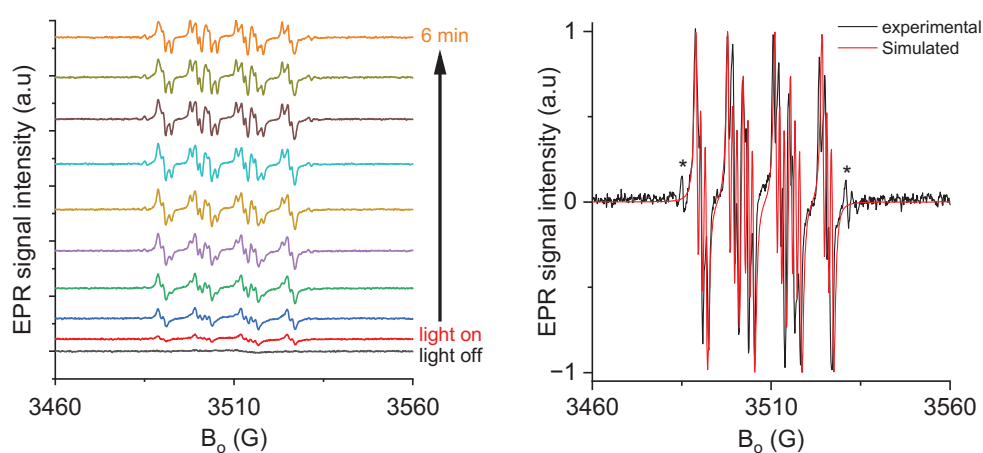


Figure S19. a) EPR spectra of $\text{Acr}^2\text{-Tf-[Ni]}^1$ in 0.5 CH_3CN in the presence of 4-iodobenzotrifluoride and DMPO during irradiation, measured with modulation amplitude of 0.3 G for better resolving the small hyperfine structures. b) simulation of the experimental spectrum after 4 min irradiation.

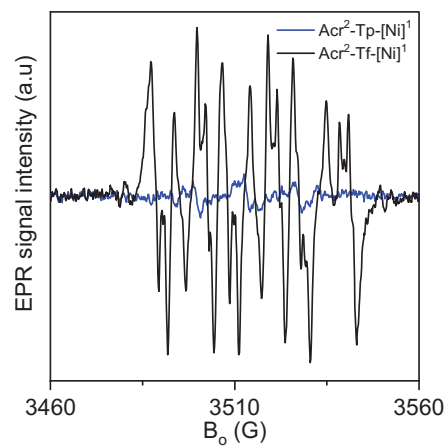


Figure S 20. EPR spectra of $\text{Acr}^2\text{-Tf-[Ni]}^1$ (black line) and $\text{Acr}^2\text{-Tp-[Ni]}^1$ in CH_3CN in the presence of 4-iodobenzotrifluoride and DMPO during irradiation for 1 min), measured with modulation amplitude of 1 G for better signal intensity.

S5. Synthesis and characterization of reference COFs

S5.1 Synthesis of bipyridine COFs

Tp-Bpy COF: A Pyrex tube (o.d. \times i.d. = 15×10 mm² and length 15 cm) is charged with trimethylphloroglucinol (**Tp**) (21 mg, 0.1 mmol), 2,2'-bipyridine-5,5'-diamine (**Bpy**) (27.9 mg, 0.15 mmol), 1.5 mL of mesitylene, 1.5 mL of 1,4-dioxane and 0.5 mL of 6 M aqueous acetic acid. This mixture was sonicated for 15 minutes in order to get a homogenous dispersion. The tube was then flash frozen at 77 K (liquid N₂ bath) and degassed by three freeze-pump-thaw cycles. The tube was sealed off and then heated at 120 °C for 3 days. An orange colored precipitate was collected by filtration and washed with acetone, methanol and cyclohexane. The powder collected was dried at 120 °C to give a dark orange colored powder (43 mg, 99 %).

DHTA-Bpy COF: A Pyrex tube (o.d. \times i.d. = 15×10 mm² and length 15 cm) is charged with 2,4-dihydroxybenzene-1,3,5-tricarbaldehyde (**DHTA**) (19.4 mg, 0.1 mmol), 2,2'-bipyridine-5,5'-diamine (**Bpy**) (27.9 mg, 0.15 mmol), 1.5 mL of mesitylene, 1.5 mL of 1,4-dioxane and 0.5 mL of 6 M aqueous acetic acid. This mixture was sonicated for 15 minutes in order to get a homogenous dispersion. The tube was then flash frozen at 77 K (liquid N₂ bath) and degassed by three freeze-pump-thaw cycles. The tube was sealed off and then heated at 120 °C for 3 days. A red colored precipitate was collected by filtration and washed with acetone, methanol and cyclohexane. The powder collected was dried at 120 °C to give a bright red colored powder (34 mg, 81 %).

HTA-Bpy COF: A Pyrex tube (o.d. \times i.d. = 15×10 mm² and length 15 cm) is charged with 2-hydroxybenzene-1,3,5-tricarbaldehyde (**HTA**) (17.8 mg, 0.1 mmol), 2,2'-bipyridine-5,5'-diamine (**Bpy**) (27.9 mg, 0.15 mmol), 1.5 mL of mesitylene, 1.5 mL of 1,4-dioxane and 0.5 mL of 6 M aqueous acetic acid. This mixture was sonicated for 15 minutes in order to get a homogenous dispersion. The tube was then flash frozen at 77 K (liquid N₂ bath) and degassed by three freeze-pump-thaw cycles. The tube was sealed off and then heated at 120 °C for 3 days. A red colored precipitate was collected by filtration and washed with acetone, methanol and cyclohexane. The powder collected was dried at 120 °C to give a bright red colored powder (40 mg, 99 %).

Tf-Bpy COF: A Pyrex tube (o.d. \times i.d. = 15×10 mm² and length 15 cm) is charged with 1,3,5-triformylbenzene (**Tf**) (16.2 mg, 0.1 mmol), 2,2'-bipyridine-5,5'-diamine (**Bpy**) (27.9 mg, 0.15 mmol), 1.5 mL of mesitylene, 1.5 mL of 1,4-dioxane and 0.5 mL of 6 M aqueous acetic acid. This mixture was sonicated for 15 minutes in order to get a homogenous dispersion. The tube was then flash frozen at 77 K (liquid N₂ bath) and degassed by three freeze-pump-thaw cycles. The tube was sealed off and then heated at 120 °C for 3 days. A yellow colored precipitate was collected by filtration and washed with acetone, methanol and cyclohexane. The powder collected was dried at 120 °C to give a bright yellow colored powder (32 mg, 82 %).

S5.2 Characterization of bipyridine COFs

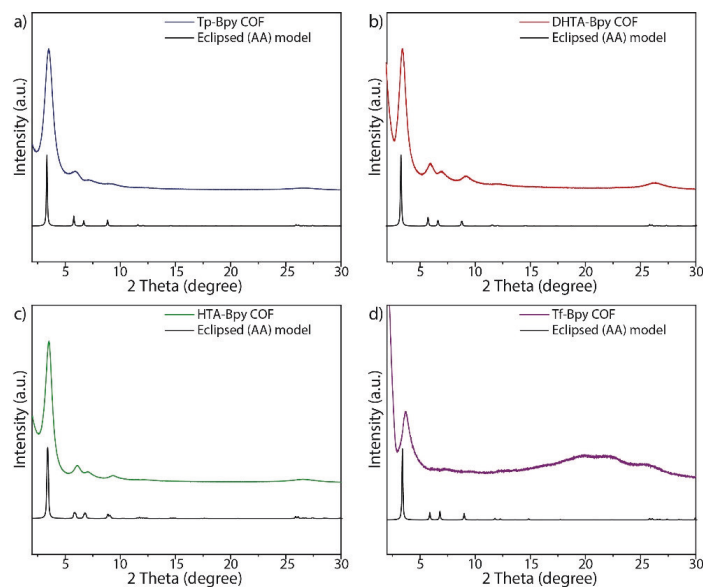


Figure S 21. Comparison between simulated and experimental PXRD patterns for a) Tp-Bpy, b) DHTA-Bpy, c) HTA-Bpy and d) Tf-Bpy COFs, showing agreement between the experimental diffractogram and the eclipsed stacking model (AA).

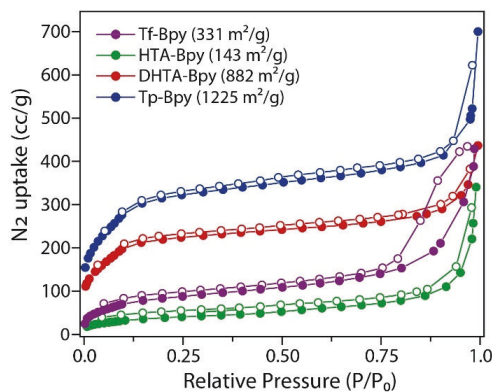


Figure S 22. N₂ sorption isotherms for Tp-Bpy, DHTA-Bpy, HTA-Bpy and Tf-Bpy COFs, calculated BET surface areas are shown in brackets.

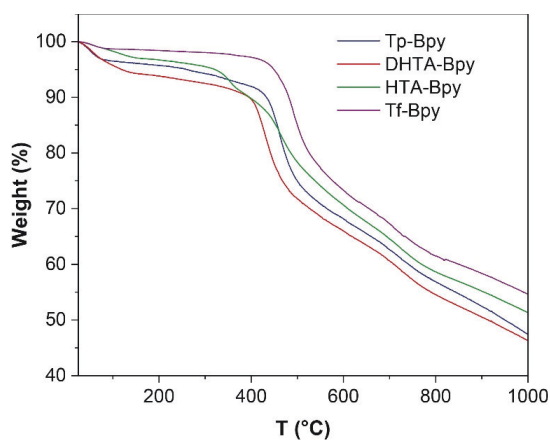


Figure S 23. Thermogravimetric analyses (TGA) for Tp-Bpy, DHTA-Bpy, HTA-Bpy and Tf-Bpy COFs, showing the thermal stability of the COFs below 350 °C, under nitrogen atmosphere.

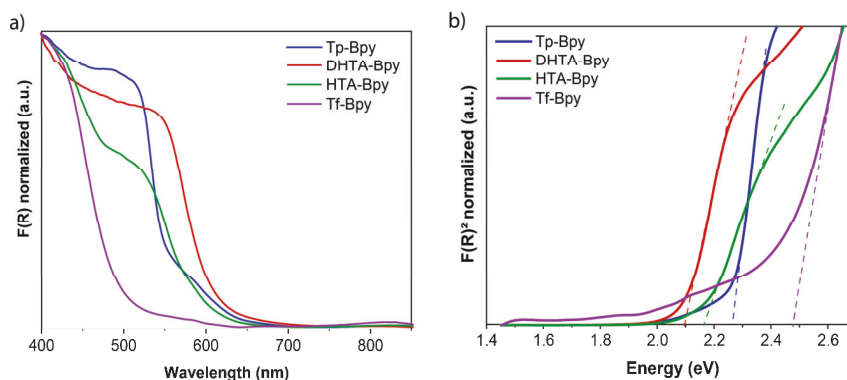


Figure S 24. a) UV-vis diffuse reflectance spectroscopy analysis of Acr¹-L-Bpy² COFs. b) Tauc plots for Acr¹-L-Bpy² COFs.

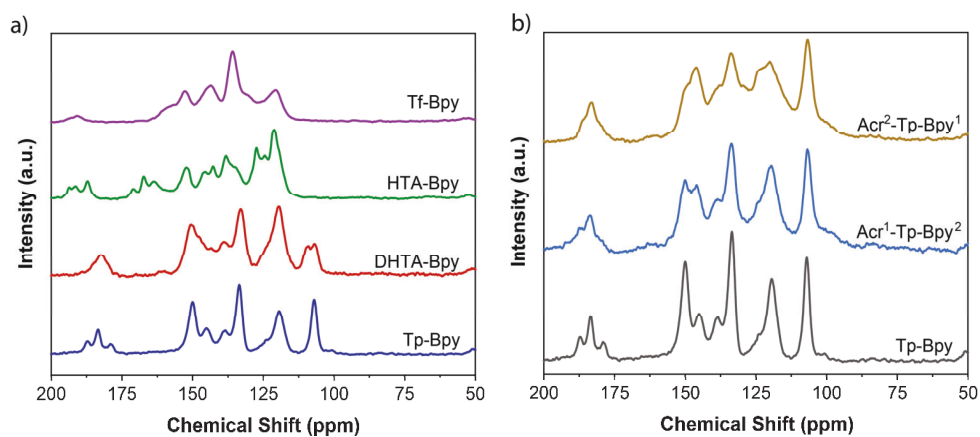


Figure S 25. a) ¹³C CP-MAS NMR spectra of Tp-Bpy, DHTA-Bpy, HTA-Bpy and Tf-Bpy COF. b) Following the trend of introduction of bipyridine units for Acr^x-Tp-Bpy^y COFs.

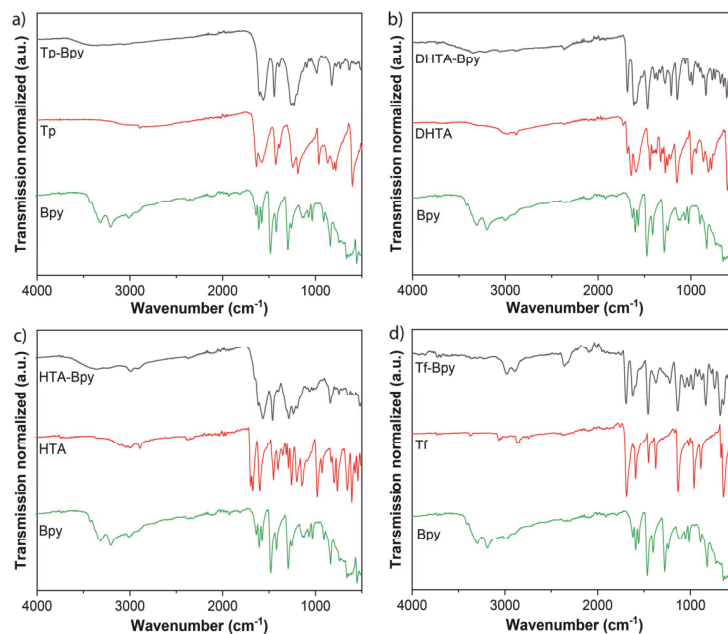


Figure S 26. FT-IR analyses of L-Bpy COFs [L = Tp (a), DHTA (b), HTA (c), Tf (d)] in comparison with the corresponding aldehydes and amine (Bpy) showing the formation of the framework structure.

S5.3 Synthesis of Tf-Acr COF

Tf-Acr COF: A Pyrex tube (o.d. \times i.d. = 15 \times 10 mm² and length 15 cm) is charged with 1,3,5-triformylbenzene (**Tf**) (16.2 mg, 0.1 mmol), 2,6-diaminoacridine (**Acr**) (31.5 mg, 0.15 mmol), 1.5 mL of *n*-BuOH, 1.5 mL of anhydrous *o*-DCB and 0.5 mL of 6 M aqueous acetic acid. This mixture was sonicated for 15 minutes in order to get a homogenous dispersion. The tube was then flash frozen at 77 K (liquid N₂ bath) and degassed by three freeze-pump-thaw cycles. The tube was sealed off and then heated at 120 °C for 3 days. A dark red precipitate was collected by filtration and washed with acetone, methanol and cyclohexane. The powder collected was dried at 120 °C to give a dark red powder (31 mg, 72 %).

S5.4 Characterization of Tf-Acr COF

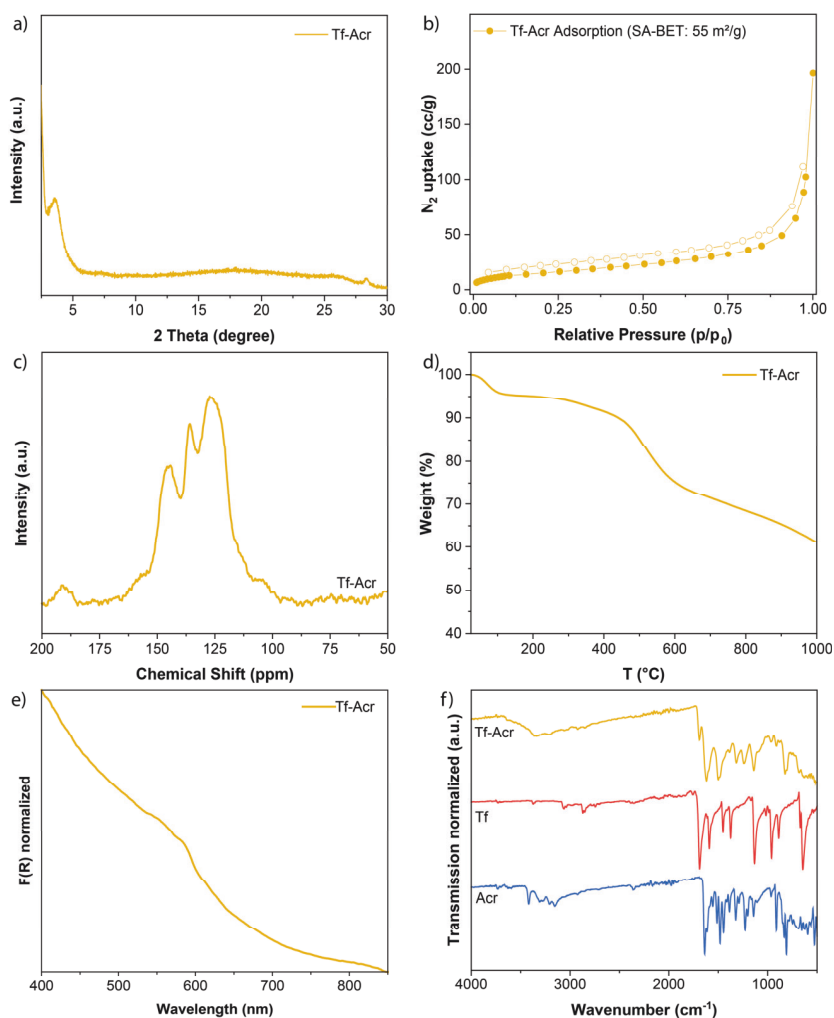
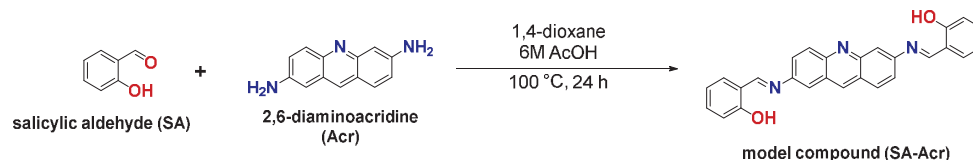


Figure S 27. Characterization of Tf-Acr COF using PXRD (a), N₂ sorption (b) ¹³C CP-MAS NMR (c), TGA (d), diffuse reflectance UV-vis (e) and FT-IR (f).

S6. Synthesis and characterization of model compounds

S6.1 Synthesis of acridine model compound (SA-Acr)



Scheme S 7. Synthesis of the model compound SA-Acr.

Model compound (SA-Acr): To a Schlenk flask were 63 mg (0.30 mmol, 1.0 eq.) of 2,6-diaminoacridine (Acr), 68 μl (0.66 mmol, 2.2 eq.) and 5 mL of 1,4-dioxane added. To the resulting suspension 1.0 mL of 6 M aqueous acetic acid were added. The flask was closed and heated to 100 $^{\circ}\text{C}$ for 24 h while stirring the reaction mixture. After cooling to room temperature, the resulting yellow-brown suspension was filtered and washed with 10 mL acetone to remove residual starting materials. The model compound was subsequently dried under vacuo to give the desired compound as a dark brown powder (71 mg, 57%).

ESI-MS $[\text{M}+\text{H}^+]$ (m/z): 418.1549 (th.: 418.1550). Due to the low solubility of this compound in common deuterated solvents, no ^{13}C NMR spectra could be recorded.

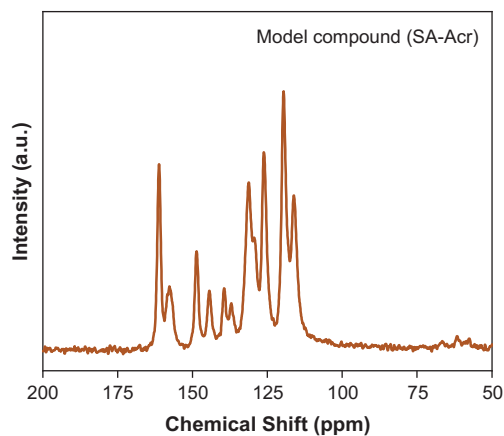
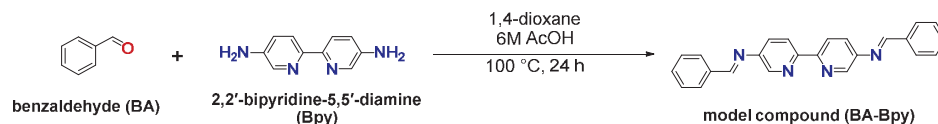


Figure S 28. ^{13}C CP-MAS solid-state NMR spectra of the model compound SA-Acr.

S6.2 Synthesis of bipyridine model compounds (BA-Bpy)



Scheme S 8. Synthesis of the model compound BA-Bpy.

Model compound (BA-Bpy): To a Schlenk flask were 56 mg (0.30 mmol, 1.0 eq.) of 2,2'-bipyridine-5,5'-diamine (Bpy), 67 μl (0.66 mmol, 2.2 eq.) of benzaldehyde and 5 mL of 1,4-dioxane added. To the resulting solution 1.0 mL of 6 M aqueous acetic acid were added. The flask was closed and heated to 100 $^{\circ}\text{C}$ for 24 h while stirring the reaction mixture. After cooling to room temperature, the resulting dark yellow suspension was filtered and washed with 10 mL of diethyl ether to remove residual starting materials. The model compound was subsequently dried under vacuo to give the desired compound as a dark yellow powder (75 mg, 69%).

^1H NMR (700 MHz, DMSO) δ 8.81 (s, 2H), 8.63 (d, J = 2.5 Hz, 2H), 8.45 (d, J = 8.4 Hz, 2H), 8.00 (dd, J = 7.9, 1.3 Hz, 4H), 7.89 (dd, J = 8.4, 2.5 Hz, 2H), 7.61 – 7.54 (m, 6H) ppm. ^{13}C NMR (176 MHz, DMSO) δ 162.9, 152.6, 147.2, 143.0, 135.8, 132.0, 129.0, 128.9, 128.7, 120.7 ppm. ESI-MS $[\text{M}+\text{H}^+]$ (m/z): 363.1603 (th.: 363.1604).

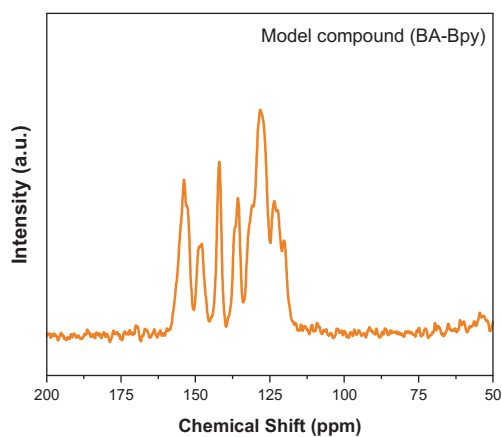


Figure S 29. ^{13}C CP-MAS solid-state NMR spectra of the model compound BA-Bpy. The peaks found are in full agreement with the liquid state NMR results.

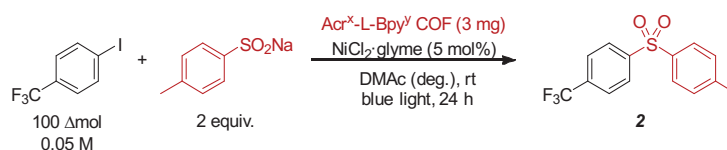
S7. Photocatalytic reaction optimization

S7.1 General experimental procedure for screening experiments

An oven dried vial (19 x 100 mm) equipped with a stir bar was charged with $\text{NiCl}_2 \cdot \text{glyme}$ (4–12 μmol), 3 mg of $\text{Acr}^x\text{-L-Bpy}^y$ COF, 4-halobenzotrifluoride (100 μmol) and nucleophile (200 μmol). The solvent (anhydrous) was added and the vessel was sealed with a septum and Parafilm. The mixture was stirred for 1 minute at high speed, followed by sonication for 5 minutes and degassing by bubbling argon for 10 minutes. The reaction mixture was stirred at 800 rpm and irradiated with 440 nm, 535 nm or 666 nm LED lamps using the reported power settings. After the respective reaction time, 1,3,5-trimethoxybenzene (1 equiv) was added to the reaction vessel, the mixture was shaken and an aliquot (200 μL) was removed, filtered, diluted with $\text{DMSO}-d_6$ and analyzed by ^1H NMR.

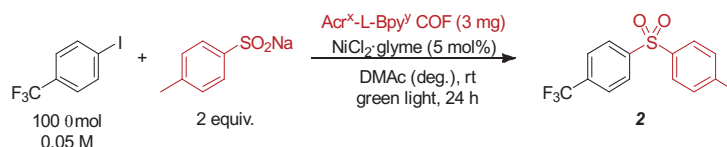
S7.2 Initial screening experiments using sodium *p*-toluensulfinate

Table S 2. Screening experiments for the coupling of 4-iodobenzotrifluoride and sodium *p*-toluensulfinate using 440 nm.^a



Entry	Variations	2 [%] ^c
MT30	Tp-Bpy	6
MT31	DHTA-Bpy	16
MT32	HTA-Bpy	28
MT33	$\text{Acr}^2\text{-Tp-Bpy}^1$	15
MT34	$\text{Acr}^2\text{-DHTA-Bpy}^1$	20
MT35	$\text{Acr}^2\text{-HTA-Bpy}^1$	34
MT36	No COF	traces

^aReaction conditions: 4-iodobenzotrifluoride (100 μmol), sodium *p*-toluensulfinate (200 μmol), $\text{NiCl}_2 \cdot \text{glyme}$ (5 μmol), COF (3 mg), DMAc (anhydrous, 2 mL), 440 nm LED (1 lamp at full power). ^bConversion of 4-iodobenzotrifluoride determined by ^1H -NMR using 1,3,5-trimethoxybenzene as internal standard. ^cNMR yields determined by ^1H -NMR using 1,3,5-trimethoxybenzene as internal standard. glyme = 1,2-dimethoxyethane. n.d. = not detected.

Table S 3. Screening experiments for the coupling of 4-iodobenzotrifluoride and sodium *p*-toluenesulfonate using 525 nm.^a

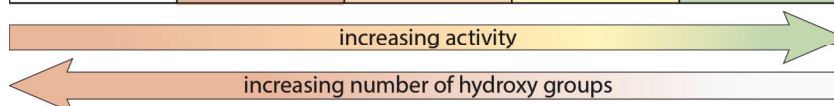
Entry	Variations	2 [%] ^c
MT30	Tp-Bpy	3
MT31	DHTA-Bpy	5
MT32	HTA-Bpy	17
MT33	Acr ² -Tp-Bpy ¹	9
MT34	Acr ² -DHTA-Bpy ¹	7
MT35	Acr ² -HTA-Bpy ¹	11
MT36	No COF	traces

^aReaction conditions: 4-iodobenzotrifluoride (100 μmol), sodium *p*-toluenesulfonate (200 μmol), NiCl₂·glyme (5 μmol), COF (3 mg), DMAc (anhydrous, 2 mL), 525 nm LED (1 lamp at full power). ^bConversion of 4-iodobenzotrifluoride determined by ¹H-NMR using 1,3,5-trimethoxybenzene as internal standard. ^cNMR yields determined by ¹H-NMR using 1,3,5-trimethoxybenzene as internal standard. glyme = 1,2-dimethoxyethane. n.d. = not detected.

S7.3 Screening experiments for different COFs

Table S 4. Screening experiments for the coupling of 4-iodobenzotrifluoride and sodium *p*-toluenesulfonate using different COFs.

Acr:Bpy (Ni mol%)				
2:1 (4 mol%)	25	33	43	55
1:2 (8 mol%)	19	29	35	49
0:1 (12 mol%)	10	30	39	59



Reaction conditions: 4-iodobenzotrifluoride (100 μmol), sodium *p*-toluenesulfonate (200 μmol), NiCl₂·glyme (4-12 mol%), COF (3 mg), DMAc (anhydrous, 2 mL), 440 nm LED (2 lamps at full power). NMR yields determined by ¹H-NMR using 1,3,5-trimethoxybenzene as internal standard.

S7.4 Screening different COFs for cross-coupling of aryl halides and nucleophiles

Table S 5. Screening experiments for the coupling of 4-iodobenzotrifluoride and methyl 3-mercaptopropionate using different COFs.

Acr:Bpy (Ni mol%)				
2:1, 2 h	4 (21)	41 (46)	59 (64)	86 (86)
2:1, 5 h	54 (54)	99 (quant.)	92 (quant.)	96 (quant.)

Reaction conditions: 4-iodobenzotrifluoride (100 μ mol), methyl 3-mercaptopropionate (200 μ mol), NiCl₂·glyme (4 mol%), COF (3 mg), *N,N*-tert-butylisopropylamine (BIPA, 500 μ mol), MeCN (anhydrous, 2 mL), 440 nm LED (2 lamp at full power). NMR yields and conversion of 4-iodobenzotrifluoride determined by ¹H-NMR using 1,3,5-trimethoxybenzene as internal standard. Conversion in brackets.

Table S 6. Screening experiments for the coupling of 4-bromobenzotrifluoride and pyrrolidine using different COFs.

Acr:Bpy = 2:1	80 (quant.)	28 (40)	14 (29)	4 (16)

Reaction conditions: 4-bromobenzotrifluoride (200 μ mol), pyrrolidine (600 μ mol), NiCl₂·glyme (4 mol%), COF (3 mg), DMAc (anhydrous, 1 mL), 440 nm LED (2 lamp at full power). Conversion of 4-iodobenzotrifluoride determined by ¹H-NMR using 1,3,5-trimethoxybenzene as internal standard; conversion noted in brackets. NMR yields determined by ¹H-NMR using 1,3,5-trimethoxybenzene as internal standard.

S7.5 Control studies

Table S 7. Control experiments

Fc1ccc(I)cc1 + COCC(=O)S
 $\xrightarrow[\text{MeCN (deg.), rt, blue light, 3 h}]{\text{Acr}^2\text{-Tf-Bpy}^1 \text{ COF (3 mg), NiCl}_2\cdot\text{glyme (4 mol\%), BIPA (5 equiv)}}$
COCC(=O)Sc1ccc(F)cc1

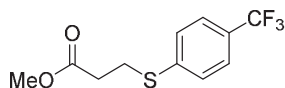
 100 μmol 0.05 M 2 equiv. **1**

Entry	Variation	Conversion [%] ^b	1 [%] ^c
1	None	quant.	98
2	No COF	12	4
3	No NiCl ₂ ·glyme	8	traces
4	No BIPA	10	n.d.
5	No light	8	n.d.
6	Pre-ligated (COF+NiCl ₂ ·glyme)	quant.	99
7	Tp-Acr + dtbppy	35	33
8	Tf-Acr (2 mg) + Tf-Bpy (1 mg)	34	34
9	green instead of blue light, 5h	74	74
10	green instead of blue light, 5h, Tf-Bpy	24	23
11	red instead of blue light, 5h	15	9
12	red instead of blue light, 48h	quant.	99

^aReaction conditions: 4-iodobenzotrifluoride (100 μmol), methyl 3-mercaptopropanoate (200 μmol), NiCl₂·glyme (4 mol%), COF (3 mg), *N,N*-tert-butylisopropylamine (BIPA, 500 μmol), MeCN (anhydrous, 2 mL), blue light (440 nm; 2 lamp at full power), green light (525 nm; 2 lamp at full power), red light (666 nm; 2 lamp at full power). ^bConversion of 4-iodobenzotrifluoride determined by ¹H-NMR using 1,3,5-trimethoxybenzene as internal standard. ^cNMR yields determined by ¹H-NMR using 1,3,5-trimethoxybenzene as internal standard. n.d. = not detected.

Experimental procedure for methyl 3-((4-(trifluoromethyl)phenyl)thio)propanoate

An oven dried vial (13 x 95 mm) equipped with a stir bar was charged with NiCl₂·glyme (2.6 mg, 12 μmol, 4 mol%), 4-iodobenzotrifluoride (0.3 mmol, 1 equiv.) and Tf-COF (9.0 mg). Subsequently, methyl 3-mercaptopropanoate (0.6 mmol, 2 equiv.), *N,N*-tert-butylisopropylamine (BIPA, 1.5 mmol, 5 equiv.), MeCN (anhydrous, 6 mL) were added and the vial was sealed with a septum and parafilm. The reaction mixture was sonicated for 5-10 min and the mixture was then degassed by bubbling N₂ for 10 min. The mixture was stirred at 800 rpm and irradiated with two LED lamps (440 nm) at full power. After the respective reaction time, one equivalent of 1,3,5-trimethoxybenzene (50.5 mg, 0.3 mmol, internal standard) was added. An aliquot (~300 μL) of the reaction mixture was diluted with DMSO-d₆ and subjected to ¹H-NMR analysis. The NMR sample was combined with the reaction mixture, diluted with H₂O (40 mL) and extracted with ethyl acetate (3 x 30 mL). The combined organic phases were washed with aqueous NaOH (1 M, 2 x 40 mL) and brine (40 mL), dried over MgSO₄ and concentrated. The product was purified by flash column chromatography (SiO₂, cyclohexane/EtOAc) on a Biotage Isolera system using a 25 g cartridge and an elution gradient of 0-5 % of ethyl acetate in cyclohexane. The product was gained in 91% yield (72 mg, 273 μmol) as a white solid. The final product was characterized by ¹H-NMR, ¹³C-NMR, ¹⁹F-NMR.



Methyl 3-((4-(trifluoromethyl)phenyl)thio)propanoate: ¹H NMR (700 MHz, CDCl₃) δ 7.52 (d, J = 8.3 Hz, 2H), 7.39 (d, J = 8.2 Hz, 2H), 3.69 (s, 3H), 3.24 (t, J = 7.4 Hz, 2H), 2.67 (t, J = 7.4 Hz, 2H) ppm. ¹³C NMR (176 MHz, CDCl₃) δ 172.0, 141.1, 128.3, 128.1 (q, J = 32.6 Hz), 125.93 (q, J = 3.7 Hz), 124.20 (q, J = 271.8 Hz), 52.1, 33.9, 27.9 ppm. ¹⁹F NMR (659 MHz, CDCl₃) δ -62.51 (s, 3F) ppm. ESI-MS [M+H⁺] (m/z): 265.0503 (th.: 265.0505).

These data are in full agreement with those previously published in the literature.^[23]

S8. Photocatalysis - recycling studies

S8.1 Reaction procedure

An oven dried vial (13 x 80 mm) equipped with a stir bar was charged with $\text{Acr}^2\text{-Tf-Bpy}^1$ (9 mg) and $\text{NiCl}_2\cdot\text{glyme}$ (2.6 mg, 12 μmol , 4 mol%). Subsequently, 4-iodobenzotrifluoride (0.3 mmol, 1 equiv.) methyl 3-mercaptopropionate (0.6 mmol, 2 equiv.), *N,N*-tert-butylisopropylamine (BIPA, 1.5 mmol, 5 equiv.), MeCN (anhydrous, 6 mL) were added and the vial was sealed with a septum and Parafilm. The reaction mixture was sonicated for 5-10 min followed by stirring for 5 min until fine dispersion of the solids was achieved and the mixture was then degassed by bubbling N_2 for 10 min. The mixture was stirred at 800 rpm and irradiated with one or two LED lamps (440 nm) at full power. After the respective reaction time, one equivalent of 1,3,5-trimethoxybenzene (50.5 mg, 0.3 mmol) was added and the mixture was stirred for 5 min. The reaction mixture was centrifuged at 3500 rpm for 10 min and the liquid phase was carefully separated and analyzed by $^1\text{H-NMR}$. The $\text{Acr}^2\text{-Tf-Bpy}^1$ COF was washed 2 times with MeCN (anhydrous, 3 mL, followed by centrifugation at 3500 rpm for 10 min and separation of the liquid phase) and reused in the next reaction.

Table S 8. Catalyst Recycling experiments of the C-S arylation with the 440 nm setup using an *in situ* generated catalyst.^a

Fc1ccc(I)cc1 + COCCSCC(=O)OC
 $\xrightarrow[\text{MeCN (deg.), rt, blue light, 3 h}]{\text{Acr}^2\text{-Tf-Bpy}^1 \text{ COF (9 mg), NiCl}_2 \text{ glyme (4 mol\%), BIPA (5 equiv.)}}$
Fc1ccc(SCCC(=O)OC)cc1

 300 μmol 0.05 M 2 equiv. 1

Entry	Cycle	Conversion [%] ^b	1 [%] ^c
1	1	quant.	96
2	2	quant.	98
3	3	quant.	97
4	4	quant.	98
5	5	quant.	97

^aReaction conditions: 4-iodobenzotrifluoride (300 μmol), methyl 3-mercaptopropionate (600 μmol), $\text{NiBr}_2\cdot\text{glyme}$ (4 mol%), COF (9 mg), *N,N*-tert-butylisopropylamine (BIPA, 1.5 mmol), MeCN (anhydrous, 6 mL), blue light (440 nm; 2 lamp at full power).

^bConversion of 4-iodobenzotrifluoride determined by $^1\text{H-NMR}$ using 1,3,5-trimethoxybenzene as internal standard. ^cNMR yields determined by $^1\text{H-NMR}$ using 1,3,5-trimethoxybenzene as internal standard. n.d. = not detected.

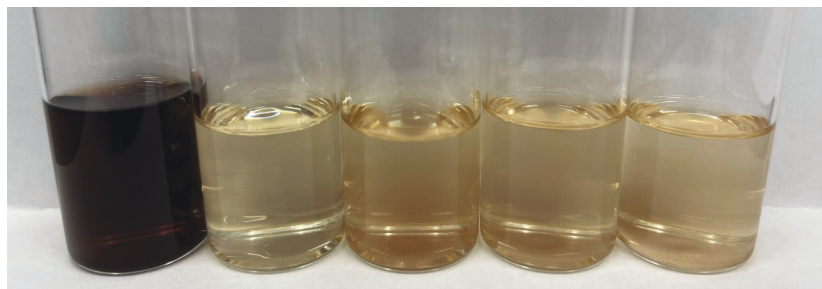
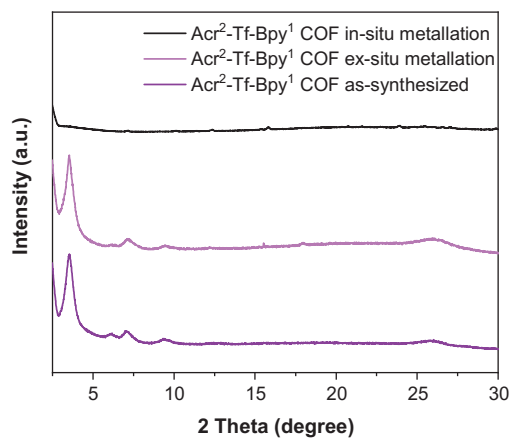


Figure S 30. Reaction mixtures (see Table S 8) by centrifugation.

S8.2 Analysis of recycled Tp-Acr COF

Table S 9. ICP-OES measurements of the nickel content of the $\text{Acr}^2\text{-Tf-Bpy}^1$ COF, $\text{Acr}^2\text{-Tf-[Ni]}^1$ COF in- and ex-situ preparation and the recovered $\text{Acr}^2\text{-Tf-Bpy}^1$ COF after 5 cycles.

Sample	Ni [mg/g catalyst]	Occupancy of Bpy sites [%]
$\text{Acr}^2\text{-Tf-Bpy}^1$ COF	0.317	-
$\text{Acr}^2\text{-Tf-Bpy}^1\text{-Ni}$ COF (in situ)	13.9	20.0
$\text{Acr}^2\text{-Tf-Bpy}^1\text{-Ni}$ COF (ex situ)	3.59	5.1
$\text{Acr}^2\text{-Tf-Bpy}^1\text{-Ni}$ COF (after 5 cycles) ^a	10.3	14.7

^a $\text{Acr}^2\text{-Tf-Bpy}^1$ COF after 5 reaction cyclesFigure S 31. PXRD analyses of $\text{Acr}^2\text{-Tf-Bpy}^1$ before and after photocatalysis (in-situ metallation), and ex-situ metallation, showing that the framework structure loses crystallinity under photocatalysis conditions, compared to metallation without light irradiation

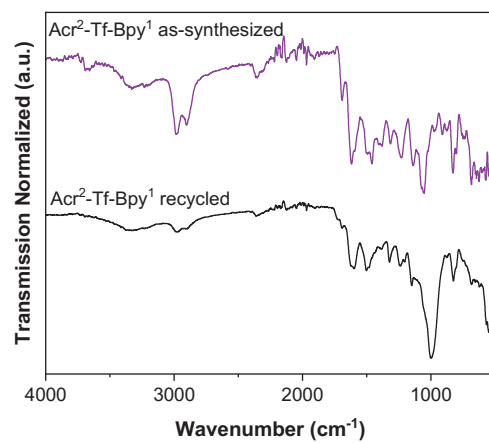


Figure S 32. FT-IR analyses of Acr²-Tf-Bpy¹ COF before and after photocatalysis, showing that the framework structure remains stable under photocatalysis conditions.

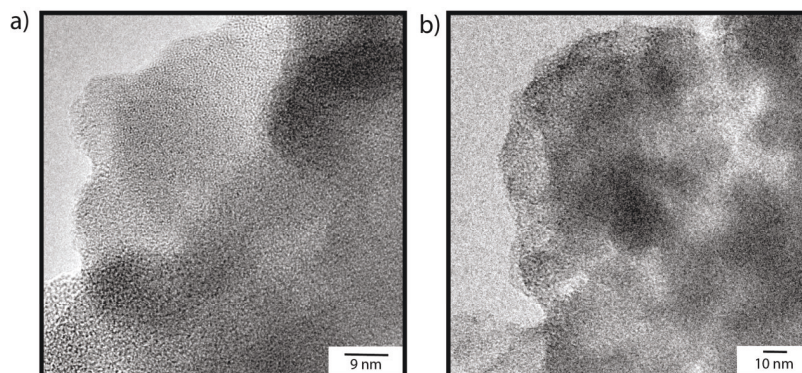


Figure S 33. TEM analyses of Acr²-Tf-Bpy¹ before (a) and after photocatalysis (b), respectively, showing the morphology and the layered structure of the COF matrix, unchanged by photocatalysis.

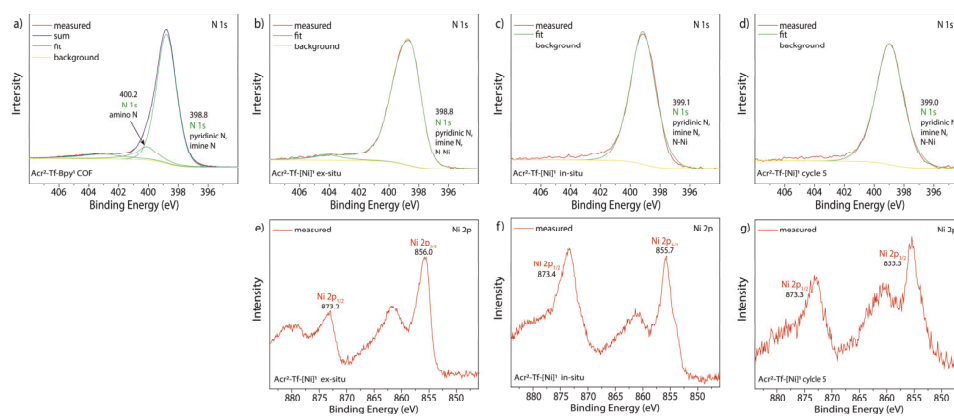


Figure S 34. (a, b, c, d) N 1s XPS core level spectra of the Acr²-Tf-Bpy¹ COF (a), ex-situ metallated Acr²-Tf-Bpy¹-Ni COF (b), in-situ metallated Acr²-Tf-Bpy¹-Ni COF (c) and Acr²-Tf-Bpy¹-Ni COF after 5 recycling cycles (d) of photocatalytic dual nickel C-S cross coupling. (e, f, g) Ni 2p XPS core level spectra of the ex-situ metallated Acr²-Tf-Bpy¹-Ni COF (e), in-situ metallated Acr²-Tf-Bpy¹-Ni COF (f) and Acr²-Tf-Bpy¹-Ni COF after 5 recycling cycles (g) of photocatalytic dual nickel C-S cross coupling.

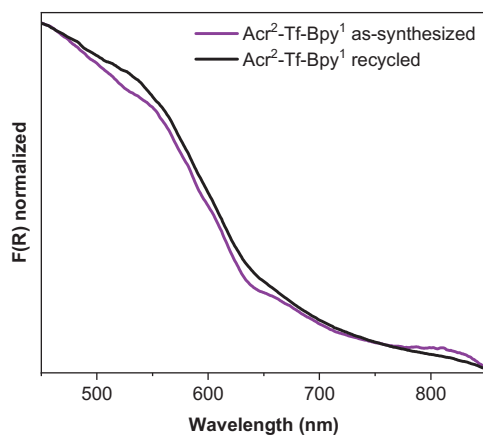


Figure S 35. UV-vis diffuse reflectance spectroscopy analysis of Acr²-Tf-Bpy¹ COF before and after in-situ metalation during photocatalysis, showing no effect of the nickel on the optical properties of the framework.

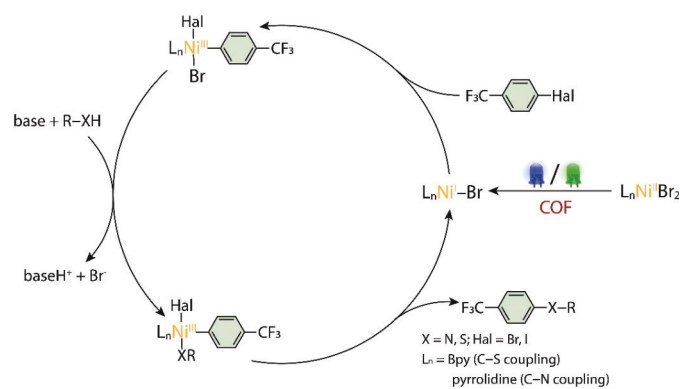


Figure S 36. Proposed mechanisms invoked in the nickel mediated metallaphotocatalytic C-X cross-coupling by a thermally sustained Ni^{II/III} cycle.

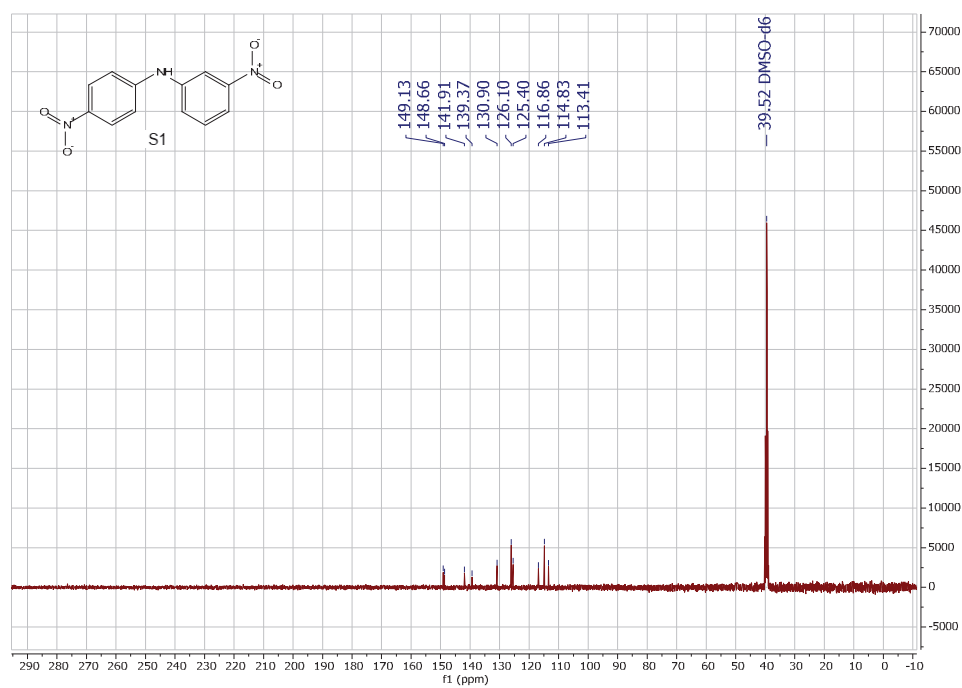
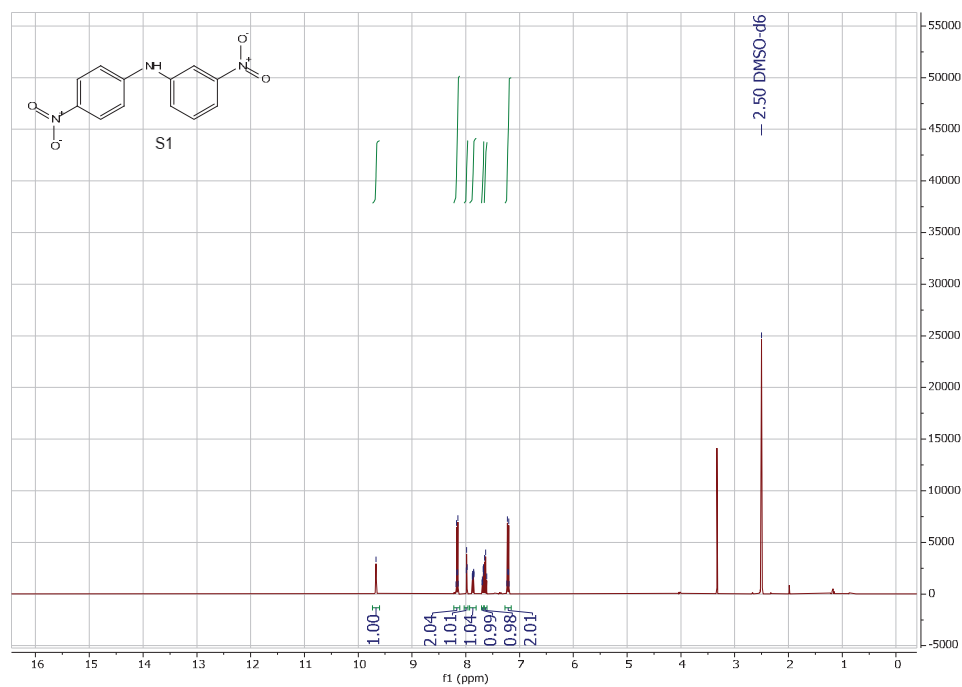
S10. References

- [1] “<https://www.kessil.com/photoreaction/PR160L.php>,” **n.d.**
- [2] D. H. O’Donovan, B. Kelly, E. Diez-Cecilia, M. Kitson, I. Rozas, *New J. Chem.* **2013**, 37, 2408–2418.
- [3] J. H. Chong, M. Sauer, B. O. Patrick, M. J. MacLachlan, *Org. Lett.* **2003**, 5, 3823–3826.
- [4] S. Haldar, D. Chakraborty, B. Roy, G. Banappanavar, K. Rinku, D. Mullangi, P. Hazra, D. Kabra, R. Vaidhyanathan, *J. Am. Chem. Soc.* **2018**, 140, 13367–13374.
- [5] A. A. Anderson, T. Goetzen, S. A. Shackelford, S. Tsank, *Synth. Commun.* **2000**, 30, 3227–3232.
- [6] M. Traxler, S. Gisbertz, P. Pachfule, J. Schmidt, J. Roeser, S. Reischauer, J. Rabeah, B. Pieber, A. Thomas, *Angew. Chem. Int. Ed.* **2022**, 61, e202117738.
- [7] G. Kresse, J. Furthmüller, *Comput. Mater. Sci.* **1996**, 6, 15–50.
- [8] G. Kresse, J. Furthmüller, *Phys. Rev. B - Condens. Matter Mater. Phys.* **1996**, 54, 11169–11186.
- [9] J. P. Perdew, K. Burke, M. Ernzerhof, *Phys. Rev. Lett.* **1996**, 77, 3865–3868.
- [10] S. Grimme, J. Antony, S. Ehrlich, H. Krieg, *J. Chem. Phys.* **2010**, 132, 154104.
- [11] S. Grimme, S. Ehrlich, L. Goerigk, *J. Comput. Chem.* **2011**, 32, 1456–1465.
- [12] P. E. Blöchl, *Phys. Rev. B* **1994**, 50, 17953–17979.
- [13] G. Kresse, D. Joubert, *Phys. Rev. B - Condens. Matter Mater. Phys.* **1999**, 59, 1758–1775.
- [14] J. Heyd, G. E. Scuseria, M. Ernzerhof, *J. Chem. Phys.* **2003**, 118, 8207–8215.
- [15] J. Heyd, G. E. Scuseria, M. Ernzerhof, *J. Chem. Phys.* **2006**, 124, 219906.
- [16] F. Neese, *WIREs Comput. Mol. Sci.* **2012**, 2, 73–78.
- [17] F. Weigend, R. Ahlrichs, *Phys. Chem. Chem. Phys.* **2005**, 7, 3297–3305.
- [18] T. Yanai, D. P. Tew, N. C. Handy, *Chem. Phys. Lett.* **2004**, 393, 51–57.
- [19] P. J. Stephens, F. J. Devlin, C. F. Chabalowski, M. J. Frisch, *J. Phys. Chem.* **1994**, 98, 11623–11627.
- [20] A. D. Becke, *J. Chem. Phys.* **1993**, 98, 5648–5652.
- [21] C. Lee, W. Yang, R. G. Parr, *Phys. Rev. B* **1988**, 37, 785–789.
- [22] E. Runge, E. K. U. Gross, *Phys. Rev. Lett.* **1984**, 52, 997–1000.
- [23] J. I. Higham, J. A. Bull, *Chem. Commun.* **2020**, 56, 4587–4590.

S11. Author Contributions

M.T. and S.R. contributed equally to this work and either has the right to list them self first in bibliographic documents. All authors contributed extensively to the work presented in this paper. M.T., S.R., B.P. and A.T. conceived the research project. M.T. conducted the synthesis of linkers as well as COFs and performed characterizations. S.R. evaluated the COFs in cross-couplings. S.V. performed and evaluated the XPS analyses. J. Roeser was responsible for simulations of the COFs. J. Rabeah carried out EPR analyses. C.P. and P.S. conducted theoretical calculations. M.T. and S.R. wrote the manuscript with the input from all authors.

S12. Copies of NMR spectra



S48

